DEVELOPMENT OF HETEROGENEOUS CATALYSTS FOR LIQUID PHASE HYDROXYALKYLATION AND OXIDATION OF PHENOLIC COMPOUNDS

A THESIS SUBMITTED TO THE

UNIVERSITY OF PUNE

FOR THE DEGREE OF DOCTOR OF PHILOSOPHY

IN CHEMISTRY

BY

AJAY JHA

RESEARCH GUIDE

DR. CHANDRASHEKHAR V. RODE

CHEMICAL ENGINEERING AND PROCESS DEVELOPMENT DIVISION

CSIR–NATIONAL CHEMICAL LABORATORY

PUNE- 411 008, INDIA

DECEMBER-2013

Certificate of the Guide

Certified that the work incorporated in the thesis entitled **"Development of heterogeneous catalysts for liquid phase hydroxyalkylation and oxidation of phenolic compounds"** submitted by **Mr. Ajay Jha** was carried out by the candidate under my supervision/guidance. Such material as has been obtained from other sources has been duly acknowledged in the thesis.

December, 2013

Dr. Chandrashekhar V. Rode
(Research Guide)

Declaration by the Candidate

I declare that the thesis entitled **"Development of heterogeneous catalysts for liquid phase hydroxyalkylation and oxidation of phenolic compounds"** submitted by me for the degree of Doctor of Philosophy is the record of work carried out by me during the period from 29-09-2010 to 31-08-2013 under the guidance of **Dr. C. V. Rode** and has not formed the basis for the award of any degree, diploma, associateship, fellowship, titles in this or any other University or other institution of Higher learning.

I further declare that the material obtained from other sources has been duly acknowledged in the thesis.

December, 2013 Ajay Jha

CSIR-National Chemical Laboratory,
Pune-411008

Dedicated to my beloved Parents and Wife…

Acknowledgement

I wish to express my sincere gratitude to my research guide, ***Dr. C. V. Rode****, Chief Scientist, Chemical Engineering and Process Development Division, CSIR-National Chemical Laboratory (NCL), Pune, for introducing me to the interesting research field of catalysis. His constant support, invaluable guidance, numerous discussions, constructive suggestions and encouragement throughout the course of this work enabled me to complete this thesis. He has been a constant source of inspiration to me during my stay at NCL. His enthusiastic attitude, innovative ideas, and scientific knowledge have inspired me profoundly. I will be remaining ever grateful to him for his teaching, guidance, and wonderful personality. It has been an intellectually stimulating and rewarding experience to work with him.*

I would like to thank former head of the Chemical Engineering and Process Development Division, Dr. B. D. Kulkarni, and Dr. V. V. Ranade, the present Chair of CEPD Division, for providing me all the divisional facilities required for my research work.

I would like to thank Dr. S. Sivaram (former Director) and Dr. S. Pal, Director, CSIR-NCL, Pune, for allowing me to carry out research and providing all infrastructural facilities at CSIR-NCL. I am grateful to Council of Scientific and Industrial Research (CSIR), New Delhi for awarding me the Junior Research Fellowship.

I would like to thank Dr. R. C. Chikate of Abasaheb Garware College, Pune for very useful scientific discussions during the period of my research.

I take this opportunity to express my deepest sense of gratitude towards Dr. K. R. Patil, Dr. C. S. Gopinath, Dr. P. N. Joshi, Dr. D. Srinivas, Dr. P. A. Joy, and Dr. (Mrs.) Mayadevi, scientists at CSIR-NCL for their timely help, constant support, and valuable guidance.

I also wish to thank my seniors and my friends, Dr. Indresh, Dr. Vikas, Dr. Ajit, Dr. Jayprakash, Dr. Anand, Dr. Jitendre, Dr. Anuj, Vivek, Amol, Narayan, Ms. Rasika, Ms. Mandakini, Ms. Dattakumar, Sachin, Sumit, Rajan, Ms. Sarada, Mrs. Aparna, Ms. Shobha, Rameshwar, Atul, Tejawansh, Ajay G., Pravin, Bhogesh, Joby, Unni, and all

other research scholars and friends in NCL who are not named in person, for their valuable suggestions and helping hand.

I owe my special thanks to all scientific and non scientific staff of NCL. I would like to thank Mr. R. K. Jha, Mrs. Rupali Waichal, Mr. Raheja, Mr. Patane, Mr. Kamble, Mr. Dure, and Mr. Shinde, for their help and cooperation in completing my research work successfully.

Words are not enough to express my love and gratitude to my family members. It gives me great pleasure to thanks my parents. Thanks to my dear wife for being patient and supportive all the time particularly during the stage of thesis writing.

Ajay Jha

List of Contents

Section A

List of Tables of Section A

List of Tables of Section B

List of Schemes of Section A

List of schemes of Section B

List of Figures of Section A

List of Figures of Section B

Chapter 1

Abbreviations

BET	Brunauer-Emmett-Teller
BJH	Barrett-Joyner-Halenda
B/L ratio	Brönsted to Lewis acid sites ratio
BPA	Bisphenol A
CP	Co-precipitation
DAM	2, 2'-methylenebis (4-methylphenol)
DTA	Differential thermal analysis
FT-IR	Fourier- transform infrared spectroscopy
FWHM	Full width at half maximum
GC	Gas chromatography
r-GO	Reduced graphene oxide
GO	Graphite oxide
$H_3PW_{12}O_{40}$ / DTP	Dodecatungstophosphoric acid
HBA	Hydroxybenzyl alcohol
HPA	Heteropolyacids
HPLC	High performance liquid chromatography
HT	High temperature
LT	Low temperature
Mont K10	Montmorillonite K10
MO	Mixed oxides
MPTMS	Mercaptopropyltrimethoxysilane
NMR	Nuclear magnetic resonance
PHBAld	*p*-Hydroxybenzaldehyde
PHBAcid	*p*-Hydroxybenzoic acid
PHBAlc	*p*-Hydroxybenzyl alcohol
PTA (PWA)	Phosphotungstic acid
S_{BET}	BET surface area
SEM	Scanning electron microscopy
SPM	Silica bound magnetite

ST	Solvothermal
TG	Thermogravimetry
TPD	Temperature programmed desorption
TPR	Temperature programmed reduction
TEOS	Tetraethylorthosilicate
XPS	X-ray photoelectron spectroscopy

ABSTRACT OF THESIS

Development of heterogeneous catalysts for liquid phase hydroxyalkylation and oxidation of phenolic compounds

Introduction

Development of tailor made solid catalysts for industrially important reactions is an active area of research in heterogeneous catalysis. In this PhD work two such reactions chosen were hydroxyalkylation of phenolic compounds with aldehyde or ketone for the production of drugs, polymers and food additives and liquid phase oxidations of side chain alkyl groups of phenols [1]. The major objective of the present thesis work was to develop variety of solid acid catalysts involving phosphotungstic acid (PTA) impregnated on different supports like MCM-41 and montmorillonite for hydroxyalkylation of phenol with phthalic anhydride to give phenolphthalein [2]. Further, sulfonic acid grafted magnetically separable solid acid catalyst was developed for hydroxyalkylation of guaiacol to give selectively vanillin alcohol. metal cations exchanged montmorillonite clay as a solid acid catalyst was also developed for *p*-cresol hydroxyalkylation to give 2, 2'-methylenebis (4-methylphenol) [DAM]. For oxidation of vanillyl alcohol various supported and unsupported spinel oxide like Co_3O_4, Mn_3O_4 $CoMn_2O_4$ as catalysts were developed. These spinel oxides catalysts were also tested for oxidation of *p*-cresol into corresponding aldehyde products which is extensively used in flavour/fragrance, food, pharmaceuticals and polymer additives. The major emphasis of the thesis is on interpretation of the observed activity results based on the characterization data obtained by using various techniques such as BET, NH_3-TPD, FTIR, pyridine IR, XRD, XPS, EDX, SEM, and by cyclic voltammetry. Optimization of reaction conditions was also carried out for the best catalysts for all the reactions studied in this work.

The thesis has been divided into two sections: Section A deals with the hydroxyalkylation and Section B deals with oxidation of phenolic compounds. **Chapter 1** of section A

provides a brief introduction to catalysis and the role of catalysts to develop industrially benign processes. It also includes general introduction to the hydroxyalkylation reactions, types of solid acid catalysts used for hydroxyalkylation of phenol and phenolic derivative compounds, summary of literature on hydroxyalkylation of phenolic compounds. At the end of this chapter, scope and objectives of sections A and B are given. **Chapter 2** includes detailed experimental procedures used for preparation of various solid acid and metal oxide catalysts, their characterization and activity testing protocol for hydroxyalkylation and oxidation of phenolic compounds. **Chapter 3** discusses the results of activity of different solid acid catalysts viz. PTA supported on MCM-41 for phenol hydroxyalkylation with phthalic anhydride to give phenolphthalein. Guaiacol hydroxyalkylation was studied over the propyl sulfonic acid grafted on silica coated magnetite catalyst. It has been found that the catalyst was more selective for vanillyl alcohol synthesis (57%) than PTA supported on silica and montmorillonite catalysts. The highest selectivity of the catalyst was due to the presence of bulkier acid group over the catalyst surface, which did not allows the further reaction of hydroxyalkylated product to the starting materials to give other byproduct. Hydroxyalkylation of *p*-cresol was studied over metal cation exchanged montmorillonite catalysts. It was found that the activity of these catalysts was in accordance with the increase in acidity of parent montmorillonite after the exchange of cations in the order of Zn^{2+}, Fe^{3+} and Al^{3+}. Among these metal cations exchanged catalysts, Al-montmorillonite showed 51 % conversion of *p*-cresol with 98% selectivity to the DAM [3].

In section B, Chapter 1 provides a general introduction to the oxidation reactions and their importance to develop industrially valuable products and types of solid catalysts used for the oxidation of side chain of phenolic compounds. A summary of literature on oxidation of phenol substituted derivatives using homogeneous and heterogeneous catalysts is also given. **Chapter 2** includes detailed experimental results and discussion of vanillyl alcohol, veratryl alcohol and *p*-cresol oxidation carried out by using different supported and unsupported metal oxide catalysts. Spinel Co_3O_4 nanoparticles prepared by solvothermal method having the particle size in the range of 12-20 nm exhibited excellent activity for the liquid phase aerobic oxidation of vanillyl alcohol with 80% conversion

and 98% selectivity to vanillin [4]. Further, we developed Mn doped Co_3O_4 catalyst and tested for aerobic oxidation of vanillyl alcohol in the absence of NaOH. The catalyst showed excellent activity and gave 63% conversion of vanillyl alcohol with 83% selectivity to vanillin in 2 h. Catalyst characterization results showed that prepared catalyst having teragonal phase of $CoMn_2O_4$ which was found to be more active and selective for vanillin alcohol oxidation than Co_3O_4 and Mn_3O_4 spinel [5]. As we observed mixed oxides catalysts has higher activity than the single metal Co_3O_4 and Mn_3O_4 oxide, further we developed mixed metal oxide catalyst supported on the reduced graphene oxide for vanillyl alcohol oxidation in the absence of a base. The same catalyst was found to catalyze efficiently *p*-cresol oxidation in the presence of a base with >72% product yield and 96% selectivity to the corresponding aldehyde. The detailed characterization results on morphology, size and structure of the prepared graphene oxide supported MnCo nanoparticles obtained by XRD, FT–IR, H_2–TPR, HR–TEM and cyclic voltammetry technique were used to understand the role of Mn and Co species in directing the selectivity towards *p*–hydroxybenzaldehyde.

Chapter 3 summarizes the work presented in sections A and B and general conclusions arrived from the discussed results.

References

1. A. C. Garade, V. S. Kshirsagar, R. B. Mane, A. A. Ghalwadkar, U. D. Joshi, C. V. Rode, *Appl. Clay Sci.* 2010, 48, 164.
2. A.Jha, A. C. Garade, C. V. Rode, *Ind. Eng. Chem. Res.* 2012, 51, 3916.
3. A. Jha, A.C. Garade, M. Shirai, C.V. Rode, *Appl. Clay Sci.* 2013, 74, 141.
4. A. Jha, C.V. Rode, *New. J. Chem.*2013, 37, 2669.
5. A. Jha, K. R. Patil, C. V. Rode, *ChemPlusChem* 2013, 78, 1384.

Section A

Hydroxyalkylation of phenolic compounds

Chapter 1

Introduction

This thesis is divided into two sections: Section A, deals with the hydroxyalkylation and Section B, deals with oxidation of phenolic compounds. This Chapter presents the general introduction to the subject area of catalysis and is particular to the hydroxyalkylation reaction of phenols and solid acid catalysts. Introduction to the catalytic liquid phase oxidation is given under Section B. However, the objective and scope of the work of both the sections is included at the end of this Chapter.

1.1. CATALYSIS

A substance which changes the kinetics of the reaction, but does not change the thermodynamics is called as catalyst and the whole process is known as catalysis. The term "catalysis" was first introduced by Berzelius in 1835 [1]. Catalysis is principally divided in two branches: (i) homogeneous catalysis, when the catalyst is in the same phase as of the reactant, and (ii) heterogeneous catalysis, when the catalyst is in a phase different from that of the reactant (typically solid/liquid, solid/gas or solid/liquid/gas). Table 1.1 summarizes a comparison between the main features of homogeneous and heterogeneous catalysis.

Table 1.1. Comparison between homogeneous and heterogeneous catalysis

Feature	**Homogeneous Catalyst**	**Heterogeneous Catalyst**
Form	metal complex	solid, often metal or metal complex
Activity	high	variable
Selectivity	high	variable
Reaction conditions	mild	drastic
Average time-life	variable	long
Sensitivity to poison	low	high
Problems of diffusion	none	possible
Recycling	difficult (and expansive)	easy
Separation from products	difficult	easy
Variation of steric and electronic feature	possible	difficult
Intelligibility of the mechanism	possible	difficult

One of the main advantages of homogeneous molecular catalysts is that their active sites are spatially well separated from one another, just as they are in enzymes. Because of such spatial separation and the self-similarity of the structures of the sites, there is a constant energetic interaction between each active site and the substrate.

Heterogeneous catalysis has a major role in the development of sustainable industrial processes, as it potentially possesses the ability to achieve the objectives of industrial catalysis, while paying attention to the principles of sustainable and green chemistry [2]. Easy separation, easy recovery, no problems in solubility and miscibility are the strengths of a heterogeneous system in order to reduce the cost of production and to set up environmentally benign processes. Heterogeneous catalysis is quite prevalent in the chemical industry, and affects our everyday life in many ways. Over 90% of all chemical manufacturing is based or relies heavily on catalytic processes and by some estimates, catalysis contributes to approximately 35% of the world's gross domestic product (GDP) [3]. Earlier, the main focus of the industry was to enhance the kinetics of the reactions. However in recent years, the trends get changed and there is a practice not only to promote a given desired conversion but also to avoid any undesirable side reactions. This is required to improve reaction yields, to simplify the overall manufacturing process, to eliminate expensive product separation steps and to minimize the generation of potentially polluting byproducts [4, 5]. Many kinds of organic reactions such as hydroxyalkylation, oxidation, hydrogenation, alkylation, etherification, cracking, dehydration, condensation, hydration, oligomerisation, esterification, isomerisation and disproportionation play a vital role for making industrially important products. For my PhD work, I studied heterogeneously catalyzed hydroxyalkylation and oxidation reactions of side chain of phenolic compounds.

1.2. HYDROXYALKYLATION

Hydroxyalkylation reaction belongs to the class of Friedel Craft reaction, which involves the condensation of aldehyde or ketones with aromatic compounds in the presence of an acid catalyst. The reaction is aimed at the introduction of one hydroxyalkyl group on the aromatic ring. The favorable condition for the reaction is that aromatic ring should have electron donating groups like $–OCH_3$ or –OH while, carbonyl compounds should possess electron attracting groups like $–NO_2$ or –CN. The general scheme for the hydroxyalkylation of aromatic compounds in presence of acidic catalysts/reagents is presented in Scheme 1.1.

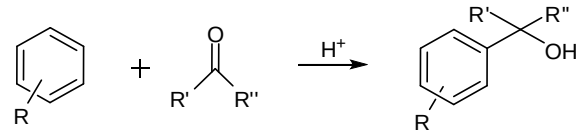

R= -OH, OCH_3
R', R'' = -H, $-NO_2$, $-CH_3$

Scheme 1.1. Hydroxyalkylation of activated arene

In the hydroxyalkylation reaction, aldehyde or ketone reacts with an aromatic compound to form an intermediate, hydroxybenzyl alcohol. The reaction usually does not stop at this stage and hydroxybenzyl alcohol which is formed initially, reacts further with another molecule of aromatic compound to give diarylmethane. (Scheme 1.2)

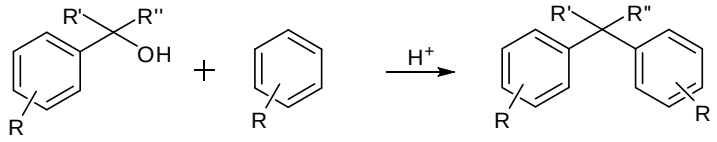

Scheme 1.2. Hydroxyalkylation of intermediate of scheme 1.1

Products obtained from hydroxyalkylation reaction are of great commercial importance and widely used as chemical intermediates in drugs, polymer, pharmaceutical and food industries. Saligenol, an intermediate in the synthesis of a variety of products, and particularly a key intermediate in the preparation of coumarin [6], an important perfume base (scheme 1.3), is the best example of the industrial application of hydroxyalkylation reaction.

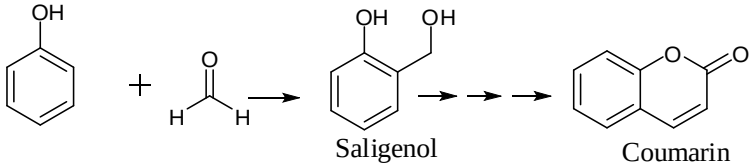

Scheme 1.3. Hydroxyalkylation of phenol

The hydroxyalkylation reaction is difficult to perform with high activity and selectivity. Firstly, because the ketone or aldehyde is a mild electrophile and aromatic ring must be

activated. Secondly, substitution generally leads to a variety of substituted sites (particularly, *ortho*, *para*-selectivity for activated aromatic compounds), and last but not the least, consecutive reactions are often observed. However, by using specially designed heterogeneous catalysts, it is possible to favor desired reaction over the others.

Phenolphthalein is a hydroxyalkylation product obtained by condensation of phenol and phthalic anhydride, having wide ranging applications in polymer industry to make polycarbonates, polyester, and poly (arylene ether) [7]. An additional advantage of phenolphthalein as a polymer backbone is that the heterocyclic pendant lactone provides chemically reactive sites for further derivatization or grafting suitable reactive moieties for making functional polymeric materials. Currently, multiblock poly (arylene ether sulfone) copolymers based on phenolphthalein are used in proton exchange membranes in fuel cell technology [8].

Polycarbonate sheets Polyester Proton-exchange membrane

Fig.1.1. Applications of phenolphthalein in polymer industry

As reported in 1997, only one company produced phenolphthalein in the United States, with an annual production of 250 tons. In 2009, phenolphthalein was produced by eight manufacturers worldwide, including one each in the United States and China and six in India (SRI 2009), and was available from 57 suppliers, including 34 U.S. suppliers (ChemSources 2009) [9]. The available processes for phenolphthalein synthesis based on the use of liquid mineral acids are energy intensive due to tedious separation and recovery steps for pure products from the reaction medium [10]. Due to immense commercial importance of phenolphthalein, developing cheaper and eco-friendly routes for its synthesis are of great practical importance. For my PhD work, I have prepared

phosphotungustic acid supported on MCM−41 as a solid acid catalyst and used it for phenolphthalein synthesis. The details of catalyst preparation and activity results are described in chapters 2 and 3 of Section A.

Another industrially important chemical compound synthesized by the hydroxyalkylation of guaiacol with formaldehyde is vanillyl alcohol, which on oxidation produced vanillin, widely used as a flavoring and fragrance agent in pharmaceutical and food industries.

Fig. 1.2. Applications of vanillin in fragrance, flavor and drugs

Among various flavoring and fragrance agents, *p*-vanillin, *p*-hydroxybenzaldehyde (PHBAld) and benzophenone derivatives are well known and commonly used in consumer products. Due to the high production cost (Table 1.2) from natural resources, these compounds are generally prepared by chemical processes e.g. the cost of vanillin extracted from vanilla pods has increased up to $1200 per kilo in 2001, in contrast to the price of synthetic vanillin, stable at < $15 per kilo [11, 12]. Global demand for synthetic vanillin is 16000 tons/year. Out of this huge demand of vanillin, only 0.2% is obtained from natural resources, 15% from delignification process and the major demand is full-filled by the synthetic route (85%). At the industrial level, guaiacol hydroxyalkylation reactions are catalyzed by Lewis-type acids, such as $AlCl_3$, and by mineral Brönsted acids, as well as by bases. Some papers have appeared in recent years, where zeolitic materials are described as catalysts for this reaction [13-15]. However, major problem associated with these catalysts is their deactivation due to deposition of bulky and higher molecular weight condensation products formed during the progress of the reaction.

Another important class of chemical compounds synthesized by the hydroxyalkylation of phenols with formaldehyde, is bisphenols also known as dihydroxydiarylmethane (DAM) which are widely used as antioxidants and chemical intermediates for the preparation of epoxide resins and polycarbonate in polymer industries [16-18]. Bisphenols are mainly produced in Japan, and its production (e.g. bisphenol F) is estimated to be about 3000 metric tons per year [19]. The most important bisphenols other than bisphenol F are bisphenol A and bisphenol Z which are produced by condensation of phenol with acetone and cyclohexanone, respectively. World capacity of bisphenol A is 2.67 million metric tons (2001) and four main global producers are, General Electric (25% of world installed capacity), Bayer (16% of world installed capacity), Shell (12% of world installed capacity) and Dow Chemical Corp. (10% of world installed capacity) [20]. The worldwide production of bisphenol Z is about 1360 metric tons per year [21] which is widely used for production of polycarbonate film. [22]

Polycarbonate sheets Epoxy-resin adhesive

Fig. 1.3. Applications of bisphenol in polymer industry

1.2.1. Conventional routes for hydroxyalkylation reaction

Hydroxyalkylation processes are conventionally carried out using strong mineral acids (HCl, HF, H_2SO_4, H_3PO_4 etc.) as well as bases (e.g. teramethylammonium hydroxide). Some of the industrially important products derived from the hydroxyalkylation of phenol using conventional reagents are summarized in Table 1.2.

Table 1.2. Industrially important products derived from hydroxyalkylation of phenol

Aromatic	Aldehyde/ Ketone	Product (s)	Reagents	Industry
Phenol Guaiacol	Formaldehyde	Hydroxybenzyl alcohol Vanillyl alcohol	Quarternary ammonium salt NaOH	The Dow Chemical Company, USA [23]; Mitsubishi Petrochemical Company Ltd., Japan [24]
Phenol	Formaldehyde	Bisphenol F	HCl, H_2SO_4 or Oxalic acid	Dainippon Ink & Chemicals, Japan [25]
Phenol	Acetone	Bisphenol A	HCl	Mitsui Toatsu Chemicals, Inc., Japan [26]
Phenol	Cyclohexa-none	Bisphenol Z	HCl or H_2SO_4	Maruzen Oil Co., Ltd., Japan [27]

Although, these reagent based processes give acceptable yields of the desired product, still they suffer from some serious drawbacks like:

i. Use of the reagents in stoichiometric or even excess quantities creating serious environmental problems.
ii. Difficulties in the separation and recovery of pure product from the reaction crude.
iii. The product in reagent-based process is isolated by hydrolysis of the complex; hence recyclability of the reagent is impossible.
iv. Formation of large amounts of corrosive waste streams due to hydrolysis of the complex.
v. Difficulties of handling of reagents due to their corrosive nature and toxicity.

The major challenges in this area are the development of cost-effective, highly active, selective and stable solid acid replacements. Presently, several conventional processes based on stoichiometric use of reagents are being replaced by solid acid catalysts in order to overcome the above mentioned drawbacks and in particular to improve the process

economics [28-30]. In total, there are 103 known industrial processes that use solid acid catalysts [31]. The types of catalysts used include zeolites, oxides, ion exchange resins, phosphates, clays, complex oxides, heteropolyacids, and sulfated zirconia.

1.3. SOLID ACID CATALYSTS

Solid acid catalysts are the materials which exhibit the Brönsted and/or Lewis acidity and can be used as an alternative to or as a replacement for homogeneous (liquid) acid catalysts and have the following advantages over conventional acid reagents:

1) Required in catalytic amount unlike mineral acids which are used in stoichiometric equivalent or in excess quantity
2) Easy separation and recovery from the reaction mixture
3) Reusability and lower toxicity
4) Higher selectivity to the desired product
5) Avoid formation of inorganic waste

In homogeneous media of hydroxyalkylation reaction, the final product is usually the bis-arylmethane (dimer), which corresponds to the reaction of the initially formed benzylic alcohol with another molecule of starting aromatic material. Heterogeneous catalysis offers the interesting possibility of avoiding these consecutive reactions. Mild acidic catalyst can be used, and tuning of the adsorption affinities of different moieties in the medium enables preferential adsorption of the starting material over the product, thus limiting consecutive reactions. The catalytic activity of solid acid catalysts mainly depends upon their acidic strength, type of acidity, acid site density which in turn depends upon the distribution of acidic sites over the surface of solid acid catalysts. In this work, three different solid acid catalysts were synthesized for hydroxyalkylation reaction of three different phenolic compounds viz. MCM-41 supported phosphotungstic acid [32], metal cations exchanged montmorillonite clay [33] and SO_3H–acid grafted silica bound magnetite catalysts. The important structural details of these catalysts are described below.

1.3.1. MCM-41 supported phosphotungstic acid

Phosphotungstic acid belongs to the class of heteropolyacids (HPAs) having Keggin structure. HPAs are mixed oxides composed of a central ion or 'heteroatom' generally P, As, Si, or Ge, bonded in a tetrahedral arrangement of oxygen atoms and surrounded by 12 MO_6 octahedra (M = Mo, W, V) arranged in four groups of three edge-sharing M_3O_{13} units.

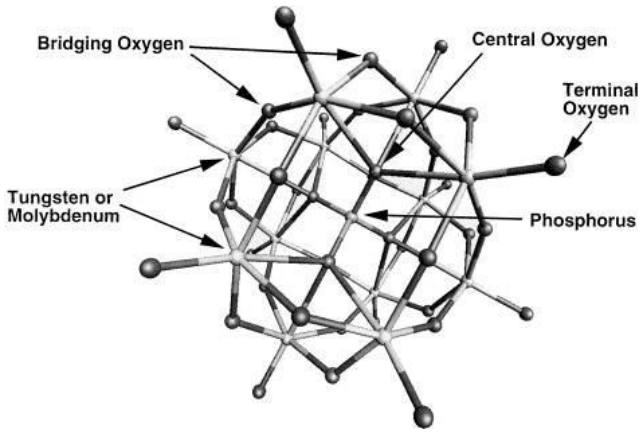

Fig. 1.4. The Keggin structure of heteropoly acid

There are four types of oxygen atoms found in the Keggin unit, the central oxygen atoms, two types of bridging oxygen atoms and terminal oxygen atoms. HPAs are much stronger acids than mineral acids (H_2SO_4, HBr, HCl, HNO_3, and $HClO_4$). Hence, they are also known as superacids. The super acidic nature of HPAs can be explained as follow: after losing one H^+, HPAs form heteropolyanions. Since in heteropolyanions, the negative charge is delocalized over much larger anions than those formed from mineral acids, the electrostatic interaction between proton and anion is much less for HPAs which facilitates the easy removal of protons and responsible for their super acidic nature. As for the acid strengths of heteropolyacids, the following order has been reported for the compounds in acetone: $H_3PW_{12}O_{40} > H_4S_{12}O_{40} \approx H_3PMo_{12}O_{40} > H_4PMo_{11}VO_{40} > H_4SiMo_{12}O_{40}$. HPAs, specifically phosphotungstic acid (PTA) catalyzed various industrially important organic reactions. Solid HPAs are pure Brönsted acids and stronger than many conventional solid acid catalysts such as mixed oxides and zeolites [34]. One important advantage of HPAs

is that they can be utilized both homogeneously and heterogeneously. The homogeneous reactions occur in polar media at ~100 ^{o}C; on the other hand, when using nonpolar solvents, the reactions proceed heterogeneously. The major problems associated with HPAs in the bulk form are (i) their low catalytic efficiency due to lower surface area (approximately 5m^2/g) having most of the acidic protons are in the interior of the solid, which are inaccessible for catalysis, (ii) rapid deactivation, and (iii) relatively poor stability in polar solvents such as water and ethanol. Attempts to improve the efficiency and stability of HPAs were made by using various supports including carbon [35], alumina [36], mesoporous aluminosilicates, [37] zirconia, [38] and mesoporous silica, [39]. Because of their basic nature, alumina and zirconia tend to decompose HPAs, resulting in deformation of the parent Keggin structure, thereby reducing the overall acidity. Supporting of HPAs on solid supports changes the acid strength and the structure of the aggregates. For the present study, MCM-41 was chosen as a support for PTA, since it is a mesoporous silica possessing very high surface area (>1000 m^2/g) and uniform large pore size (2−8 nm), which would allow the PTA acid cluster having ~1.2 nm diameter to be introduced inside the pores giving an excellent dispersion [40]. Formation of crystal phase was not seen even at PTA loadings as high as 40 wt% on MCM-41, which enables to develop catalysts with a wide range of PTA loadings necessary for excellent activity and shape selectivity in industrial applications e.g. liquid-phase phenol alkylation (Scheme 1.4) [41].

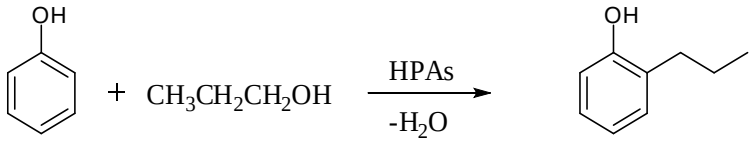

Scheme 1.4. Hydroxyalkylation of phenol

MCM-41 belongs to the class of M41S mesoporous molecular sieves, possesses a hexagonal array of uniform mesopores. These materials were developed originally by scientists at Mobil corporation, US. The general acid strength of these materials is speculated to be lower than some of the zeolitic materials. MCM-41 has been synthesized

with uniform channels varying from approximately 1.5 nm to >10 nm in size. The larger pore materials typically have surface areas >1000 m^2/g. A liquid crystal templating mechanism (LCT) in which surfactant liquid crystal structures serve as organic templates, has been also proposed for the formation of these materials. Like in zeolites, the framework of MCM-41 is based on an extensive three-dimensional network of oxygen ions that occupied tetrahedral cation sites, and in addition to the Si^{4+}, other cations can also occupy these sites. MCM-41 with bigger pore size can provide better mass transport than zeolites.

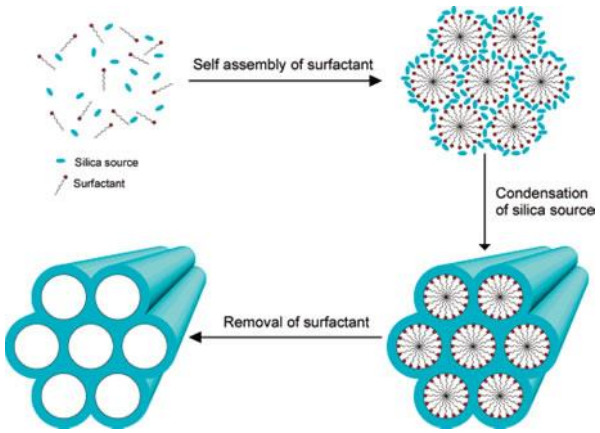

Fig. 1.5. Schematic presentation of MCM−41 synthesis

1.3.2. Metal cations exchanged montmorillonite clay

Clay minerals represent a convenient source to prepare potential solid acid catalysts because of their environmental compatibility, low cost and easy availability. Pillared and metal cation-exchanged clays with modified porosity, acidity and thermal stability have been explored for the wide range of acid catalyzed reactions [42- 44]. Montmorillonite is a member of the smectite clay family [45] and has 2:1 structure i.e. octahedral layer of Al or Mg is sandwiched between two tetrahedral layers of silicon coordinated with oxygen (TOT) [46] (Fig. 1.6). Montmorillonite clay could be dioctahedral or trioctahedral, based on the number of octahedral sites per unit cell occupied, which in turn depends essentially on the cations present (for example, Al^{3+} or Mg^{2+}) in the octahedral sheets. Replacing Si with Al, lead to a net negative charge over the layer of aluminosilicate,

which is balanced by hydrated cations (Na^+, K^+ or Ca^{2+}) in the interlayer spaces of montmorillonite clay [47].

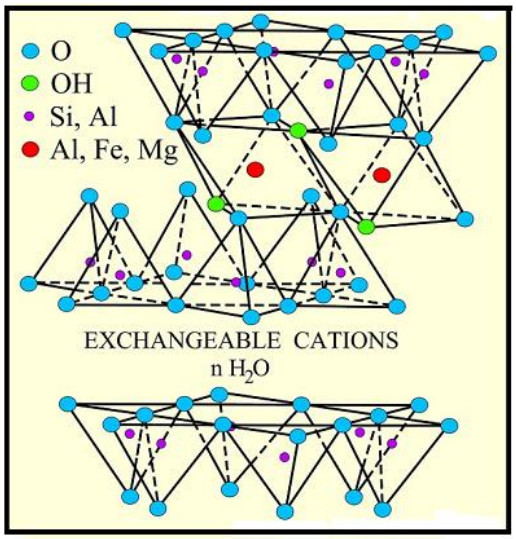

Fig. 1.6. Schematic presentation of montmorillonite clay structure

The most interesting features of the smectite clay are their intercalation, swelling and cation-exchange capacity which can improve the catalytic properties of smectite clay. Immersion in water results in a swelling of the clay and exposure of the intercalated cations making them accessible for cation-exchange. When smectite clay is immersed into the solution of metal cations, the suspended clay can freely exchange its interlayer cations for other metal cations in solution. The interlamellar cations are largely responsible for the clay's Brönsted and/or Lewis acidity [48]. Amount and strength of Brönsted and Lewis acidity can be enhanced by cation exchange or treatment with a mineral acid, e.g. H_2SO_4. Natural montmorillonite clay has limited activity. These clays are often acid activated by treatment with acids such as sulfuric acid. This results in a change in the textural properties of the clay such as surface area, porosity and the type and concentrations of the ions in the exchange sites. The acidity is due to either the free acid, e.g. in acid-treated clays, or the dissociation of water molecules in the interlayer. Acid treated clay like Mont K10 or KSF (from Sud-Chemie or Fluka, respectively) have been widely used as acid catalysts for Friedel−Crafts alkylation reaction (Scheme 1.5).

[49] Montmorillonite is also reported as an effective support for Lewis acids such as $ZnCl_2$ or $FeCl_3$ [50]. The substitution of exchangeable cations, by highly polarizing species of small radius such as aluminum, zinc or iron, results in the alteration of Brönsted and Lewis acid sites as well as clay architecture. For example, Al^{3+}-exchanged montmorillonite, is as active as concentrated sulfuric acid in promoting acid−catalyzed reactions (Scheme 1.5).

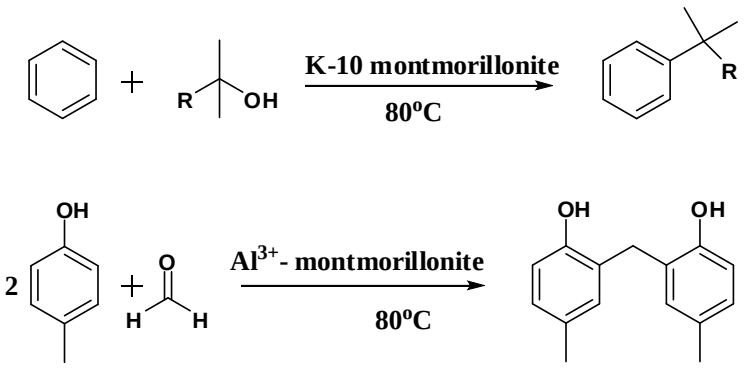

Scheme1.5. Friedel−Crafts reactions

1.3.3. SO_3H–acid grafted silica bound magnetite

Recovery and reuse of expensive catalysts after catalytic reactions are important factors for sustainable process development. Compared with conventional solid acids, magnetic solid acids can be separated more easily in presence of an external magnetic field, particularly in viscous or solid reaction mixtures. The most common method used for synthesis of magnetic solid acid catalysts is sulfonation of a mesoporous structure with a magnetic core, generally Fe_3O_4 [51]. Recently, magnetically separable materials have generated a significant research interest due to their potential technological applications in diverse fields such as electronics, life sciences as well as new generation catalysts mainly exploiting their inherent magnetic property for efficient recycling [52, 53]. This approach may prevent the agglomeration of the catalyst particles during recovery and can increase the durability of the catalysts. We have designed magnetically separable solid acid catalyst comprising organo sulfonic acid ($-CH_2CH_2CH_2SO_3H$) grafted on to the pore walls of mesoporous silica bound iron oxides (Fe_3O_4@MCM 41). The activity of the sulfonic acid functionalized catalyst was evaluated for guaiacol hydroxyalkylation

reaction. Iron oxides are themselves well known as catalysts. It is necessary to build up a strong barrier between the iron oxides and the molecular catalysts to circumvent unwanted interactions with molecular catalysts bound to the surface of the iron oxides. Coating of iron oxides with silica prevents particle aggregation. Furthermore, the presence of surface silanol groups allows surface functionalization with a variety of functional groups such as amino propyl, mercapto propyl, cyanopropyl, etc.

Guaiacol hydroxyalkylation has been carried out in the presence of formaldehyde (Scheme 1.6). When formaldehyde is one of the reactants, the main problem is the presence of water, since water leads to the deactivation of the acid sites and in fact, most solid acids lose their catalytic activity in aqueous solutions. The development of new water-tolerant solid acids is expected to minimize this problem.

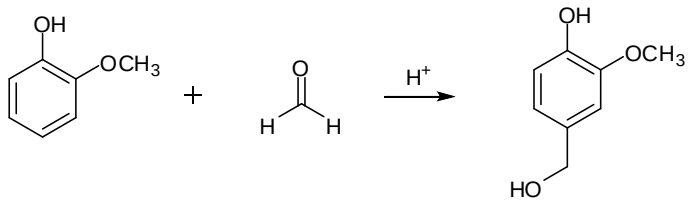

Scheme 1.6. Hydroxyalkylation of guaiacol

We have overcome this difficulty by designing solid acid catalysts comprising organo sulfonic acid ($-CH_2CH_2CH_2SO_3H$) grafted on to the pore walls of mesoporous silica bound magnetite. The as prepared catalyst was hydrophobic as well as acidic in nature. We found that the acidic proton in the hydrophobic environment of organo modified mesoporous silica was active for hydroxyalkylation of guaiacol. Since the catalyst possesses magnetic property, it could be quantitatively recovered by simply applying a strong magnetic field using a bar magnet (Fig. 1.7).

Two methods are commonly employed for grafting active molecules: i) covalent binding and, ii) simple adsorption of the active molecules. Covalent binding is preferred because it is generally sufficiently robust to survive the harsh reaction conditions, minimizes catalyst leaching and allows the catalyst to be reused several times.

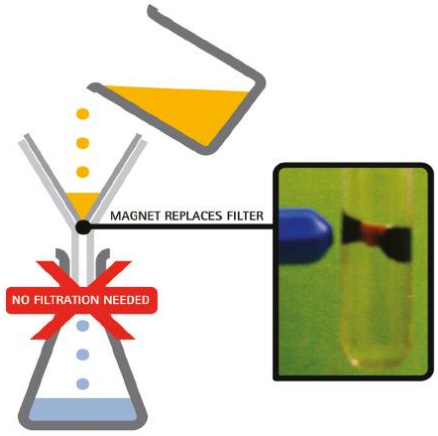

Fig. 1.7. Catalyst separation by magnetic field

1.4. LITERATURE SURVEY ON HYDROXYALKYLATION OF PHENOLIC COMPOUNDS

Several solid acid catalysts as well as reagents have been reported in the literature (Table 1.2) for the hydroxyalkylation reaction. In the past, mainly three mineral acids like HCl, H_2SO_4, H_3PO_4 have been reported for the hydroxyalkylation of phenolic compounds to give the corresponding products [54-57]. However, these reagents based processes suffer from serious drawbacks like strong corrosiveness, difficulties in separation from homogeneous reaction mixtures, toxicity and formation of huge amount of inorganic wastes as mentioned in section 1.2.1. Alternatively, solid acids including solid Brönsted acids (e.g., SO_3H functionalized carbon and polymers) in addition to solid Lewis acids (transition-metal (W, Zr, Nb) oxides) are easily separated from the reaction mixture and can be reused. Thus, solid acids have been used as catalysts to replace liquid mineral acids in several reactions. Furthermore, they can be designed to give higher activity, selectivity, and longer catalyst life. The first work on heterogeneous hydroxyalkylation was conducted by Venuto and Landis. [58] They worked on the hydroxyalkylation of the phenol with formaldehyde, benzaldehyde and acetone using HY zeolite at 180 ^{o}C. The major product was always the bis-arylmethane. In the eighties, Corma and then Van Backum [59] studied hydroxyalkylation of phenol, toluene and anisole with formaldehyde [60], acetaldehyde [61], benzaldehyde and acetophenone [62] at high

temperature (160 ^{o}C) using a variety of solid acid catalysts. The major product was always the bis-arylmethane adduct. At the end of the eighties, Mitsui Toatsu [63] claimed synthesis of *para*-hydroxymethyl phenol from phenol and trioxane using the H^+ type Y zeolite at 160 ^{o}C for 3 h to give 65% conversion of trioxane and 88% *para*-hydroxymethylphenol selectivity. Among these catalysts, ion exchange resins play an important role for the hydroxyalkylation of phenol. Inaba et al. reported Lewatit SC-102 ion exchange resin which showed 96% conversion of acetone with 85% selectivity to bisphenol A [64] while sulfonated styrene ion exchange resin was reported by Faler and Loucks which showed 66% conversion of acetone with 99% selectivity to bisphenol A [65]. Several other ion exchange resin catalysts were also reported for hydroxyalkylation of phenols such as sulfonic acid-type cation exchange resin (Diaion SK104) along with 3-pyridinemethanethiol which showed higher activity giving 93% conversion of acetone with 95% selectivity to bisphenol A [66]. Polysiloxane catalyst having $–SO_3H$ group showed 88% conversion of acetone with 96% selectivity to bisphenol A for the hydroxyalkylation of phenol with acetone [67]. Although these ion exchange resin catalysts showed better activity, they suffer from major disadvantages like thermal instability and reusability. Another important class of catalysts, i.e. zeolites were also used for hydroxyalkylation of various phenolic compounds. Alvaro et al. reported USY-zeolite which gave 47% yield of diphenylmethane [68] while protonic zeolites like MOR, MFI and BEA were reported by Barthel *et al.* which showed 46% total product yield with 57% selectivity to diarylmethane [69]. ZSM-5 catalyst showed 40% total product yield with 90% selectivity to bisphenol F [70] for the hydroxyalkylation of phenol to give bisphenol F. β-type zeolite for hydroxyalkylation of phenol gave selectivity to bisphenol F as high as 99% with 95% conversion of formaldehyde in hydroxyalkylation of phenol [71]. Perego and De Angelis reported HSH-320 HUA zeolite with modified acidity by varying Si/Al ratio which showed 90% conversion of acetone and 60% selectivity to bisphenol A [72]. For bisphenol A formation, the same group of Perego *et al.* reported amorphous aluminosilcate which gave 72% conversion of acetone with 62% selectivity to bisphenol A [73]. Various other zeolites like Al:MCM-41 and H-β have been reported by Jana *et al.* for bisphenol F with 91% selectivity and 34 and 68% product yield

respectively [74, 75]. Cavani *et al.* studied another industrially important hydroxyalkylation reaction of guaiacol to vanillyl alcohol (VAlc), by varying Si/Al ratio in H-mordenite catalysts [76, 77]. They found that the highest selectivity of 60-70% to vanillyl alcohol could be achieved for an optimum Si/Al ratio of 23. Corma *et al.* reported layered zeolite ITQ-2 catalyst comprising balanced combination of acidity and strength as the highly active and selective catalyst (100% conversion of paraformaldehyde with 91% selectivity to diarylmethane) for the hydroxyalkylation of bis-1, 1′-(2-methoxy-naphthyl) methane with paraformaldehyde to give diarylmethane [78].

In case of heteropolyacid supported catalysts, Udayakumar *et al.* reported 30% HPA/MCM-41 catalyst for hydroxyalkylation of phenol which gave 34% yield of dihydroxy-diarylmethane [79]. Yadav and Kirthivasan have reported HPA-K10 catalysts for hydroxyalkylation of phenol to give bisphenol A with 23% conversion of phenol and 60% selectivity to bisphenol A [80]. Garade *et al.* studied HPA loading in the range of 10-40% on various supports like fumed silica, Mont K10, Mont KSF/O and bentonite clay and tested catalytic activity for *p*-cresol hydroxyalkylation. Among these, 20% HPA supported on bentonite gave 95% product yield with 94% selectivity to 2, 2′-methylenebis (4-methylphenol), DAM [81-85].

Since, heteropolyacid based solid catalysts are not much explored for the hydroxyalkylation of phenol due to their low surface area (5-8 m^2/g) and high solubility in polar solvent, the present work is undertaken to improve activity and reusability of heteropolyacids by impregnating them on appropriate supports. In this thesis, three different solid acid catalysts were prepared with tuned acidity and strength suitable for hydroxyalkylation of phenol and its derivatives under mild reaction conditions.

Table 1.3. Summary of the literature for the hydroxyalkylation of phenols

Sr. No	Catalyst/ Reagent	Reactant	Product	Reaction Conditions	Yield/ Conv. (%)	Product Sel. (%)	Ref.
1	HCl	Phenol, Acetone, 15% MeSNa solution	Bisphenol A	323 K	11 (DY)	-	54
2	Conc. HCl	Phenol, Acetone	Bisphenol A	318 K; 2 h	9 (TPY)	98	55
3	H_2SO_4, HCl	Phenol, Acetone	Bisphenol A	333 K; 10 min	87 (AC)	92	56
4	Phosphoric acid	Phenol, Formald-ehyde	Bisphenol F	323-353 K; P to F mole ratio, 6-50	91 (DY)	91	57
5	Acidic ion exchange resin (Lewatit SC-102)	Phenol, Acetone	Bisphenol A	358 K; 8 h	96 (AC)	85	64
6	Sulfonated styrene ion exchange resin	Phenol, Acetone	Bisphenol A	348 K; 1 h	66 (AC)	99	65
7	Sulfonic acid-type cation exchange resin (Diaion SK104) along with 3-Pyridinemeth-anethiol	Phenol, Acetone	Bisphenol A	358 K; 1h	93 (AC)	95	66

8	Polysiloxane catalyst having –SO_3H group	Phenol, Acetone	Bisphenol A	348 K; 24 h	88 (AC)	96	67
9	USY zeolite (Si/Al= 17.5)	Benzene/ Anisole/ N,N-Dimethyl aniline, Benzalde-hyde	Diphenyl methane	383-423 K; 8 h	47 (DY)	-	68
10	Protonic Zeolites (Y-FAU, MOR, MFI & BEA)	Anisole, Chloral	Diaryl methane	323 K; 8 h	46 (TPY)	57	69
11	ZSM-5	Phenol (85),40% Formald-ehyde	Bisphenol F	393 K; 4 h	40 (TPY)	90	70
12	β-type zeolite	Phenol, Formald-ehyde	Bisphenol F	393 K; 4 h	95 (FC)	99	71
13	Zeolite (Toyosoda HSH-320 HUA)	Phenol (100), Acetone (20)	Bisphenol A	453 K;P to A mole ratio, 5; 12 h	90 (AC)	60	72
14	Amorphous aluminosili-cate	Phenol, Acetone	Bisphenol A	423 K; P to A mole ratio, 5; 6 h	72 (AC)	62	73
15	H-β-zeolite (Si/Al=75)	Phenol, Formald-ehyde	Bisphenol F	363 K; P to F mole ratio, 30; 15 min	68 (TPY)	91	74
16	Al:MCM-41 (Si/Al=70)	Phenol, Formald-ehyde	Bisphenol F	363 K; P to F mole ratio, 30; 15 min	34 (TPY)	91	75

17	H-mordenite (Si/Al=23)	Guaiacol, Formald-hyde	VAlc	353 K; 2 h	41 (GC)	70	76
18	H-mordenite (Si/Al=23)	Guaiacol, Formald-ehyde	VAlc	338 K; 2 h	41 (GC)	70	77
19	ITQ-2	Bis-1,1'-(2-methoxy-naphthyl) methane (5), Paraform-aldehyde	Diaryl methane	323 K; 24 h	100 (PFC)	91	78
20	HPA/Si-MCM-41	Phenol, Benzald-ehyde	DAM	393 K; PH/ ALD mole ratio, 3; 3h	34 (DY)	-	79
21	DTP-K10	Phenol, Acetone	Bisphenol A	408 K; P to A mole ratio, 5; 4 h	23 (AC)	60	80
22	Mont KSF/O	*p*-cresol, Formald-ehyde	2,2'-methyleneb is-(4-methylphen ol)	343 K; PC to F mole ratio,5;flow rate, 3 mL/h	26 (PCC)	91	81
23	20% DTP/SiO_2	Phenol, Formald-ehyde	Bisphenol F	353 K; P to F mole ratio, 5; 1 h	34 (TPY)	90	82
24	20% DTP/Mont K10	Phenol, Formald-ehyde	Bisphenol F	353 K; P to F mole ratio, 5; 1 h	28 (PC)	90	83
25	20% DTP/Bento-nite	*p*-cresol, Formald-ehyde	2,2'-Methylene bis-(4-methylp-henol)	353 K; PC to F mole ratio,5; 1 h	95 (TPY)	94	84

26	Sn/Si-MCM-41	*p*-cresol, Formald-ehyde	2,2'-Methylene bis-(4-methylp-henol)	363 K; PC to F mole ratio,5; 2 h	70 (TPY)	88	85

Note: AC = Acetone Conversion; FC = Formaldehyde conversion; DY = Diarylmethane Yield; TPY = Total Product Yield; GC = Guaiacol Yield; PFC = Paraformaldehyde Conversion; PCC = *p*-cresol Conversion; PC = Phenol Conversion.

1.5. SCOPE AND OBJECTIVES OF PRESENT INVESTIGATION

As mentioned earlier, this thesis presents the study on catalyst development for two industrially important reactions viz. (1) hydroxyalkylation and (2) oxidation. In order to give a proper perspective of each of these studies, the thesis is divided into two sections A and B. However, the scope and objectives of both the parts are given together below to facilitate the reader to understand overall scientific content of the thesis.

Hydroxyalkylation is an industrially important reaction nevertheless, traditionally it has been practiced using inorganic reagents in stoichiometric quantities. Hence, there is a scope to develop active, selective and reusable solid acid catalysts for the hydroxyalkylation of phenolic compounds by tuning the acid strength, acid density and particle size of the catalysts. Similarly liquid phase oxidation is also a core unit process practiced industrially for the manufacture of variety of value-added products. Like hydroxyalkylation process, classical liquid phase oxidation process also involved reagent based chemistry. Although catalytic oxidation have become common, but this research area remains active for the further development of new generation non-noble metal based heterogeneous catalysts for the existing as well as for new liquid phase oxidations. The overall objective of this thesis is to design and develop highly active and selective solid catalysts for hydroxyalkylation of phenol derivatives and for liquid phase oxidation. For both these reactions, the specific objectives are:

- Development of new, sophisticated catalyst systems such as PTA supported on MCM−41, metal cation exchanged montmorillonite and magnetically separable solid acid catalysts for hydroxyalkylation of *p*-cresol, phenol and guaiacol.
- Development of new heterogeneous catalysts based on non-noble transition metal for liquid phase oxidation of vanillyl alcohol, veratryl alcohol and *p*-cresol.
- Preparation of catalysts by different methods and their comparative catalytic activity study for oxidation reactions.
- Study the role of support in the oxidation reactions.
- Detail characterization of the prepared catalysts using various techniques such as BET, NH_3-TPD, FTIR, pyridine IR, cyclic voltammetry, chemisorption study, XRD, XPS, and by HR-TEM.
- Mechanistic understanding of the functioning of these catalysts based on the characterization data.
- Optimization of reaction conditions for the best catalysts.

1.6. REFERENCES

1. J. J. Berzelius, *Ann. Chim. Phys.* 1836, 61, 146.
2. G. Centi, S. Perathoner, *Catal. Today* 2003, 77, 287.
3. J. N. Armor, *Catal. Today* 2011, 163, 3.
4. F. Zaera, *J. Phys. Chem. B* 2002, 106, 4043.
5. G. Somorjai, C. Kliewer, React. Kinet. *Catal. Lett.* 2009, 96, 191.
6. P. M. Boisde, W. C. Meuly, "Coumarin" in Encyclopedia of Chemical Technology, John Wiley and sons, IV edition,1993, 7, 647.
7. P. W. Morgan, *J. Polym. Sci., Part A* 1964, 2, 437.
8. R. Guo, O. Lane, D. Van Houten, J. E. McGrath, *Ind. Eng. Chem. Res*. 2010, 49, 12125.
9. Report on Carcinogens, Twelfth Edition, 2011.
10. R. M. Basale, B. Ganesan, A. S. Shyadligeri, V. Srinivasan, *US* 2008/0177091 Al. 2008, 24.
11. D. G. Diddams, J. K. Krum in: Kirk–Othmer *Encyclopedia of Chemical Technology,* 2nd ed., Vol. 21, Interscience: New York, 1970, p. 183.
12. W. Haynes, *This Chemical Age,* 2nd ed., Knopf: New York, 1942, p. 37.
13. A. Corma, H. Garcia, *J. Chem. Soc., Dalton Trans.* 2000, 1381.
14. M. J. Climent, A. Corma, H. Garcia, J. Primo, *J. Catal.* 1991, 130, 138.
15. J. Lecomte, A. Finiels, P. Geneste, C. Moreau, *J. Mol. Catal.* 1998, 133, 283.
16. M. Okihama, J. Kunitake, *Japanese Pat.* 08268943, 1996.
17. M. Okihama, J. Kunitake, *Japanese Pat.* 09067287, 1996.
18. M. Huglin, G. Knight, W. Wright, *Die Makromolekulare Chemie*. 1972, 152, 67.
19. E. O. Camara, T. Kaelin, G. Toki, Bisphenol A, Chemical economics handbooks, *SRI International, Menlo Park,* CA, 2001.
20. A. de Angelis, P. Ingallina, C. Perego, *Ind. Eng. Chem. Res.* 2004, 43, 1169.
21. B. Suresh, M. Yoneyama, Cyclohexanol-cyclohexanone, Chemical economics handbook, *SRI International, Menlo Park,* CA, 2002.
22. W. Hesse, Ullmann's encyclopedia of industrial chemistry, Vol A19, *Wiley-VCH, Weinheim,* Germany, p. 313.

23. W. C. Muench, T. S. Hormel, P. M. Kirchhoff, L. A. Robbins, *US Pat. 4205188*, 1980.
24. H. Iwane, T. Sugawara, N. Suzuki, K. Kaneko, *US Pat. 5220079*, 1993.
25. M. Okihama, J. Kunitake, *Japanese Pat. 08198790*, 1996.
26. K. Takashi, I. Shigeru, M. Yoshio *Japanese Pat. 01211544*,1989.
27. Maruzen Oil Co., Ltd., Japan, *Japanese Pat. 57035532*,1982.
28. A. Chakrabarti, M. M. Sharma, *React. Polym.* 1993, 20, 1.
29. A. Corma, *Chem. Rev.* 1997, 97, 2373.
30. J. H. Westbrook, R. L. Fleischer, Intermetallic Compounds, *John Wiley and Sons*: New York, 2000.
31. K. Tanabe, W. F. Hoelderich, *Appl. Catal. A* 1999,181, 399.
32. A. Jha, A. C. Garade, S. P. Mirajkar, C. V. Rode, *Ind. Eng. Chem. Res.* 2012, 51, 3916.
33. A. Jha, A. C. Garade, M. Shirai, C.V. Rode, *Appl. Clay Sci.* 2013, 74, 141.
34. M. Misono, N. Mizuno, K. Katamura, A. Kasai, Y. Konishi, K. Sakata, T. Okuhara, Y. Yoneda, *Bull. Chem. Soc. Jpn.* 1982, 55, 400.
35. F. Lefebvre, P. Dupont, A. Auroux, *React. Kinet. Catal. Lett.* 1995, 55, 3.
36. Y. Wu, X. Ye, X. Yang, X. Wang, W. Chu, Y. Hu, *Ind. Eng. Chem. Res.* 1996, 35 2546.
37. L. R. Pizzio, C. V. Caceres, M. N. Blanco, *Appl. Catal. A: Gen.* 1998, 167, 283.
38. A. Oulmekki, F. Lefebvre, *React. Kinet. Catal. Lett.* 1992, 48, 601.
39. I. V. Kozhevnikov, *Catal. Lett.* 1995, 30, 241.
40. S. Udayakumar, S. Ajaikumar, A. Pandurangan, *Appl. Catal. A Gen.* 2006, 302, 86.
41. I. V. Kozhevnikov, A. Sinnema, R. J. J. Jansen, K. Pamin, H. van Bekkum, *Catal. Lett.* 1995, 30, 241.
42. C. R. Reddy, G. Nagendrappa , B. S. Jai Prakash, *Catal. Commun.* 2007, 8, 241.
43. B. M. Choudary, M. Sateesh, M. Lakshmi Kantam, K. V. R. Prasad, *Appl. Catal. A Gen.* 1998, 171, 155.
44. A. Gil, L. M. Gandía, M. A. Vicente, *Catal. Rev. Sci. Eng.* 2000, 42, 145.

45. P. F. Luckham, S. Rossi, *Adv. Coll. Int. Sci.* 1999, 82, 43.
46. O. B. Ayodele, J. K. Lima, B. H. Hameeda, *Appl. Catal. A: Gen.* 2012, 413, 301.
47. F. Salles, O. Bildstein, J. M. Douillard, M. Jullien, J. Raynal, H. Van Damme, *Langmuir* 2010, 26, 5028.
48. T. Cseri, S. Bèkássy, F. Figueras, S. Rizner, E. Cseke, L. C. de Menorval, R. Dutartre, *Appl. Catal. A Gen.* 1995, 132, 141.
49. C. N. Rhodes, D. R. Brown, *J. Chem. Soc. Faraday Trans.* 1992, 88, 2269.
50. J. H. Clark, A. P. Kybett, D. J. Macquarrie, S. J. Barlow, P. Landona, *J. Chem. Soc., Chem. Commun.* 1989, 1353.
51. R. Schlögl, S. B. Abd Hamid, *Angew. Chem. Int. Ed.* 2004, 43, 1628.
52. M. V. Barmatova, I. D. Ivanchikova, O. A. Kholdeeva, A. N. Shmakov, V. I. Zaikovskii, M. S. Melg̀unov, *J. Mater. Chem.* 2009, 19, 7332.
53. W. Teunissen, A. A. Bol, J. W. Geus, *Catal. Today,* 1999, 48, 329.
54. F. Matsunaga, T. Nishimura, E. Miyake, K. Baba, *Japanese Pat. 61012640,* 1986.
55. Mitsui Toatsu Chemicals, Inc., Japan, *Japanese Pat. 60038335*, 1985.
56. Mitsubishi Chemical Industries Co., Ltd., Japan, *Japanese Pat. 57112588*, 1982.
57. M. Okihama, Y. Kunitake, *Japanese Pat. 9067287*, 1997.
58. P. B. Venuto, P. S. Landis, *J. Catal.* 1966, 6, 237.
59. W. H. M. Burgers, H. Van Bekkum, *Stud. Surf. Sci. Catal.* 1963, 78, 567.
60. J. M. Climent, A. Corma, H. Garcia, J. Primo, *Appl. Catal.* 1989, 51, 113.
61. J. M. Climent, A. Corma, H. Garcia, J. Primo, *J. Catal,* 1991, 130, 138.
62. J. M. Climent, A. Corma, H. Garcia, S. Iborra, J. Primo, *Appl. Catal. A: Gen.* 1995, 130, 5.
63. T. Kiyora, JP 04275246, A2, 1988.
64. S. Inaba, T. Yamamori, Y. Morimoto, *Japanese Pat. 61078741*, 1986.
65. G. R. Faler, G. R. Loucks, *US Pat. 4424283*, 1984.
66. T. Maki, T. Masuyama, T. Yokoyama, Y. Fujiyama, *Eur. Pat. 45959,* 1982.
67. H. Nakamura, M. Inomata, K. Takahashi, S. Yoshinaga, *Japenese Pat. 2000281607*, 2000.

68. M. Alvaro, H. Garcia, A. Sanjuan, M. Espla, *Appl. Catal., A: Gen.* 1998, 175, 105.
69. N. Barthel, A. Finiels, C. Moreau, R. Jacquot, M. Spagnol, Top. Catal. 2000, 13 269.
70. M. G. Clerici, G. Bellussi, *US pat. 4895988*, 1990.
71. T. Shimizu, K. Tsumura, *Japanese Pat. 11269113*,1999.
72. C. Perego, A. De Angelis, *US pat. 6872859*, 2005.
73. C. Perego, A. De Angelis, A. Carati, C. Flego, R. Millini, C. Rizzo, G. Bellussi, *Appl. Catal. A: Gen.* 2006, 307, 128.
74. S. K. Jana, T. Okamoto, T. Kugita, S. Namba, *Appl. Catal. A: Gen*. 2005, 288, 80.
75. S. K. Jana, T. Kugita, S. Namba, *Appl. Catal. A: Gen.* 2004, 266, 245.
76. M. Bolognini, F. Cavani, L. Dal Pozzo, L. Maselli, F. Zaccarelli, B. Bonelli, M. Armandi, E. Garrone, *Appl. Catal. A: Gen.* 2004, 272, 115.
77. F. Cavani, M. Corrado, R. Mezzogori, *J. Mol. Catal. A: Chem*. 2002, 182-183, 447.
78. A. Corma, H. Garcia, J. Miralles, *Micropor. Mesopor. Mater.* 2001, 43, 161.
79. S. Udayakumar, S. Ajaikumar, A. Pandurangan, *Appl. Catal. A: Gen.* 2006, 302, 86.
80. G. D. Yadav, N. Kirthivasan, *Appl. Catal. A: Gen.* 1997, 154, 29.
81. A. C. Garade, A. M. Hengne, T. N. Deshpande, S. V. Shaligram, M. Shirai, C. V. Rode, *J. Chem. Eng. Jpn.* 2009, 42, 782.
82. A. C. Garade, V. S. Kshirsagar, C. V. Rode, *Appl. Catal. A: Gen*. 2009, 354, 176.
83. A. C. Garade, V. S. Kshirsagar, R. B. Mane, A. A. Ghalwadkar, C. V. Rode, *Appl. Clay Sci.* 2010, 48, 164.
84. A. C. Garade, V. S. Kshirsagar, A. Jha, C. V. Rode, *Catal. Commun.* 2010, 11, 942.
85. A. C. Garade, P. S. Niphadkar, P. N. Joshi, C. V. Rode, *Chem. Lett*. 2010, 39, 126.

Chapter 2

Experimental and physico-chemical characterization

2.1. INTRODUCTION

The design and preparation of catalysts is a crucial issue in heterogeneous catalysis, which dramatically influence their surface area, morphology, nature of acidity, acid site density, redox properties etc. All of these structural and electronic properties are the function of preparation and pretreatment protocols. Hence, the present chapter describes details of preparation and activity testing procedures, characterization of various catalysts, and the analytical methods used for liquid product identification in both hydroxyalkylation (section A) and oxidation reactions (section B) studied in this work.

2.2. MATERIALS

Fumed silica (SiO_2), montmorillonite K10, *p*-vanillyl alcohol, (99%), bentonite (99%), cetyltrimethylammonium bromide (CTAB), veratryl alcohol, veratraldehyde, cobalt acetate tetrahydrate, manganese acetate terahydrate and tetraethylorthosilicate (TEOS) were purchased from Sigma-Aldrich, Bangalore, India. Montmorillonite KSF/O, montmorillonite K10 and Amberlyst-15 were purchased from Fluka, Germany. Phenol (98%), *p*-cresol (98%), formalin solution (37% formaldehyde, 10-13% methanol, 50-55% water), toluene (98%), ferric chloride (98%), aluminium nitrate (98%), and phosphotungstic acid, PTA (98%) were purchased from Loba chemie, Mumbai, India. Guaiacol, Anhydrous sodium carbonate (Na_2CO_3), 30% aqueous ammonia, phthalic anhydride and phenolphthalein were purchased from Thomas Baker, India.

2.3. CATALYST PREPARATION

2.3.1. Solid acid catalysts

2.3.1.1. MCM-41 supported phosphotungstic acid (PTA)

First, MCM-41 support was prepared by a hydrothermal synthesis method as described earlier [1, 2]. In a typical synthesis, 2.46 g of NaOH was dissolved in 146 mL of deionized water and stirred for 5 min. To this solution, 5.96 g of CTAB was added, and the mixture was stirred for 15 min. 14 g portion of TEOS was added drop wise, and the

pH of the solution was maintained in a range of 9−10 by adding dilute H_2SO_4. The resulting reaction mixture was stirred for 5 h at room temperature. Thereafter, the entire reaction mixture along with the mother liquor was transferred into the teflon-lined autoclave and heated under static conditions at 100 ^oC for 48 h. The resulting solid product was recovered by filtration, washed several times with deionized water, dried at 80 ^oC overnight, and calcined at 540 ^oC for 6 h to remove the template from MCM-41.

A series of PTA (10−30 wt %) impregnated on MCM-41 catalysts were prepared by a wet impregnation method. In a typical procedure, the calculated quantity of PTA was dissolved in 40 mL of methanol, which was stirred for 5 min, followed by the slow addition of MCM-41 to the solution. The resulting mixture was kept for 6 h at room temperature under stirring conditions. The solvent was evaporated on a rotavap and then the catalysts were calcined at 300 ^oC for 3 h. A schematic presentation of catalyst preparation is shown in Fig.2.1.

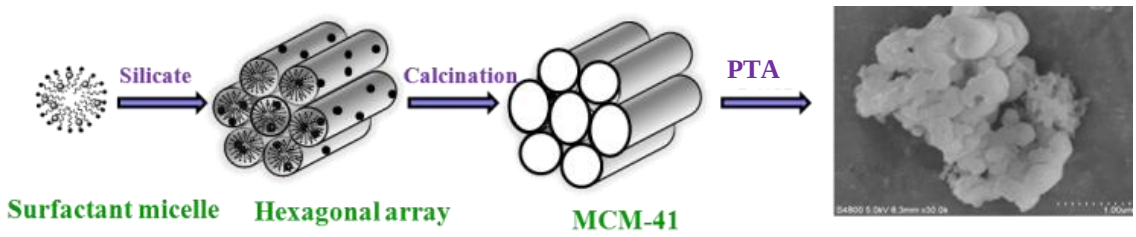

Fig. 2.1. Preparation of PTA/MCM-41 catalyst

PTA impregnated on various other supports such as montmorillonite K10, Mont KSF etc. were also prepared in a similar way, as follows; 4 g of mont K10 was added to the solution of 1 g of PTA in 100 mL methanol with constant stirring over a period of 20 min. The dispersion was stirred for 6 h at room temperature and the solvent was evaporated under vacuum. The catalyst was dried at 100 ^oC for 2 h and then calcined at 300 ^oC for 6 h [3].

2.3.1.2. Preparation of SO_3H-Fe_3O_4@MCM-41

SO_3H-Fe_3O_4@MCM-41catalyst was prepared in two steps. The first step involves the synthesis of silica bound magnetite particles (SMPs) while, the second step involves the

grafting of mercaptopropyltrimetoxysilane (MPTMS) over the SMPs followed by oxidation. Silica bound magnetite particles were prepared by in situ condensation of magnetite particles with silica. The schematic presentation of synthesis of SMPs is shown in Scheme 2.1. In a typical synthesis procedure, 3 g (0.0082 mol) cetyltrimethylammonium bromide (CTAB) was dissolved in 400 mL of distilled water, followed by drop wise addition of 1 M NaOH solution to maintain the pH at 10−11. The resulting solution was stirred for 30 min at room temperature followed by sonication with 0.2 g of magnetite (size < 1 μm) for 30 min. In the resultant mixture, 13.95 g of

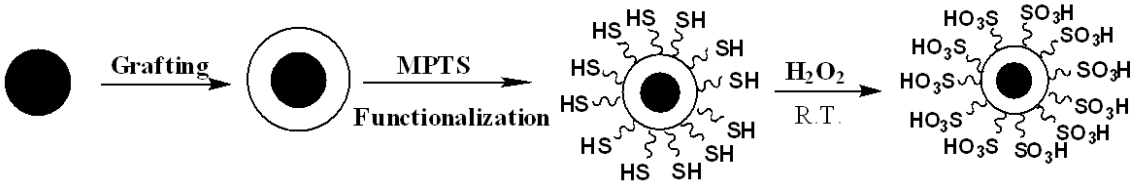

Scheme 2.1. Preparation of SO_3H-Fe_3O_4@MCM-41

teraethylorthosilicate (TEOS) was added drop wise, and this solution was stirred (700−800 rpm) at room temperature for 4 h. The resultant SMPs designated as Fe_3O_4@MCM-41, was filtered, washed with 1.5 L of distilled water, dried in vacuum oven at 100 ^oC for 12 h, and calcined at 540 ^oC for 6 h to remove the template from the SMPs. Second step involved the functionalization with MPTMS, in which 5 mL of MPTMS was added drop wise into the suspension of SMPs (0.4g) in toluene, and reflux it for 24 h. After filtration and thorough washing with dry toluene, the grafted product was dried overnight under vacuum. The as obtained material was afterwards oxidized with 30 wt.% aqueous hydrogen peroxide (15 mL per 0.3 g of catalyst) at room temperature for 24 h under inert atmosphere, filtered off and washed several times with water and ethanol. The wet material was finally suspended in 1 M sulfuric acid for 2 h, collected by filtration, washed with water and ethanol and dried at 60 °C under vacuum for several hours to obtain the final product SO_3H-Fe_3O_4@MCM-41.

2.3.1.3. Preparation of metal cation-exchanged montmorillonite clay

The catalysts prepared by cation-exchange process were according to the method reported in the literature [4]. In a typical preparation, 5 g of montmorillonite clay was slowly added to 80 mL of 0.3 M concentration of respective metal nitrate aqueous solution. The resulting mixture was stirred for 4 h at room temperature. The final product was filtered, washed 2 times with 80 mL of distilled water and then dried in vacuum oven at 100 ^{o}C for 2 h. As prepared catalysts were powdered and then calcined in a furnace at 300 ^{o}C for 3 h. Schematic presentation of catalyst synthesis is shown in Fig. 2.2. For *p*-cresol hydroxyalkylation we developed Al, Zn and Fe exchanged montmorillonite catalysts.

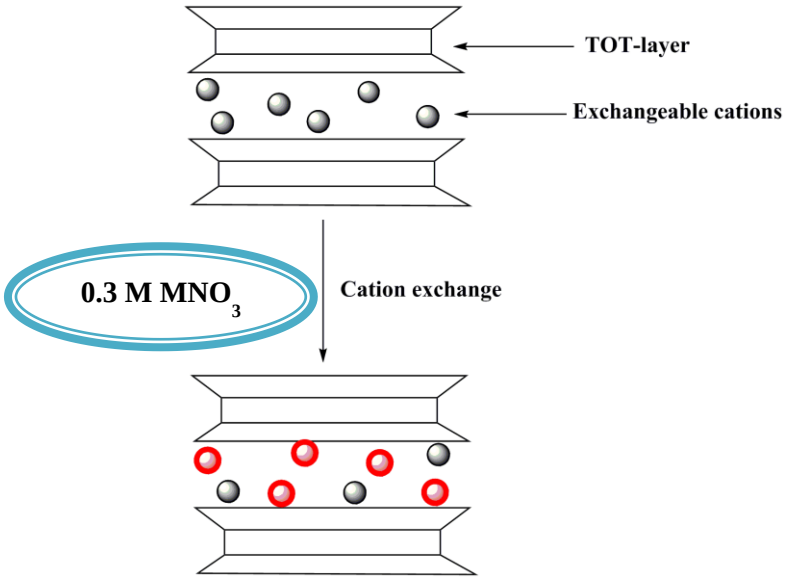

Fig. 2.2. Preparation of metal cation-exchanged montmorillonite clay

2.3.2. Metal oxide catalysts for oxidation reactions

2.3.2.1. Co_3O_4 nanoparticles

Co_3O_4 nanoparticles were prepared by solution-phase method as described earlier. [5] In a typical synthesis, 4.98 g of cobalt acetate tetrahydrate was dissolved in 60 mL of

ethylene glycol and the solution was gradually heated to 160 ^{o}C. To this, 200 mL of aqueous 0.2 M Na_2CO_3 solution was added drop wise and the slurry was further aged for 1 h under nitrogen atmosphere. The resulting solid was filtered, thoroughly washed with distilled water until neutralization, and dried overnight at 100 ^{o}C, then calcined at 450 ^{o}C for 4 h in a horizontal furnace.

2.3.2.2. Manganese oxide (MnO_x)

MnOx catalyst was prepared by solvothermal method. In a typical synthesis, 4.98 g of manganese acetate tetrahydrate was dissolved in 60 mL of ethylene glycol and the solution was gradually heated from room temperature to 160 ^{o}C. To this, 200 mL of aqueous 0.2 M Na_2CO_3 solution was added drop wise and the slurry was further aged for 1 h under nitrogen atmosphere. The resulting solid was filtered, thoroughly washed with distilled water until neutralization, and dried overnight at 100 ^{o}C, then calcined at 450 ^{o}C for 4 h.

2.3.2.3. Synthesis of mixed CoMn-oxide

Manganese-doped cobalt oxide catalyst was also prepared by a solvothermal method keeping the molar ratio of Co/Mn = 2. In a typical synthesis, manganese acetate tetrahydrate (2.45 g) and cobalt acetate tetrahydrate (4.98 g) were dissolved in ethylene glycol (60 mL), the solution was heated gradually from room temperature to 160 ^{o}C, and then 0.3M aqueous Na_2CO_3 solution (200 mL) was added drop wise. The resulting slurry was further aged for 1 h under a nitrogen atmosphere. The product was isolated by filtration, washed thoroughly with distilled water until neutralization, dried at 100 ^{o}C for 12 h, and then calcined at 450 ^{o}C for 4 h. The obtained catalyst was labeled as MnCo-MO. The experimental set up of the catalyst preparation is shown in Fig. 2.3.

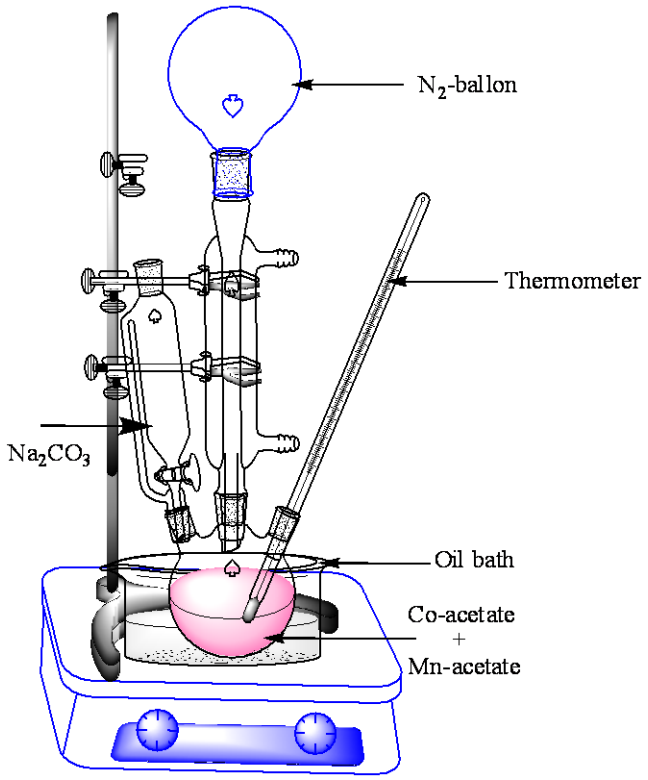

Fig. 2.3. Synthesis of mixed Co-Mn oxide

2.3.2.4. Reduced graphene-MnCo composite oxide

2.3.2.4.1. Graphene oxide (GO)

A modified 'Hummers' method was used to synthesize graphite oxide in which 1g of graphite powder was put into the already prepared $NaNO_3$ (0.5g) solution in concentrated H_2SO_4 (30ml) and cooled to 0°C. To this, 3 g KMnO4 was added, during which temperature of the mixture was kept below 20ºC. Successively, the mixture was stirred at 35 ºC for 1 h, and then diluted with 46 ml deionized water by keeping the temperature under 85 ºC and then increased to 100 ºC for 30 min. 140 ml deionized warm water was then added to the mixture, followed by 15 ml 50% H_2O_2 drop by drop and the solution was left for 30 min. under stirring. The mixture was then centrifuged and washed with 5% aqueous HCl solution (1 L) to remove metal ions followed by 2 L of deionized water to remove the acid. The resulting solid was dried in air for 12 h at 60ºC.

2.3.2.4.2. r-GO-MnCo nanocoposite

r-GO-MnCo nanocomposite was synthesized by solvothermal method. In a typical synthesis, GO was dispersed into 60 mL of ethylene-glycol and sonicated for 1 h, followed by subsequent addition of 1.6 mL aqueous NH_3 and stirred again for 1 h. To this, manganese and cobalt acetates were added in 1:1 ratio and the solution was gradually heated to 160 ^oC. After the temperature reached 160 ^oC, 200 mL of aqueous 0.3 M Na_2CO_3 solution was added drop wise and the slurry was further aged for 2 h under nitrogen atmosphere. The resulting product was filtered, thoroughly washed with distilled water until neutralization, and dried overnight at 100 ^oC, then calcined at 350 ^oC for 4 h. The schematic presentation of catalyst synthesis is shown in Fig. 2.4.

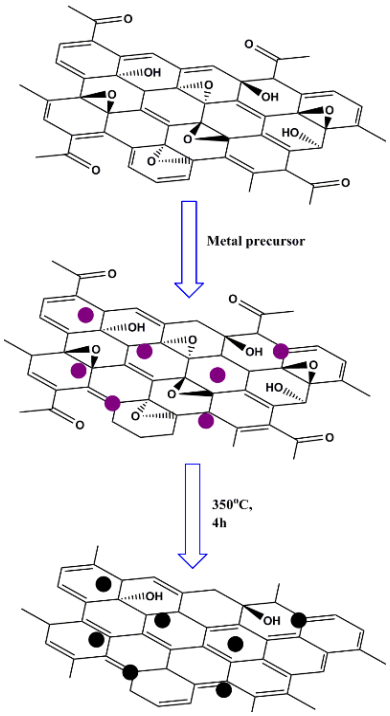

Fig. 2.4. Schematic presentation of synthesis of r-GO-MnCo nanocoposite

2.4. CHARACTERIZATION METHODS FOR SOLID ACID CATALYSTS

2.4.1. X-ray diffraction

X-ray diffraction (XRD) is a non-destructive technique for the qualitative and quantitative analysis of the crystalline materials, in form of powder or solid. It helps in determining the crystallinity, phase purity, crystal structure and crystallite size of catalyst materials [6].The XRD method involves interaction between the incident monochromatized X-rays (like Cu Kα or Mo Kα) with the atoms of a periodic lattice (Fig. 2.5). X-rays scattered by the atoms in an ordered lattice interfere constructively as described by Bragg's law: $n\lambda = 2d \sin\theta$, where, λ is the wavelength of the X-rays, *d* is the distance between two lattice planes, θ is the angle between the incoming X-rays and the normal to the reflecting lattice plane and n is an integer known as the order of reflection [6, 7].

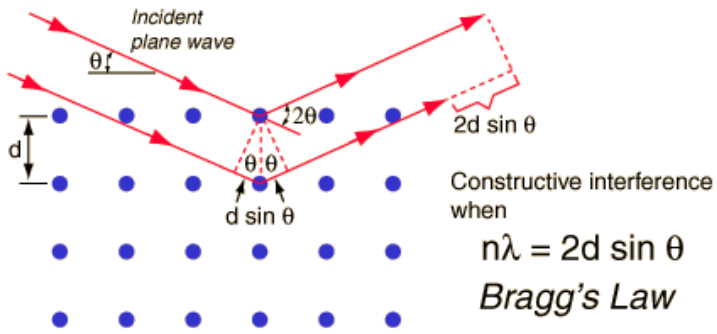

Fig. 2.5. X-ray diffraction from crystal planes

The mesoporous materials were characterized using an X'Pert Pro (Philips) diffractometer with Cu-Kα radiation (λ = 0.15406 nm) and a proportional counter as a detector. A divergent slit of 1/32◦ on the primary optics and an anti-scatter slit of 1/16◦ on the secondary optics were used to measure the data in the low-angle region. The rest of the catalysts were analyzed using a Rigaku Geigerflex X-ray diffractometer with Ni-filtered Cu-Kα radiation (40 kV, 30 mA). The XRD patterns were measured in the 2θ range of 0.5–10º in the case of mesoporous (PTA/MCM 41 and SO_3H-Fe_3O_4@MCM-41) materials and 5 – 80° in the case of metal cation-exchanged montmorillonite clay catalyst

at a scan rate of 5.3º min^{-1}, respectively. Crystallite size of the materials was determined using the Scherrer equation: $L = K\lambda/\beta\cos\theta$, where θ and λ are the Bragg's angle and wavelength of incident X-ray radiation, respectively. K is a constant approximately taken as 0.9; β is the line width on the 2θ scale in radians. Qualitative phase analysis of the catalysts was done based on the comparison of the line positions and intensity distributions of a set of reflections of the catalyst sample with a data base (JCPDS).

In case of mixed oxides, XRD is the best technique to study the effect of dopant on the host oxide. It can measure the newly form crystalline phase due to the dopant present in the mixed oxide. Peak widths are fitted to the Debye−Scherrer equation to determine crystallite size. Shifts due to the substitutional doping are often interpreted using Vegard's rule, which states that there is a linear relationship between the concentration of a substitutional dopant and the change in the lattice parameter. As an added complication, the lattice parameters of small nanocrystals depend on crystallite size, and it is not sure whether the observed lattice parameters shift is due to doping or to the small size of the crystallites.

2.4.2. Nitrogen Physisorption–Textural Characterization

Physisorption is the most common type of adsorption. Physisorbed molecules are fairly free to move around the surface of the sample. As more gas molecules are introduced into the system, the adsorbate molecules tend to form a thin layer that covers the entire adsorbent surface. Based on the well-known Brunauer, Emmett and Teller (BET) theory, one can estimate the number of molecules required to cover the adsorbent surface with a monolayer of adsorbed molecules, Nm. Multiplying Nm by the crosssectional area of an adsorbate molecule yields the sample's surface area. The BET equation can be represented as:

$$P/V\,(Po-P) = 1/V_mC + [(C-1)/V_mC]\,(P/Po) \quad \ldots\ldots (2.1)$$

Where, P is the adsorption equilibrium pressure (Pa),

P_o is the saturation vapor pressure of the adsorbate at the experimental temperature (Ta),

V is the volume of gas adsorbed at pressure P (cm^3),

V_m is the volume of adsorbate required for monolayer coverage (cm^3), and

C is constant related to the heat of adsorption and liquefaction [8].

A plot of P/V (P_o-P) vs. (P/P_o) yields a straight line usually in the range $0.05 \leq P/P_o \leq 0.35$. The monolayer volume V_m is given by 1/(S+I), where S is the slope, which is equal to $(C-1)/V_mC$ and I is the intercept, which is equal to $1/V_mC$. The surface area of the catalyst (S_{BET}) is related to V_m by the equation:

$$S_{BET} = (V_m/22414)\, N_a\, \sigma \ldots\ldots. (2.4)$$

Where, N_a is the Avogadro number and σ is mean cross sectional area covered by one adsorbate molecule. The σ value generally used for N_2 is 0.162 nm^2. Surface area and porosity are important properties in the field of heterogeneous catalysis. Total surface area is a crucial criterion for solid catalysts since it determines accessibility of active sites and is thus often related to catalytic activity. The pore architecture of a heterogeneous catalyst controls transport phenomena and governs selectivity in catalyzed reactions. Properties, such as pore volume and pore-size distribution, are therefore essential parameters especially in shape selective catalysis. The first important information about surface and porosity obtained from a physisorption experiment is the isotherm. It can reveal the kind of porosity present in unknown samples. The IUPAC recommended the following six types of the adsorption isotherms, as shown in Fig. 2.6. The type I isotherm represents presence of micropores where molecules are adsorbed by micropore filling. The type II isotherm is indicative of the multilayer adsorption process, suggesting the presence of nonporous or macroporous surfaces. The type III isotherm arises from nonporous or macroporous surfaces which interact very weakly with the adsorbent molecules. The type IV isotherm gives useful information on the mesopore structure through its hysteresis loop that is, non-overlapping of the adsorption and desorption branches. The type V isotherm is close to the type IV isotherm instead of very weak adsorbent-adsorbate interaction. The type VI isotherm is the stepped adsorption isotherm

which comes from phase transition of the adsorbed molecular layer or adsorption on the different faces of crystalline solids. Several computational procedures are available for the derivation of pore size distribution of mesoporous samples from physisorption isotherms. Most popular among them is the Barrett-Joyner-Halenda (BJH) model, which allows the computation of pore sizes from equilibrium gas pressures. One can therefore generate experimental curves (or isotherms) linking adsorbed gas volumes with relative

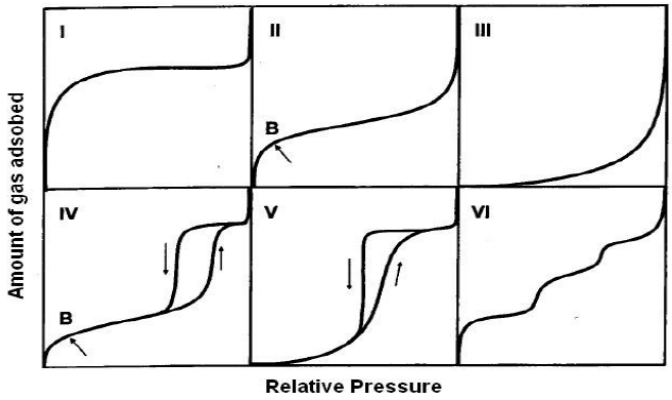

Fig. 2.6. IUPAC classification of isotherms

saturation pressures at equilibrium, and convert them to cumulative or differential pore size distributions [9]. As the equilibrium adsorbate pressures approach saturation, the pores become completely filled with adsorbate. Knowing the density of the adsorbate, one can calculate the volume it occupies and consequently, the total pore volume of the sample. Since adsorption and desorption mechanisms differ, adsorption and desorption isotherms rarely overlay each other. The resulting hysteresis leads to isotherm shapes that can be mechanistically related to those expected from particular pore shapes. Adsorption of nitrogen measured by Brunauer-Emmett-Teller (BET) equation at low pressure (10-4 Torr) and liquification temperature of N_2 (77 K) is the standard method for determination of surface area, pore volumes and pore size distribution of molecular sieves. All these measurements were conducted on Autosorb 1, Quantachrome instrument (Fig. 2.7).

Fig. 2.7. Autosorb 1, Quantachrome instrument

2.4.3. Temperature programmed desorption of ammonia (NH_3-TPD)

In contrast to physisorption, chemical adsorption (chemisorption) involves the formation of strong chemical bonds between adsorbate molecules and specific surface locations known as chemically active sites. Chemisorption is thus used primarily to count the number of surface active sites which are likely to promote chemical and catalytic reactions. NH_3-TPD technique is one of the examples of chemisorption, generally used to determine the acidity and acid strength of the solid catalysts and involves monitoring surface or bulk interaction between the solid catalyst and its gaseous environment via continuous analysis of the gas phase composition as the temperature is raised linearly with time [10]. Instrument used for ammonia-TPD study consists of a sample holder charged with the catalyst in a furnace that can be temperature programmed and a thermal conductivity detector (TCD) to measure the amount of desorbed NH_3 gas in the carrier gas mixture.

NH_3-TPD measurements of all the catalysts were done on a Micromeritics 2720 by (i) pre-treating the sample at 473 K in a flow of helium for removing surface

contaminants, (ii) adsorption of ammonia at 50 ^{o}C temperature, and (iii) desorption of adsorbed ammonia with a heating rate 10 K min^{-1} starting from the adsorption temperature to 700 ^{o}C. The (%) distribution of acidic sites was calculated by measuring the area of desorption peaks in a low and high temperature regions using Origin 6.1 software.

2.4.4. Pyridine FT-IR technique

Pyridine FT-IR is the most widely used technique for determining the nature of acidic sites i.e. Brönsted and/or Lewis present on the catalyst surface [11]. The infrared spectrum in the 1400 to 1700 cm^{-1} region has been determined for pyridine adsorbed on acidic solids. The spectrum of pyridine coordinately bonded to the surface is markedly different from that of the pyridinium ion. This permits the differentiation of acid type on the surface of acidic solids. Since NH_3 is a strong base (pK_b ~ 5), it can react with extremely weak acid sites, though pyridine is also a relatively strong base, it is significantly weaker than ammonia (pK_b pyridine ~ 9), and thus will not react with some of the weaker sites that would react with ammonia. Therefore, pyridine is used for distinguishing type of acid sites. The pyridinium ion gives a band at approximately 1540 cm^{-1} which is not present in either pyridine or coordinately bonded pyridine ($Py \rightarrow BH_3$). Both coordinately bonded pyridine and hydrogen-bonded pyridine have a band in the 1440-1465 cm^{-1} region. The catalyst having Brönsted acidity shows a peak at 1540 cm^{-1}, while peak at 1450 cm^{-1} can be assigned to Lewis acidity [12]. In this thesis, the Brönsted and Lewis acid sites were determined by ex-situ FTIR spectroscopy with chemisorbed pyridine. For this purpose, catalyst samples were dried at 110 ^{o}C for 1 h and then saturated with pyridine vapors in a desiccator containing pyridine for 8 h. Physically adsorbed pyridine was removed by heating the samples at 120 ^{o}C for 2 h in a continuous flow of nitrogen. FTIR spectra of the samples were recorded on a Shimadzu (Model-820 PC) spectrophotometer under DRIFT (diffuse reflectance infrared Fourier transform) mode.

2.4.5. Thermal analysis

Thermal analysis is a group of techniques that study the changes in the properties of a sample occurring while the sample is subjected to a controlled temperature program. The thermal techniques most commonly used to investigate the acid – base or redox character of solid surfaces are: differential thermal analysis (DTA), thermogravimetric (TG) and differential thermogravimetric (DTG), differential scanning calorimetry (DSC) and calorimetry. Techniques such as DTA, TG or DSC study the thermal behavior of a catalyst as it undergoes heating at a constant rate. For example, DTA relies on the measurement as function of time i.e. of the difference between the temperature of the sample (Ts) and that of a reference material (Tr), upon heating both materials in a furnace. $\Delta T = Ts - Tr$ is related to the heat evolved (or absorbed) by the sample at a time when the sample undergoes an endothermic or exothermic reaction, which includes phase transitions, dehydration, decomposition, redox, or solid state reactions. The area under a DTA peak can be proportional to the enthalpy change and is not affected by the heat capacity of the sample [13]. In the TG and DTG methods, the variation of the sample mass with time (dm or dm /dt) is measured as a function of temperature while the sample is heated at a constant rate [14]. In this work, thermal analysis (TGA/DTA) was performed on Perkin-Elmer TGA-7 analyzer at a 10 ^{o}C/min scan rate in nitrogen atmosphere.

2.4.6. Transmission Electron Microscopy

In the 1940s, it was realized that interaction between electrons and atoms might change the phase of an electron wave and make possible the observation of single atoms using phase contrast. This is the theoretical foundation of high–resolution transmission electron microscopy (HRTEM). It was also established by O. Scherzer [15]. TEM is typically used for high resolution imaging of thin films of a solid sample for micro structural and compositional analysis. The principles of TEM and HRTEM can be understood in brief as follow: A TEM column can be described using a ray diagram as shown in Fig. 2.8, which is very similar to that for an optical microscope. The most important components

in an electron microscope are the electron source (normally called the electron gun) and a group of electromagnetic lenses.

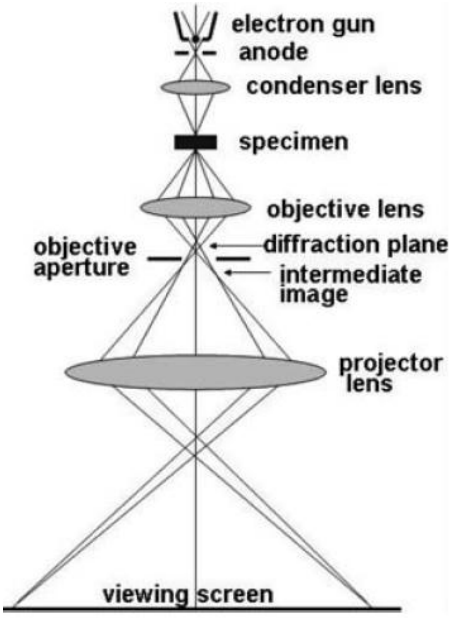

Fig. 2.8. Ray diagram of TEM set-up

Electrons are emitted from the electron gun and accelerated by a potential difference (a typical value for HRTEM is 200 to 300 kV). These electrons are focused by the condenser lenses to form a parallel beam. The electron beam strikes a specimen, creating different forms of energy. The transmitted and scattered electrons are then recombined and focused by the objective lens to form a diffraction pattern and an intermediate image at different stages. The beams then diverge and are focused by the projective lenses to form the final image. Typical operating conditions of TEM instruments are 100-200 KeV electrons, 10-6 mbar vacuum, 0.5 nm resolutions and a magnification of about 105. The topographic information obtained by TEM in the vicinity of atomic resolution can be utilized for structural characterization and identification of various phases of mesoporous materials, viz., hexagonal, cubic or lamellar [16]. TEM also provides real space image on the atomic distribution in the bulk and surface of a nano-crystal. TEM of the samples were recorded using a JEOL-model 1200 EX instrument operating at 100 KV. Details of characterization results of different catalysts are reported in the respective chapters.

2.4.7. Inductively coupled plasma atomic emission spectroscopy (ICP-AES)

Inductively coupled plasma atomic emission spectroscopy (ICP-AES), also referred to as inductively coupled plasma optical emission spectrometry (ICP-OES), is an analytical technique used for the detection of trace metals. It is a type of emission spectroscopy that uses the inductively coupled plasma to produce excited atoms and ions that emit electromagnetic radiation at wavelengths characteristic of a particular element. [17, 18] The intensity of this emission is indicative of the concentration of the element within the sample.

The W content in PTA/MCM-41 catalyst was determined from inductive coupled plasma (ICP) analysis with a Spectro 165 high resolution ICP-OES Spectrometer (model no. ARCOSFHS 12). 25 mg of catalyst was treated with aqua regia (HNO_3–HCl = 1 : 3) with few drops of HF at 60 °C on a sand bath for 2 h and the obtained solid was dissolved in 10 mL distilled water.

2.4.8. X-ray Photoelectron Spectroscopy (XPS)

XPS is based on the observation of the photoelectric effect and also known as electron spectroscopy for chemical analysis (ESCA), in which a photon reaching a sample can liberate an electron, which subsequently escapes into the vacuum (Fig. 2.9). XPS detects only those electrons that have actually escaped into the vacuum of the instrument. This technique biased towards the top few atomic layers (∼1−10 nm) of the solid. [19] XPS is a quantitative spectroscopic technique that measures the elemental composition, empirical formula, chemical state and electronic state of the elements that present at the surface in concentration greater than approximately 1 atomic percent. Furthermore, XPS can provide information regarding the elemental stoichiometry of the near-surface region, which is often different from the bulk composition. The catalytic function is acknowledged to be essentially dependent on the surface composition and electronic properties, which make XPS a popular surface analytical tool. The intensity of an XPS peak (I_A) is a strong function of (i) the incoming photon flux, (ii) the concentration of the

given element, (iii) its photoionization cross-section (which is excitation-energy dependent), (iv) the mean free path of the emitted photoelectron, and

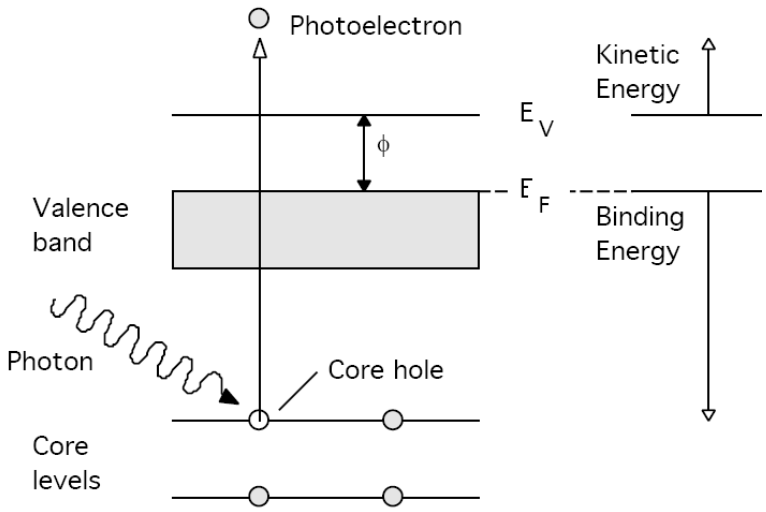

Fig. 2.9. Schematic presentation of XPS

(v) further instrumental parameters (such as photoelectron collection and detection efficiency). By defining atomic sensitivity factors (S, as an overall factor summing up the effects of iii – v), the atom fraction of any element in a sample can be calculated as:

$$X_A = \frac{I_A}{S_A} / \sum (I_i / S_i) \qquad (2.1)$$

XPS data of different catalysts were collected on a VG Scientific ESCA-3000 spectrometer using a non-monochromatised Mg Kα radiation (1253.6 eV) at a pressure of about 1 x 10^{-9} Torr (pass energy of 50 eV, electron take off angle 55) and overall resolution 0.7 eV determined from the full width at half maximum of the $4f_{7/2}$ core level of the gold surface. The error in the binding energy values were within 0.1 eV. The binding energy values were charge-corrected to the C1s signal (284.6 eV).

2.4.9. Fourier transforms infrared spectroscopy (FT-IR)

IR spectroscopy techniques are widely used for chemical analysis. It gives only partial information on the vibrational structure of most polyatomic species. In fact, selection rules apply to IR light absorption phenomena, so that only vibrational modes that are associated with changes of the molecular dipolar moment can be directly excited. The application of IR spectroscopy to catalysis and surface chemistry was reported in 1937 by Buswell and coworkers [20]. Most metal oxides only absorb radiation in the low - energy IR region (below 1000 cm^{-1}) while most gaseous or volatile molecules absorb strongly in the higher energy IR region (4000–1000 cm^{-1}). The formation of metal oxide was determined using FTIR spectroscopy. The spectra were recorded on a Shimadzu FTIR-8201 PC spectrophotometer in the wave number range of 400 – 4000 cm^{-1}. The samples were made into KBr pellets (1 wt. %) or as such in DRIFT mode. In general, neat KBr was used as a reference material.

2.4.10. Temperature programmed reduction (TPR) and oxidation (TPO)

The technique temperature programmed oxidation and reduction typically involves monitoring surface (or bulk) processes between the solid catalysts and its gaseous environment via continuous analysis of the gas phase composition as the temperature is raised. TPR is a widely used tool for the characterization of metal oxides, mixed metal oxides, and metal oxides dispersed on a support. A thermal conductivity detector (TCD) is used to measure changes in the thermal conductivity of the gas stream. TPR is a method in which a reducing gas mixture (5% H_2 in argon) flows over the sample while the tempereture is increased linearly. The experiments permits the determination of the total amount of hydrogen consumed, from which the degree of reduction and, thus the average oxidation state of the solid material after reduction can be calculated. However, reduction of metal oxide is strongly dependent on the morphology and particle size [21]. Similarly in TPO experiment, pre-reduced sample was subjected to oxygen flow (10% O_2 in He, 25 ml/min.) with linear heating. The amount of oxygen consumption gives the

reduced species in a catalyst material. In the present work both the TPR/TPO experiment was carried on Micromeritics 2720 chemisorb instrument, Fig. 2.10.

Fig. 2.10. Micromeritics 2720, instrument

2.4.11. Cyclic Voltammetry (CV)

Cyclic voltammetry (CV) is the most widely employed tool for obtaining qualitative information about electrochemical reactions [22]. It gives information about the redox potentials of the electrochemically active species. CV is a simple type of potentio-dynamic electrochemical measurement. In a cyclic voltammetry experiment, the potential of working electrode is ramped linearly vs. time. CV takes the experiment a step further than linear sweep voltammetry which ends when it reaches a set potential. The current at the working electrode is plotted versus the applied voltage to give the cyclic voltammogram trace. Actually in this case the voltage is swept between two values (V_1 and V_2) at a fixed scan rate (mV/sec). When the voltage reaches V_2 the scan is reversed and the voltage is swept back to V_1. A typical cyclic voltammograms recorded for study redox behavior of lab synthesized Co_3O_4 nanoparticles at a scan rate of 50 mV s^{-1} over the potential range of 0–0.6 V in 0.1M KOH solution by using a quasi reference electrode. When the scan is reversed we simply move back through the equilibrium positions gradually converting the adsorption state of cations and anions into free state (cations and anions back transferred in electrolyte from electrode interface).

2.5. CATALYST ACTIVITY MEASUREMENT

2.5.1 Hydroxyalkylation reaction

2.5.1.1. Phenolphthalein synthesis from hydroxyalkylation of phenol with phthalic anhydride

Phenolphthalein synthesis was carried out by condensation of phenol with phthalic anhydride using a catalyst in a magnetically stirred glass reactor (capacity 50 mL), fitted with a reflux condenser and an arrangement for temperature control. In a typical experiment, phenol (34 mmol), phthalic anhydride (16 mmol), and 20% PTA/MCM-41 catalyst (0.1 g/cm^3) were added to the reactor, which was then heated to 150 ^{o}C for 3 h. Conversion of phthalic anhydride and products selectivity were determined by a Hewlett-Packard model 1050 chromatograph equipped with an ultraviolet detector (λ_{max} = 254 nm) on a 25 cm RP-18 column.

2.5.1.2. Hydroxyalkylation of guaiacol to *p*-vanillyl alcohol

The hydroxyalkylation of guaiacol with formaldehyde was carried out in a magnetically stirred glass reactor (capacity 50 mL) fitted with a reflux condenser and an arrangement for temperature control. In a typical experiment, 1:7 molar ratio of guaiacol to formaldehyde and SO_3H-Fe_3O_4@MCM-41 catalyst (0.11 g/mL) were added to the reactor which was then heated to 70 ^{o}C for 3 h. The guaiacol conversion and product selectivity were determined by liquid sample analysis using a Hewlett-Packard model high pressure liquid 1050 chromatograph equipped with an ultraviolet detector (λ_{max} = 278) on a 25 cm RP-18 column.

2.5.1.3. Hydroxyalkylation of *p*-cresol with formaldehyde to give bisphenol

The hydroxyalkylation reaction of *p*-cresol was carried out in a round bottom glass reactor (50 mL capacity) fitted with a reflux condenser and an arrangement for temperature controller as shown in Fig. 2.11. In a typical procedure, calculated quantities

of *p*-cresol, formaldehyde, toluene as a solvent and Al-montmorillonite catalyst were added and the reaction mixture was stirred at 80 ^{o}C temperatures for 2 h. The *p*-cresol conversion and selectivity of the products were determined by using a gas chromatograph (HP 6890) equipped with flame ionization detector (FID) and an HP-5 capillary column (0.25 μm cross-linked methyl silicone gum, 0.32 mm×30 m).

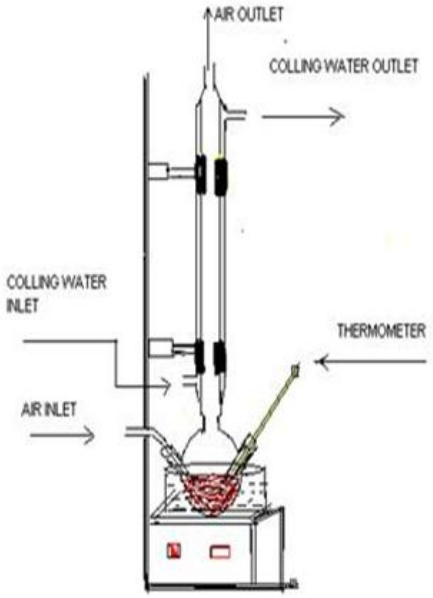

Fig. 2.11. Atmospheric experimental set-ups for hydroxyalkylation reactions

2.5.2. Oxidation reactions

2.5.2.1. Vanillyl alcohol to vanillin

In a typical experiment, 0.5 g of NaOH and 70 mL of isopropanol were heated in a flask with a reflux condenser until the NaOH dissolved completely. This NaOH solution was charged with 0.5 g of vanillyl alcohol and 0.1 g catalyst into a 300 mL Parr autoclave. The reaction mixture was heated to 80 ^{o}C. After the desired temperature was attained, the reactor was pressurized with 6.8 bar air. Then the reaction was started by agitating the contents at 1000 rpm and was continued for 6 h. After 6 h, the reactor was cooled to room

temperature and the unabsorbed air was vented out. Then the contents of the reactor were discharged and the final volume was recorded.

2.5.2.2. Vanillyl alcohol to vanillin under base free condition

In a typical experiment, vanillyl alcohol (0.5 g), catalyst (0.1 g) and acetonitrile (70 mL) were charged into a 300 mL Parr autoclave. The reaction mixture was heated to 140 ^{o}C. After the desired temperature was attained, the reactor was pressurized with 21 bar air pressure. Then the reaction was started by agitating at 1000 rpm. The reaction was continued for up to 2 h, then the reactor was cooled to room temperature and the unabsorbed air was vented out. The content of the reactor was discharged and the final volume was noted.

2.5.2.3. *p*-cresol to *p*-hydroxybenzaldehyde

In a typical experiment, 6.0 g *p*-cresol, 6.2 g NaOH and 50 ml methanol were heated in a round bottom flask with a reflux condenser until the NaOH dissolved completely. This reaction mixture was charged to a 300 mL par autoclave. Then 0.2 g catalyst was added, and the reaction mixture was heated to 373 K. After the desired temperature was attained, the reactor was pressurized with 2.7 bar oxygen. Then the reaction was started by agitating at 1000 rpm. When the pressure decreased, the reactor was again filled by oxygen. This was continued up to 1 h. The progress of the reaction was monitored by observing the pressure drop in the reservoir vessel as a function of time. After 1 h the reactor was cooled to room temperature and the unabsorbed oxygen gas was vented out. Then the content of the reactor was discharged and the final volume was noted down. The final samples were analyzed by HPLC.

2.5.2.4. Veratryl alcohol to veratraldehyde

In a typical experiment, 0.5 g veratryl alcohol, 0.1 g catalyst and 60 ml acetonitrile were charged into a 300 ml Parr autoclave. The reaction mixture was heated to 120 ^{o}C. After the desired temperature was attained, the reactor was pressurized with 21 bar air pressure.

Then the reaction was started by agitating at 1000 rpm. The reaction was continued up to 90 min. After 90 min. the reactor was cooled to room temperature and the unabsorbed air was vented out. Then the content of the reactor was discharged and the final volume was noted down.

2.6. ANALYTICAL METHODS

Analysis of phenol and vanillyl alcohol and their hydroxyalkylation products was done using Hewlett-Packard model 1050 liquid chromatograph equipped with an ultraviolet detector. HPLC analysis was performed on a 25 cm RP-18 column supplied by Hewlett-Packard. The products and reactants were detected using a UV detector at λ_{max}, 254 nm using 35% acetonitrile-water as mobile phase at a column temperature of 35 ^{o}C and the flow rate of 0.8 mL/min. Samples of 10 μL were injected into the column using an auto sampler. The *p*-cresol conversion and product yield (sum of DAM and trimer based on formaldehyde) and selectivity were determined with an HP 6890 series GC System (Hewlett Packard) coupled with FID detector and capillary column (HP-1 capillary column, 30 m length x 0.32 mm i.d.). The injector and detector temperatures were kept at 250 ^{o}C. The oven temperature was programmed as follows: 80 ^{o}C (3 min), then 110 ^{o}C (2 min, with ramp rate of 10 ^{o}C min^{-1}) and finally 300 ^{o}C with ramp rate of 10 ^{o}C min^{-1}. Helium gas was used as a carrier gas with the flow rate of 20 mL min^{-1}. Authentic samples were used for calibration and quantifying the data.

Analysis of the substrate and product of the oxidation reactions was carried out by using Thermo Scientific HPLC, model AS3000, liquid chromatograph equipped with an ultraviolet detector. All the analysis was performed on 25 cm RP-18 column supplied by Hewlett-Packard. The products and reactant were detected using a UV detector at λ_{max} = 254 nm. Aqueous methanol (50%) was used as a mobile phase at a column temperature of 35 ^{o}C and a flow rate of 0.7 mL min^{-1}. Samples of 20 μL were injected into the column using an auto sampler.

2.7. REFERENCES

1. J. K. Satyarthi, L. Saikia, D. Srinivas, P. Ratnasamy, *Appl. Catal. A* 2007, 330, 145.
2. A. Thangaraj, R. Kumar, P. Ratnasamy, *J. Catal.* 1991, 131, 294.
3. A. C. Garade, V. S. Kshirsagar, R. B. Mane, A. A. Ghalwadkar, C. V. Rode, *Appl. Clay Sci.* 2010, 48, 164.
4. J. Wang, Y. Yoichi Masui, M. Onaka, Euro. *J. Org. Chem.* 21, 1763.
5. X. Xie, Y. Li, Z. Liu, M. Haruta, W. Shen, *Nature* 2009, 458, 746.
6. W. H. Bragg, W. L. Bragg, The Crystalline State, Vol. 1, McMillan, New York 1949.
7. G. Bergeret, in: Handbook of Heterogeneous Catalysis, Vol. 2, Eds: G. Ertl, H. Knozinger, J. Weitkamp, Wiley-VCH, Weinheim, 1997, pp. 464.
8. S. Brunauer, P. H. Emmett, E. Teller, *J. Am. Chem. Soc.* 1938, 60, 309.
9. E. P. Barrett, L. G. Joyner, P. P. Halenda, *J. Am. Chem. Soc.* 1951, 73, 373.
10. Y. Kamiya, Y. Ooka, C. Obara, R. Ohnishi, T. Fujita, Y. Kurata, K. Tsuji, T. Nakajyo, T. Okuhara, *J. Mol. Catal. A: Chem.* 2007, 262, 77.
11. E. Modrogan, M. H. Valkenberg, W. F. Hoelderich, *J. Catal.* 2009, 261, 177.
12. S. Udayakumar, S. Ajaikumar, A. Pandurangan, *Appl. Catal. A: Gen.* 2006, 302, 86.
13. P. Gabbott, Principles and Applications of Thermal analysis, Wiley- Blackwell, 2007.
14. P. D. Garn: Thermoanalytical Methods of Investigation, Academic Press, New York, 1965.
15. O. Scherzer, *J. Appl. Phys.* 1949, 20, 20.
16. J. M. Thomas, O. Terasaki, P. L. Gai, W. Zhou, J. Gonzalez-Calbet, *Acc. Chem. Res.* 2001, 34 583.
17. A. Stefánsson, I. Gunnarsson, N. Giroud, *Anal. Chim. Acta* 2007, 582, 69.
18. J. M. Mermet, J. Anal. At. *Spectrom.* 2005, 20, 11.
19. A. M. Venezia, *Catal. Today* 2003, 77, 359.

20. A. M. Krebs, K. Buswell, W. H. Rodebush, *J. Ame. Chem. Soc.*1937, 59, 2603.

21. X. Xie, W. Shen, *Nanoscale* 2009, 1, 50.

22. J. Xu, P. Gao, T. S. Zhao, *Energy Environ. Sci.* 2012, 5, 5333.

Chapter 3

Solid acid catalysts for hydroxyalkylation reactions

3.1. INTRODUCTION

Hydroxyalkylation reactions are of great interest in fine chemistry, because they enable functionalization of aromatic compounds and offer a wide range of possibilities for the preparation of high value-added compounds that find applications in areas including medicine and pharmacy, agriculture, dye industry, and many others as discussed in chapter 1of Section A (section 1.2). In this chapter, study on detailed catalyst characterization, activity evaluation and acidity–activity relationship of solid acid catalysts for the industrially important hydroxyalkylation reactions is discussed. Three different solid acid catalysts developed were:

a) MCM-41 supported phosphotungstic acid (PTA/MCM-41) for the hydroxyalkylation of phenol to phenolphthalein.
b) SO_3H-MCM-41@Fe_3O_4 catalyst for the hydroxyalkylation of guaiacol to vanillyl alcohol.
c) Metal cation-exchanged montmorillonite clay catalysts for the hydroxyalkylation of *p*-cresol to 2, 2′-methylenebis (4-methyl phenol).

The reasons for the selection of these three catalysts were:

(a) HPA is known to have excellent acidic properties. However, in a polar medium HPA gets dissolved hence MCM-41 was used as a matrix to hetrogenize HPA in a polar medium also and this approach gave very good results.

(b) MCM-41 itself was then functionalized with SO3H and Fe3O4 was also incorporated to make the catalyst separation more easy, merely by applying the magnetic field.

(c) Montmorillonite clay possesses some acid sites however, the strength may not sufficient for catalyzing the hydroxyalkylation reaction, which generally needs Brönsted acidity. Hence, the montmorillonite clay was modified by incorporating suitable metal cations.

Each of the three catalysts was evaluated for three different industrially important hydroxyalkylation reactions, the discussion of which is presented below.

3.2. MCM-41 SUPPORTED PHOSPHOTUNGSTIC ACID FOR THE HYDROXYALKYLATION OF PHENOL TO PHENOLPHTHALEIN

Condensation of phenol with phthalic anhydride in the presence of acid catalyst give phenolphthalein (Scheme 3.1), which has wide ranging applications in polymer industry as already discussed in Section A (section 1.2) of chapter1.The available processes for phenolphthalein synthesis utilizing mineral or Lewis acids are time-consuming (15−20 h) and energy intensive due to tedious separation and recovery steps for pure products from homogeneous reaction crude. The most commonly used Lewis acid for phenolphthalein manufacture is $ZnCl_2$ required in relatively large amounts (0.6 moles for per mole of phthalic anhydride), [1] which increases the viscosity with the progress of the reaction. Hence, it was desirable to develop a suitable heterogeneous catalyst.

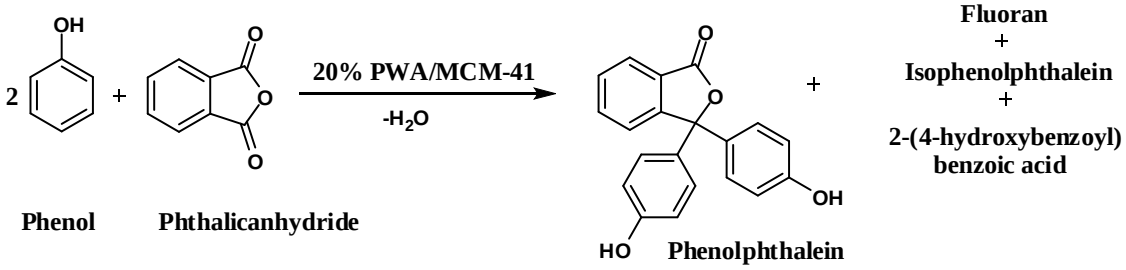

Scheme 3.1. Synthesis of phenolphthalein from phenol and phthalic anhydride

Phosphotungstic acid (PTA) is one of the best solid materials having strong acidity for catalyzing various organic reactions of practical interest. Two major drawbacks of PTA, namely, (i) very low surface area and (ii) their instability in polar solvents, limit their applicability on a wide scale. In our work, MCM-41 was chosen as a matrix to impregnate the PTA, in order to enhance catalyst stability in polar media as well as higher dispersion for better exposure of the acid sites [2]. This approach was found to be successful giving an active and selective solid acid catalyst for condensation of phenol and phthalic anhydride to form phenolphthalein. The activity of PTA/MCM-41 has been

also compared with those of different other solid acid catalysts like PTA/Mont K10, and Mont KSF/O. The versatility of our catalyst system was also proven by its activity for hydroxyalkylation of phenol and *p*-cresol to the corresponding dihydroxydiarylmethane (DAM) compounds.

3.2.1. Experimental

PTA with different loadings (10−30%) dispersed on MCM-41 were prepared by wet impregnation method and the detail experimental procedure of their preparation has been described in chapter 2 of Section A (section 2.3.1.1). The catalysts were characterized by XRD, N_2 adsorption-desorption isotherm, NH_3-TPD, and pyridine-FTIR techniques according to the procedure described in chapter 2 of Section A (sections 2.4.1, 2.4.2, 2.4.3 and 2.4.4). The activity testing of prepared catalysts was carried out in a magnetically stirred glass reactor (capacity 50 mL), fitted with a reflux condenser for the hydroxyalkylation of phenol to phenolphthalein following the experimental procedure described in chapter 2 of Section A (sections 2.5.1.1). Liquid samples were analyzed by a Hewlett-Packard model 1050 chromatograph equipped with an ultraviolet detector (λ_{max} = 254 nm) on a 25 cm RP-18 column.

3.2.2. Results and discussion

3.2.2.1. Catalyst characterization

Low angle XRD diffractograms of pure MCM-41 and PTA/MCM-41 samples are shown in Fig. 3.1. The pure MCM-41 sample (Fig. 3.1. a) showed three (100), (110), and (200) diffraction peaks below 10° (2θ), which indicate the formation of an ordered hexagonal mesoporous structure [3, 4]. Interestingly, 10%, 20%, and 30% PTA/MCM-41 samples also showed XRD peaks (Fig. 3.1. b-d) similar to that of parent MCM-41; however, the intensity of (100) reflection peak of the MCM-41 diminished with an increase in PTA loading from 10 to 30% (Fig. 3.1). This decrease in the intensity of (100) peaks could be due to the beginning of disorder in the hexagonal structure of MCM-41 support with the increase in PTA loading [5].

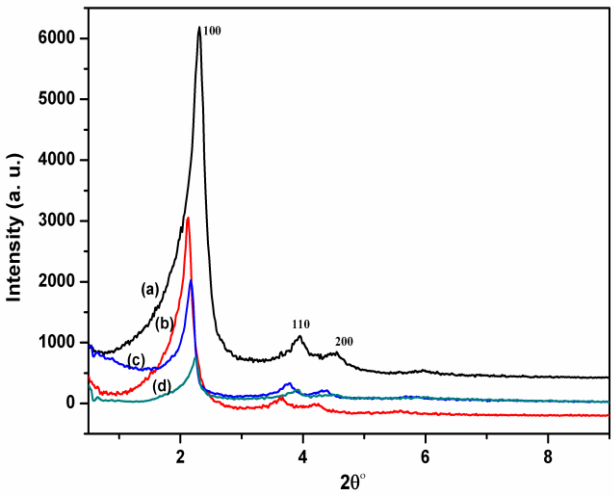

Fig. 3.1. Low angle XRD patterns of calcined materials: (a) MCM-41, (b) 10% PTA/MCM-41, (c) 20% PTA/MCM-41, and (d) 30% PTA/MCM-41

Wide angle X-ray diffraction patterns of MCM-41, PTA/MCM-41, and bulk PTA are shown in Fig. 3.2. The parent MCM-41 shows a broad band in the range of 2θ = 15−40°, which is a characteristic of siliceous material [6]. All PTA/MCM-41 samples (10−30% PTA loading on MCM-41) showed XRD patterns (Fig. 3.2b −d) similar to that of parent MCM-41. No separate crystal phase characteristic of bulk PTA exists in the 10%, 20%, and 30% PTA/MCM-41 samples due to the larger surface area of MCM-41. This also confirms the high dispersion of PTA on MCM-41 support.

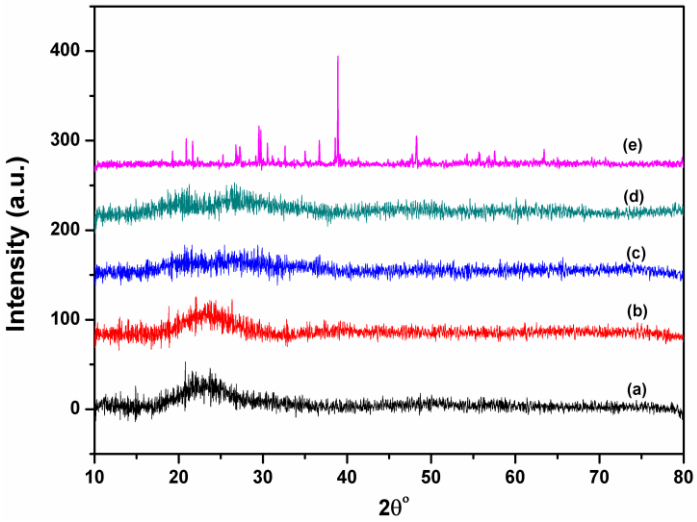

Fig. 3.2. Wide angle XRD patterns of (a) MCM-41, (b) 10% PTA/MCM-41, (c) 20% PTA/MCM-41, (d) 30% PTA/MCM-41, and (e) bulk PTA

The acidic properties of the samples with PTA loading ranging from 10 to 30% were investigated by FT-IR spectroscopy of adsorbed pyridine and NH_3-TPD measurements. FT-IR spectra of chemisorbed pyridine showed both Brönsted as well as Lewis acid sites in these samples (Fig. 3.3). The band at 1545 cm^{-1} (pyridinium ion) was assigned to Brönsted acid sites, whereas bands at 1610 and 1450 cm^{-1} (pyridine coordinated to Lewis acid sites) were assigned to Lewis acid sites. The band at 1490 cm^{-1} (hydrogen bonded pyridine) is common to both types of acidic sites [7, 8]. The surface of MCM-41 contained only Lewis acid sites, but as PTA was dispersed on MCM-41, both Brönsted as well as Lewis acid sites were observed. The acidity increased gradually with increasing PTA loading, as revealed by the acidity measurement (NH_3-TPD) shown in Fig. 3.4. Parent MCM-41showed (Fig. 3.4a) a very small hump indicating low acidity which was in accordance with the results of pyridine IR (Fig. 3.3) while PTA/MCM-41 samples with various PTA loadings, showed broad desorption peaks near 573 K (Fig. 3. 4b−d).

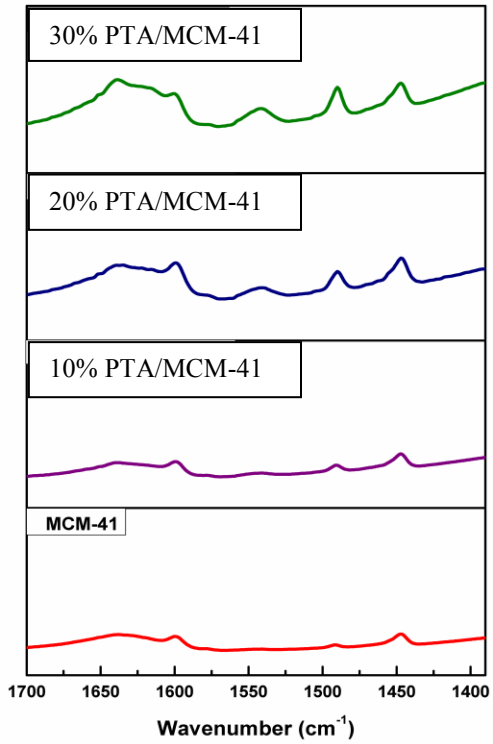

Fig. 3.3. FT-IR pyridine spectra of MCM-41 and 10−30% PTA/MCM-41catalysts

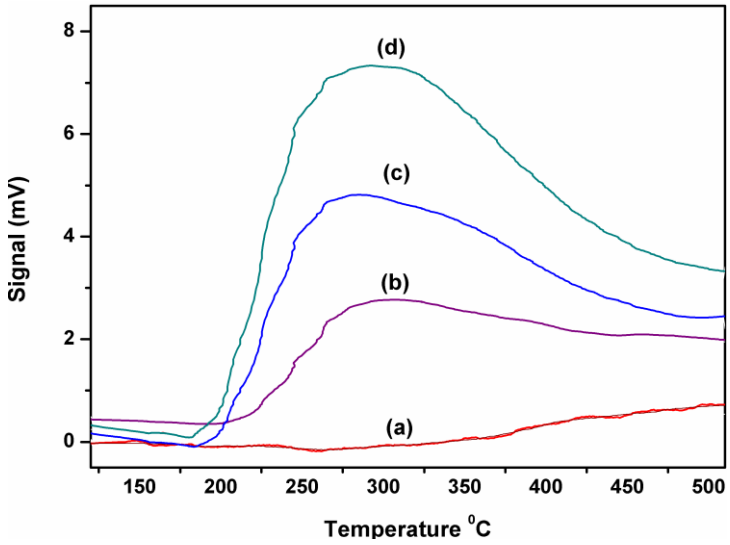

Fig. 3.4. NH_3-TPD profiles of (a) MCM-41, (b) 10% PTA/MCM-41, (c) 20% PTA/MCM-41, and (d) 30% PTA/MCM-41 catalysts

The concentration of acid sites (in terms of NH_3 desorbed) of parent MCM-41 increased from 0 to 0.9 μmol S^{-1} with an increase in PTA loading from 0 to 30% (Table 3.1).

Table 3.1. Textural properties of the catalysts

Catalysts	Surface area (m^2/g)	Pore size BJH_{des}(nm)	Pore volume BJH_{des} (cc/g)	NH_3 desorbed (μmol/S)
MCM-41	1250	3.98	1.28	Nil
10%PTA/MCM-41	1050	3.84	0.98	0.2
20%PTA/MCM-41	1036	3.72	0.96	0.4
30%PTA/MCM-41	619	3.57	0.55	0.9
Bulk PTA	8.3	-	-	93.6
20%PTA/Mont K10	130	-	-	4.8
Montmorillonite KSF/O	128.4	-	-	6

Nitrogen adsorption–desorption measurements were used to study the textural properties of the prepared catalysts. A typical isotherm of the MCM-41 and 20% PTA/MCM-41 samples are shown in Fig. 3.5 curves a and b, respectively. Isotherms of MCM-41 and

20% PTA/MCM-41 showed a type IV isotherm having a hysteresis loop at p/po = 0.3−0.4, which is a characteristic of mesoporous materials [9]. With increasing PTA loading, the hysteresis loop became gradually shorter corresponding to a reduction in the pore volume. A bend in the adsorption−condensation region, at p/po = 0.3−0.4 for the 20% PTA/MCM-41 sample could be due to dispersion of PTA over the walls of MCM-41 [10]. Table 3.1 shows values of BET surface area, pore size, and pore volume for MCM-41 and supported PTA catalysts. It was observed that parent MCM-41 had the highest surface area and pore volume among the prepared catalysts, [11] while an increase in PTA loading caused a reduction in the pore volume and notable compression of the pore size distribution, which seems logical as the impregnated PTA was dispersed and deposited on the support surface, decreasing the pore diameter and thus diminishing the surface area [12].

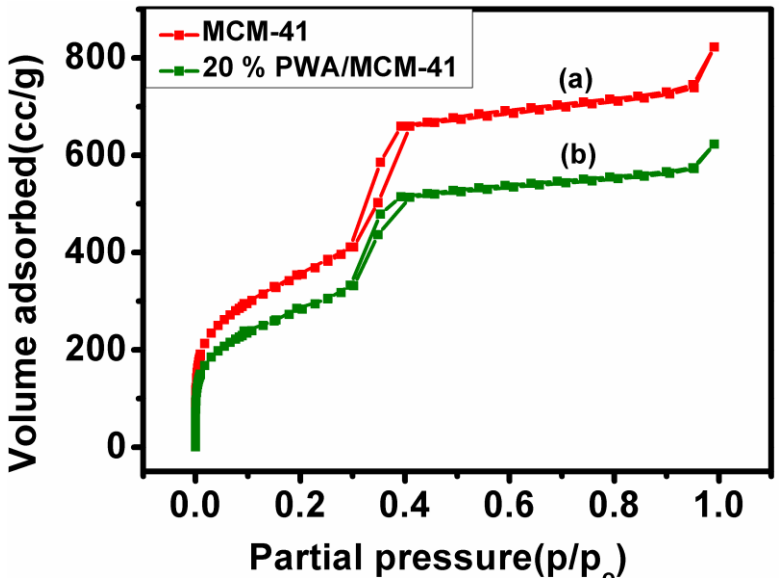

Fig. 3.5. Adsorption isotherms of (a) MCM-41 and (b) 20% PTA/MCM-41 catalysts

These observations were also consistent with the low angle XRD results, which showed a decrease in intensity of the (100) diffraction peak due to diminishing hexagonal order structure with PTA loading. However, the average pore size distribution of the prepared catalysts was centered at about 24.5 Å, the same as that of parent MCM-41 (Fig. 3.6).

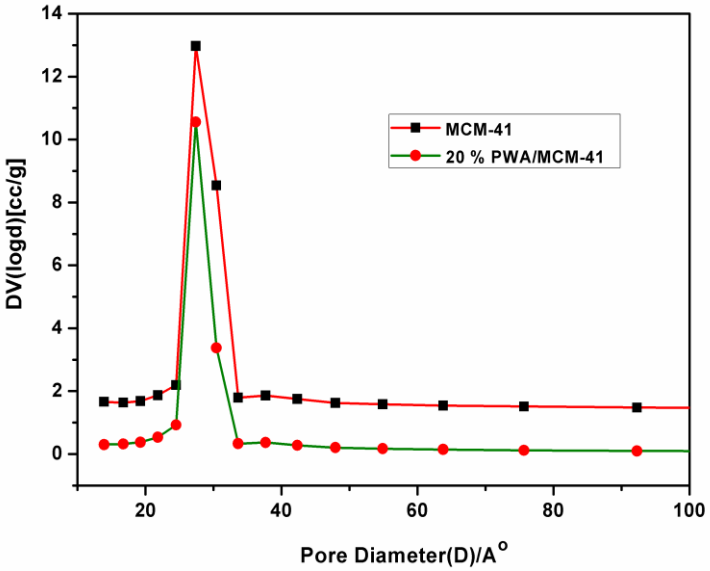

Fig. 3.6. Pore size distribution of MCM-41 and 20% PTA impregnated MCM-41 catalysts

3.2.2.2. Catalytic activity of 20% PTA/MCM-41

Phenolphthalein synthesis is an acid-catalyzed condensation reaction of phenol and phthalic anhydride, for which various solid acid catalysts were screened (Fig. 3.7). Among these, 20% PTA/MCM-41 catalyst showed better activity and selectivity to phenolphthalein. Almost negligible activity of MCM-41 (not shown in the figure) was due to its extremely low concentration of acidic sites (Figs. 3.3 and 3.4) which was a more predominant factor than its surface area (Table 3.1). On the other hand, bulk PTA showed lowest activity as compared to the supported PTA catalysts despite its strong Brönsted acidity. The very low surface area (<10 m^2/g) of bulk PTA causes limited availability of acidic sites on the surface, [8] hence lower activity for acid catalyzed hydroxyalkylation of phenol and phthalic anhydride. When bulk PTA was dispersed on MCM-41, a number of active sites on the surface increased considerably leading to higher activity of supported PTA catalysts as compared to bulk PTA.

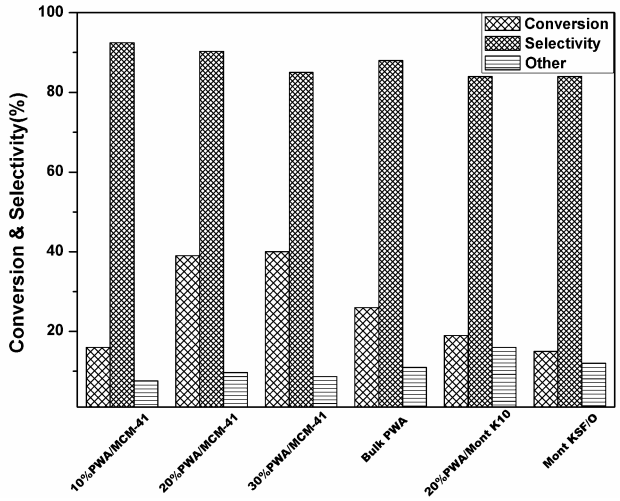

Fig. 3.7. Catalyst screening for the synthesis of phenolphthalein. Reaction conditions: phenol, 34.0 mmol; phthalic anhydride, 16.2 mmol; catalyst concentration, 0.1 g/cm^3; temperature, 423 K; time, 3 h; mole ratio of phenol to phthalic anhydride, 2:1

In case of 20% PTA/Mont K10 and Mont KSF/O catalysts, conversion of phthalic anhydride was less than that of PTA supported catalysts but higher than bulk PTA. This result could be due to the lower surface areas of 20% PTA/Mont K10 and Mont KSF/O catalysts as compared to the PTA/MCM-41catalysts but higher than bulk PTA. The catalyst performance of 20% PTA/MCM-41 was also evaluated for the hydroxyalkylation of phenol and *p*-cresol with formaldehyde (Schemes 3.2 and 3.3, respectively) to give corresponding DAM. For the hydroxyalkylation of phenol, 20% PTA/MCM-41 showed 31% conversion of phenol with 94 and 6% selectivity to bisphenol F and trimers, respectively. While for the *p*-cresol hydroxyalkylation reaction, it gave 34% conversion with 97 and 3% selectivity to DAM and trimer, respectively. The catalyst activity and reusability results of 20% PTA/MCM-41 for the hydroxyalkylation of phenol and *p*-cresol are discussed in the later section (Fig. 3.13. a,b).

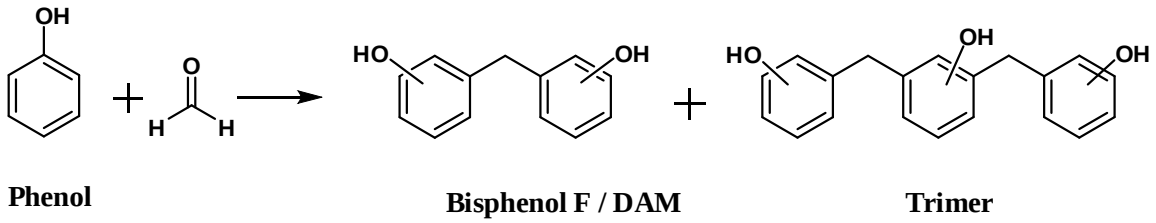

Scheme 3.2. Hydroxyalkylation of phenol with formaldehyde

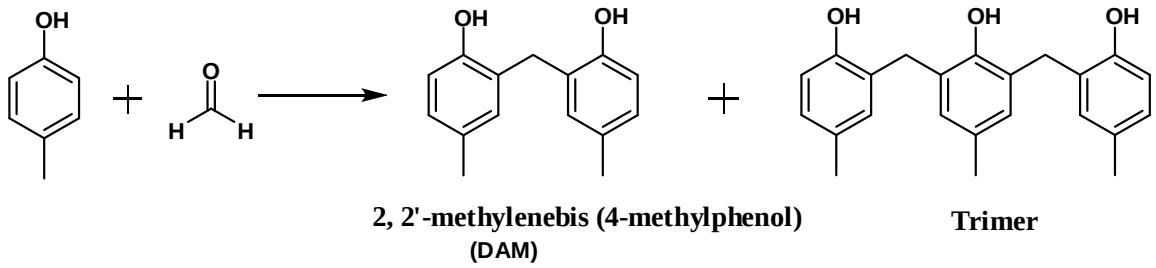

Scheme 3.3. Hydroxyalkylation of *p*-cresol with formaldehyde

The effect of the mole ratio of phthalic anhydride to phenol on conversion and phenolphthalein selectivity were studied in the range of 1:1 to 1:3 for 20% PTA/MCM-41 catalyst by varying the concentration of phenol at a constant phthalic anhydride concentration, and the results are presented in Fig. 3.8.

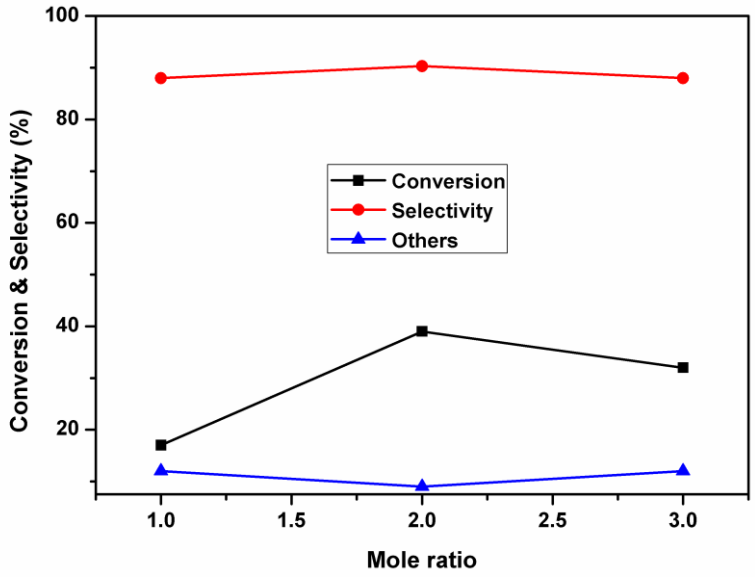

Fig. 3.8. Influence of mole ratio of phenol to phthalic anhydride on the conversion of phthalic anhydride catalyzed by 20% PWA/MCM-41.Reaction conditions: temperature, 150 ^{o}C; time, 3 h; catalyst weight, 0.1 cm^{3}/g; mole ratio of phenol to phthalic anhydride, 1:1 to 1:3.

The conversion of phthalic anhydride increased from 17 to 40% as the mole ratio of phthalic anhydride to phenol increased from 1:1 to 1:2. Since the formation of phenolphthalein involves the condensation of two moles of phenol with one mole of phthalic anhydride, conversion of the latter was facilitated with an increase in phenol amount from 1:1 to 1:2. With a further increase in the mole ratio from 1:2 to 1:3, the conversion of phthalic anhydride decreased from 40 to 32%, while selectivity to phenolphthalein remained almost constant (91%). This could be explained based on the competition between phenol and phthalic anhydride molecules for active acid sites of the catalyst. Since nucleophilicity of the phenol molecule is higher than that of phthalic anhydride, causing better adsorption of the former rather than the latter on active acid sites resulted in lower conversion of phthalic anhydride.

The effect of the catalyst concentration in the range of 0.02−0.1 g/cm^3 on the conversion of phthalic anhydride and phenolphthalein selectivity was also studied, and the results are presented in Fig. 3.9.

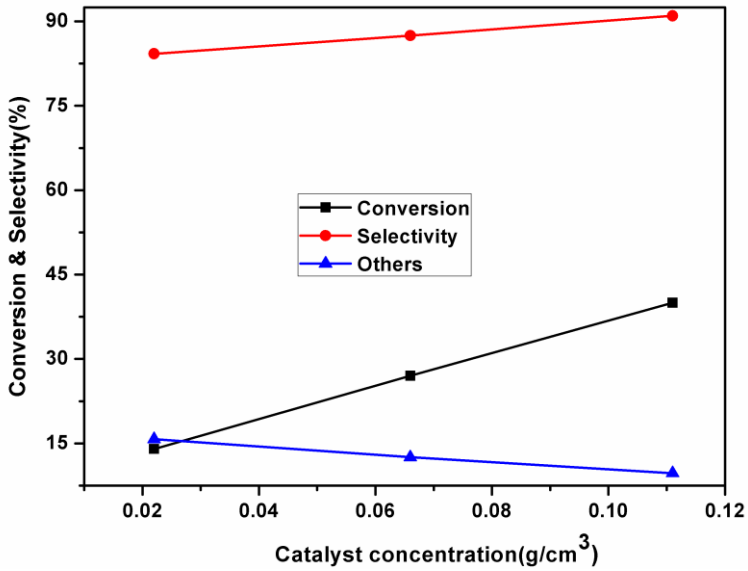

Fig. 3.9. Effect of catalyst amount on conversion and selectivity. Reaction conditions: phenol, 34.0 mmol; phthalic anhydride, 16.2 mmol; catalyst concentration, 0.02−0.1 g/cm^3; temperature, 150 ^{o}C; time, 3 h; mole ratio of phenol to phthalic anhydride, 2:1; catalyst, 20% PTA/MCM-41

The conversion of phthalic anhydride and selectivity to phenolphthalein increased from 14 to 40% and 84 to 91%, respectively, with an increase in catalyst concentration from 0.02 to 0.1 g/cm^3. This is obvious since with the increase in catalyst concentration; the acidic sites also increased, which facilitated the reaction of initially formed carbinol with a second molecule of phenol to give phenolphthalein.

The effect of temperature on both conversion of phthalic anhydride and phenolphthalein selectivity was studied in the temperature range of 393−453 K (Fig. 3.10). The conversion of phthalic anhydride increased from 33 to 51%, while selectivity to phenolphthalein decreased from 91 to 80% with an increase in temperature from 393 to 453 K. The low phenolphthalein selectivity could be due the formation of undetected tarry product by further reaction of phenolphthalein with available phenol. This also led to a lowering of the material balance from 98 to 81%.

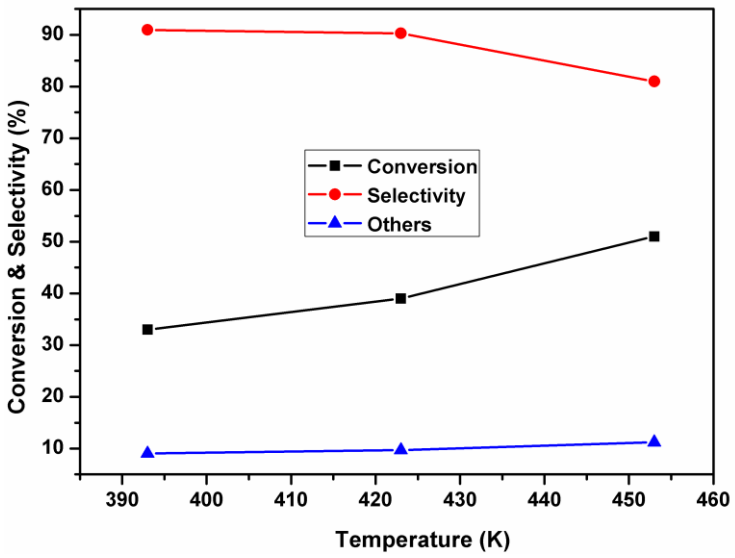

Fig. 3.10. Effect of temperature on conversion and selectivity. Reaction conditions: phenol, 34.0 mmol; phthalic anhydride, 16.2 mmol; catalyst concentration, 0.1 g/cm^3; temperature, 393−423 K; time, 3 h; mole ratio of phenol to phthalic anhydride, 2:1; catalyst, 20% PTA/MCM-41.

The effect of reaction time on the phthalic anhydride conversion and phenolphthalein selectivity was studied for a mole ratio of 1:2 (Fig. 3.11). The conversion of phthalic anhydride increased from 26 to 40%, while selectivity to phenolphthalein remained almost constant (91%) with an increase in reaction time from 1 to 3 h. With further increase in reaction time from 3 to 5 h, the conversion of phthalic anhydride increased from 40 to 48%; however, undetected tarry products were also observed.

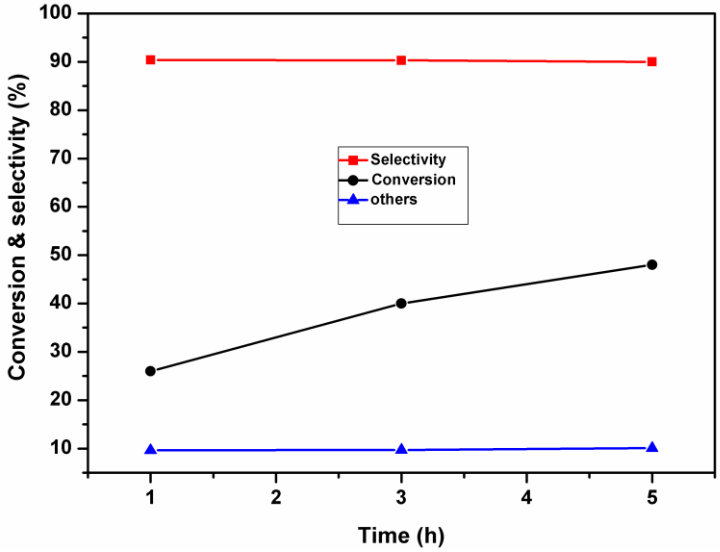

Fig. 3.11. Effect of time on conversion and selectivity. Reaction conditions: phenol, 34.0 mmol; phthalic anhydride, 16.2 mmol; catalyst concentration, 0.1 g/cm^3, temperature, 423 K; time, 1−5 h; mole ratio of phenol to phthalic anhydride, 2:1; catalyst, 20% PTA/MCM-41.

Catalyst recycling experiments for 20% PTA/MCM-41catalyst were carried out by separating the catalyst of the first run by filtration. It was then washed with dichloromethane and reused after calcination at 573 K for 3 h. Fig. 3.12 shows the results on catalyst recycle for phenolphthalein synthesis in which the conversion of phthalic anhydride decreased from 40 to 31% after first recycle experiment. Interestingly, the conversion only marginally decreased from 31 to 26% after the fourth recycle experiment. The initial loss of substantial activity was due to the leaching and dissolution of the supported PTA as confirmed by ICP−OES analysis. The elemental analysis of W present in PTA by ICP−OES showed 5.4% leaching of PTA from the support after the

first recycle experiment. The extent of leaching was marginal as indicated by 2.1%, 0.7%, and 0.2% after the second, third, and fourth recycles experiments. This was also reflected by the fact that used catalyst showed the same conversion of 26% after the third and fourth recycles experiments. Such type of leaching of PTA from the support was reported by many researchers in the case of PTA-supported catalysts [13−15].

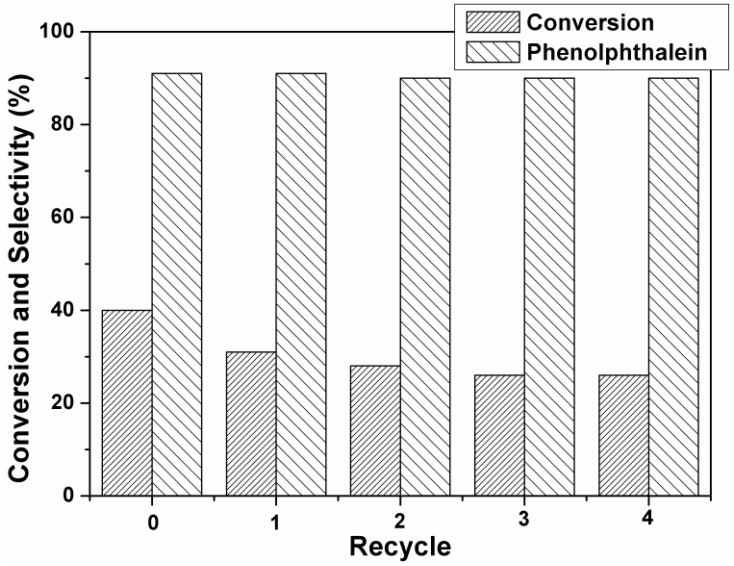

Fig. 3.12. Recycle experiments for synthesis of phenolphthalein. Reaction conditions: phenol, 34.0 mmol; phthalic anhydride, 16.2 mmol; catalyst concentration, 0.1 g/cm3; temperature, 423 K; time, 3 h; mole ratio of phenol to phthalic anhydride, 2:1.

The reusability of 20% PTA/MCM-41 was also studied for the hydroxyalkylation of phenol and *p*-cresol, and the results are presented in Fig. 3.13. a, b. The catalyst was found to retain its activity even after a fourth recycle experiment for the hydroxyalkylation of phenol (Fig.3.13a) and *p*-cresol (Fig.3.13b) with formaldehyde. The conversion of phenol and *p*-cresol was marginally decreased from 31 to 28% and 34 to 32%, respectively, after the fourth recycle experiment. This slight decrease in the activity could be due to the handling loss of the catalyst as well as partial leaching of PTA from the support (<1.5% after the first recycle experiment).

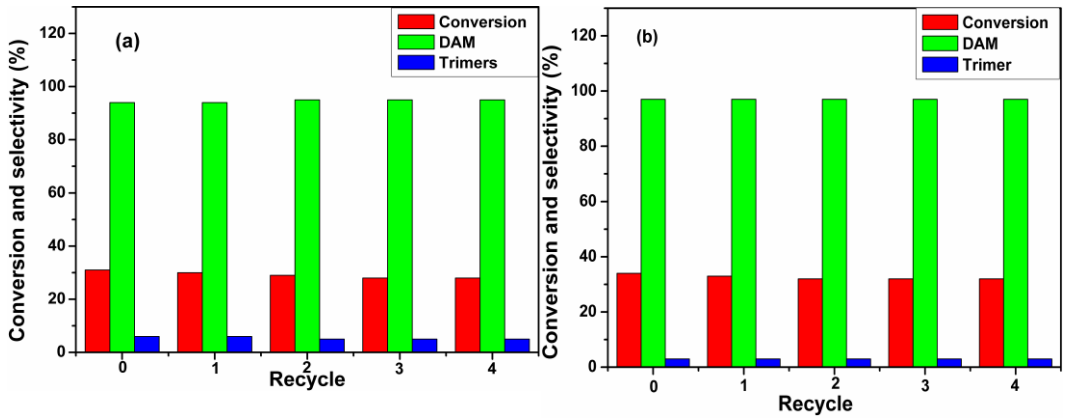

Fig. 3.13. Recycle experiments for the hydroxyalkylation of **(a)** phenol and **(b)** *p*-cresol with formaldehyde. Reaction conditions: phenol/*p*-cresol, 40 mmol; formaldehyde, 5 mmol; catalyst concentration, 0.03 g/cm^3; temperature, 353 K; time, 2 h; mole ratio of phenol to formaldehyde, 5; solvent, toluene (12 mL).

A separate hydroxyalkylation experiment was also performed using a physical mixture of 20% PTA and 80% MCM-41 under similar reaction conditions, which showed a very low activity (17% conversion of phthalic anhydride with 90% selectivity to phenolphthalein) as compared to 20% PTA/MCM-41 catalyst in 3 h. This indicated that the dispersion of PTA over the MCM-41 in the case of 20% PTA/MCM-41, resulting into redistribution of acid sites, is mainly responsible for the catalytic activity.

3.2.2.3. Plausible mechanistic pathway

A plausible mechanistic pathway for the hydroxyalkylation of phenol with formaldehyde to give Bisphenol F (4, 4'-isomer) is shown in Scheme 3.4. In a commercial aqueous solution of formaldehyde (37%), the monomeric form of formaldehyde (around 40% with respect to total formaldehyde) is mostly present in the form of methylene glycol while, the remaining 60% of formaldehyde is in oligomeric form (polyoxymethylene glycols and polyoxymethylene hemiacetals). In the first step, methylene glycol is activated by a proton from the catalyst to form methyol cation (I) with release of a water molecule. The electrophilic attack of methyol cation on phenol takes place in the second step to form a resonance-stabilized carbocation (II). This is followed by a proton transfer from

carbocation (II) to the catalyst and a carbinol (*p*-hydroxy benzyl alcohol) (III) is formed with regeneration of the catalyst. The hydroxymethyl group of the carbinol abstracts a proton from the catalyst to form hydroxy benzyl carbocation (IV). Finally, the electrophilic attack of hydroxy benzyl carbocation on the second molecule of phenol followed by a proton transfer to catalyst gives bisphenol F (4, 4'-isomer) (V) with regeneration of the catalyst [16].

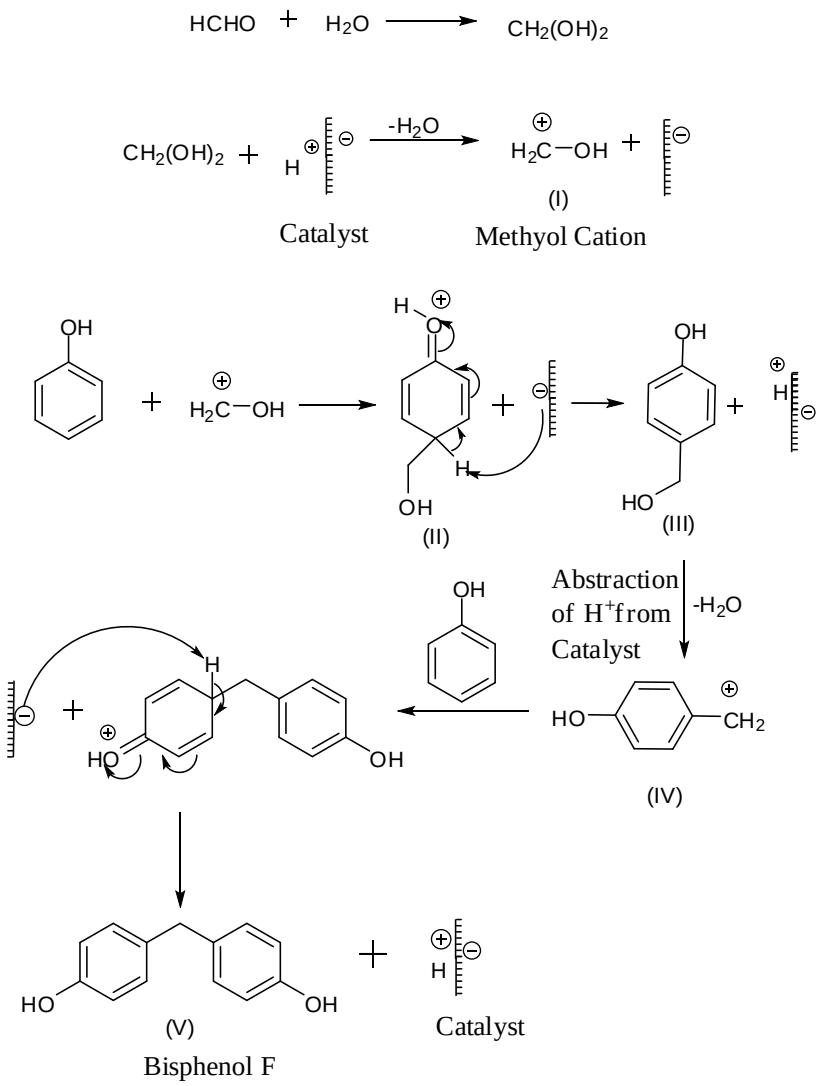

Scheme 3.4. Plausible mechanistic pathway for hydroxyalkylation of phenol

3.3. MAGNETICALLY SEPARABLE SOLID ACID CATALYST FOR THE HYDROXYALKYLATION OF GUAIACOL TO VANILLYL ALCOHOL

Another novel solid acid catalyst developed for the hydroxalkylation reaction was a ferrite based MCM-41 functionalized with SO_3H- group. This catalyst was evaluated for hydroxyalkylation of 2-methoxyphenol (guaiacol) to 3-methoxy-4-hydroxy benzyl alcohol (*p*-vanillyl alcohol) which involved in the multi stage synthesis of 3-methoxy-4-hydroxybenzaldehyde (vanillin), an environmentally friendly process for the production of this important food additive (Scheme 3.5) [17]. Vanillin has wide ranging applications in foods and perfumes because of its flavor and also finds use in medicinal applications or as platform chemicals for pharmaceuticals production [18].

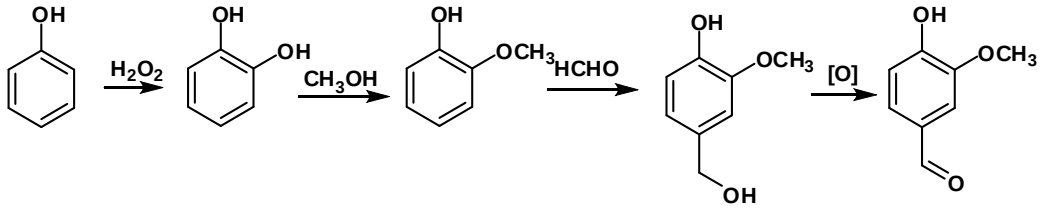

Scheme 3.5. Multi-step synthesis of vanillin starting from phenol

Vanillyl alcohol is conventionally prepared by the hydroxyalkylation of guaiacol with formaldehyde or glyoxylic acid in presence of strong mineral acids like hydrochloric acid, or quarternary ammonium salts [19]. Although these reagents based process gave acceptable yields of the desired product, the procedure has some major drawbacks like difficulties in the separation and recovery of pure product from the reaction medium, handling of the reagents, problems due to corrosive nature of reagents and formation of inorganic wastes due to use of reagents in the stoichiometric quantities [20]. Among various solid acid catalysts, explored for this reaction zeolites were extensively used for the hydroxyalkylation of guaiacol to vanillyl alcohol [21]. Cavani *et al.* demonstrated that HM-45 zeolite is able to catalyze hydroxyalkylation of guaiacol, give 40% conversion and 70% selectivity to vanillyl alcohol [22]. Zeolites in their H^+ form are the most widely used solid acids in petrochemistry and gas phase reactions. However, when moving to fine chemistry and for liquid phase, batch wise reactions typical of organic synthesis,

zeolites are not the universal acid catalysts. The main drawback of zeolites as general solid acids is their microporous nature (<1.0 nm) that imposes a severe restriction for the diffusion of substrates and products through the pores of the zeolites, it leads to a substantial decrease in the reaction rate [23]. Other solid acid catalysts like HPAs possess strong acidity having potential applications in acid catalyzed reaction [24]. Nevertheless, commercial applications of HPAs are rather restricted due to their very low surface area and high solubility in polar solvents [25]. Hence, there is a scope to develop such catalysts which can minimize the diffusion problem and show the catalyst stability during the reaction.

As already discussed in chapter 1, selective hydroxyalkylation is a more challenging reaction due to its consecutive nature that lead to the predominant formation of dihydroxydiarylmethane as a by-product and deactivation of the catalyst was due to deposition of bulky and higher molecular weight condensation products on the catalyst surface. In this respect, hydroxyalkylation of guaiacol is still more challenging, in which a very high mole ratio (1:15 to 1:20) of guaiacol to formaldehyde is necessary to achieve the highest selectivity to the intermediate vanillyl alcohol [22]. When formaldehyde (37% aqueous) is one of the reactants, the major problem is the presence of water, which blocks the active sites of the catalyst, causing loss of catalytic activity. The development of hydrophobic solid acid catalyst is expected to minimize this problem. Therefore, we developed a solid acid catalyst comprising organo sulfonic acid ($-CH_2CH_2CH_2SO_3H$) grafted on to the porous walls of the mesoporous silica bonded magnetite. The acidic proton in the hydrophobic environment of organo modified mesoporous silica was active for hydroxyalkylation of guaiacol that gave 20% conversion and 60% selectivity to vanillyl alcohol (Scheme 3.6).

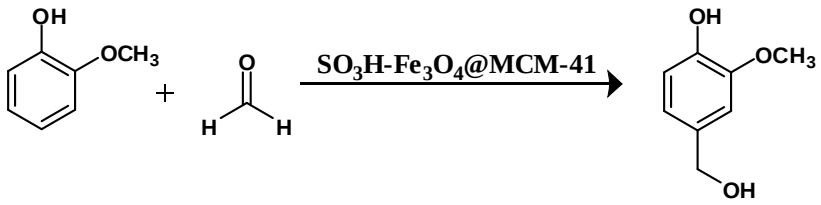

Scheme 3.6. Hydroxyalkylation of guaiacol with formaldehyde

Catalyst activity comparison study was carried out using various solid acids catalysts such as amberlyst-15, PTA supported on different supports like fumed SiO_2, Mont K10, Mont KSF and sulfonic acid grafted on mesoporous silica bonded magnetite. These catalysts were characterized by BET surface area measurement, IR, HR-TEM, and by XRD. Effect of various reaction parameters like mole ratio of guaiacol to formaldehyde, reaction temperature, catalyst concentration and reaction time on guaiacol conversion and on product selectivity were also studied for the hydroxyalkylation of guaiacol. The reusability of the catalyst (SO_3H-Fe_3O_4@MCM-41) was also evaluated by the catalyst recycle experiments.

3.3.1. Experimental

The magnetically separable solid acid catalyst was prepared through a direct synthetic method involving the co-condensation of tetraethoxysilane (TEOS) and mercaptopropyl trimethoxysilane (MPTMS) in the presence of commercial available magnetite and post oxidation of mercapto groups to sulfonic acids by using 30% hydrogen peroxide at room teperature. The detailed synthesis procedures are discussed in chapter 2 of Section A (section 2.3.1.2). Activity testing of the prepared catalysts was carried out in a magnetically stirred glass reactor (capacity 50 mL), fitted with a reflux condenser for the hydroxyalkylation of guaiacol to vanillyl alcohol following the experimental procedure described in sections 2.5.2. Liquid samples were analyzed by a Hewlett-Packard model 1050 HPLC chromatograph equipped with an ultraviolet detector (λ max = 254 nm) on a 25 cm RP-18 column. The catalysts were characterized by XRD, FTIR, TGA and HR-TEM techniques according to the procedure described in chapter 2 of Section A (sections 2.4.1, 2.4.9, 2.4.5 and 2.4.6).

3.3.2. Results and discussion

3.3.2.1. Catalyst characterization

The low angle XRD patterns of SO_3H-Fe_3O_4@MCM-41, synthesized by condensation and grafting methods are shown in Fig. 3.14. For Fe_3O_4@MCM-41sample, the three diffraction peaks in the low-angle XRD region were indexed as (100), (110) and (200),

respectively, are due to the hexagonal array of parallel mesoporous channels. After introducing the sulfonic groups onto the mesoporous wall of Fe_3O_4@MCM-41, the main peak (100) could still be observed clearly, but with slight decrease in intensity. This indicates the existence of the long-range order pores for the derivative sample also [26].

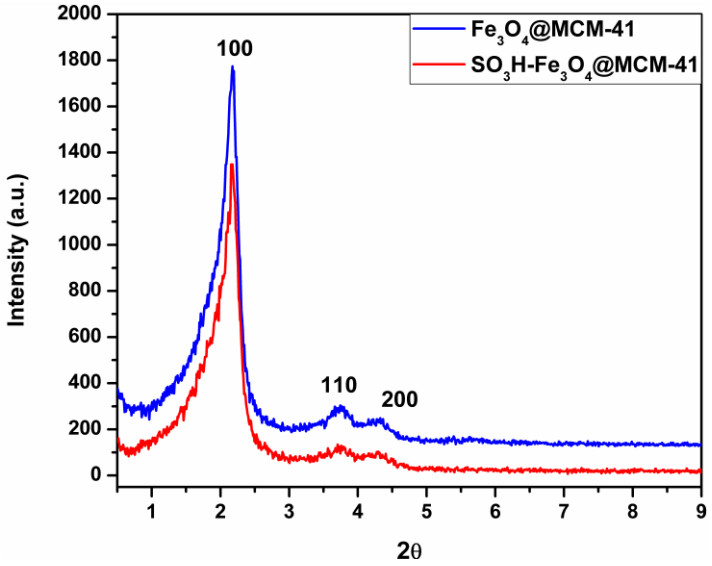

Fig. 3.14. Low angle XRD patterns of Fe_3O_4@MCM-41and SO_3H-Fe_3O_4@MCM-41

Fig. 3.15 shows the wide angle XRD patterns of Fe_3O_4@MCM-41 and SO_3H-Fe_3O_4@MCM-41.

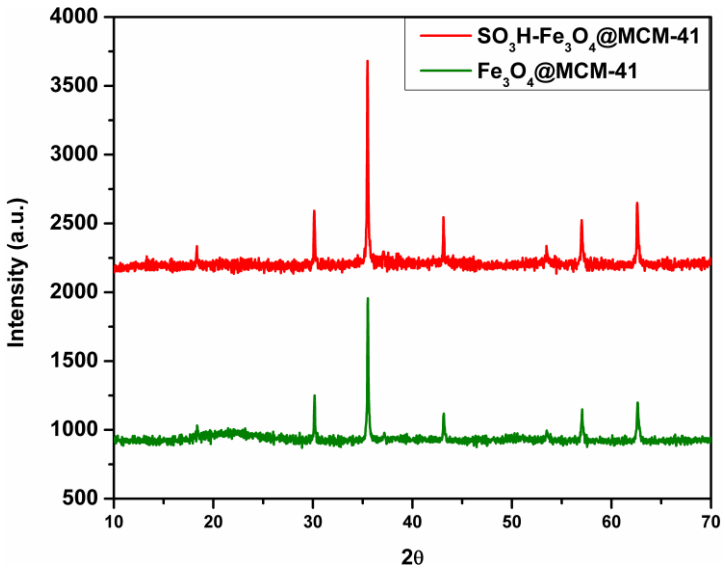

Fig. 3.15. XRD patterns of Fe_3O_4@MCM-41and SO_3H-Fe_3O_4@MCM-41

Both the samples showed diffraction peaks at 2θ = 30.3°, 35.7°, 41.1°, and 49.5° which could be attributed to the parent magnetite. We did not observe any extra peaks due to other iron oxide phases (α- or γ- Fe_2O_3), which are thermodynamically stable and very prone to form when exposed in air. This indicates that iron oxide was covered with MCM-41.

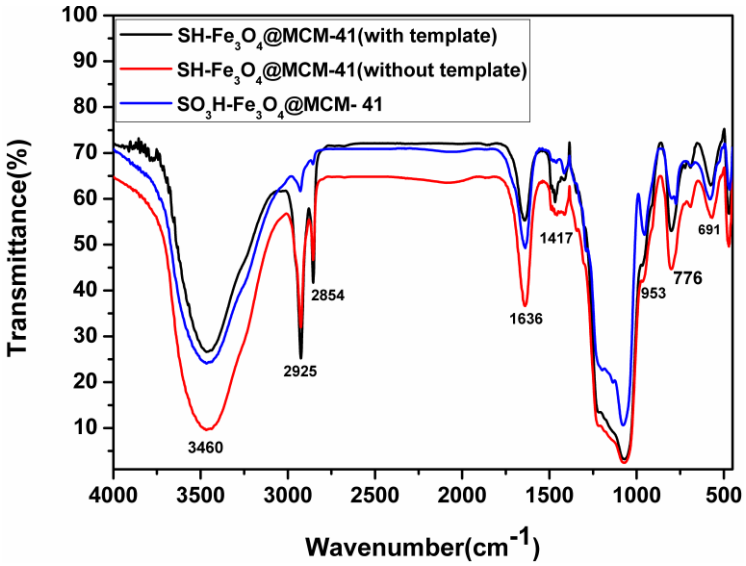

Fig. 3.16. FT-IR spectra of functionalized materials

Due to the paramagnetic nature of the nanoparticle Fe_3O_4, nuclear magnetic resonance (NMR) technique could not be used to confirm surface modifications on the SO_3H-Fe_3O_4@MCM-41 (SO_3H-MS). Instead, FT-IR technique was used to characterize organic functionalities. FTIR analysis of the functionalized materials showed similar spectra as seen in the literature [27]. The O–H stretching of surface hydroxyl groups and physisorbed water were present as broad peaks at 3000–3700 cm^{-1} and a sharper peak at 1636 cm^{-1}, respectively. An intense peak at 1000–1250 cm^{-1} corresponded to the Si–O stretch in the mesoporous silica shell. Evidence of the surface functionalization was could be made by the presence of C–H stretch and C–H bend in the spectra at 2800–3000 cm^{-1} and 1417 cm^{-1}, respectively (Fig. 3.16).

The inclusion of the mercaptopropyl residue into the siliceous framework is clearly demonstrated with thermogravimetric measurements as shown in Fig. 3.17. Typical

weight loss curves of SH-Fe_3O_4@MCM-41 sample in air observed were: 1st weight loss below 200 ^oC, corresponding to hydrated water in the catalyst and 2nd weight loss at 343 ^oC, corresponding to the mercaptopropyl group. However, SO_3H- Fe_3O_4@MCM-41 sample showed one additional weight loss near to 460 ^oC, corresponding to SO_3H- group. These observations indicate that sulfonic groups were grafted on the mesoporous material.

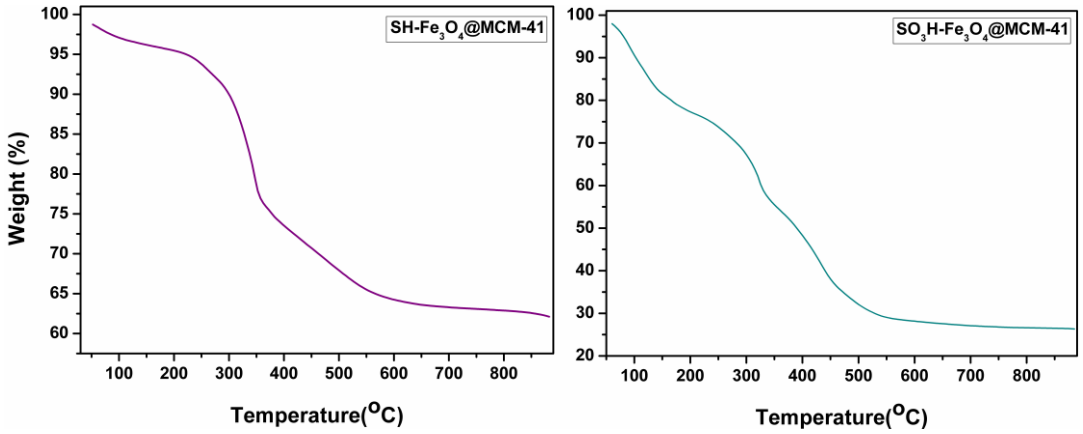

Fig. 3.17. TGA curves of SH-Fe_3O_4@MCM-41 and SO_3H-Fe_3O_4@MCM-41samples

TEM images of SO_3H-Fe_3O_4@MCM-41 catalyst display dark magnetic nanoparticles (50−80 nm) dispersed on the mesoporous silica shell (Fig. 3.18). The aggregation pattern

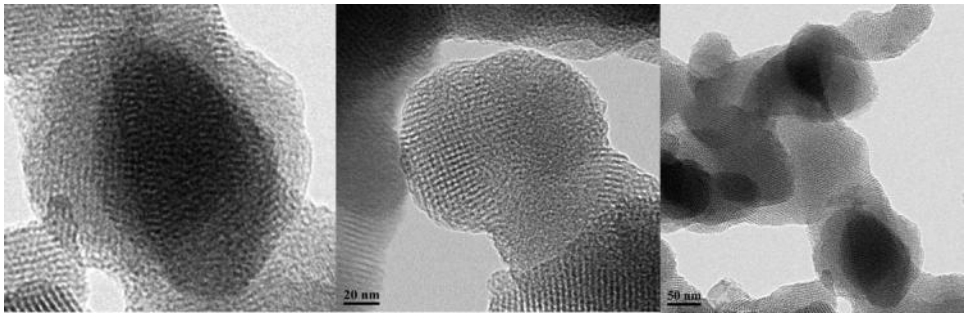

Fig. 3.18. HR-TEM images of SO_3H-Fe_3O_4@MCM-41catalyst

of these magnetic particles determines the shape and size of the final catalyst particles. Thus, these magnetic nanoparticles were successfully embedded in the mesoporous silica, leading to particles ranging in size from 150 to 300 nm. Moreover, the clear lattice fringes observed in the HR-TEM images further confirm the highly ordered hexagonal

arrays and two-dimensional mesoporous parallel channels. These results are in good agreement with the low angle XRD observations.

3.3.2.2. Catalytic Activity

The activity results of various solid acid catalysts screened for the hydroxyalkylation of guaiacol are shown in Fig. 3.19. Among the various catalysts screened, SO_3H-Fe_3O_4@MCM-41 catalyst showed the maximum (60%) selectivity to vanillyl alcohol (after 3 h) while DTP (or PTA) supported on fumed SiO_2 and Mont K10, showed negligible activity for this reaction. However, DTP supported on Mont KSF/O showed the activity but it gave maximum selectively to the dimer product (DAM). Among all the screened catalysts, amberlyst-15 showed the highest conversion of guaiacol with maximum selectivity to DAM (78%). The lesser activity in case of DTP supported on SiO_2, Mont K10 and Mont KSF/O can be explained on the basis of hydrophilic nature of catalysts.

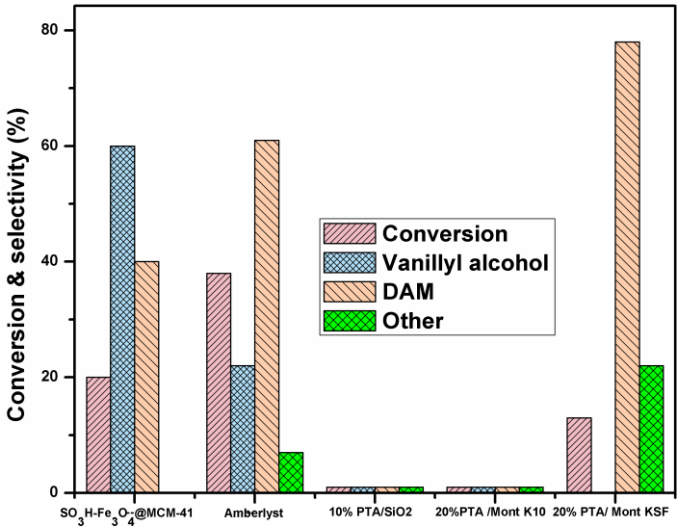

Fig. 3.19. Catalyst screening for vanillyl alcohol synthesis. Reaction conditions: molar ratio of guaiacol to formaldehyde (1:7); catalyst concentration, 150 mg; temperature, 70 ^oC; time, 3 h.

As commercial formaldehyde has 63% water, competitive adsorption of water and the substrate may retard the hydroxyalkylation reaction, since, the nucelophilicity of water

oxygen is greater than formaldehyde oxygen, facilitating the co-ordination of water molecules with the acidic sites of the catalyst. Among amberlyst-15 and SO_3H-Fe_3O_4@MCM-41catalysts, former has the strong acidity than the latter and that is why it gave highest conversion of guaiacol. However, it also promotes the further reaction of vanillyl alcohol with guaiacol and yields DAM (62%). Due to mild acidity of SO_3H-Fe_3O_4@MCM-41 as compared to that of amberlyst 15 and its hydrophobic nature, it gave the highest selectivity to the desired product i.e. vanillyl alcohol (60%). The observed activity and selectivity patterns of various catalysts studied in this work strongly indicate that mild acidity and hydrophobicity of the catalyst was highly desirable for the selective hydroxyalkylation of guaiacol to vanillyl alcohol. Since SO_3H-Fe_3O_4@MCM-41showed the highest selectivity (60%) to vanillyl alcohol, further optimization of reaction conditions was carried out by using SO_3H-Fe_3O_4@MCM-41 catalyst.

The effect of reaction time on the guaiacol conversion and product selectivity was studied for guaiacol to formaldehyde mole ratio of 1:7 at 70 ^oC. It was found that the guaiacol conversion increased from 12 to 30% with increase in reaction time from 2 to 6 h (Fig. 3.20).

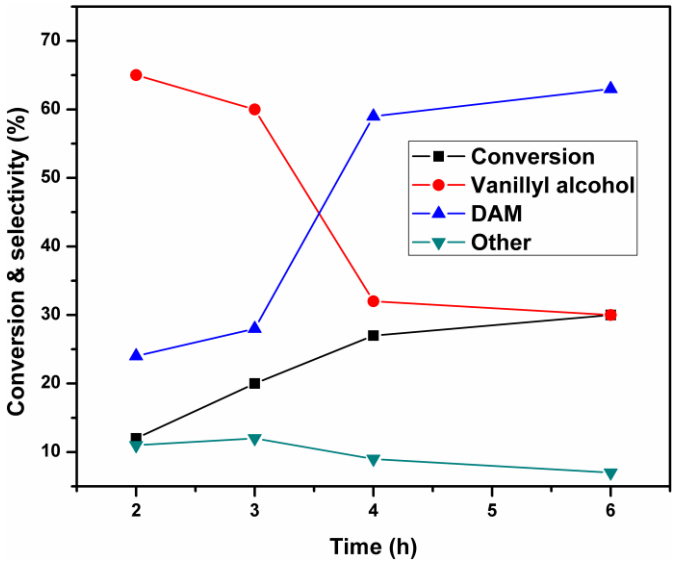

Fig. 3.20. Effect of time on conversion and selectivity. Reaction conditions: molar ratio of guaiacol to formaldehyde (1:7); catalyst concentration, 150 mg; temperature, 70 ^oC; time, 6 h.

However, this led to the decrease in vanillyl alcohol selectivity from 65 to 30%. This decrease in vanillyl alcohol selectivity was mainly because of the reaction of initially formed vanillyl alcohol with guaiacol to give DAM and its higher homologues. The optimum reaction time of 3 h was found to give the high catalyst activity (20% conversion of guaiacol) with 60% vanillyl alcohol selectivity.

Effect of mole ratio of guaiacol to formaldehyde on the conversion and product selectivity was studied in the range of 1:3 to 1:10 using SO_3H-Fe_3O_4@MCM-41catalyst by varying the concentration of formaldehyde at a constant guaiacol concentration and the results are shown in Fig. 3.21. The conversion of guaiacol decreased from 40 to 15% as the mole ratio of guaiacol to formaldehyde increased from 1:3 to 1:10, but this leads to the increase of vanillyl alcohol selectivity from 29 to 63% and decrease of dihydroxydiarylmethane (DAM) selectivity from 61to 27% . The other products formed were mainly ether of vanillyl alcohol e.g. 2-methoxy-4-(methoxymethyl) phenol and 2-methoxy-6- (methoxymethyl) phenol. The lower guaiacol conversion (15%) was mainly because of the blockage of active sites of the catalyst by more polar water molecules present in excess amount of formaldehyde for a mole ratio of 1:10 as compared to 1:3, 1:5 and 1:7 mole ratios. The formation of vanillyl alcohol (60 and 64%) at moles ratio of 1:7 and 1:10 respectively, was due to the availability of formaldehyde in excessive amount which minimizes the formation of DAM. Mole ratio of 1:7 shows the best compromise between high catalyst activity (20% conversion of guaiacol) and selectivity to vanillyl alcohol (60%). It is interesting to note that the highest selectivity to vanillyl alcohol (60-70%) has been reported in the literature for a very high mole ratio (1:15 to 1:20) of guaiacol to formaldehyde [22].

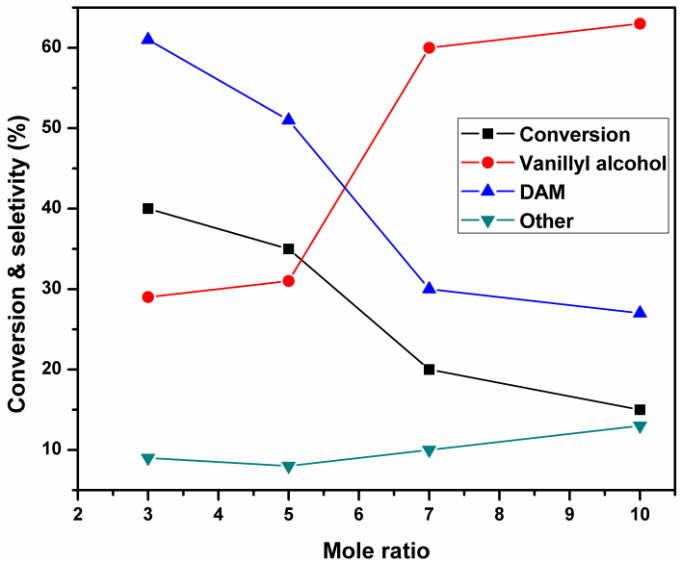

Fig. 3.21. Influence of mole ratio of guaiacol to formaldehyde. Reaction conditions: molar ratio of guaiacol to formaldehyde (1:3 to 1:10); catalyst concentration, 150 mg; temperature, 70 ^{o}C; time, 3 h.

Effect of catalyst concentration in the range of 0.014 to 0.028 g/cm^3 on guaiacol conversion and product selectivity was also studied and the results are shown in Fig. 3.22. The guaiacol conversion increased from 15 to 28% with increase in catalyst concentration from 100 to 200 mg with 1:7 mole ratio of guaiacol to formaldehyde. This is obvious since with increase in catalyst concentration enhance the availability of the acidic sites which facilitate the conversion of guaiacol to the products. However, the selectivity to vanillyl alcohol decreased significantly from 65 to 43% and that of DAM increased from 28 to 56% as the catalyst concentration increased from 100 to 200 mg. The decrease in vanillyl alcohol selectivity was due to its further conversion to DAM because of increase in acidic sites at higher catalyst concentration. The selectivity to other products remained almost constant (7%).

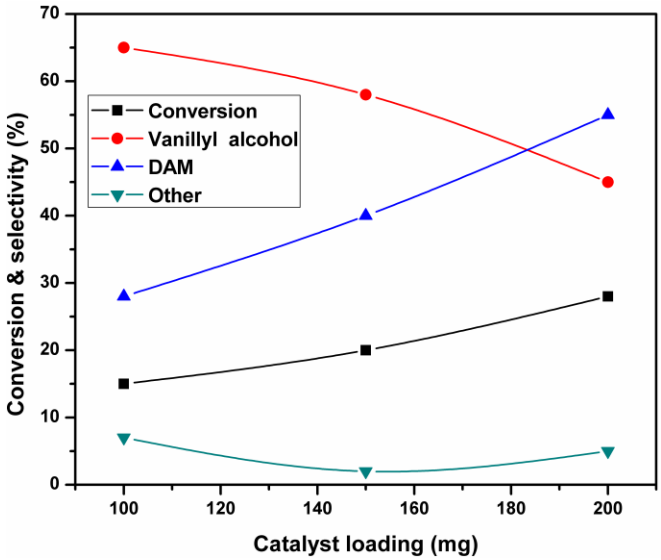

Fig. 3.22. Effect of catalyst amount on conversion and selectivity. Reaction conditions: molar ratio of guaiacol to formaldehyde, 1:7; catalyst concentration, 100-200 mg; temperature, 70 ^{o}C; time, 3 h.

The stability of the catalyst under the reaction conditions was studied by catalyst recycle study. Since, this was a magnetically separable catalyst it could be quantitatively recovered by simply applying a strong magnetic field using a bar magnet as shown in Fig. 3.23. The magnetic characterization of the catalyst done by VSM at room temperature showed no hysteresis loop of the SO_3H-Fe_3O_4@MCM-41catalyst (Fig. 3.24), suggesting the super-paramagnetic characteristics of the catalyst can be exploited for its separation. The catalyst thus recovered was then washed two times with 20 mL of methanol, dried at 100 ^{o}C in a vacuum oven for 3 h, and then reused for subsequent recycle experiments. The reused catalyst was found to retain its activity even after 3rd recycle experiment as shown in Fig. 3.25, giving 20% conversion of guaicol with 60% selectivity to vanillyl alcohol. Efficient recyclability of the catalyst proved the successful grafting of SO_3H- on silica coated magnetite, exhibiting its stability under reaction conditions.

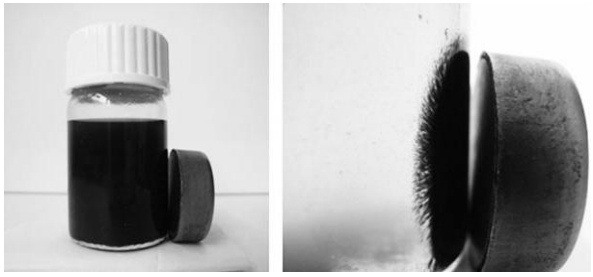

Fig. 3.23. Magnetic separation of finely dispersed SO_3H-MS catalyst

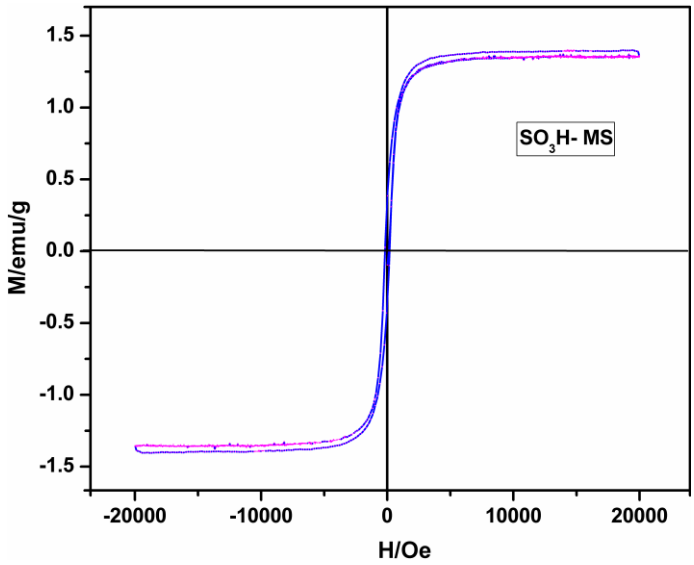

Fig. 3.24. VSM of the SO_3H-MS catalyst at room temperature

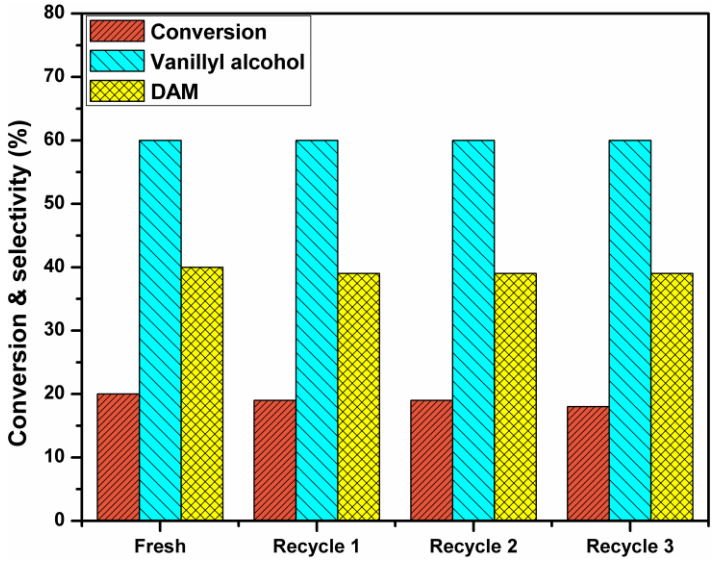

Fig. 3.25. Recycle study for vanillyl alcohol synthesis. Reaction conditions: molar ratio of guaiacol to formaldehyde, 1:7; catalyst loading, 150 mg; temperature, 70 ^{o}C; time, 3 h.

3.4. METAL CATION-EXCHANGED MONTMORILLONITE CLAY CATALYST FOR HYDROXYALKYLATION OF *p*-CRESOL TO 2, 2′-METHYLENEBIS (4-METHYL PHENOL)

Clay material like mont KSF/O, mont K10, mont K30 etc. are well known to catalyze many organic transformations which otherwise require acid reagents [28]. Clay minerals represent a convenient source to prepare potential solid acid catalysts because of their environmental compatibility, low cost and easy availability. Pillared and metal cation-exchanged clays with modified porosity, acidity and thermal stability have been well reported for acid catalyzed reactions. [29] Between the two, metal cation-exchanged clays are relatively less explored as catalysts except cation-exchanged montmorillonite for acylation and alkylation reactions. [30, 31] As PTA impregnated on montmorillonite and fumed silica were reported to be the efficient catalysts for the hydroxyalkylation of phenols [32]. Here we report for the first time, the montmorillonite clay exchanged with a series of metal cations (Al^{3+}, Fe^{3+} and Zn^{2+}) for the hydroxyalkylation of *p*-cresol with formaldehyde (Scheme 3.6).

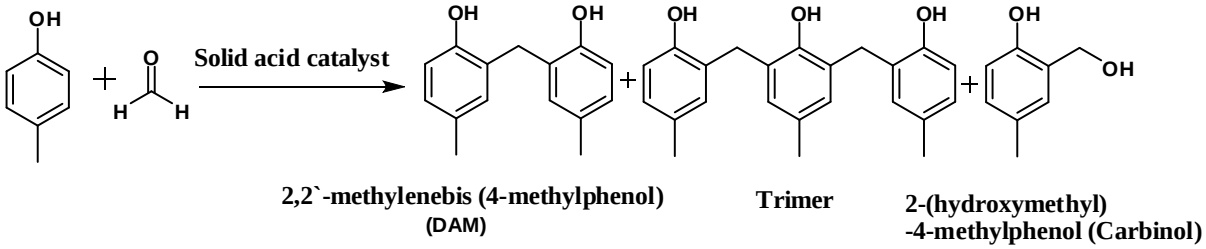

Scheme 3.7. Hydroxyalkylation of *p*-cresol to 2, 2′-methylenebis (4-methylphenol).

Montmorillonite is a member of the smectite clay family [33] and has 2:1 structure i.e. octahedral layer of Al is sandwiched between two tetrahedral layers of silicon coordinated with oxygen (TOT) exhibiting overall weak acidity. The crystalline sheets of negatively charged aluminosilicates are balanced by hydrated cations (Na^{+}, K^{+} or Ca^{2+}) in the interlayer spaces of montmorillonite as already discussed in chapter 1 of section A (1.3.2). The most interesting features of the smectite clay are their intercalation, swelling and cation exchange capacity which improve the catalytic properties of smectite clay.

When smectite clay is immersed into the solution of metal cations, both the intercalation of water molecule and swelling occur. The suspended clay can also freely exchange its interlayer cations for other metal cations in solution, which can substantially increase the acidity of the clay [34]. The substitution of exchangeable cations, by highly polarizing species of small radius such as Al, Zn or Fe, [35, 36] results in the alteration of Brönsted and Lewis acid sites as well as clay architecture (delamination), which subsequently influences the activity–selectivity pattern for the hydroxyalkylation of *p*-cresol. The aim of our present work is to study the effect of metal cations exchange on textural properties of montmorillonite clay and thereby on the pattern of activity–selectivity. In the present study, Al, Zn and Fe metal cation-exchanged clay catalysts were prepared and evaluated for the hydroxyalkylation of *p*-cresol. The stability and life-time of the catalyst were studied by catalyst recycle experiments.

3.4.1. Experimental

The catalysts were prepared by cation-exchange process and the detail experimental procedure of their preparation has been described in Section A (2.3.1.3) of chapter 2. The catalysts were characterized by various techniques including BET surface area measurements, X-ray powder diffraction (XRD), ammonia temperature programmed desorption (NH_3-TPD) and pyridine-IR techniques according to the procedure described in sections 2.4.2, 2.4.1, 2.4.3 and 2.4.4. The activity testing of prepared catalysts was carried out in a magnetically stirred glass reactor (capacity 50 mL), fitted with a reflux condenser for hydroxyalkylation of *p*-cresol with formaldehyde to give 2, 2′-methylenebis (4-methyl phenol) (DAM) following the experimental procedure described in sections 2.5.3. Liquid samples were analyzed by using a gas chromatograph (HP 6890) equipped with flame ionization detector (FID) and an HP-5 capillary column (0.25 μm cross-linked methyl silicone gum, 0.32 mm×30 m).

3.4.2. Results and discussion

3.4.2.1. Catalyst characterization

The X-ray diffraction (XRD) measurements provide a powerful tool to understand the changes in the interior of the clay microenvironment. Powder XRD-pattern of montmorillonite and different cation-exchanged montmorillonite samples are shown in Fig. 3.26. The d_{001} basal spacing from the XRD patterns was used to examine the structural changes that occurred during the preparation of the cation exchanged clay [37]. The d_{001}-values for the basal reflection at $2\theta = 9.1°$ in Zn^{2+} and Fe^{3+}-exchanged montmorillonite samples were almost similar to the parent montmorillonite (9.63 Å), indicating that the interlayer separation was not affected by the Zn^{2+} and Fe^{3+} exchange process. However, in the case of Al^{3+}, a slight shift in the position of the 001 reflection at $2\theta = 8.8°$ from a d-value of 9.63 to 9.95 Å was recorded, which was also accompanied by a decrease in intensity of the 001 reflection from 51 to 27% as compared to the same reflection in the parent montmorillonite sample. This was because of the delamination of montmorillonite layers taking place due to a higher extent of polarizability of Al^{3+} cations. A similar observation was reported as irregular stacking of the layers in the case of acid-activated montmorillonite clay [38]. Further evidence for delamination was the increase in surface area of parent montmorillonite from 19 to 47 m^2/g after Al^{3+} exchange (Table 3.2) [39]. During cation exchange process, the layered structures of mont clay are separated from each other and after drying, the sheets do not come to their original position, which lead to the change in morphology and characterized by high surface area. The non-basal X-ray reflections, which are a characteristic of montmorillonite (M in Fig. 3.26) were found at $2\theta = 19.5$ and $35.5°$. Other reflections at $2\theta = 20.8$, 26.5 and 27.9° can be attributed to quartz phase (Q in Fig. 3.26), which was present as an impurity [40].

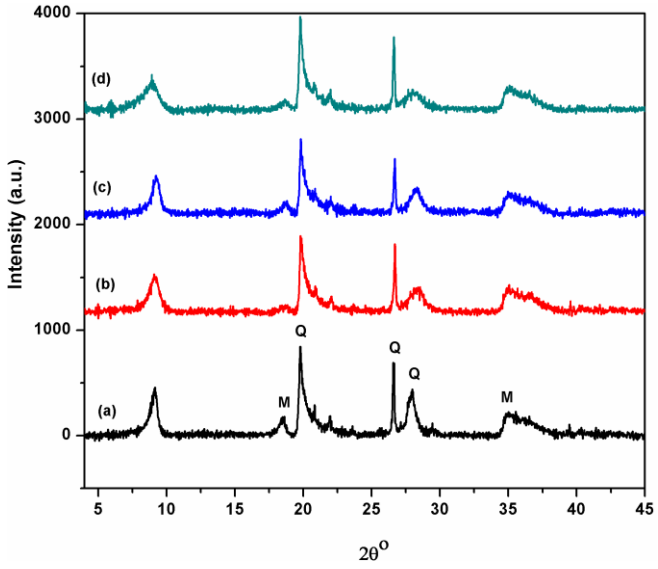

Fig. 3.26. Wide angle XRD patterns of: (a) Montmorillonite, (b) Zn-montmorillonite, (c) Fe-montmorillonite and (d) Al-montmorillonite

Table 3.2 Textural properties of the metal cation exchanged catalysts

Catalysts	Surface area (m^2/g)	Amount of NH_3 desorbed (mmol/g)	NH_3-TPD (%) distribution of acidic sites	
			Region I (LT-peak)	Region II (HT-peak)
Montmorillonite	19	0.06	97	3
Zn-montmorillonite	21	0.09	96	4
Fe-montmorillonite	35	0.14	89	11
Al-montmorillonite	47	0.25	87	13

As the hydroxyalkylation reaction is catalyzed by acid sites, the total acidity as well as the nature of acid sites of our catalysts were determined by NH_3-TPD and pyridine IR, respectively. The increase in total acidity of various montmorillonite samples observed by the NH_3-TPD measurements was in the following order: montmorillonite < Zn-montmorillonite < Fe-montmorillonite < Al-montmorillonite. As the trivalent cations

possess the highest polarizability, Al-exchanged clay with higher acidity was expected to be more active than divalent or monovalent ion-exchanged clays. The maximum acid sites in all the samples were found to be in the medium temperature range of 330 to 550 K (Table 3.2). As illustrated in Fig. 3.27, a progressive shift of medium temperature peak was observed while going from montmorillonite, Zn^{2+}, Fe^{3+} and Al^{3+}, indicating the increase in strength of acid sites as also evidenced by increase in values of NH_3 desorption from 0.06 to 0.25 mmol/g in the same order.

The pyridine IR spectrum of parent montmorillonite and cation-exchanged montmorillonite samples is shown in Fig. 3.28. The pyridine-IR of the parent montmorillonite showed a broad hump in the region of 1600–700 cm^{-1} and a small peak at 1490 cm^{-1} indicating the combination of Brönsted and Lewis acidities [41]. With change in cations from Zn^{2+}, Fe^{3+} and Al^{3+} the intensity of the peak at 1490 cm^{-1} increased progressively indicating an increase in the strength of the mixed acid sites. At the same time, the intensity of the peak at 1550 cm^{-1} increased in the same order confirming the increase in acidity was due mainly to the contribution from Brönsted acid sites which was maximum for Al-montmorillonite. This was mainly responsible for the highest catalytic activity of Al-montmorillonite, as discussed later. Brönsted acidity arises as per the reaction shown below.

$$[M(OH_2)_x]^{m+} \rightarrow [M(OH)\,(OH_2)_{x-1}]^{(m-1)} + H^+ \qquad (3.1.)$$

Where x is the number of water molecules directly bonded with the metal cation M and m+ is the charge on the cation. The hydrated cations in the interlayer space are dissociated producing protons which exhibit the Brönsted acidity [42]. The increase of acidity of cation-exchanged montmorillonite was possible because of the polarization of the interlayer hydration sphere with small size and highly-charged metal cations (Al^{3+}, $Fe^{3+}$and Zn^{2+}). Since among the three cations, Al^{3+} has the highest ability for polarization owing to its smallest size with a maximum charge density distribution, the release of a proton was easily facilitated and responsible for the Brönsted acidity.

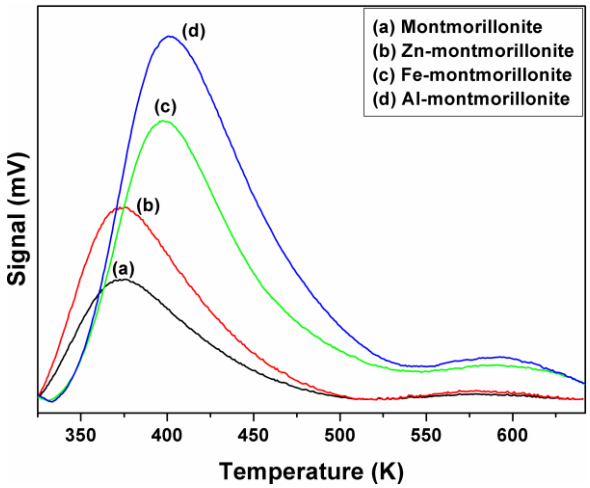

Fig. 3.27. NH_3-TPD profiles of: (a) Montmorillonite, (b) Zn-montmorillonite, (c) Fe-montmorillonite and (d) Al-montmorillonite

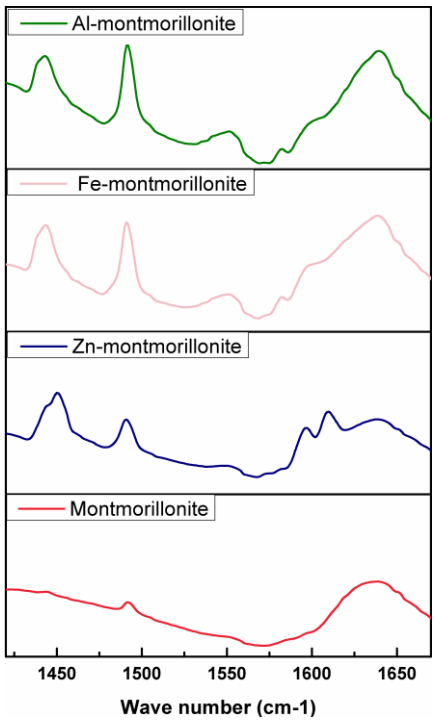

Fig. 3.28. FT-IR pyridine spectra of montmorillonite and different metal cation exchanged montmorillonite clay

3.4.2.2. Catalytic Activity

The results of activities of montmorillonite, Zn, Fe and Al-montmorillonite catalysts for the hydroxyalkylation of *p*-cresol are presented in Fig. 3.29. Among the various catalysts screened, Al-montmorillonite showed the highest *p*-cresol conversion of 51% with 98% selectivity to DAM, while parent montmorillonite showed negligible activity for the hydroxyalkylation of *p*-cresol. The highest activity of Al-montmorillonite could be due to its highest acidity (0.25 mmol of NH_3/g) arising by the exchange of interlayer hydrated cation by Al^{3+} as well as delamination of montmorillonite clay confirmed by XRD result. The negligible activity for parent montmorillonite could be attributed to its lowest acidity of 0.06 mmol/g of NH_3.

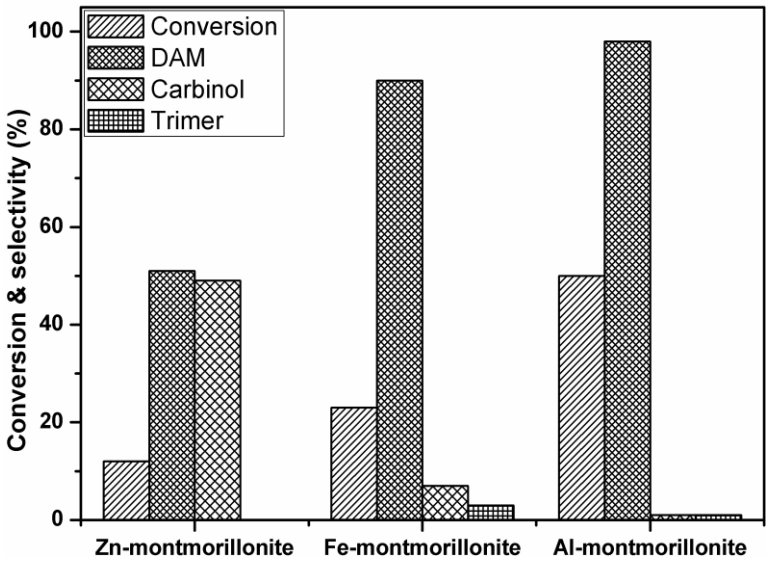

Fig. 3.29. Catalyst screening for hydroxyalkylation of *p*-cresol. Reaction conditions: *p*-cresol, 25.5 mmol; formaldehyde 8.5 mmol; catalyst concentration, 0.038 g/cm^3; temperature, 353 K; time, 2 h; and mole ratio of *p*-cresol to formaldehyde, 3:1.

As can be seen from Fig. 3.29, intermediate *p*-cresol conversions were observed for Zn^{2+} and Fe^{3+} exchanged montmorillonite. The progressive increase in conversion of *p*-cresol from 12 to 25% for Zn^{2+} and Fe^{3+}-exchanged montmorillonite was in accordance with the increase in their acidity from 0.09 to 0.14 mmol/g respectively. The activity along with the pyridine IR results (Fig. 3.27) also indicates that Brönsted acidity played an important role in the hydroxyalkylation of *p*-cresol. The selectivity pattern was different for each of the three catalysts. For Zn-montmorillonite, the intermediate carbinol formed was almost in equal amount (48% selectivity) to that of final product DAM (Fig. 3.29). This could be due to the higher strength of Lewis acid sites as shown by pyridine IR in Fig. 3.27. In the case of Fe-montmorillonite catalyst, the selectivity to final product DAM increased substantially to 90% with only 7% carbinol however, a small amount of trimer (3% selectivity) was also observed. The higher conversion of carbinol to DAM and its further conversion to trimer can be attributed to the higher Brönsted acidity of Fe-montmorillonite. As the highest Brönsted acidity was observed for Al-montmorillonite, a higher extent of the formation of trimer was expected. On the contrary, Al-

montmorillonite was found to give almost a complete selectivity to DAM with less than 1% selectivity to trimer. As delamination was observed in the case of Al-montmorillonite, this also might have resulted in a change in porosity and morphology, which would be favorable for the shape selective product formation. As Al-montmorillonite catalyst gave highest *p*-cresol conversion and DAM selectivity, further work on the optimization of reaction parameters was carried out using this catalyst; the results are discussed below.

The effect of the mole ratio of *p*-cresol to formaldehyde in the range of 1:1 to 1:5 on conversion and selectivity to DAM were studied by varying the concentration of *p*-cresol at constant formaldehyde concentration; the results are presented in Fig. 3.30.

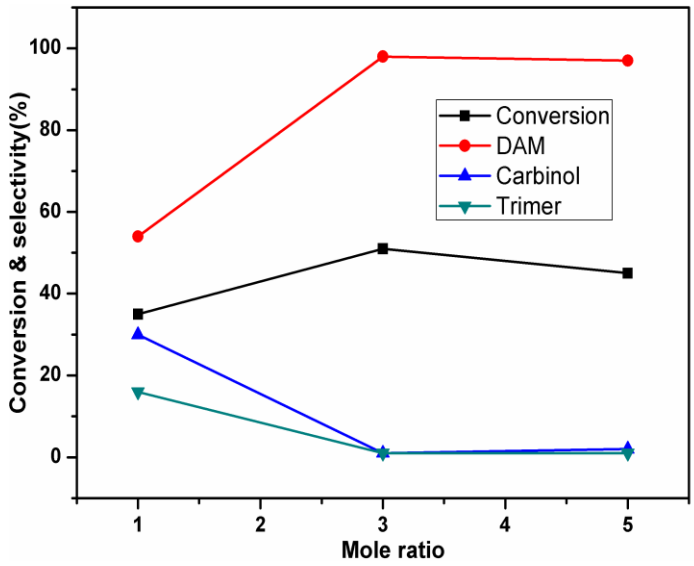

Fig. 3.30. Influence of mole ratio of *p*-cresol to formaldehyde on the conversion of *p*-cresol over Al-montmorillonite. Reaction conditions; temperature, 353 K; time, 2 h; catalyst concentration, 0.038 cm^3/g.

The conversion of *p*-cresol increased from 35 to 51% as the mole ratio of *p*-cresol to formaldehyde increased from 1 to 3 and selectivity to DAM increased from 54 to 98%. At 1:1 mole ratio, the selectivity to intermediate carbinol was as high as 23%. This may be due to the lower stoichiometric amount of *p*-cresol (two moles of *p*-cresol reacting with one mole of formaldehyde) giving lower selectivity to DAM. For the mole ratio of

3:1, the selectivity to the intermediate carbinol decreased steeply from 23 to 1%, due to the presence of excess of *p*-cresol which reacts with intermediate carbinol to give DAM. With further increase in the mole ratio from 3:1 to 5:1, the conversion of *p*-cresol decreased from 51 to 45% while the selectivity to DAM remained almost constant (97%). This could be explained by the preferential adsorption of *p*-cresol molecule on active acid sites of the catalyst compared to formaldehyde with increase in *p*-cresol concentration.

The effect of reaction time on *p*-cresol conversion and selectivity to DAM was studied for the optimum mole ratio of 3:1 at 353 K temperature (Fig. 3.31).

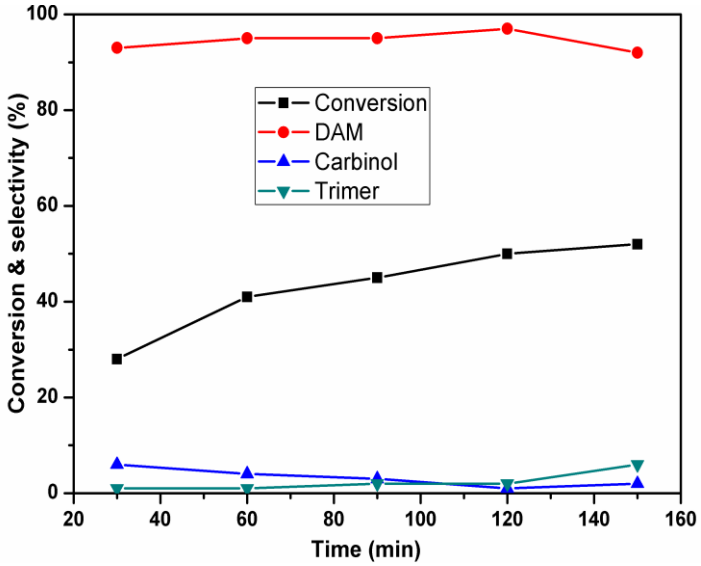

Fig. 3.31. Effect of reaction time on conversion and selectivity for Al-montmorillonite catalyst. Reaction conditions: *p*-cresol, 25.5 mmol; formaldehyde 8.5 mmol; catalyst concentration, 0.038 g/cm^3; temperature, 353 K; time, 0–150 min; and mole ratio of *p*-cresol to formaldehyde, 3:1.

The conversion of *p*-cresol increased from 0 to 51% with an increase in the reaction time from 0 to 120 min; thereafter it increased slightly from 51 to 53% as the reaction time further increased from 120 to 150 min. During the entire reaction time, selectivity to DAM remained almost constant (98%) indicating that the optimum reaction time was 120

min. and longer reaction time did not show any appreciable change in conversion and selectivity.

The catalyst concentration was varied in the range of 0.007–0.053 g/cm^3 for studying its effect on the conversion of *p*-cresol and selectivity to DAM. Both the conversion of *p*-cresol and selectivity to DAM increased from 39 to 51% and from 87 to 95% respectively, with an increase in catalyst concentration from 0.007 to 0.038 g/cm^3, as shown in Fig. 3.32. This is expected since with an increase in catalyst concentration the acidic sites also increased, which facilitated the reaction of the initially formed carbinol with another molecule of *p*-cresol to give DAM. Further increase up to 0.053 g/cm^3 in catalyst concentration, caused the increase in *p*-cresol conversion to 56%, however, DAM selectivity decreased to 90% due to the increased formation of trimer (9% selectivity).

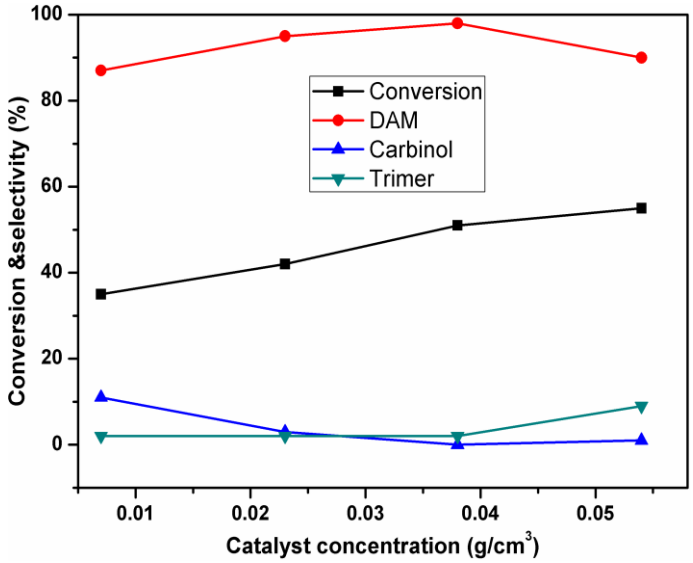

Fig. 3.32. Effect of catalyst concentration on conversion and selectivity. Reaction conditions: *p*-cresol, 25.5 mmol; formaldehyde 8.5 mmol; temperature, 353 K; time, 120 min; and mole ratio of *p*-cresol to formaldehyde, 3:1.

The effect of temperature on both the conversion of *p*-cresol and selectivity to DAM in the range of 333–373 K is shown in Fig. 3.33. With an increase in temperature from 333

to 353 K, the conversion of *p*-cresol increased from 34 to 51% with an increase in DAM selectivity from 85 to 98% at the cost of carbinol selectivity (decreased from 15 to 1%). With further increase in temperature to 373 K, the conversion of *p*-cresol increased up to 61% but DAM selectivity decreased from 98 to 90% due to the formation of trimer in a substantial amount (10% selectivity)

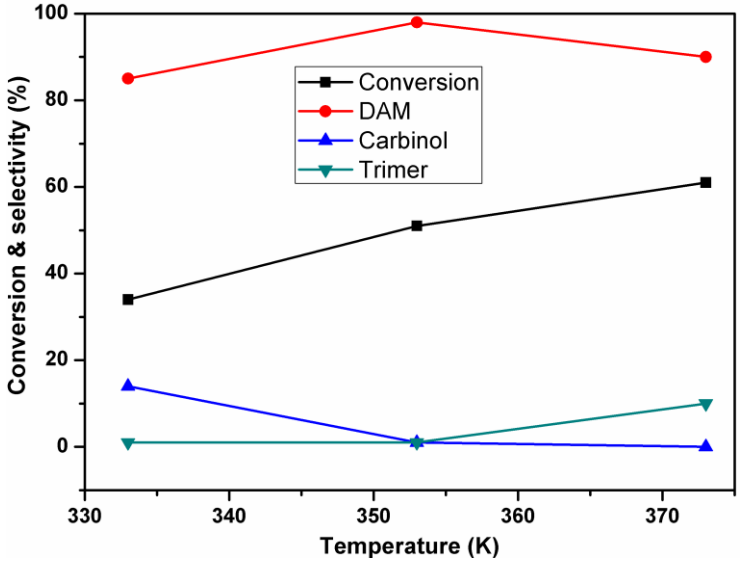

Fig. 3.33. Effect of reaction temperature on conversion and selectivity for Al-montmorillonite catalyst. Reaction conditions: *p*-cresol, 25.5 mmol; formaldehyde 8.5 mmol; catalyst concentration, 0.038 g/cm^3; time, 120 min; and mole ratio of *p*-cresol to formaldehyde, 3:1.

For practical applications of heterogeneous catalyst systems, the stability and reusability of the catalyst are important factors. A recycle study of Al-montmorillonite catalyst was carried out at 353 K with *p*-cresol to formaldehyde mole ratio of 3:1 and the results are presented in Fig. 3.34. After the first hydroxyalkylation run, the catalyst was filtered and washed several times with methanol, dried under IR lamp for 2 h and reused for the subsequent runs. The catalyst was found to retain its activity even after the 8th recycle experiment without any loss of activity indicating the high efficiency of Al-montmorillonite as a solid acid catalyst for the hydroxyalkylation of *p*-cresol.

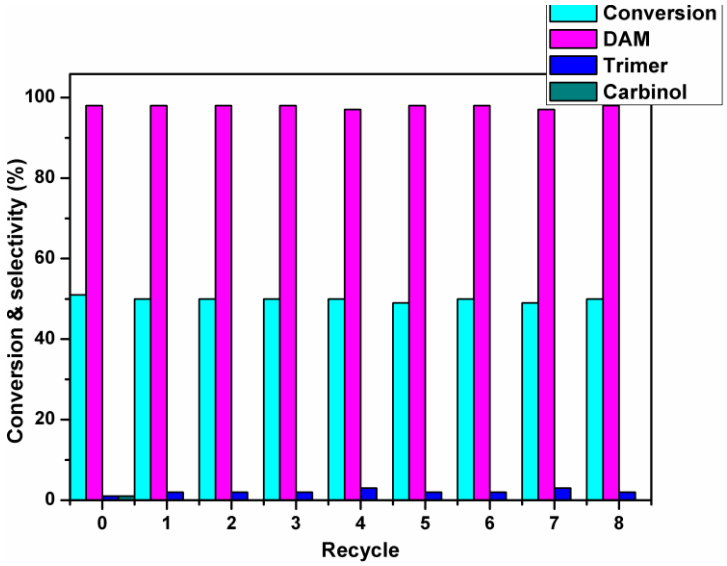

Fig. 3.34. Catalyst recycle studies. Reaction conditions: *p*-cresol, 25.5 mmol; formaldehyde 8.5 mmol; catalyst concentration, 0.038 g/cm^3; temperature: 353 K; time, 120 min; and mole ratio of *p*-cresol to formaldehyde, 3:1.

3.5. CONCLUSIONS

Three different solid acid catalysts were developed viz. PTA/MCM-41, SO_3H-Fe_3O_4@MCM-41, and metal cation-exchanged montmorillonite clay and were evaluated for hydroxyalkylation of different phenolic compounds of industrial importance. In case of phenolphthalein synthesis, 20% PTA/MCM-41 gave the highest conversion (40%) of phthalic anhydride with maximum selectivity of 91% to phenolphthalein due to the presence of both Brönsted and Lewis acidity as revealed by pyridine−FTIR studies. The activity and reusability of 20% PTA/MCM-41 was also studied for the hydroxyalkylation of phenol and *p*-cresol with formaldehyde which gave 31and 34% conversion of phenol and *p*-cresol with 94 and 97% selectivity to DAM, respectively. The catalyst was found to retain its activity even after the fourth recycle experiment for both the reactions. Water tolerant sulfonic acid functionalized magnetically separable solid acid catalyst (SO_3H-Fe_3O_4@MCM-41) was synthesized and evaluated for guaiacol hydroxyalkylation. The catalyst was found to be mildly acidic and gave 20% conversion with 60% selectivity to the desired product (vanillyl alcohol). Functionalization of -SO_3H acid was confirmed by FT-IR and TGA. In another attempt of developing a solid acid catalyst, the effect of

exchange of metal cations (Al^{3+}, Zn^{2+} and Fe^{3+}) in montmorillonite clay was studied. All these catalysts were also evaluated for the acid-catalyzed hydroxyalkylation of *p*-Cresol. The total acidity measured by NH_3-TPD was found to be the maximum (0.25 mmol/g) for Al-montmorillonite sample and minimum of 0.06 mmol/g for parent montmorillonite. The pyridine-IR studies showed that the highest Brönsted acidity was achieved with Al-montmorillonite due to the polarization of interlayer water molecule by the distribution of highly charged Al^{3+} cations over its smallest size as compared to other metal cations. The XRD characterization showed the delamination of Al-montmorillonite due to a higher extent of polarizability of Al^{3+}. As a result of highest acidity and delamination, Al-montmorillonite gave a highest *p*-cresol conversion of 51% with almost complete selectivity of 98% to DAM. For Zn-montmorillonite catalyst, almost the same selectivity to the intermediate carbinol and DAM were obtained, while for Fe-montmorillonite, DAM formation was accompanied with carbinol along with a trimer to the extent of 7%. Our Al-montmorillonite catalyst was shown to retain the original activity even after the 8^{th} recycle.

3.6. REFERENCES

1. R. M. Basale, B. Ganesan, A. S. Shyadligeri, V. Srinivasan, *US 2008/0177091 Al*. 2008.
2. S. Udayakumar, Ajaikumar, S. Pandurangan, *Appl. Catal. A* 2006, 302, 86.
3. I. V. Kozhevnikov, A. Sinnema, R. J. J. Jansen, K. H. Van Bekkum, *Catal. Lett.* 1995, 30, 241.
4. A. Jha, A. C. Garade, S. P. Mirajkar, C. V. Rode, *Ind. Eng. Chem. Res.* 2012, 51, 3916- 3922.
5. G. Kamalakar, K. Komura, Y. Sugi, *Appl. Catal. A: Gen.* 2006, 310, 155.
6. K. C. Souza, N. D. S. Mohallem, E. M. B. Sousa, *J Sol. Gel Sci. Technol.* 2010, 53, 418.
7. B. R. Jermy, A. Pandurangan, *Appl. Catal. A* 2005, 295, 185.
8. K. Rajasekar, K. Balkis Ameen, A. Pandurangan, *Catal. Commun.* 2008, 10, 150.
9. K. S. W. Sing, D. H. Everett, R. A. W. Haul, L. Moscou, R. A. Pierotti, J. Rouquerol, T. Siemieniewska, *Pure Appl. Chem.* 1985, 57, 603.
10. A. Ghanbari-Siahkali, A. Philippou, J. Dwyer, M. W. Anderson, *Appl. Catal. A* 2000, 192, 57.
11. A. Corma, A. Martinez, V. Martinez-Soria, J. B. J. Morton, *J. Catal.* 1995, 153, 25.
12. K. Rajasekar, A. Pandurangan, *Catal. Commun.* 2007, 8, 635.
13. J. C. Juan, J. Zhang, M. A. Yarmo, *J. Mol. Catal. A* 2007, 267, 265.
14. L. Yang, C. Wei, C. Muhua, H. Jinyan, *J. Wuhan Univ. Technol.* 2008, 23, 234.
15. Q. Y. Liu, W. L. Wu, J. Wang, X. Q. Ren, Y. R. Wang, *Micro. Meso. Mater.* 2004, 76, 51.
16. A. C. Garade, V. S. Kshirsagar, C. V. Rode, *Appl. Catal. A: Gen.* 2009, 354, 176.
17. P. Metivier, in: Fine Chemicals through Heterogeneous Catalysis, R.A. Sheldon and H. van Bekkum (Eds.), Wiley-VCH, 2001, p. 173.
18. A. S. Amarasekara, B. Wiredu, A. Razzaq, *Green Chem.* 2012, 14, 2395.

19. W. C. Muench, T. S. Hormel, P. M. Kirchhoff, L. A. Robbins, *US Pat. 4205188*, 1980.
20. C. Moreau, S. Razigade-Trousselier, A. Finiels, F. Fajula, L. Gilbert, *US Pat. 5811587*, 1998.
21. M. Bolognini, F. Cavani, L. Dal Pozzo, L. Maselli, F. Zaccarelli, B. Bonelli, M. Armandi, E. Garrone, *Appl. Catal. A: Gen.* 2004, 272, 115.
22. F. Cavani, M. Corrado, R. Mezzogori, *J. Mol. Catal. A: Chem.* 2002, 447, 182.
23. G. Perot, M. Guisnet, *J. Mol. Catal.* 1990, 61, 173.
24. M. H. Bhure, I. Kumar, A. D. Natu, R. C. Chikate, C. V. Rode, *Catal. Commun.* 2008, 9, 1863.
25. T. Okuhara, *Chem. Rev.* 2002, 102, 3641.
26. Y. Wang, G. Wang, M. Yang, L. Tan, W. Dong, R. Luck, *J. Colloid Interface Sci*. 2011, 353, 519.
27. G. H. Du, Z. L. Liu, X. Xia, Q. Chu, S. M. Zhang, *J. Sol–Gel Sci. Technol.* 2006, 39, 285.
28. M. P. Hart, D. R. Brown, *J. Mol. Catal. A: Chem.* 2004, 212, 315.
29. A. Moronta, T. Oberto, G. Carruyo, R. Solano, J. Sánchez, E. González, L. Huerta, *Appl. Catal. A: Gen.* 2008. 334, 173.
30. B. Chiche, A. Finiels, C. Gauthier, P. Geneste, *J. Mol. Catal. A* 1987, 42, 229.
31. T. Cseri, S. Bèkássy, F. Figueras, S. Rizner, *J. Mol. Catal. A: Chem.* 1995, 98, 101.
32. A. C. Garade, V. S. Kshirsagar, R. B. Mane, A. A. Ghalwadkar, U. D. Joshi, C. V. Rode, *Appl. Clay Sci.* 2010, 48, 164.
33. P. F. Luckham, S. Rossi, *Adv. Colloid Interface Sci.*1999, 82, 43.
34. A. Jha, A. C. Garade, M. Shirai, C. V. Rode, Appl. Clay Sci. 2013, 74, 141–146.
35. M. Kawai, M. Gnaka, Y. Izumi, *Chem. Lett.* 1986, 381.
36. R. S. Varma, *Tetrahedron* 2002, 58, 1235.
37. P. Stathi, I. T. Papadas, A. Enotiadis, R. Y. N. Gengler, D. Gournis, P. Rudolf, Y. Deligiannakis, *Langmuir* 2009. 25, 6825.
38. P. Pushpaletha, S. Rugmini, M. Lalithambika, *Appl. Clay Sci.* 2005. 30, 141.

39. F. Figueras, *Catal. Rev.* 1988, 30, 457.
40. G. W. Brindley, G. Brown, Longman Scientific and Technical, London, 1980.
41. M. H. Zahedi-Niaki, S. M. Javaid Zaidi, S. Kaliaguine, *Micro. Meso. Mater.* 1999, 32, 251.
42. L. Jankovič, P. Komadel, *J. Catal.* 2003, 218, 227.

Section B

Liquid phase oxidation of phenolic compounds

Chapter 1

Introduction

1.1. OXIDATION

The chemical term ‘oxidation’ can be defined as the take-up of oxygen by organic and inorganic materials or removal of hydrogen from a substrate [1]. More specifically, oxidation reaction is a part of redox reaction that involves electron transfer between a pair of substances. In this process, the species that loses electron(s) is said to be oxidized, i.e. it undergoes oxidation and the species that accepts the electron(s) is said to be reduced, i.e. it undergoes reduction. Oxidation reactions are among the most useful and commonly practiced reactions in industrial processes, since these can produce diverse chemicals from petroleum as well as biomass feedstock [2]. Oxidation processes can be divided into following categories:

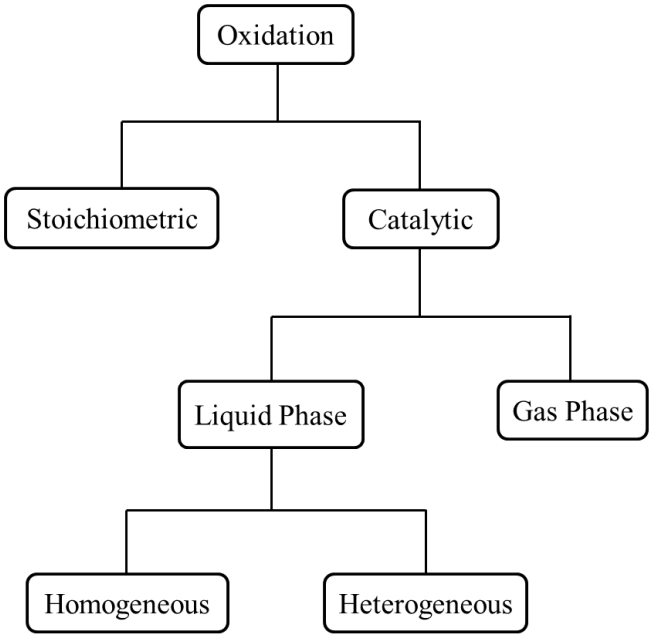

Fig.1.1. Classification of oxidation processes

Traditionally, oxidation in the liquid phase is not a ‘‘green’’ or environment friendly method, when considering the stoichiometric use of inorganic (or organic) oxidants and solvents. The process generally involves the use of chromium (IV) reagents, permanganate, manganese dioxide and periodate, resulting in the concomitant generation of copious amounts of inorganic salt-containing effluents. Currently, there is considerable pressure, to replace these antiquated technologies with cleaner catalytic alternatives [3,

4]. Catalysis provides the unique opportunity to make oxidation processes not only more atom-efficient but also more economic and less harmful for the environment. There are several requirements for a selective catalytic oxidation process to fulfill, so that it can be considered to be ‘‘green’’. One of the most challenging is the use of molecular oxygen as an oxidant. This holds true for selective oxidations in the gas phase as well as in the liquid phase. Particularly, in selective oxidations of relatively big and thermally sensitive molecules as often encountered in fine chemical synthesis, liquid phase oxidation cannot be circumvented because the substrates cannot easily be evaporated and oxidized in the gas- or vapor-phase and the use of solvents may become inevitable. This often makes it difficult to develop a green process. In that case, there is need to develop such catalysts which are able to decrease the activation energy of the reaction for carrying it at milder condition. The key characteristics of a green oxidation technology are the use of an easily recyclable catalyst, clean oxidants such as molecular oxygen or hydrogen peroxide without any additive such as co-reductant or co-oxidant, and high atom efficiency. The use of a solid catalyst often has technical advantages concerning catalyst handling and separation. For liquid phase oxidation, both homogeneous and heterogeneous types of catalysts have been reported but in practice, the overwhelming majority of processes are homogeneous, i.e. they involve the use of soluble metal salts or complexes as the catalysts. e.g.

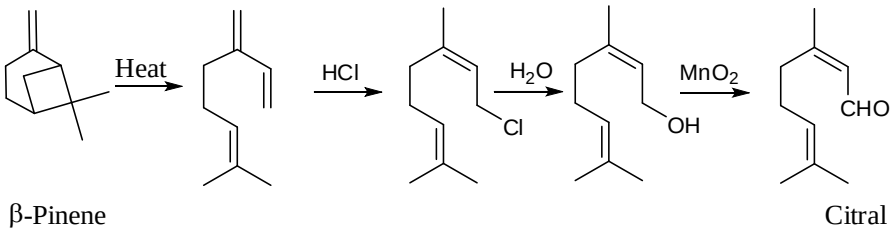

Scheme 1.1. Classical route for pinene oxidation

Depending on the reactant phase, the catalytic oxidation is classified in two types as liquid and gas phase. In gas phase oxidation, substrate concentrations are much lower and radical chain oxidation pathway is less favored. It takes place by the adsorption of dioxygen on the surface of a heterogeneous catalyst, leading to the formation of surface

oxo species. These surface oxo species (Scheme 1.2 A) are highly reactive once adsorbed on defective, coordinatively unsaturated surface sites. This chemisorbed oxygen can be exploited for the oxidation of, e.g., ethylene to ethylene oxide [5], CO to CO_2 [6, 7] or in catalytic combustion [8], i.e. in oxidation reactions where selectivity is either not a problem or poor selectivity can be economically tolerated.

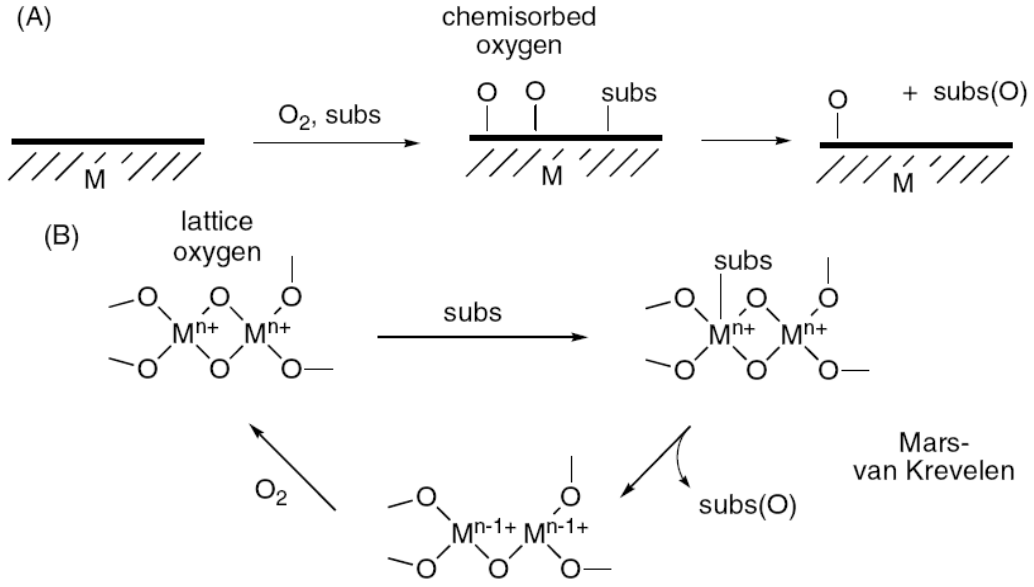

Scheme 1.2. Oxygen activation on the surface of heterogeneous catalysts: (A) Through chemisorption; (B) by replenishing consumed lattice oxygen [9].

In the same way, metal-oxide or mixed-metal-oxide catalysts generally employ their already existing surface oxo species (lattice oxygen) for the high temperature oxidation of hydrocarbons. This is typical for n-type semiconductor oxides (e.g., Ti, V, and Mo) where a lower oxidation state is easily accessible to the central metal atom (Scheme 1.2 B). Oxygen vacancies are subsequently replenished by molecular dioxygen. This two-step process is known as the Mars–Van Krevelen mechanism [9]. Because lattice oxygen is more tightly bound than chemisorbed oxygen, it can be delivered in a more controlled fashion opening the way to selective oxidation and this mechanism is involved in processes like, e.g., synthesis of acrolein or acrylonitrile [10]. Among various substrates, selective oxidation of unfunctionalized hydrocarbons (C−H bonds), is still a major

challenge [11] The difficulty lies in the activation of the poorly reactive C−H bonds. There are several large scale industrial vapor phase oxidation processes in operation nevertheless, it has certain disadvantages such as very high operating temperature and the formation of a large amount of carbon dioxide, contributing to the global warming. Further, the conversion has to be kept low to attain a high selectivity of aldehydes, and the low concentration of substrates in the feed stock mixture poses the problem of recovery. In case of vapor phase oxidation of cyclohexane to cyclohexanol/cyclohexanone – the starting material for adipic acid used on a million tonnes scale for the manufacture of nylon-66 – is more challenging. Since the substrate is reactive unlike C−H bonds and the oxidation product is not stable, the reaction is stopped at conversions <10% to prevent further oxidation, affording a roughly 1:1 mixture of cylohexanol/cyclohexanone with 80% selectivity [12].

Liquid-phase oxidation reactions are also operated commercially in the presence of supported metal catalysts and they are potentially very attractive for the preparation of intermediates and fine chemicals because high selectivities can be obtained with environmentally clean processes e.g. *p*-xylene to terephthalic acid, cyclohexane to cyclohexanol/cyclohexanone and adipic acid, n-butane to acetic acid, oxidation of isobutane to *tert*-butyl hydroperoxide (TBHP)/*tert*-butanol, diisopropyl benzene to hydroquinone, epoxidation of propylene to propylene oxide, oxidation of alcohols to aldehydes, *p*-cresol to *p*-hydroxybenzaldehyde, *o*-hydroxybenzylalcohol to salicylaldehyde, vanillyl alcohol to vanillin etc. Due to relatively milder reaction conditions, liquid phase oxidations are easy to operate while giving the quantitative conversions of the substrate. Since, liquid phase oxidation operates through free radical pathway; it is always associated with the formation of coupling as well as over oxidation products. This is even more imperative in the production of fine chemicals since the recovery of the desired oxidation product of highest purity is required due to their applications in health care, fragrance, flavors and pharmaceutical formulations [13, 14]. Nowadays, sustainability is also becoming an important economic driver along with its inclusion in the twelve principles of Green Chemistry for developing a green process[15].

1.2. ENVIRONMENTALLY BENIGN OXIDANTS

Replacement of technologies based on soluble catalysts with heterogeneous ones is intrinsically more likely to lead to important technical improvements in terms of catalyst design, process simplification, milder or more sustainable reaction conditions, use of cheaper or more environmentally friendly oxidants. Going green implies an evaluation of the properties of common oxidants. Table 1.1 reports an analysis of the byproduct formed, the atom efficiency and the cost for a series of them [16, 17]. Two oxidants stand out in terms of environmental acceptability: oxygen (air) and hydrogen peroxide giving either no byproduct or water as a byproduct and atom efficiency close to or above 50%. An analysis of their E-factor leads to similar conclusions (Table 1.1) [18, 19]. Although the E-factor refers to a specific reaction, it is strongly influenced by the choice of the oxidant.

Table 1.1. Comparisons between different terminal oxidants in terms of green character [16].

Oxidant	Byproduct[a]	Atom effeiciency (%)[a]	E-factor[b]	Cost ($/kg) or ($/1)[c]
O_2	H_2O (none)	50(100)	0	57.5
H_2O_2	H_2O	47	0	103.5
$CH_3C(O)OOH$	$CH_3C(O)OH$	27	1.03	640.8
t-BuOOH	*t*-BuOH	22	1.27	246.4
NaClO	NaCl	21	101	26.3
Pyridne-*N*-oxide	Pyridine	17	1.36	739.4
CumOOH	CumOH	12	2.34	180.7
$KMnO_4$	MnO_2+H_2O	10	1.50	146.2
$2KHSO_5+KHSO_4+K_2SO_4$(Oxoxne®)	$3KHSO_4+K_2SO_4$	10[d]	10.03	119.9
m-CPBA	*m*-CBA	9	2.70	755.8
PhIO	PhI	7	3.52	e

a = One O-atom transfer, in parenthesis two O-atoms transfer.

b =Calculated for the epoxidation of propene.

c =Data from www.sigmaaldrich.com for the most concentrated sold version of the oxidant, May 2012.

d =Two O-atoms are transferred to the products.

e =Not sold

Sustainability of an industrial catalytic process is measured by two parameters, these are:

a) Atom economy (atom efficiency)

The atom economy or atom efficiency concept was first introduced by Barry Trost in1991 [19]. It can be defined as "the percentage of atoms in the reactants that end-up in the product". Atom economy can be written as:

$$\text{Atom efficiency (\%)} = \frac{\text{Moecular mass of desired product}}{\text{Molecular mass of all reactants}} \text{ X } 100\%$$

b) E-factor

E-factor concept was first introduced by Roger Sheldon for assessing the environmental impact of chemical processes and can be defined as "the ratio of the mass of waste per unit of product" [3].

$$\text{E} - \text{factor} = \frac{\text{Total waste (kg)}}{\text{Product (kg)}}$$

1.2.1. Oxygen (Air)

From the point of view of green and sustainable chemistry, molecular oxygen is considered as an ideal oxidant due to its natural, inexpensive, and environment friendly characteristics [20]. In addition, it exhibits a highly atom-efficient oxidant per unit weight. In contrast to other simple diatomic molecules such as N_2 or H_2, the oxygen molecule (or dioxygen) is paramagnetic as it has two unpaired electrons in the ground state (Fig. 1.2). The highest occupied molecular orbitals (HOMOs) are a pair of π^* orbitals of identical energy, so that the two highest energy electrons have no reason to spin-pair [21].

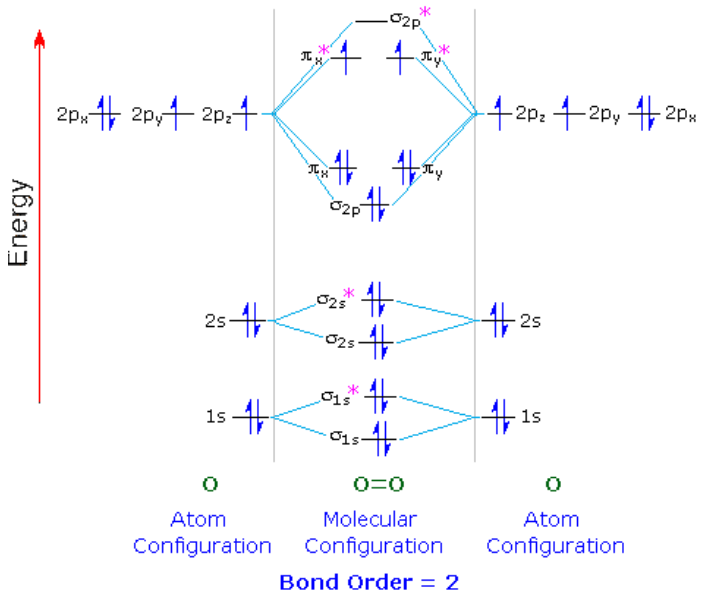

Fig. 1.2. Molecular orbital diagram of oxygen molecule

Most of the reactions involving O_2 proceed in one-electron step: electrons added to the O_2 molecule populate anti-bonding (π*) orbitals and weaken the O−O bond (Scheme 1.3) i.e. decreasing the bond energy from 118 kcal/mol to 88 kcal/mol [22]. This effect is evident in both the O−O bond length and its dissociation energy making the resulting superoxo ($O_2^{\bullet -}$) and peroxo (O_2^{2-}) species more reactive and kinetically more easy to control.

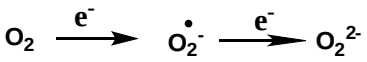

bond energy (kcal/mol)	118	88	46
length (Å)	1.21	1.26	1.49

Scheme 1.3. Basic data on the dioxygen molecule and the superoxo and peroxo anions

1.3. MECHANISM OF METAL-CATALYZED OXIDATIONS

The ground state of dioxygen is a triplet containing two unpaired electrons with parallel spins. The direct reaction of $^3O_2$ with singlet organic molecules to give singlet product is

a spin forbidden process with a very low rate. One way to circumvent this activation energy barrier involves a free radical pathway in which a singlet molecule reacts with $^3O_2$ to form two doublets (free radicals) in a spin allowed process as shown in reaction 1.1.

$$RH + {}^3O_2 \longrightarrow R^{\bullet} + HO_2^{\bullet} \qquad (1.1)$$

This process is possible only with very reactive molecules that afford resonance stabilized radicals. A second alternative to overcome this spin conservation obstacle is via reaction of $^3O_2$ with a paramagnetic (transition) metal ion, affording a superoxoxmetal complex as shown in reaction 1.2.

$$M^n + {}^3O_2 \longrightarrow M^{n+1}(O_2^{\bullet}) \qquad (1.2)$$

Subsequent inter- or interamolecular electron-transfer processes can lead to the formation of a variety of metal-oxygen species which may play a role in the oxidation of the organic substrates. (Fig. 1.3)

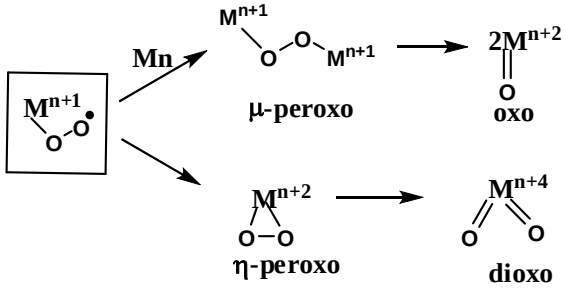

Fig.1.3. Metal–oxygen species

As rationalized by Sheldon and Kochi [23], all metal catalyzed oxidations under homogeneous or heterogeneous conditions, can be divided into two types on the basis of their mechanism: homolytic and heterolytic which are discussed below.

1.3.1. Homolytic mechanism

Homolytic oxidations involve free-radical intermediates and in solution, are catalyzed by first-row transition metals mediated by one-electron redox steps (e.g., Co^{II}/Co^{III},

Mn^{II}/Mn^{III}, Cu^{I}/Cu^{II}). In homolytic reactions, the hydrocarbon to be oxidized is generally not coordinated to the metal and is oxidized outside the coordination sphere via a radical chain. The main role of the metal is generally to decompose organic hydroperoxides, formed in solution either spontaneously or by the action of an initiator. In such processes the metal ion acts as an initiator rather than a catalyst. This behavior is also known as the Haber–Weiss mechanism (Fig.1.4).

$$RO_2H + Co^{II} \longrightarrow RO^{\cdot} + Co^{III}OH$$

$$RO_2H + Co^{III} \longrightarrow RO_2^{\cdot} + Co^{II} + H^{+}$$

Fig.1.4. Metal initiated and mediated autoxidation

These radical processes are common and constitute the basis for several very important industrial applications (e.g., the synthesis of adipic [24] and terephthalic [25] acids). However, radical chains are difficult to control, and lead to the formation of a wide variety of products as a consequence of a series of consecutive reactions because the reaction product is generally more easily oxidizable than the reactant itself.

1.3.1.1. Direct homolytic oxidation of organic substrate

This metal catalyzed autoxidation involves the direct one-electron oxidation of the substrate by the oxidized form of the metal catalyst e.g. cobalt is usually added as Co^{II}, reactive substrates such as aldehyde or ketone are often added as promoters to generate the high concentration of Co^{III} necessary for initiation of the reaction (Fig. 1.5).

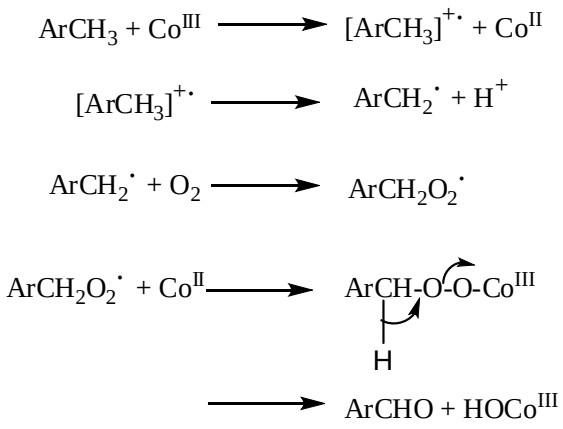

Fig. 1.5. Direct homolytic oxidation of benzylic compounds

1.3.2. Heterolytic mechanism

This metal catalyzed oxidation involves a two-electron oxidation of a (coordinated) substrate by a metal ion. The oxidized form of the metal is subsequently regenerated by reaction of the reduced form with dioxygen e.g. Pd(II)–catalyzed oxidation of alkene (Wacker process) (Fig. 1.6).

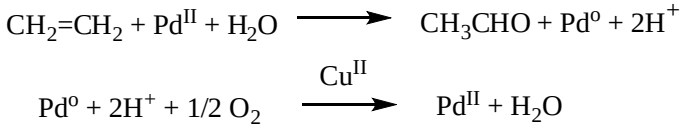

Fig.1.6. Wacker oxidation of alkenes

In a variation on this theme, which pertains mainly to the gas phase oxidations, where, an oxometal species oxidizes the substrate and the reduced form is the subsequently re-oxidized by dioxygen (Fig. 1.7).

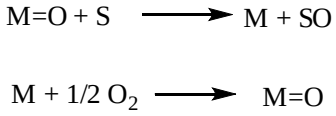

Fig. 1. 7. Mars-van Krevelen mechanism

1.3.2.1. Catalytic oxygen transfer

Reduced forms of dioxygen, such as H_2O_2 or RO_2H, are considered as a single oxygen donor. Such a reaction is referred to as a catalytic oxygen transfer process [26].

$$S + XOY \xrightarrow{\text{Catalyst}} SO + XY \qquad (1.3)$$

S = substrate; SO = oxidized substrate

XOY = H_2O_2, RO_2H, R_3NO, NaOCl, $KHSO_5$, etc.

Catalytic oxygen transfer processes are widely applicable in organic synthesis. Heterolytic oxygen transfer processes can be divided into two categories based on the nature of the active oxidant: an oxometal or a peroxometal species (Fig. 1.8). Catalysis by early transition metals (Mo, W, Re, V, Ti, Zr) generally involves high-valent peroxometal complexes whereas later transition metals (Ru, Os), particularly first row elements (Cr, Mn, Fe) mediate oxygen transfer via oxo metal species.

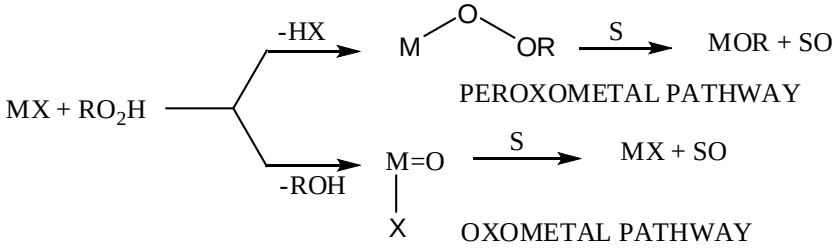

Fig. 1.8. Peroxometal versus oxometal pathways

1.4. SIDE CHAIN OXIDATION OF PHENOLIC COMPOUNDS

The oxidation of alkyl side chain of phenol derivatives to the corresponding carbonyl compounds is of fundamental importance in organic synthesis, due to the wide ranging utility of the oxidation products as important precursors and intermediates for many drugs, vitamins and fragrances e.g. liquid phase oxidation of veratryl alcohol gives

veratryl aldehyde which is used as a flavoring agent and also as an important pharmaceutical intermediate for the manufacture of angiocardiopathy drugs such as donepezil [27]. Another example of liquid phase oxidation is of vanillyl alcohol giving vanillin, which has major applications in the food and perfumery sectors because of its flavor and it also finds use in medicinal applications serving as a platform chemical for pharmaceutical production [28]. Traditionally, oxidations of alcohols have been performed with high-valent metal oxides or their mineral salts, notably of middle first row transition metals [29]. Common reagents of this type are: chromium (VI) oxide (CrO_3), potassium chromate (VI) (K_2CrO_4), potassium dichromate (VI) ($K_2Cr_2O_7$), manganese (IV) oxide (MnO_2) and potassium permanganate (VII) ($KMnO_4$). Potassium ferrate (VI) (K_2FeO_4) has recently also been added to this list [30]. In most instances, these inorganic oxidants are required in stoichiometric amounts and are usually toxic, hazardous or both. Moreover, purification of the reaction product is often demanding and laborious. In recent years, there has been great interest in the search for new catalytic systems for the oxidation of alcohols using hydrogen peroxide [31] or dioxygen [32, 33] as the ultimate stoichiometric oxidant, due to their obvious economic and ecological advantages (‘‘green chemistry’’). However, the number of metal compounds capable of mediating dioxygen activation (through metal–O_2 adduct formation), thus leading to alcohol oxidation [34, 35].

1.5. LITERATURE SURVEY ON LIQUID PHASE OXIDATION REACTIONS

Catalytic liquid phase oxidation of side chains of phenolic compounds is an active research area and several types of catalysts have been reported in the literature, which can be broadly classified as follows:

1) Supported noble-metal catalysts

2) Non-noble metal oxides

3) Mixed metal oxides

Most of the reactions catalyzed by these catalysts have been carried out in a batch reactor in the presence of stoichiometric excess NaOH. The reason for the use of sodium hydroxide is that it prevents the formation of dimeric by-products and hence is beneficial for the selective oxidation [36]. Main importantly, free base is necessary for preforming the phenolate ion, which helps to anchor the substrate on catalyst surface [23].

1.5.1. Supported noble-metal catalysts

Supported noble-metal catalysts find wide applications as liquid phase oxidation catalysts. The catalytic active sites of metal, supported on high-surface-area oxides, consist of dispersed surface metal oxide species [37]. Supported metal oxide catalysts have been extensively investigated since 1950 and the literature on supported noble-metal catalysts published till date is summarized in Table 1.2. These catalysts are employed in numerous large-volume industrial catalytic applications [38]: e.g. liquid phase oxidation of *p*-cresol and oxidation of 1-pheny ethanol to acetophenone over hydrotalcite-supported gold nanoparticles [39]. The highlights of studies on noble metal catalyzed liquid phase oxidation are given below.

1.5.1.1. Pd-catalysts

Nanoparticles of Pd have been supported on a variety of materials, including hydroxyapatite (HAP), [40] carbon, [41] Al_2O_3, [40] SiO_2, [40] pumice, [42] and SiO_2-Al_2O_3 mixed oxide. The role of the support for Pd catalysts was investigated by Mori *et al.* [40] and Chen *et al.* [43] Mori *et al.* found that benzyl alcohol (BA) conversion and the benzaldehyde selectivity depended on the support; with hydroxyapatite (HAP)-as a support, the catalyst gave the highest conversion (99%) and selectivity to benzaldehyde (99%).

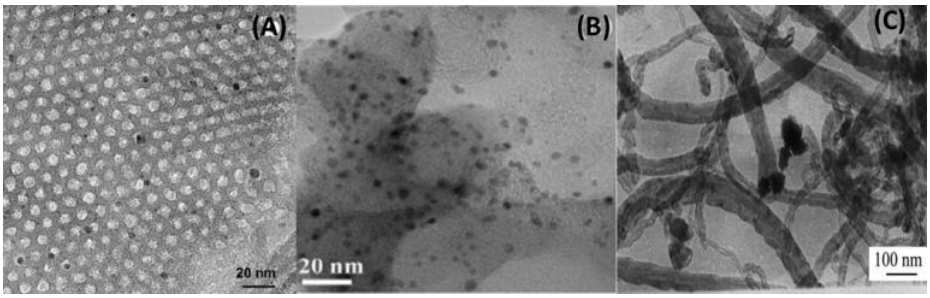

Fig. 1.9. TEM images of (A) Pd-SiO_2, (B) Pd-C and (c) Pd-CNT [40, 44, 45].

The other supports examined (Al_2O_3, SiO_2, and C) produced the aldehyde with less than 50% selectivity (Fig.1.9 A). The highest conversion was achieved over Pd/Al_2O_3, though the selectivity was the lowest (38%), while highest selectivity of 47% was achieved with Pd/SiO_2 catalyst however the conversion was only 71%. The Pd/C (Fig. 1.9 B) produced the lowest conversion (46%) and selectivity (42%). Uozumi *et al.* utilized a novel support, an amphiphilic resin, in the oxidation of aqueous alcohols [44]. The corresponding catalyst gave 97% yield of aldehyde product after 1.5 h. The high selectivity to the aldehyde in an aqueous medium is interesting particularly, because sequential oxidation to the carboxylic acid readily occurs in water. Apparently the hydrophobic nature of the resin prevents the conversion of the aldehyde in water over Pd. The investigation of the role of solvent was studied by Villa *et al.* for Pd on activated carbon (AC) or on carbon nanotubes (CNT) as oxidation catalysts (Fig. 1.9 C) [45]. An increased rate of reaction was noted in neat alcohol (TOF 0.83 s^{-1}) as opposed to a mixture of 80% water and 20% alcohol (TOF 0.023 s^{-1}) over Pd/AC catalyst, though the product distribution remained unchanged.

From the literature survey, it appears that the support material for Pd nanoparticles has a substantial effect on the product selectivity. Interestingly, the appropriate choice of support can suppress the sequential oxidation of aldehyde to carboxylic acid in aqueous solution.

1.5.1.2. Au-catalysts

Although bulk gold has for a long time being regarded as a poorly active metal, surprisingly the high activity of gold nanoparticles has initiated intensive research into their use for aerobic oxidation reactions [46]. Much of the literature on benzyl alcohol oxidation over Au catalysts describes results obtained in the presence of a homogeneous base. Buonerba *et al.* [47] supported Au nanoparticles on block copolymers and used the resulting catalysts in the oxidation of BA in a water and chloroform solvent with added KOH. They attained >99% conversion of BA and 97% selectivity to the aldehyde product after 6 h at mild conditions (308 K, 100 kPa O_2). Very recently, Guo *et al.* reported successful aerobic oxidation of BA over unsupported bulk Au [48]. The oxidation of BA was performed in aqueous NaOH, and the distribution of products was a function of the reaction temperature and concentration of NaOH. For BA oxidation at 333 K, the major product was the ester, benzyl benzoate, for lower concentrations of base (<0.6 M NaOH) while at higher concentrations of 1.2 M NaOH, benzoic acid was predominantly formed, Increasing the temperature to 363 K, resulted in a majority of the aldehyde product over the range of NaOH concentrations. The authors hypothesize that the π-electrons in BA enhance interactions with Au, facilitating the oxidation. The effect of acid and base sites on the support in Au catalysis for BA oxidation has been investigated in the absence of additional homogeneous base [49, 50, 51]. Low conversion of benzyl alcohol was observed after 3 hours (maximum conv. 7%, over Au/Fe_2O_3), which is typical of oxidation reactions in the absence of a homogeneous base. Selective oxidation to benzaldehyde was achieved over Au on SiO_2, TiO_2, and CeO_2, (Fig 1.10) with the best results obtained in case of Au/CeO_2 (3.4%conversion, 100% selectivity to aldehyde after 3 h at 373 K and 200 kPa O_2).

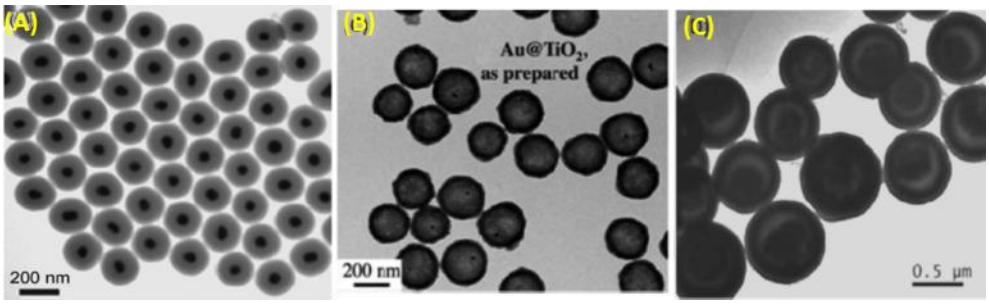

Fig. 1.10. TEM images of (A) Au-SiO_2, (B) Au-TiO_2 and (c) Au-CeO_2 [50,51]

The lowest conversion was observed over Au/TiO_2 catalyst (0.65% conversion and 100% selectivity to aldehyde in 3 h). Gold catalysts supported on nanosized NiO (3–5 nm) were more active than Au on commercial micrometer sized NiO (55% conversion vs. 6% conversion, in 6 h), likely due to both an increase in basicity of the support (basicity per square meter of nanosized NiO: 0.21 mmol g^{-1}; of commercial NiO: 0.12 mmol g^{-1}) and also a cooperative effect of metal and support [52]. Fang *et al.* investigated amphoteric materials and the effects of their acidity/basicity on BA oxidation in *p*-xylene solvent at 393 K in the absence of an oxidant [50]. Au/Al_2O_3, Au/MgO, Au/HAP, and Au/Hydrotalcite (HT) catalysts demonstrated BA conversion of about 20-30%; the selectivity to the aldehyde over each catalyst was compared at this conversion. The Au/Al_2O_3 catalyst showed the highest conversion (32%) but the lowest aldehyde selectivity (18%), whereas Au/MgO showed the highest selectivity (99%) but the lowest conversion (20%). The Au/HT exhibited selectivity similar to that of Au/MgO, but at approximately 10% higher conversion. Au/HT had both strong acid and strong base sites, Au/SiO_2 had neither acid nor base sites, and Au/MgO had only strong base sites. The catalysts with neither acid nor base sites were almost inactive, whereas the catalyst with the highest acidity and basicity (Au/HT) had the highest conversion of alcohol and selectivity to aldehyde. Moreover, a catalyst with stronger basicity in absence of any acidity (Au/MgO) showed higher selectivity to aldehyde, but a catalyst with strong acidity (Au/Al_2O_3) was more active. In summary, the oxidation of benzyl alcohol exhibited the highest rates over Au catalysts in the presence of a homogeneous base. Although the oxidation of alcohol to aldehyde to acid is greatly accelerated by the

presence of homogeneous base, the sequential oxidation of aldehyde to acid may be inhibited through careful selection of the solvent and the catalyst support.

1.5.1.3. Ru-catalysts

Zeolite impregnated with RuO_2 nano clusters (RuO_2-FAU) was reported to be an effective and selective catalyst for for oxidation of a wide variety of both activated and unactivated substrates [52]. These materials display strong shape selectivity due to uniform pore size distribution [53]. Kobayashi developed a polymer incarcerated ruthenium (PI Ru), based on the technique of microencapsulation and cross-linking from a polystyrene-based copolymer and ruthenium chloride hydrate as the metal source [54]. However, this catalyst needed the presence of 15 mol% of TEMPO to show wide applicability, and leaching of Ru metal was observed in some cases, which is typical of polymer supported catalysts, that suffer from low chemical and/or mechanical resistance. Ruthenium is less expensive than Au, Pd or Pt; and one of the few studies on Ru/C-catalyst done recently by Sajiki and co-workers showed that 10% Ru/C in toluene (at 50 °C) under an oxygen atmosphere was able to convert various secondary and primary benzylic alcohols to the corresponding carbonyl compounds and primary aliphatic alcohols to carboxylic acids when water was added as a co-solvent [55].

Table 1.2. Supported noble-metal catalysts for oxidation of benzyl alcohol

Entry	**Catalysts**	**Reaction conditions**		**Conv. (%)**	**Sel. (%)**		**Ref.**
		Temp (^{0}C)	**Time (h)**		**ALD**	**ACID**	
1.	[a]Au/HT	27	6	99	99	-	39
2.	Pd/HAP	90	1	99	99	-	40
3.	Pd/C	60	3	46	42	58	41
4.	Pd/Al_2O_3	90	1	96	38	62	40
5.	Pd/SiO_2	90	1	71	47	53	40

6.	ARP-Pd	100	1.5	99	97	3	44
7.	Pd/AC	80	15 min	90	74	26	45
8.	AuNPs	35	1	>99	96	4	47
9.	Bulk Au	110	3	60	90	10	48
10.	[a]Au/Fe_2O_3	100	3	7	87	13	50
11.	[a, b]RuO_4^- /CPSIL	80	5	99	>99	-	52
12.	RuO_2/FAU	35	1	100	>99	-	53
13.	[c]PI-Ru	80	2.5	>99	96	-	54
14.	10%Ru/C	50	24	90	85	15	55

a = without base

b = cross linked polymer supported ionic liquid

c = polymer incarcerated ruthenium (PI-Ru)

1.5.2. Non-noble metal oxide catalysts

Metal oxides represent one of the most important and widely employed categories of solid catalysts, either as active phases or as supports. Metal oxides are utilized both for their acid–base and redox properties and constitute the largest family of catalysts in heterogeneous catalysis. Metal oxide catalysts have numerous industrial applications for liquid phase oxidation reactions [56,57]. Several noble metal-based heterogeneous catalysts such as Au/CeO_2, Pd/C, Ru/TiO_2 etc. have been explored for this purpose and such reactions are mediated by the use of alkali [58, 59]. Although noble metal catalysts exhibit high activity for oxidation reactions, they can be expensive therefore, minimizing their potential for commercial applications [60]. Oxides of other transition metals, such as copper, cobalt, manganese, and chromium, are also known to be effective catalysts for oxidation reactions. Among these metals, cobalt is the most attractive because of its

strong capability for dioxygen activation (through metal–O_2 adduct formation) and because it is more cost effective compared to noble metals. Cobalt has been known as an excellent catalyst for the relatively inert hydrocarbon C–H bond activation in the oxidation reactions [36]. Nanostructured Co_3O_4 catalyst (6–8 nm) having high surface area (95m^2/g) was developed for liquid phase air oxidation of *p*-cresol which gave 83% selectivity to *p*-hydroxybenzaldehyde in 1 h [61]. Co-saponite catalysts reported for the air oxidation of *p*-vanillyl alcohol were prepared by varying Co content in the range of 5% to 30% using in situ precipitation method. The highest activity (conv. 55%) and selectivity of 99% to *p*-vanillin was obtained for 13% Co-saponite in *p*-vanillyl alcohol oxidation [62]. Monometallic cobalt and manganese supported on hexagonal mesoporous silicas (HMS) prepared by incipient-wetness impregnation were examined as catalysts for partial oxidation of 4-*tert*-butyltoluene with dioxygen as oxidizing agent in acetonitrile solvent. The catalysts showed 30 and 18% conv. of *tert*-butyltoluene with 75 and 69% selectivity to corresponding aldehyde respectively [63]. A series of Mg–Mn–Al ternary hydrotalcite with (Mg+Mn)/Al atomic ratios of ∼3 and Mg:Mn atomic ratios ranging from 3:0 to 0:3 were synthesized by a co-precipitation method and evaluated for liquid phase oxidation of toluene using *tert*-butyl hydroperoxide as the oxidant. Benzaldehyde and benzoic acid were the major products with minor amounts of benzyl alcohol [64]. Co_3O_4 catalyst supported on activated carbon showed ∼100% BA conversion even in the absence of any promoter (e.g., NaOH) [65]. Nano-structured, spinel Co_3O_4 catalyst was developed for the aqueous phase oxidation of veratryl alcohol, which showed the highest conversion of 85% with 96% selectivity to veratryl aldehyde [66].

Table 1.3. Non-noble metal oxide catalysts for liquid phase oxidation reactions

Substrates	Catalysts	Reaction conditions			Conv. (%)	Sel. (%)			Ref.
		T, °C	t, h	NaOH mmol		ALD	ACID	OTH	
BA	Co-Al-HT	100	1	-	12	97	0.5	2.2	56
p-cresol	Co_3O_4	95	1	111	40	44	-	56	61
vanillyl alcohol	Co-saponite	65	3	26	55	99	1	-	62
tert-butyltoluene	Co-HMS	70	5	-	30	75	17	8	63
tert-butyltoluene	Mn-HMS	70	5	-	18	69	25	6	63
toluene	Mn-LDH	80	4	-	14	24	75	1	64
BA	Co_3O_4/AC	100	3	-	100	87	10	3	65
veratryl alcohol	Co_3O_4	140	7	-	85	96	4	-	66

1.5.3. Mixed-metal oxides

Oxides containing two or more different kinds of metal cations are known as mixed metal oxides. Oxides can be binary, ternary and quaternary with respect to the presence of the number of different metal cations. Mixed metal oxides play a very important role in academic as well as industrial research due to their acid–base and redox properties, having significant contributions in heterogeneous catalysis. Mixed metal oxides are better in terms of their catalytic activity than single metal oxides in various reactions. It could be due to increasing active acidic or basic sites, and increasing surface area, which reduces the reaction time, increases the yield of reaction or conversion of reactants. [67] Mixed-metal oxides are widely employed in industry as heterogeneous catalysts for selective oxidation reactions e.g. methanol oxidation to formaldehyde, propylene oxidation/ammoxidation to acrolein/acrylonitrile, propane oxidation/ ammoxidation to acrolein/acrylonitrile, n-butane oxidation to maleic anhydride, etc. (Fig. 1.11).

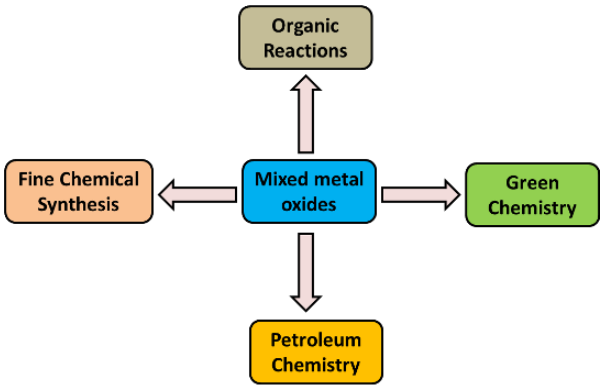

Fig. 1.11. Application of mixed metal oxides in various sectors

The spinel type chromites MCr_2O_4 (M = Co, Ni and Cu) were synthesized by the co-precipitation method and have been studied for the oxidation of benzyl alcohol by molecular oxygen wherein it has been observed that benzaldehyde is formed with 100% selectivity. The catalytic activity of the chromites follows the order Co > Cu > Ni [68]. Song and co-workers have reported a Cu–Mn mixed oxide catalyst supported on carbon which was prepared using the incipient wetness method. The catalyst along with TEMPO was used for the selective aerobic oxidation of alcohols to corresponding aldehydes or ketones [69]. Jayaram *et al.* very recently reported MoO_3/SiO_2 as a heterogeneous bi-functional catalyst for sequential oxidation of alcohols to their corresponding aldehydes/ketones using H_2O_2 as a green oxidant [70]. Mn–Ni mixed hydroxide was synthesized by a facile co-precipitation method and the catalytic performance in the aerobic oxidation of benzyl alcohol using molecular oxygen was examined. This catalyst showed the best selectivity for benzaldehyde (99%) at 100 ^oC within 1 h [71]. Parida *et al.* reported the liquid phase oxidation of benzyl alcohol by using vanadium phosphate as a heterogeneous catalyst, with remarkable catalytic activity of 97% conversion and 99% selectivity to aldehyde [72]. Synthesis of *p*-hydroxybenzaldehyde from *p*-cresol and molecular oxygen was reported by Feng *et al.* over a CuMn-mixed oxides catalyst supported on carbon gave a high conversion of *p*-cresol (99%) and a high selectivity to *p*-hydroxybenzaldehyde (96%) [73]. CuCo- mixed oxides supported on carbon provides a single step synthesis of salicyladehyde from *o*-cresol. The catalyst gave 74% conversion

of *o*-cresol with 57% selectivity to salicylaldehyde [74]. Oxidation of benzyl alcohol was reported on alumina supported CuMn-mixed oxide catalyst gave 91% conversion of benzyl alcohol with almost complete selectivity to benzaldehyde [75]. Cu–Mn oxides in combination of 2,2,6,6-tetramethyl-piperidyl-1-oxy (TEMPO) were used to catalyze selective aerobic oxidation of alcohols to carbonyl compounds by Guanyu Yang *et al.* [76].

Table 1.4. Non-noble mixed metal oxide catalysts for liquid phase oxidation reactions

Substrates	**Catalysts**	**Reaction Conditions**			**Conv. (%)**	**Sel. (%)**			**Ref.**
		T,^{o}C	**t,h**	**NaOH (g)**		**ALD**	**ACID**	**OTH**	
BA	$CoCr_2O_4$	100	24	-	65	100	-	-	68
BA	$NiCr_2O_4$	100	24	-	20	100	-	-	68
BA	$CuCr_2O_4$	100	24	-	35	100	-	-	68
BA	CuMn/C	100	6	TEMPO	99	>99	-	-	69
BA	MnNi(OH)x	100	1	-	89	99	1	-	71
BA	$VO(PO_3)_2$	80	4	TBHP	97	99	1	-	72
p-cresol	CuMn/C	75	3	23	99	96	4	-	73
o-cresol	CuMn/C	80	1	Pyridine	74	57	22	21	74
BA	$CuMn/Al_2O_3$	100	4	-	91	>99	-	-	75
BA	CuMnOx	120	6	TEMPO	63	97	3	-	76

Based on the literature survey on the solid catalysts for liquid phase oxidation reactions, we concluded that non-noble transition metal catalysts also can perform the same catalytic activity as noble metal catalysts. However, proper tuning of the catalysts composition, morphology and particles size are the important factors contributing to the

activity and selectivity of the catalysts. We observed from the Tables 1.2, 1.3 and 1.4, that mixed oxide catalysts gave better catalyst activity than that of single metal oxides. The higher activity of these mixed oxides could be due to the synergism effect among them. In this work, the major focus was on the liquid phase oxidation of phenolic compounds; viz. vanillyl alcohol, veratryl alcohol and *p*-cresol. Among them, the first two are the lignin derived platform molecules. There are number of catalysts reported for the liquid phase oxidation of *p*-cresol, such as Co-saponite [77], Co-salen complex [78], CuMn-mixed oxide catalyst supported on carbon [73]. Most of these reactions are carried out with high concentration of homogenous base (NaOH) and longer reaction time. The catalysts reported for vanillyl and veratryl alcohols oxidation are mostly enzyme based [79-81] and few are noble metal based catalysts [82, 83]. Hence, the attempt was made to develop single and mixed non-noble metal oxides as catalyst and to understand the structure-activity correlation in the oxidation of various practically important molecules.

1.6. REFERENCES

1. R. A. Sheldon, D. H. R. Barton, A. E. Martell, D. T. Sawyer, The Activation of Dioxygen and Homogeneous Catalytic Oxidation, Eds., Plenum Press, New York, 1993.
2. T. Punniyamurthy, S. Velusamy, J. Iqbal. *Chem. Rev.* 2005, 105, 2329.
3. R. A. Sheldon, R. A. van Santen (Eds.), Cataltic oxidation: Principles and applications, Wourld Scientific, Singapore, 1995.
4. R. A. Sheldon, *CHEMTECH* 1991, 21, 566; 1994, 24, 38.
5. K. Weissermel, H.J. Arpe, Industrial Organic Chemistry, 4th edn. Wiley-VCH, Weinheim, 2003, p. 148.
6. E. S. J. Lox, B. H. Engler, In: Handbook of Heterogeneous Catalysis, Vol. 4. G. Ertl, H. Knoetzinger, J. Weitkamp, eds. VCH, Weinheim, 1997, pp. 1559–1633.
7. J. Kummer In: Catalysts for the Control of Automotive Pollutants. J. McAvoy, ed. ACS Series 143. American Chemical Society, Washington, DC, 1975, pp. 178–192.
8. R. A. Dalla Betta, *Catal. Today* 1997, 35, 129.
9. J. Hagen, Industrial Catalysis. Wiley-VCH, Weinheim, 1999, p. 148.
10. J. D. Burrington, C. T. Kartisek, R. K. Grasselli, *J. Catal.* 1984, 87, 363.
11. R. A. Sheldon, H. van Bekkum, Fine Chemicals through Heterogeneous Catalysis, Wiley-VCH, Weinheim, 2001, p 1.
12. K. Tanaka, *CHEMTECH*, 1974, 4, 555.
13. R. A. Sheldon, I. W. C. E. Arends, A. Dijksman, *Catal. Today* 2000, 57, 157.
14. D. Riley, M. Stern, J. Ebner, D. H. R. Barton, A. E. Martell and D. T. Sawyer, in The Activation of Dioxygen and Homogeneous Catalytic Oxidation, Eds., Plenum Press, New York, 1993.
15. P. T. Anastas, J. C. Warner, Green Chemistry: Theory and Practice. Oxford University Press, New York, 1998.
16. B. M. Trost *Science* 1991, 254, 1471.
17. B. M. Trost *Angew. Chem. Int. Ed.* 1995, 34, 259.

18. R. A. Sheldon, *Green Chem*. 2007, 9, 1273.
19. R. A. Sheldon, *Chem. Commun*. 2008, 3352.
20. S. S. Stahl, *Science* 2005, 309, 1824.
21. J. E. Huheey, Inorganic Chemistry, 3rd ed. Harper & Row, New York, 1983.
22. G.W. Parshall, Homogeneous Catalysis. Wiley, New York, 1980, p. 188.
23. R. A. Sheldon, J. K. Kochi, Metal Catalyzed Oxidations of Organic Compounds. Academic Press, New York, 1981.
24. M. T. Musser, In: Ullmann's Encyclopedia of Industrial Chemistry, Vol. A8, 5th edn. Wiley-VCH, Weinheim, 1995, pp. 217.
25. R. J. Sheehan, In: Ullmann's Encyclopedia of Industrial Chemistry, Vol. A26, 5th Edn. Wiley-VCH, Weinheim, 1995, pp. 193.
26. R. A. Sheldon, *Top. Curr. Chem.* 1993, 164, 21.
27. A. L. Gutman, G. Nisnevich, E. Shkolnik, B. Tishin, I. Zaltzman, US Patent, 2002, 6,492,522.
28. J. F. Stanzione, J. M. Sadler, J. J. La Scala, K. H. Reno, R. P. Wool, *Green Chem.* 2012, 14, 2346.
29. D. Benson, Mechanisms of Oxidation by Metal Ions, Elsevier Scientific Publishing Co., Amsterdam, 1976.
30. L. Delaude, P. Laszlo, *J. Org. Chem.*1996, 61, 6360.
31. G. Rothenberg, G. Barak, Y. Sasson, *Tetrahedron* 1999, 55, 6301.
32. C. Y. Lorber, S. P. Smidt, J. A. Osborn, *Eur. J. Inorg. Chem.* 2000, 655.
33. I. E. Markó, P. R. Giles, M. Tsukazaki, I. Chellè-Regnaut, C. J. Urch, S. M. Brown, *J. Am. Chem. Soc.* 1997, 119, 12661.
34. I. E. Markó, P. R. Giles, M. Tsukazaki, S. M. Brown, C. J. Urch, *Science* 1996, 274, 2044.
35. I. E. Markó, M. Tsukazaki, P. R. Giles, S. M. Brown, C. J. Urch, *Angew. Chem. Int. Ed.* 1997, 109, 2297.
36. F. Wang, G. Yang, W. Zhang, W. Wu, J. Xu, *Chem. Commun.* 2003, 1172.

37. B. M. Weckhuysen, I. E. Wachs, Catalysis by supported metal oxides, in Handbook of Surfaces and Interfaces of Materials (ed. H.S. Nalwa), Academic Press , New York , 2001, p. 63 .
38. I. E. Wachs, *Catal. Today* 1999, 51, 271.
39. T. Mitsudome, A. Noujima, T. Mizugaki, K. Jitsukawa, K. Kaneda, *Adv. Synth. Catal.* 2009, 351, 1890.
40. K. Mori, T. Hara, T. Mizugaki, K. Ebitani and K. Kaneda, *J. Am. Chem. Soc.* 2004, 126, 10657.
41. N. Dimitratos, A. Villa, D. Wang, F. Porta, D. Su and L. Prati, *J. Catal.* 2006, 244, 113.
42. F. Liotta, A. M. Venezia, G. Deganello, A. Longo, A. Martorana, Z. Schay and L. Guczi, *Catal. Today* 2001, 66, 271.
43. Q. Chen, Y. Zhang, F. Wang, H. Wan, *Adv. Synth. Catal.* 2008, 350, 453-464.
44. R. Uozumi, Nakao, *Angew. Chem. Int. Ed.* 2003, 42, 194.
45. A. Villa, D. Wang, N. Dimitratos, D. Su, V. Trevisan, L. Prati, *Catal. Today*, 2010, 150, 8.
46. C. Parmeggiani, F. Cardona, *Green Chem*. 2012, 14, 547.
47. A. Buonerba, C. Cuomo, S. O. Sanchez, P. Canton, A. Grassi, *Chem. Eur. J.* 2012, 18, 709.
48. H. Guo, A. Al-Hunaiti, M. Kemell, S. Rautiainen, M. Leskela, T. Repo, *ChemCatChem*, 2011, 3, 1872.
49. W. Fang, J. Chen, Q. Zhang, W. Deng, Y. Wang, *Chem. Eur. J.* 2011, 17, 1247.
50. D. I. Enache, D. W. Knight, G. J. Hutchings, *Catal. Lett.* 2005, 103, 43.
51. A. Villa, C. E. Chan-Thaw, G. M. Veith, K. L. More, D. Ferri, L. Prati, *ChemCatChem*, 2011, 3, 1612.
52. Y. Xie, Z. Zhang, S. Hu, J. Song, W. Li, B. Han, *Green Chem.* 2008, 10, 278.
53. B. Z. Zhan, M. A. White, T. K. Sham, J. A. Pincock, R. J. Doucet, K. V. Ramana Rao, K. N. Robertson, T. S. Cameron, *J. Am. Chem. Soc.* 2003, 125, 2195.
54. T. Matsumoto, M. Ueno, J. Kobayashi, H. Miyamura, Y. Mori, S. Kobayashi, *Adv. Synth. Catal.* 2007, 349, 531.

55. S. Mori, M. Takubo, K. Makida, T. Yanase, S. Aoyagi, T. Maegawa, Y. Monguchi, H. Sajiki, *Chem. Commun.* 2009, 5159.
56. V. R. Choudhary, P. A. Chaudhari, V. S. Narkhede, *Catal. Comm.* 2003, 4, 171.
57. T. Miyahara, H. Kanzaki, R. Hamada, S. Kuroiwa, S. Nishiyama, S. Tsuruya, *J. Mol. Catal. A: Chem.* 2001,176, 141.
58. Y. Zhang, X. Cui, F. Shi, Y. Deng, *Chem. Rev.* 2012,112, 2467.
59. Y. Shen, S. Zhang, H. Li, Y. Ren, H. Liu, *Chem. Eur. J.* 2010, 16, 7368.
60. U. Menon, V. V. Galvita, G. B. Marin, *J. Catal.* 2011, 238, 1.
61. V. S. Kshirsagar, S. Vijayanand, H. S. Potdar, P. A. Joy, K. R. Patil, C. V. Rode, *Chem. Lett.* 2008, 37, 310.
62. A. C. Garade, N. S. Biradar, S. M. Joshi, V. S. Kshirsagar, R. K. Jha, C.V. Rode, *Appl. Clay Sci.* 2011, 53, 157.
63. W. Yu, C. Zhou, D. shen Tong, T. ning Xu, *J. Mol. Catal. A: Chem.* 2012,365, 194.
64. S. Velu, N. Shah, T.M. Jyothi, S. Sivasanker, *Micro. Meso. Mater.* 1999, 33, 61.
65. J. Zhu, K. Kailasam, A. Fischer, A.Thomas, *ACS Catal.* 2011, 1, 342.
66. V. R. Mate, M. Shirai, C. V. Rode, *Catal. Comm.* 2013, 33, 66.
67. A. V. Biradar, S. B. Umbarkar, M. K. Dongare, *Appl. Catal. A* 2005, 285, 190.
68. K. Premalatha, P. S. Raghavan, B. Viswanathan, *Appl. Catal. A Gen.* 2012, 419-420, 203.
69. G. Yang, W. Zhu, P. Zhang, H. Xue, W. Wang, J. Tian, M. Song, *Adv. Synth. Catal.* 2008, 350, 542.
70. K. D. Parghi, R. V. Jayaram, *Catal. Commun.* 2010, 11, 1205.
71. Q. Tanga, C. Wu, R. Qiao, Y. Chen, Y. Yang, *Appl. Catal. A Gen.* 2011, 403 136.
72. G. C. Behera, K.M. Parida, *Appl. Catal. A Gen.* 2012, 413-414, 245.
73. F. Wang, G. Yang, W. Zhang, W. Wu, J. Xu, *Adv. Synth. Catal.* 2004, 346, 633 .
74. F. Wang, J. Xu, S. Liao, *Chem. Commun.* 2002, 626.
75. Q. Tang, X. Gong, P. Zhao, Y. Chen, Y. Yang, *Appl. Catal. A Gen.* 2010, 389 101.

76. G. Yang, J. Ma, W. Wang, J. Zhao, X. Lin, L. Zhou, X. Gao, *Cat. Lett.* 2006, 112, 83.
77. V. S. Kshirsagar, A. C. Garade, K. R. Patil, R. K. Jha, C. V. Rode, *Ind. Eng. Chem. Res.* 2009, 48, 9423.
78. C. V. Rode, V. S. Kshirsagar, J. M. Nadgeri, K. R. Patil, *Ind. Eng. Chem. Res.* 2007, 46, 8413.
79. M. Lahtinen, P. Heinonen, M. Oivanen, P. Karhunen, K. Kruus, J. Sipilä, *Org. Biomol. Chem.* 2013, 11, 5454.
80. C. Crestini, G. G. Sermanni, *J. Biotech.* 1995, 39, 175.
81. H. H. Robert, A. M Willy, R. Stefano, J. H. Willem, *J. Biol. Chem.* 2004, 279, 33492.
82. C. Crestini, M. C. Caponi, D. S. Argyropoulos, R. Saladino, *Biorg. Med. Chem.* 2006, 14, 5292.
83. C. Crestini, P. Pro, V. Neri, R. Saladino, *Bioorg. Med. Chem. Lett.* 2005, 13, 2569.

Chapter 2

Metal oxide catalysts for oxidation reactions

2.1. INTRODUCTION

Metal oxides which constitute the largest family of catalysts in heterogeneous catalysis play a very important role in academic as well as in industrial applications because of their acid–base and redox properties [1]. For example, several industrial oxidation reactions are catalyzed by metals and metal oxides such as benzyl alcohol oxidation to benzaldehyde by silver vanadate, *p*-cresol to *p*-hydroxybenzaldhyde by manganese dioxide, propane oxidation/ammoxidation to acrolein/acrylonitrile by molybdates and antimonates, *p*-xylene to terephthalic acid by cobalt with a co-oxidant [2-4]. Transition metals in particular noble metals are frequently used as catalysts and their activity has been attributed due to the partially filled *d*-orbital of the metal ions or/ and due to the influence of the oxide ligand field on this partially filled *d*-orbital [5]. Single metal oxides crystallize forming different morphologies (isotropic, anisotropic or amorphous) and local co-ordination. The majority of single metal oxides crystallize with an isotropic morphology (without preferential orientation) and the surface may terminate with M–OH, M–O–M, M=O or M-( ) functionalities, where M-( ) represents an oxygen vacancy. Although noble metal catalysts exhibit high activity for oxidation reactions, they can be expensive, minimizing their potential for commercial applications [6]. Apart from cost considerations, noble metal residues (e.g. Pt and Pd) in pharmaceutical and nutritional products are highly problematic, and thus should be avoided. Oxides of other transition metals, such as copper, cobalt, manganese, and chromium, are occupying a predominant place in catalysis owing to their low cost of production, easy regeneration and selective action.

Mixed metal oxides are also widely employed in industry as heterogeneous catalyst for selective oxidation reactions. Mixed metal oxides with a structure of spinel can be obtained by the substitution of metal cations from the host spinel oxide with other similar metal cations (dopants). This substitution may restructure chemical bonding at the surface of the host oxides, which modifies the electronic properties as well as the chemistry of the host metal oxides [7]. For example, doping of manganese into Co_3O_4 spinel leads to an increase in catalytic activity compared with the material that contains

only a single metal either cobalt or manganese as an active phase [8]. The higher activity of the mixed metal oxides may be a cooperative effect towards an increment in the mobility of the oxygen as well as stabilizing the more active species and favoring the redox cycles, which also permit the reactivation of the catalyst [9].

A great deal of research is focused on designing heterogeneous catalysts for liquid-phase aerobic oxidation for developing ecologically sustainable processes for fine chemicals [10, 11]. Liquid phase aerobic oxidations provide a green route as aerial O_2 is one of the cheapest and greenest oxidants available and water is the only by-product formed [12, 13]. A major challenge for liquid-phase air oxidation is the activation of molecular oxygen under mild conditions to achieve the highest selectivity to the desired products. Although homogeneously catalyzed liquid-phase air oxidations are commonly practiced in industry using organometallic complexes as catalysts. The major drawbacks of such oxidations are: (i) poor selectivity to the desired product, as a variety of oxygenated products are formed because of the formation of free radical intermediates; (ii) fast deactivation of homogeneous catalysts due to formation of μ-oxo dimers; (iii) contamination of the product due to trace metal impurities during catalyst separation protocol [14,15]. These problems can be overcome by designing a suitable heterogeneous catalyst because they offer many advantages over their homogenous counterparts such as easy handling, separation and reusability. Therefore, development of functionalized heterogeneous catalysts is highly desirable from an environmental point of view. This can be achieved through a simplified preparation protocol for low-cost, highly active and reusable heterogeneous catalysts with the capability to form a strong redox couple and give controlled oxidation products.

The main objective of the present PhD work was to develop non-noble transition metal based single and mixed metal oxide catalysts for the liquid phase oxidation reaction in presence of molecular oxygen. The catalyst was completely characterized for its physico-chemical properties based on which the observed activity results have been discussed. Effect of various reaction parameters on conversion and selectivity of the corresponding product has been also studied. We prepared Co_3O_4 nanoparticle catalyst by

solvothermal method and tested for vanillyl alcohol oxidation in the presence of NaOH. Further, manganese doped cobalt mixed oxide (MnCo-MO) catalyst was also prepared and tested to for vanillyl alcohol oxidation under base free condition. Mixed oxide catalyst (MnCo-MO) was made as a composite with reduced graphene oxide and its activity was evaluated for *p*-cresol oxidation. Manganese oxide catalyst was also synthesized by sovothermal and co-precipitation methods. Comparative studies of these preparation methods on catalytic activity and selectivity were done in case of veratryl alcohol oxidation reaction in the absence of a base. The detailed discussions about these prepared catalysts and their performances for liquid phase oxidation reactions are discussed in detail under the following sections.

2.2. MONO METALLIC COBALT OXIDE (Co_3O_4) CATALYST FOR LIQUID-PHASE AEROBIC OXIDATION OF VANILLYL ALCOHOL TO VANILLIN

Cobalt oxide is the most versatile catalyst in liquid phase oxidation, because of its strong capability for dioxygen activation (through metal– O_2 adduct formation) and more cost effective compared to noble metals. As compared to their bulk counterparts, nanostructured materials are more efficient as catalysts due to increased number of corner and edge atoms with decreasing crystal domains, leading to higher adsorption rates and activation of the reactants [16, 17]. The catalytic performance is extremely sensitive to the particle size because the surface structure and electronic properties change considerably at the nanometer size scale. Hence, this work was undertaken to explore and understand the mechanism by which nanostructured materials govern their performance, especially their role in directing the selectivity pattern in a consecutive oxidation reaction. For this purpose, we prepared nanostructured Co_3O_4 by solvothermal method and investigated its catalytic performance for aerobic oxidation of vanillyl alcohol in the liquid phase (Scheme 2.1).

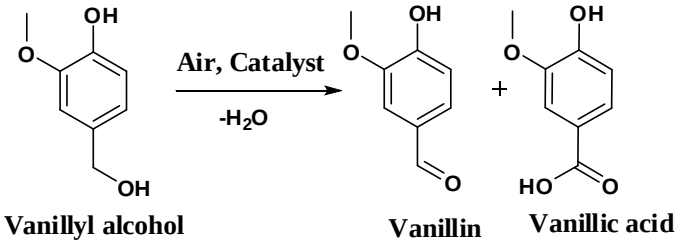

Scheme 2.1. Aerobic oxidation of vanillyl alcohol

Vanillin has major applications in the food and perfumery sectors because of its flavor and it also finds use in medicinal applications serving as a platform chemical for pharmaceutical production [18]. Traditionally, vanillin was synthesized from guaiacol through (i) the nitrose, and (ii) the glyoxylic method [19, 20] (Scheme 2.2).

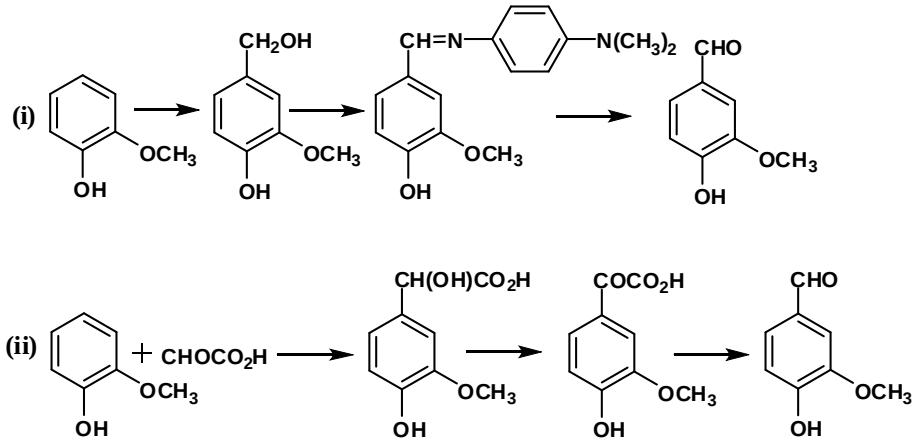

Scheme 2.2. Traditional vanillin synthesis; (i) Nitrose and (ii) glyoxylic, methods

Though these methods gave higher selectivity to vanillin, the formation of undesirable side products (nitrile and *p*-aminodimethyl aniline) in the case of the nitrose method, and the use of toxic oxidants (CuO, PbO_2 and MnO_2) in case of the glyoxylic method, and lower product yields (57%) are the serious drawbacks of these methods [21]. Hu *et al.* reported the synthesis of vanillin from oxidation of 4-methylguaiacol by using [Co-(salen)(py)][PF6]$_2$ (salen = bis(salicylidene)ethylenediamine, py = pyridine) as the catalyst, to afford complete conversion with 86% selectivity to vanillin in 18 h with mediation of the reaction by NaOH [22]. Thereafter, a combination of cobaltous chloride

and *N*-hydroxyphthalimide catalyzed oxidation in the presence of NaOH was also reported for vanillin synthesis with complete conversion of 4-methylguaiacol and 90% product yield (vanillin) in 7 hours [23]. However, catalyst preparation in both the processes was complicated, requiring a longer reaction time, and suffered a major problem in its recovery and recyclability. These drawbacks could be overcome by our successful synthesis of Co_3O_4 nanoparticles as efficient catalyst for the aerobic liquid phase oxidation of vanillyl alcohol to vanillin. The structural characterization of the catalyst was also done to explain the observed activity results. The reusability of the catalyst was achieved by the thermal regeneration step during the catalyst recycle study.

2.2.1. Experimental

Co_3O_4 nanoparticles were prepared by solvothermal method and the details of which has been described in chapter 2 of Section A (section 2.3.2.1). The catalyst was characterized by XRD, FT-IR, H_2-TPR, HR-TEM and cyclic voltammetry technique and the detailed characterization procedure is described in chapter 2 of Section A (sections 2.4.1, 2.4.9, 2.4.10, 2.4.6, and 2.4.11). The activity of Co_3O_4 catalysts for vanillyl alcohol oxidation was carried out in batch-reactor and experimental procedure is described in chapter 2 of Section A (2.5.2.1).

2.2.2. Results and discussion

2.2.2.1. Catalyst characterization

XRD diffractograms of the uncalcined and calcined samples of the prepared nano Co_3O_4 and commercial Co_3O_4 are displayed in Fig. 2.1. The as-synthesized material showed broad and asymmetric peaks at 2θ ~17.2^o, 33.6^o and 39.3^o, which are characteristic of the cobalt hydroxycarbonate phase [24]. However, the diffractogram of the calcined sample was completely different from the as-synthesized sample. The broad XRD diffraction peaks observed for calcined Co_3O_4 oxide at 2θ ~19^o, 31.4^o, 36.9^o, 44.9^o, 59.5^o and 65.4^o, were ascribed to the cubic phase of the Co_3O_4 (JCPDS No. 74-1657). The average crystallite size of Co_3O_4 nanoparticles estimated from the full width at half maximum of

the 311 diffraction peak by applying the Scherrer equation was about 14 nm, which was much smaller (six times) than that observed for the commercial Co_3O_4 (86 nm). The broader XRD diffraction peaks observed for our Co_3O_4 oxide indicate the nanocrystalline nature of the prepared catalyst.

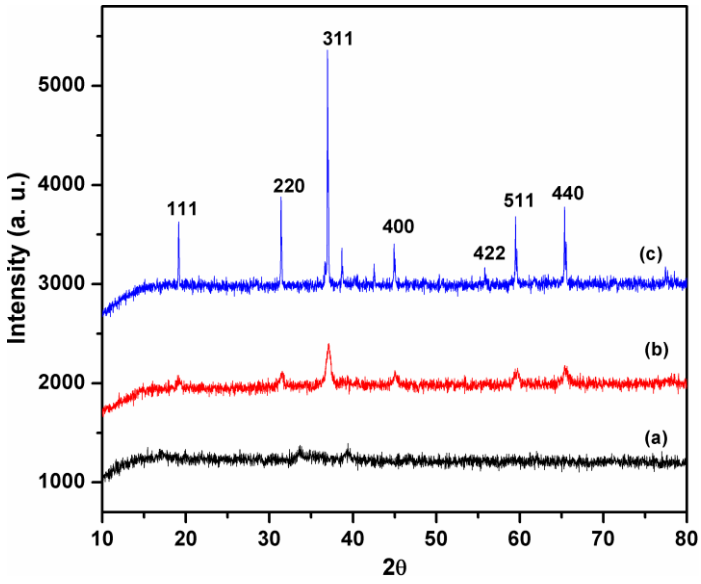

Fig. 2.1. XRD patterns of: (a) as synthesized cobalt hydroxycarbonate (b) Co_3O_4 nanoparticles (c) commercial Co_3O_4

The various cobalt oxide species possibly formed during the preparation of Co_3O_4 spinel were postulated from the temperature-programmed reduction analysis (TPR). TPR profiles of Co_3O_4 showed a two-step reduction process initiated at approximately 200 ^oC as shown in Fig. 2.2. The first reduction peak was very sharp and symmetrical and the temperature maximum was centered at about 325 ^oC. This peak was associated with the reduction of trivalent cobalt oxide (Co_3O_4) to divalent cobalt oxide (CoO) (2.1). The second reduction peak was broad and unsymmetrical with the temperature maxima centered at about 548 ^oC. This could be attributed to the subsequent reduction of divalent cobalt oxide (CoO) to metallic cobalt (Co^o) (2.2) [25, 26].

$$Co_3O_4 + H_2 - 3CoO + H_2O \qquad (2.1)$$

$$3CoO + 3H_2 - 3Co + 3H_2O \qquad (2.2)$$

The amount of hydrogen consumed at low temperature (325 ^{o}C) was about one third (3.83 mmol g^{-1}) of that for the higher temperature (548 ^{o}C, 11.8 mmol g^{-1}). The ratio of hydrogen consumed between the 1st and 2nd peaks was close to 1:3, which is consistent with the stoichiometry of Co_3O_4 reduction.

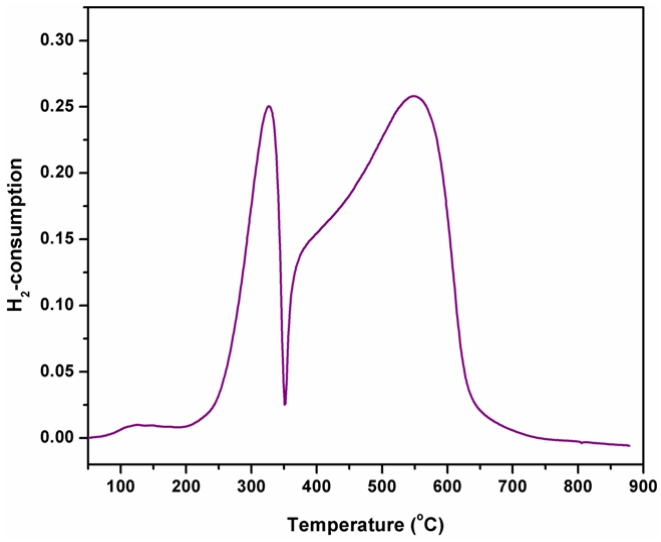

Fig. 2.2. H_2-TPR profile of Co_3O_4 nanoparticles

The reduction of CoO to metallic Co was strongly dependent on the morphology of Co_3O_4. As reported earlier, in case of nanoparticles, the reduction of CoO to Co metal initiated at 400 ^{o}C, was completed at 550 ^{o}C while for nanotube morphology, it started from 500 ^{o}C and completed at 650 ^{o}C. However in our case, CoO reduction started at 350 ^{o}C and was completed at around 650 ^{o}C, which clearly shows that the prepared Co_3O_4 existed with mixed nanocomposite morphology giving an unsymmetrical reduction peak as observed during reduction of CoO to metallic Co^{o} (Fig. 2.2). HR-TEM images (discussed later, Fig. 2.4) also suggest the mixed nanocomposite morphology of the prepared Co_3O_4 spinel.

Formation of Co_3O_4 spinel was also evident from the FT-IR characterization. Fig. 2.3 shows FTIR spectra of the as synthesized material (cobalt hydroxycarbonate) and Co_3O_4 nanoparticles. As compared with the cobalt hydroxy carbonate, the IR spectrum of the Co_3O_4 nanoparticles displayed two sharp bands at 563 and 667 cm^{-1}, originating from the

stretching vibrations of the metal–oxygen bonds. The former band at 563 cm^{-1} was attributed to Co^{3+} in an octahedral hole and the latter band at 667 cm^{-1} for Co^{2+} in a tetrahedral hole [27, 28]. The fingerprint of IR absorption at 563 and 667 cm^{-1} for the Co_3O_4 spinel was fully developed after calcination at 450 ^oC.

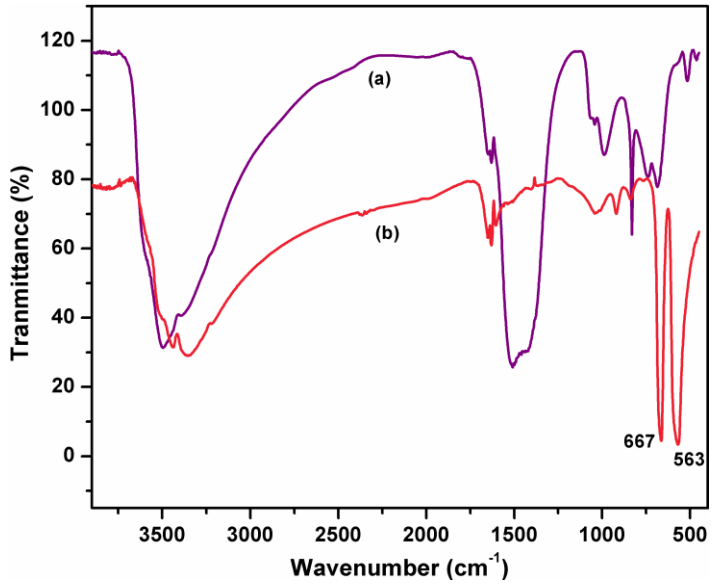

Fig. 2.3. FT-IR spectra for (a) cobalt hydroxy carbonate and (b) Co_3O_4 nanoparticles

Fig. 2.4 shows HR-TEM images of Co_3O_4 nanoparticles synthesized by the solvothermal method and subsequent calcination at 450 ^oC. The as-synthesized material had a fully developed rod-like morphology (Fig. 2.4a), while the calcined nanoparticles showed a mixed morphology which included cubic, tubular and truncated polyhedron shapes (Fig. 2.4b). These cobalt oxide nanoparticles were arranged in chain-like fashion with particle size ranging from 12–20 nm, which matched well with the crystallite size calculated from XRD. The fringe patterns of the prepared Co_3O_4 nanoparticles obtained by HR-TEM are shown in Fig. 2.4c. According to this, the dominant exposed planes were (111) with a lattice space of 0.46 nm. The other exposed planes observed were (220) and (311) with lattice spaces of 0.28 and 0.24 nm, respectively. Fig. 2.4d shows the cross-section view near the (110) orientation exhibiting a rectangular shape with a long edge parallel to (001). These 001 planes were constructed from (220) planes. Selected area ED analysis

was also carried out to understand the crystallographic orientation of the Co_3O_4 nanocystallites. Fig. 2.4f displayed the ED patterns of the cube present in the Co_3O_4 nanocomposite. The lattice constants obtained from the ED patterns are in excellent agreement with those from the XRD analysis.

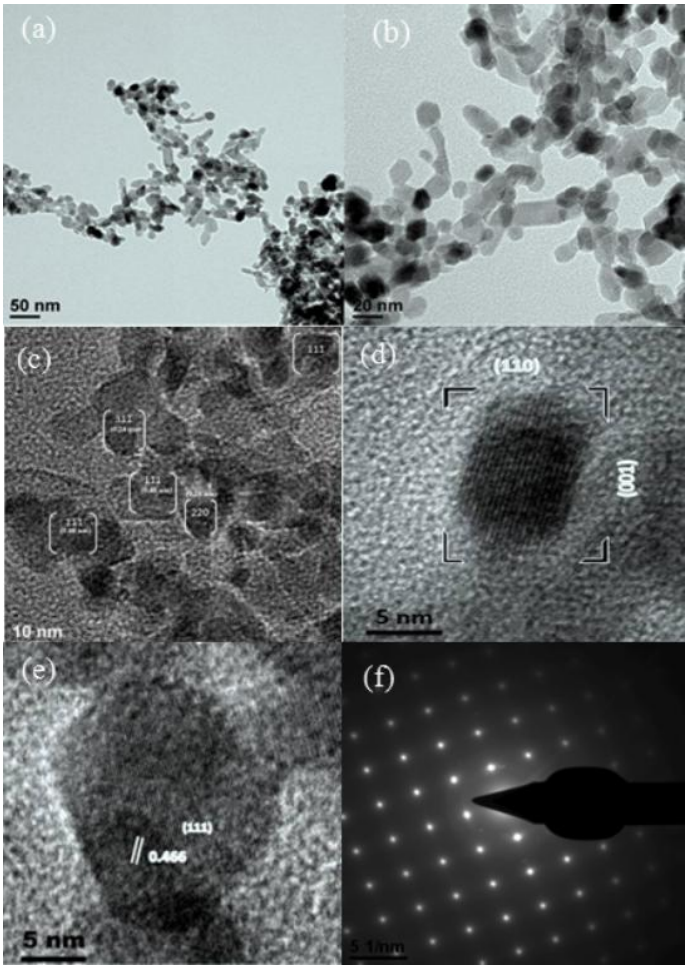

Fig. 2.4. HR-TEM images of Co_3O_4 nanoparticles and (f) SAED pattern of Co_3O_4 nanoparticles

The active sites present in Co_3O_4 could be approximately estimated by the Co^{3+}/Co^{4+} redox profiles obtained by cyclic voltammetry (CV). CV measurements were performed at a scan rate of 50 mV s^{-1} over the potential range of 0–0.6 V in 0.1M KOH solution by using a quasi-reference electrode. As can be seen in Fig. 2.5, during the positive scanning, a broad hump was observed which could be associated with the oxidation of

Co^{3+} on the surface of Co_3O_4. Corresponding to the oxidation process, a similar broad hump was observed at the cathode near 0.45 V, which was attributed to the reduction of Co^{4+} to Co^{3+} [29]. The broad peak may be due to the mixed morphology of Co_3O_4, as it was also confirmed by H_2-TPR and HR-TEM measurements.

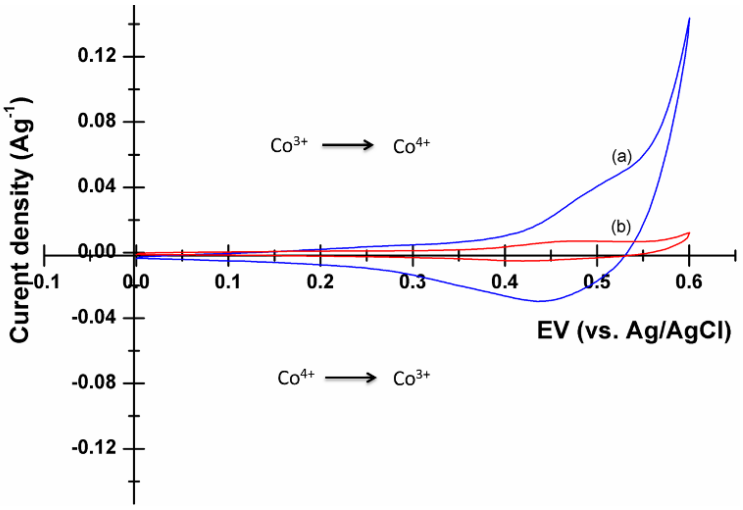

Fig. 2.5. CV curve in 0.1 M KOH solution (a) prepared Co_3O_4 oxide and (b) commercial Co_3O_4 oxide

These results are characteristic of the surface confined redox couple as shown by the reaction in Fig. 2.5. Morphology and crystallite size of the Co_3O_4 has a significant influence on the exposed number of Co^{3+} species. From the integrated area of the Co^{3+} oxidation peaks shown in Fig. 2.5, it could be evaluated that the exposed surface area of Co^{3+} in Co_3O_4 was higher in our nano Co_3O_4 sample than in the commercial Co_3O_4 sample. The area of the oxidation–reduction peak for the commercial Co_3O_4 sample was very much less, which was attributed to its higher crystallite size.

2.2.3. Catalytic performance of Co_3O_4 nanoparticles

The comparison of the activity and selectivity of different catalysts for the liquid-phase air oxidation of vanillyl alcohol is shown in Table 2.1. All the reactions were performed under optimum reaction conditions in alkaline medium except entry 4. The role of base is probably to deprotonate the phenolic –OH to form the phenoxy anion, which is the

reactive species and favors coordination to the cobalt (III) species, increasing the activity [30]. Oxidation of vanillyl alcohol in an alkaline medium without catalyst did not show any activity. However, oxidation in the presence of catalyst and a base led to the selective formation of vanillin (98%), with 80% conversion of vanillyl alcohol. This could be possible by active participation of the Co^{3+} species. As observed in the HR-TEM images of the material, the presence of (110) plane was revealed. According to Xie et al., (110) planes of Co_3O_4 are a characteristic of Co^{3+} species, which is the active component for the oxidation reaction. A comparable oxidation activity of the homogeneous precursor was also observed (entry 1, Table 2.1), but it suffers a major problem of difficult recovery and then recyclability. A control experiment with commercial Co_3O_4 gave a much lower conversion (45%) with almost the same selectivity pattern as shown in Table 2.1 (entry 3). The lower activity of the commercial Co_3O_4 was due to its higher crystallite size (86 nm), which would offer less Co^{3+} active species for the oxidation, as is also supported by its CV measurement.

Table 2.1.Catalyst screening for aerobic oxidation of vanillyl alcohol

Entry	Catalyst	Conv. (%)	Selectivity (%)	
			Vanillin	Vanillic acid
1.	[a] $Co(ac)_2$	82	96	4
2.	Co_3O_4 nanoparticles	80	98	2
3.	Commercial Co_3O_4	45	98	2
4.	[b] Co_3O_4 nanoparticles	25	88	12

[a] Homogeneous catalyst. [b] Reaction without NaOH.

In addition, the surface area of nanosize Co_3O_4 was found to be 87 m^2/g, about 17 times higher than that of the commercial Co_3O_4 sample (5 m^2/g). Secondly, the lattice fringe patterns of nano Co_3O_4 showed the presence of the (111) plane, which was absent in the commercial Co_3O_4, in which 'd' spacing of 0.28 nm was characteristic of the (220) plane (Fig 2.6). Hence both the factors viz. higher surface area as well as a dominant (111) plane exposing the active Co^{3+} sites of nano Co_3O_4, are responsible for its higher specific

activity. TOF calculated for Co_3O_4 nanoparticles was 6.4 h^{-1} while that for commercial Co_3O_4, it was 1.2 h^{-1}. Under the same reaction conditions, oxidation of vanillyl alcohol in the absence of a base leads to the lower conversion of vanillyl alcohol (25%) with 88% selectivity to vanillin and 12% vanillic acid, as shown in Table 1 (entry 4). It seems that in the oxidation of the vanillyl alcohol, the catalytic role of cobalt in the absence of base is weak but not absent because abstraction of the *β*-proton from the vanillyl alcohol depends on the formation of the superoxo-Co(III) species [31].

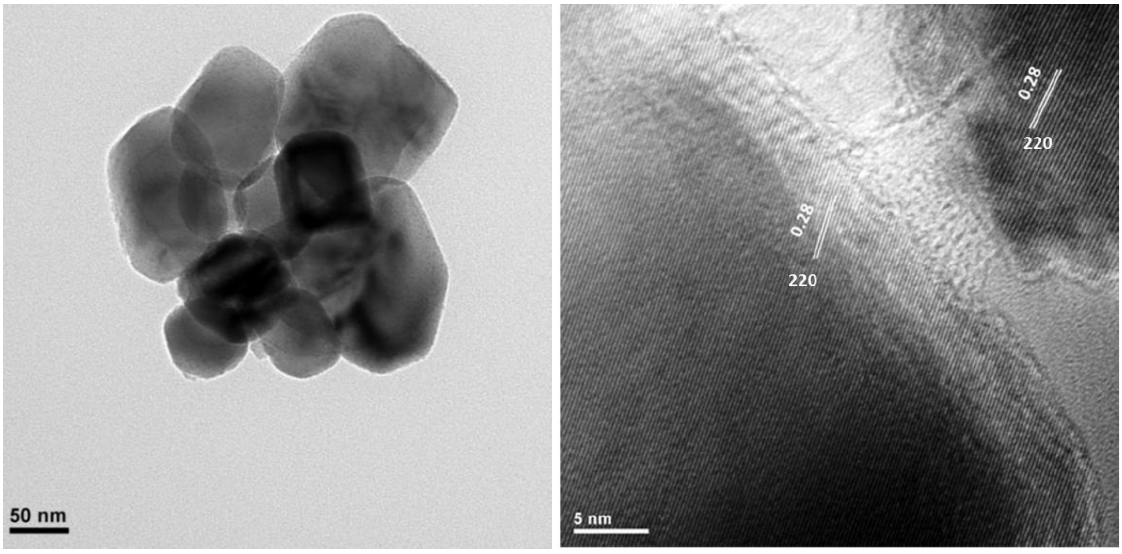

Fig. 2.6. HR-TEM images of commercial Co_3O_4

The effect of reaction time on vanillyl alcohol conversion and selectivity to vanillin was also studied for Co_3O_4 nanocatalyst and the results are shown in Fig. 2.7. The conversion of vanillyl alcohol increased from 49 to 80% with a consistent selectivity (98%) to vanillin. While an increase in reaction time from 2 to 6 h, conversion became low (86%) with a decrease in selectivity to vanillin from 98 to 94% in 8 h. The decrease in conversion and selectivity to vanillin might be due to the formation of polymeric materials over the catalyst surface as observed by the increase in the catalyst weight after the reaction.

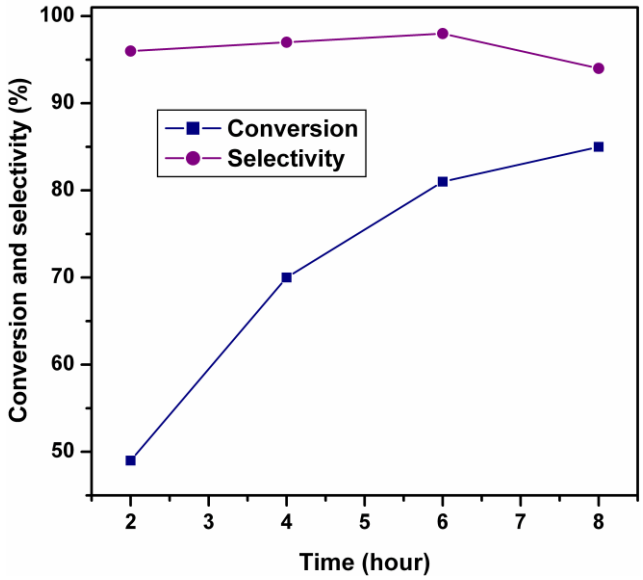

Fig. 2.7. Effect of time on conversion and selectivity. Reaction conditions: mole ratio of NaOH/vanillyl alcohol, 3.8; Co_3O_4 nanoparticles catalyst (0.1 g), 353 K, iso-propyl alcohol (70 ml), O_2-pressure (6.8 bar)

In order to study the stability of this heterogeneous catalyst, its recycle experiments were carried out in the following way: after the first oxidation run with fresh Co_3O_4 catalyst, it was filtered out and washed several times with methanol, dried under vacuum at 100 ^oC for 2 h and then reused after calcination at 450 ^oC for 1 h. The procedure was followed for three subsequent oxidation experiments, and the results are shown in Fig. 2.8. The conversion of vanillyl alcohol was found to decrease from 80 to 69% after the 3rd recycle study, however, selectivity to vanillin remained constant (98%). XRD and HR-TEM image of the used catalyst after the 3rd recycle showed that the particle size of the catalyst remained intact while, the morphology of the Co_3O_4 was changed from mixed morphology, which included cubic, tubular and truncated polyhedron, to roughly spherical (Fig 2.9 a and b). The decrease in the catalytic activity of the used catalyst might be due to the change in the morphology, which leads to the change in the crystal planes of the catalyst, which are responsible for exposing the active sites on the surface [32]. The selectivity of the product did not change during recycling of the catalyst. This

implies that the morphology affects the reaction rate significantly but has no influence on the reaction pathway.

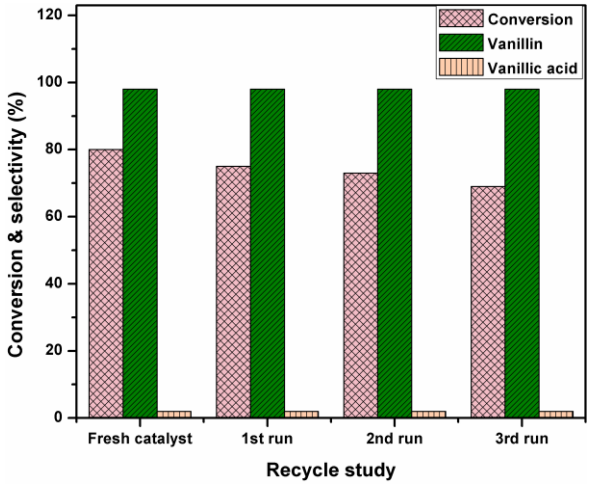

Fig. 2.8. Recycle study of vanillyl alcohol oxidation. Reaction conditions: mole ratio of NaOH/vanillyl alcohol, 3.8; Co_3O_4 nanoparticles catalyst (0.1 g), 353 K, iso-propyl alcohol (70 ml), O_2-pressure (6.8 bar).

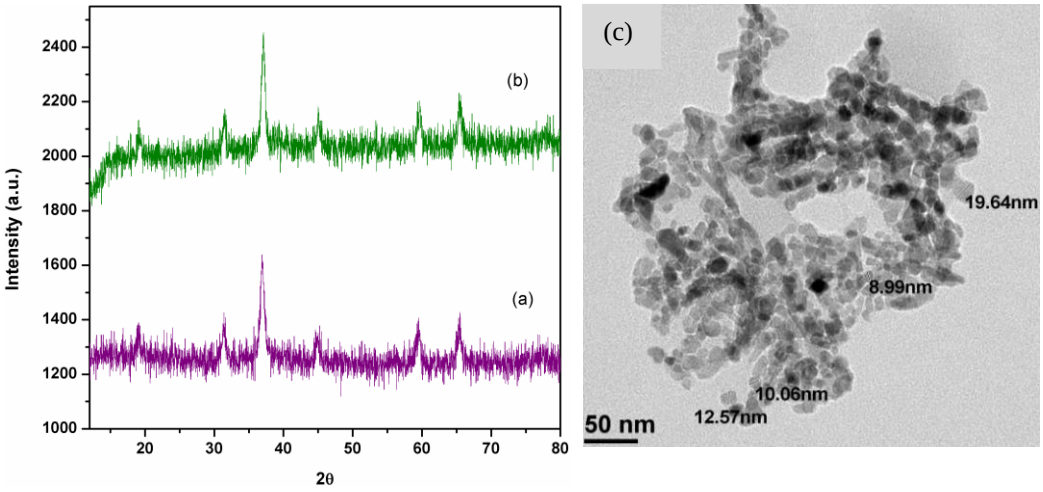

Fig. 2.9. XRD pattern of (a) fresh Co_3O_4 nanoparticles (b) after 3rd times reused Co_3O_4 nanoparticles, and (c) HR-TEM image of 3rd times reused Co_3O_4

In order to eliminate the possibility of a homogeneously catalyzed reaction due to the dissolution of cobalt oxide, a leaching test was performed as follows. The nano Co_3O_4 catalyst was separated from the reaction mixture by simple filtration after a partial

conversion of 45% in 2 h, and the filtrate was then continued for further reaction under similar conditions (6.8 bar air pressure at 80 ^{o}C), which did not give any conversion (Fig. 2.10). The absence of any cobalt species in the filtrate was also confirmed by inductively coupled plasma spectrometry. These results clearly support the fact that the oxidation of vanillyl alcohol, catalyzed by Co_3O_4, is truly heterogeneous in nature.

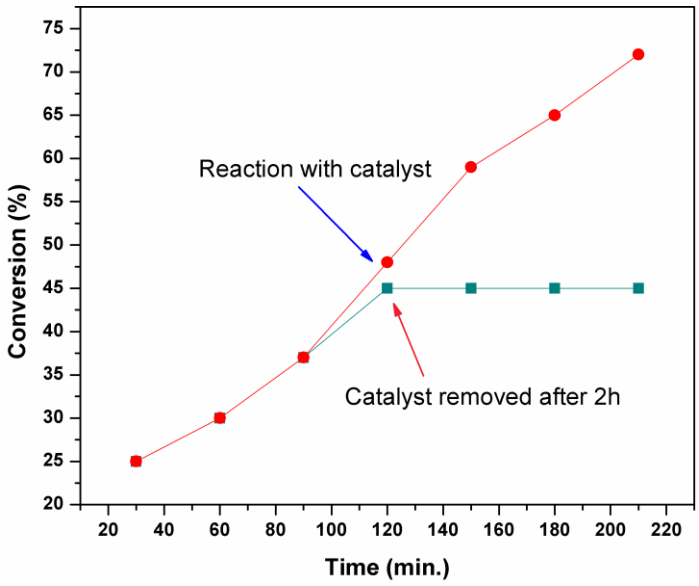

Fig. 2.10. Catalyst leaching test

2.3. MIXED Co–Mn OXIDE CATALYSED SELECTIVE OXIDATION OF VANILLYL ALCOHOL TO VANILLIN IN BASE-FREE CONDITIONS

The catalytic properties of Mn-mixed cobalt oxide catalyst are attributed to the ability of manganese to form oxides of different stoichiometries or mixed-valence compounds and their high oxygen storage capacity [33]. These metals (Co and Mn) are commonly used for oxidation reactions and also are more economical than noble-metal-based catalysts. Despite the large number of studies on single-component manganese [34, 35] and cobalt oxides [36] and very few on mixed cobalt and manganese oxides for oxidation of volatile organic compounds (e.g., benzene and toluene), there is hardly any report addressing the catalytic properties based on the structural attributes of combinations of these two oxides for the aerobic liquid phase oxidation of vanillyl alcohol, which is an industrially

important reaction. As we observed Co_3O_4 nanoparticles were active for vanilyl alcohol oxidation, but use of an excess amount of sodium hydroxide is mandatory, because firstly, it reacts with the phenolic −OH and prevents oxidation on the benzene ring; secondly, it prevents the formation of dimeric by-products and hence is beneficial for selective oxidation [37]. Nevertheless, the use of a large excess of sodium hydroxide has two major drawbacks: (i) catalyst deactivation owing to the formation of an inactive hydroxyl-bridged cobalt complex in the presence of water, and (ii) formation of huge amounts of waste inorganic salt during product neutralization. Hence, there is a genuine need to develop catalytic oxidation route without using a base. This would require a multifunctional solid catalyst designed in such a way that different active sites are present in the same catalyst for performing more than one function. As in case of bulk mixed metal oxide, the surface could be bifunctional, with one component responsible for the dissociation of molecular O_2 and the second component responsible for the chemisorption of hydrocarbons (C-H bond breaking and oxygen insertion). Hence, we developed manganese doped cobalt mixed oxide (MnCo-MO) catalyst, synthesized by a solvothermal method, which showed an excellent activity for liquid-phase air oxidation of vanillyl alcohol to vanillin without using a base.

2.3.1. Experimental

Manganese-doped cobalt oxide (MnCo-MO) catalyst was prepared by solvothermal method, the details of which were described in Section A (section 2.3.2.3) of chapter 2. As obtained catalysts were characterized by XRD, XPS, H_2-TPR, O_2-TPO and HR-TEM techniques and the detailed characterization procedure is described in chapter 2 of Section A (sections 2.4.1, 2.4.8, 2.4.10, and 2.4.6). The activity of MnCo-MO catalysts for vanillyl alcohol oxidation without using a base was carried out in a batch reactor and the experimental procedure is described in Section A (2.5.2.2) of chapter 2.

2.3.2. Results and discussion

2.3.2.1 Catalyst characterization

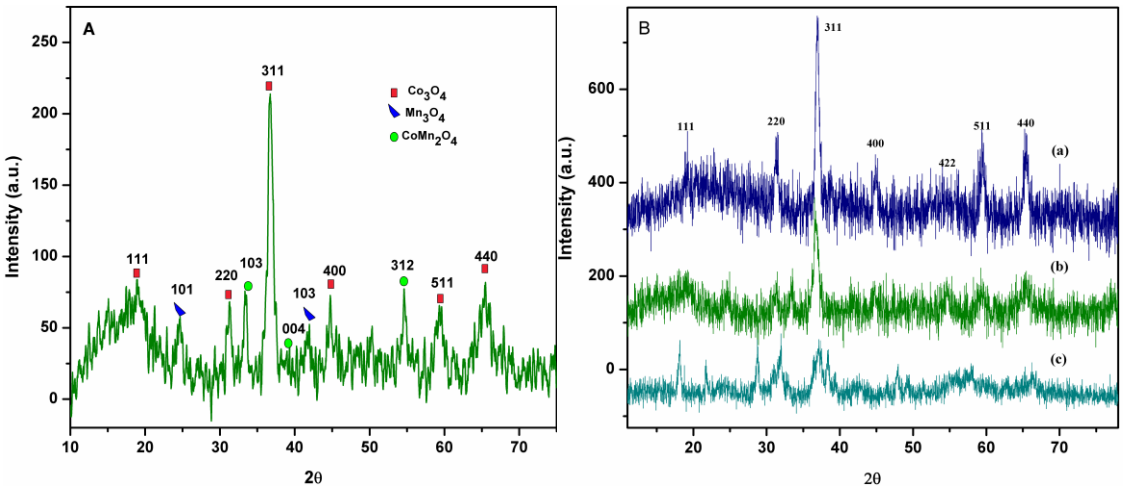

Fig. 2.11. A. XRD pattern of MnCo−MO and **B**. XRD patterns of (a) Co_3O_4, (b) mixed oxide and (c) Mn_3O_4

The XRD pattern of MnCo-MO catalyst in Fig. 2.11 A shows diffraction peaks at 2θ = 33.4^o (103), 39.1^o (004) and 54.68^o (312) corresponding to the tetragonal phase of $CoMn_2O_4$ (JCPDS: 77-0471). The peaks at 2θ = 24.7 ^{o} (101) and 41.5^o (103) were attributed to the tetragonal phase of Mn_3O_4 (JCPDS: 24-0734) and those at 2θ = 19^o, 31.4^o, 36.9^o, 44.9^o, 59.5^o and 65.4^o were ascribed to the cubic phase of Co_3O_4 (JCPDS: 74-1657). Thus, the catalyst contained three different spinel oxides, viz. $CoMn_2O_4$, Mn_3O_4 and Co_3O_4. Fig. 2.11 B shows XRD profiles of both single and mixed metal oxides. Single-component cobalt and manganese samples on calcination showed diffraction phases that were related to Co_3O_4 and Mn_3O_4, respectively. The cobalt sample exhibited peaks at 2θ = 19^o (111), 31.4^o (220), 36.9^o (311), 44.9^o (400), 59.5^o (511) and 65.4^o (440), ascribed to the cubic phase of Co_3O_4 according to JCPDS No. 74-1657. The manganese sample exhibited a broad peak at 2θ = 37^o corresponding to the (112) plane of Mn_3O_4. The other peaks of lower intensity were also identical and matched those of the tetragonal hausmannite phase (JCPDS card No. 08-0017). In the case of MnCo-MO catalyst, the diffraction peaks of Co_3O_4 became weaker and broader after doping of manganese. The intensities of broad and small peaks in the XRD patterns of mixed oxides indicated that manganese caused some deformation in the crystal structure of Co_3O_4 that resulted in a decrease of particle size [38] (the crystallite size of Co_3O_4 was 14

nm, whereas it was 10 nm for MnCo-MO catalyst, calculated by using the Scherrer equation). Doping of manganese into the Co_3O_4 resulted in a slight shift in position from $2\theta = 36.9^o$ towards a lower diffraction angle of $2\theta = 36.7^o$ (311), which might result from the insertion of manganese oxide in the octahedral framework of Co_3O_4 [39].

X-ray photoelectron spectroscopy (XPS) was used to monitor the oxidation states and the relative percentages of different constituent elements in the MnCo-MO catalyst and the results are shown in Table 2.2. A broad signal of Co $2p_{3/2}$ could be fitted satisfactorily to three principal peaks and one satellite peak after deconvolution, as shown in Fig. 2.12a. The peak at 779.2 eV was assigned to the Co^{3+} of Co_2O_3 whereas the peak at 780 eV was assigned to the Co^{2+} of $CoMn_2O_4$ [40]. Formation of $CoMn_2O_4$ was also confirmed by XRD and high-resolution transmission electron microscopy (HRTEM) results. $CoMn_2O_4$ is an incomplete normal spinel with a tetragonal structure in which Co^{2+} mainly occupies the tetrahedral sites and Mn^{3+} mainly occupies the octahedral sites. Another peak at 780.9 eV was also present owing to Co^{2+}, but from spinel Co_3O_4. A satellite peak at 782.8 eV was indicative of Co^{2+} in both the spinel Co_3O_4 and $CoMn_2O_4$. In the case of undoped Co_3O_4, the Co $2p_{3/2}$ peak could be deconvoluted into two major peaks, one at 780.2 eV (Co^{3+}) and the other at 782 eV (Co^{2+}); the very low intensity peak at 784 eV resulted from the 3d→4s shake-up satellite (Fig. 2.12b), which was a characteristic of Co_3O_4 [41]. We observed that doping of manganese into Co_3O_4 led to a decrease in the binding energy of cobalt species, which might be a result of formation of a Co–Mn compound ($CoMn_2O_4$), and it also reversed the Co^{2+}/Co^{3+} ratio in a mixed oxide relative to that in undoped cobalt oxide (Table 2.2).

Table 2.2. Surface composition calculated from XPS

Catalysts	Atomic ratio (Co/Mn)	$CoMn_2O_4$	Co_3O_4		At.(%) [a]	
		Co^{2+} [%]	Co^{2+} [%]	Co^{3+} [%]	Mn	Co
MnCo-MO	2.6	40	27	33	27	73
Co_3O_4	–	–	33	67	–	–

[a] At.% = Atomic percent of Mn and Co in mixed oxide (MnCo-MO).

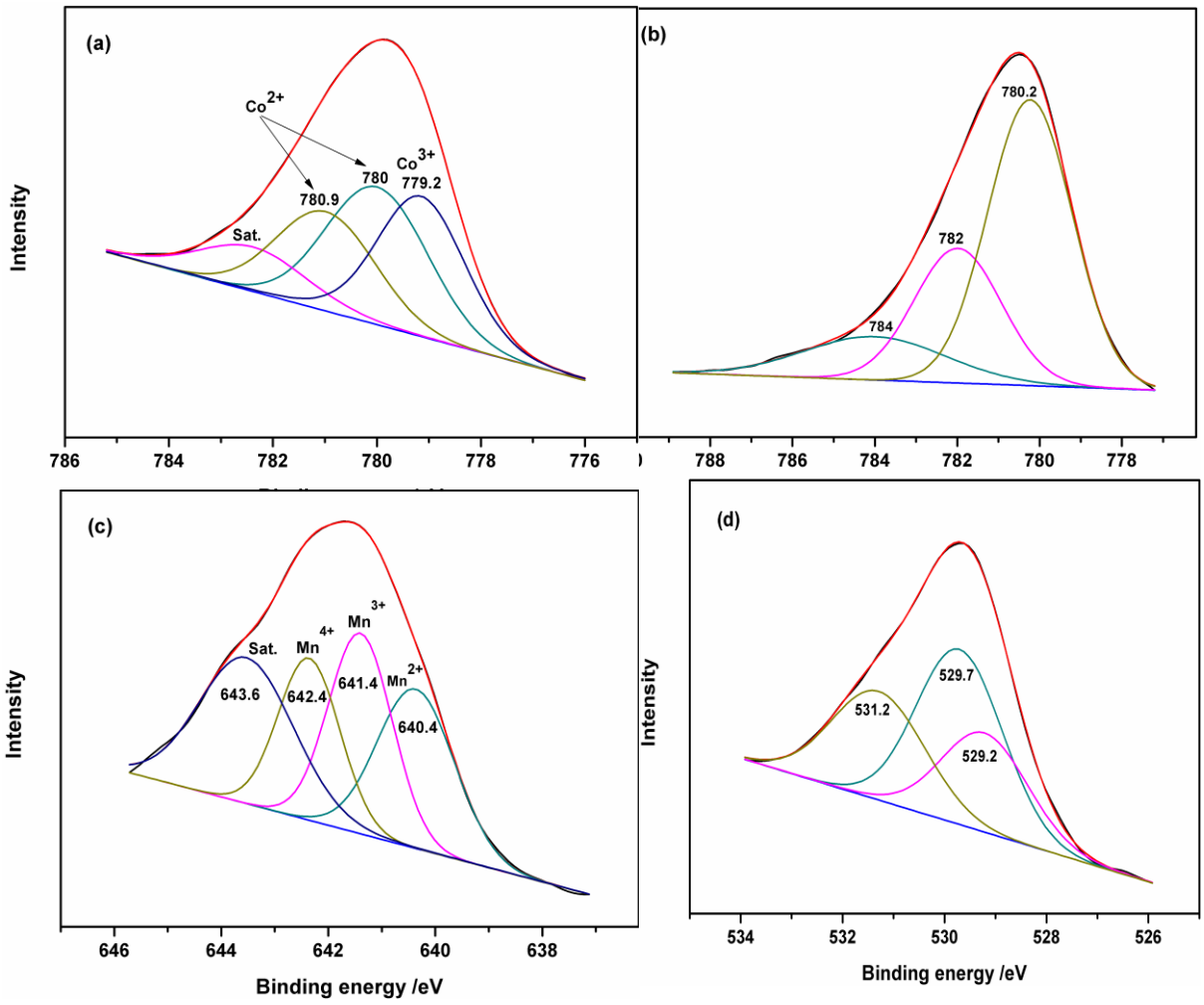

Fig. 2.12. XPS of (a) Co $2p_{3/2}$ of MnCo–MO, (b) Co $2p_{3/2}$ of Co_3O_4 (c) Mn $2p_{3/2}$, and (d) O1s of MnCo–MO catalyst

The MnCo-MO catalyst also showed a broad signal of Mn $2p_{3/2}$, which could be fitted satisfactorily to three major peaks and one satellite peak after deconvolution, as shown in Fig. 2.12c. The peaks at 640.4, 641.4 and 642.4 eV correspond to Mn^{2+}, Mn^{3+} and Mn^{4+}, respectively,[42, 43] whereas the small peak at 643.6 eV corresponds to the satellite of Mn^{4+}. It is reasonable, therefore, to conclude that Mn element exists as Mn^{2+} and Mn^{3+} in both Mn_3O_4 and $CoMn_2O_4$ spinel oxides. The presence of these spinel oxides in MnCo-MO catalyst was also confirmed by XRD peaks at $2\theta = 24.7^o$ (101) and 33.4^o (103),

respectively. However, the presence of Mn^{4+} indicates the possibility of MnO_2, which we did not observe in XRD pattern because of peak broadening.

The manner in which oxygen is bonded to metals in metal oxides can be determined through XPS of oxygen. In this series, the O1s spectrum was used to identify the types of metal oxides present in MnCo-MO catalyst. In the O1s spectrum of MnCo-MO, three peaks were fitted satisfactorily after deconvolution, as shown in Fig. 2.12d. The peaks at lower binding energies of 529.2 and 529.7 eV could be assigned to the lattice oxygen and must therefore correspond to Co-O and Mn-O bonds, respectively [44]. However, the peak at the higher binding energy of 531.2 eV was assigned to the surface adsorbed oxygen (O^{2-} or O^{-}) or hydroxyl group or oxygen vacancies.[45]

Fig. 2.13 shows HRTEM images of MnCo-MO catalyst, synthesised by the solvothermal method and subsequent calcination at 450 ^{o}C. As can be seen in Fig. 2.13b, the calcined sample displayed a roughly nanorod-like structure, whereas the as-synthesised sample showed a fully rod-like morphology with 79 nm length and 11 nm diameter (Fig. 2.13a).

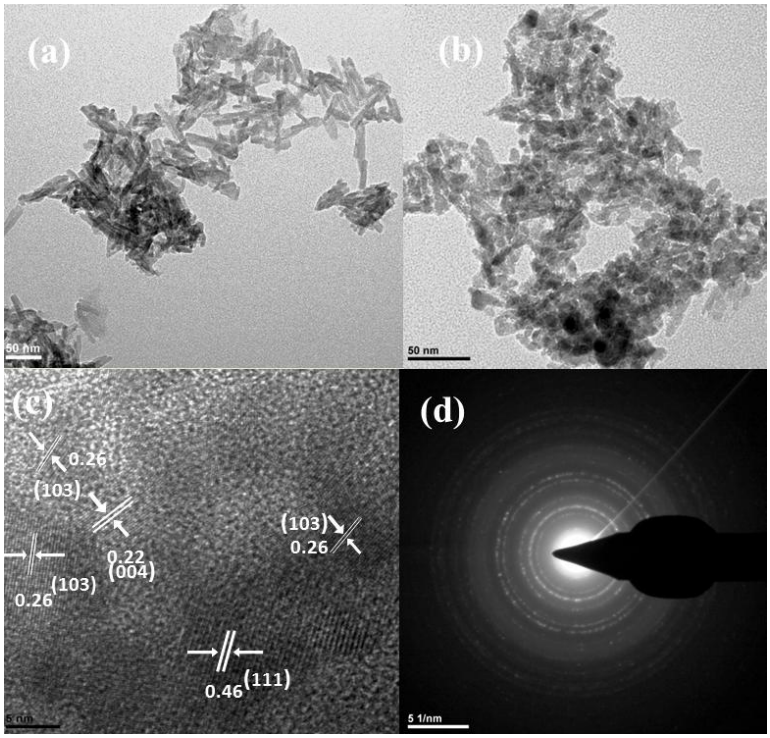

Fig. 2.13. HR-TEM images of MnCo–MO catalysts: (a) as synthesized catalyst (b) calcined sample (c) lattice fringe patterns and (d) SAED pattern

The average dimensions of calcined MnCo-MO nanorods were approximately 20–30 nm in length with a diameter of 4–7 nm. The lattice fringe patterns of the MnCo-MO catalyst are shown in Fig. 2.13c. The dominant exposed plane of MnCo-MO nanorods was (103) with a lattice spacing of 0.26 nm, which was related to the spinel $CoMn_2O_4$. The other exposed planes were (111) and (004) with a lattice spacing of 0.46 and 0.22 nm, related to the spinel Co_3O_4 and $CoMn_2O_4$, respectively. Fig. 2.13d, shows the selected-area electron diffraction (SAED) pattern of the MnCo-MO catalyst, which was used to determine the lattice constants; the results were in excellent agreement with those obtained from XRD analysis.

To evaluate the reducibility and re-oxidisability as a function of the composition, both temperature-programmed reduction (TPR) and temperature-programmed oxidation (TPO) studies were performed for single and mixed metal oxides from 100 to 800 ^{o}C and the results are displayed in Fig.s 2.14 and 2.15, respectively.

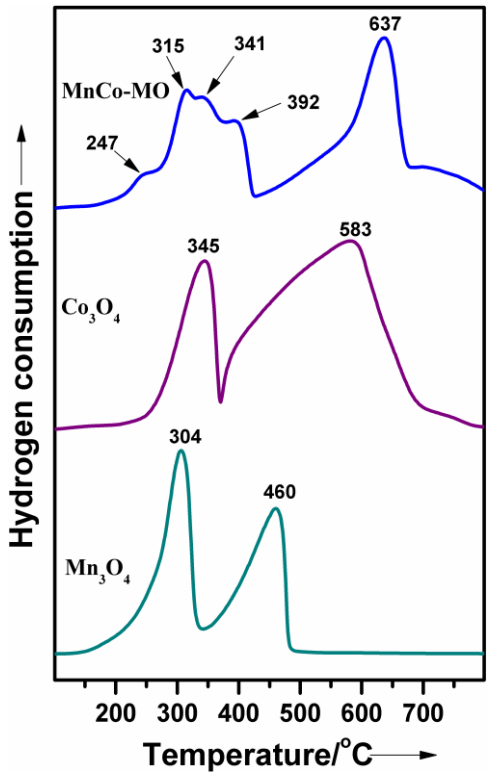

Fig. 2.14. H_2-TPR of Mn_3O_4, Co_3O_4 and MnCo–MO catalysts

TPR of the manganese oxide sample exhibited two peaks at 304 and 460 ^{o}C ascribed to the two-step reduction of MnO_2 [46]. The H_2-TPR profile of Co_3O_4 was also characterized by two reduction peaks located at 345 and 583 ^{o}C (Fig. 2.14), which resulted from a progressive reduction of Co_3O_4 as follows (3.3) [47].

$$Co_3O_4 \rightarrow CoO \rightarrow Co^{o} \qquad (3.3)$$

The first reduction peak was very sharp and symmetrical with the temperature maximum centred at about 345 ^{o}C. This peak was associated with the reduction of trivalent cobalt oxide (Co_3O_4) to a divalent cobalt oxide (CoO) (3.3). The second reduction peak was broad and unsymmetrical with a temperature maximum at about 583 ^{o}C, attributable to the subsequent reduction of divalent cobalt oxide (CoO) to metallic cobalt (Co^{o}) [48]. Four overlapping peaks at 247, 315, 341 and 392 ^{o}C were observed in the case of the manganese-doped cobalt oxide sample in a temperature range from 200 to 400 ^{o}C. It was noticed that the peak at 247 ^{o}C was observed only in the MnCo-MO sample, not for Co_3O_4 and Mn_3O_4 samples. It is reasonable to deduce that the peak at 247 ^{o}C resulted from the reduction of surface oxygen species generated by the presence of oxygen vacancies in MnCo-MO oxides. A similar observation as also reported by Shi et al. for $Mn_xCo_{3-x}O_4$ oxide used for formaldehyde oxidation [49]. The hydrogen consumption in a lower temperature range of 200–400 ^{o}C could be a result of the stepwise reduction of Co^{3+} to Co^{2+} and also of Mn^{4+} to Mn^{3+}. However, the peak in a higher temperature range of 400–700 ^{o}C could result from the reduction of Co^{2+} to Co^{o} and Mn^{3+} to Mn^{2+} in a MnCo-MO sample [50]. The presence of the reduction peak at a higher temperature of approximately 637 ^{o}C in the TPR profiles of MnCo-MO catalysts (Fig. 2.14) is additional evidence of the formation of mixed Co–Mn oxides.

After reduction of single (Co_3O_4 and Mn_3O_4) and mixed metal oxides (MnCo-MO) to the corresponding metallic forms during TPR experiments, TPO experiments were also performed and the results are displayed in Fig. 2.15. The addition of manganese to cobalt oxide led to remarkable changes in the TPO profiles of single metal oxides with respect to the amount of oxygen consumed, number of oxidation peaks and the oxidation temperature.

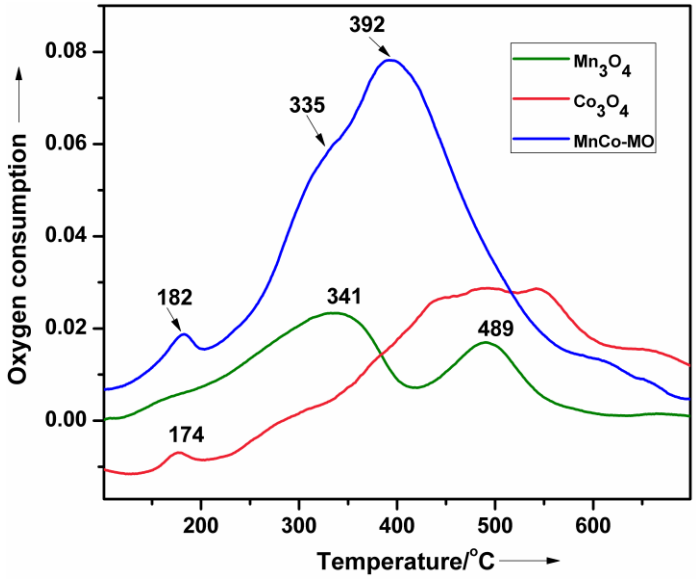

Fig. 2.15. O_2-TPO profile of Mn_3O_4, Co_3O_4 and MnCo–MO catalysts

If the reduced MnCo-MO catalyst was exposed to oxygen, manganese was oxidised to a great extent and the resulting manganese oxide covered the cobalt oxide peaks. So we could not distinguish the separate oxidation peaks for Mn and Co oxides. As can be seen from Fig. 2.15, the area of the oxygen consumption peak for MnCo-MO catalyst was much higher than that of the oxygen consumption peak for single metal oxides. This observation indicates that the addition of manganese to cobalt oxide enhanced the consumption of oxygen in mixed metal oxides, which is the favourable condition for the oxidation reaction.

2.3.3. Catalytic activity of MnCo-MO

The activity of single metal oxides (Co_3O_4 and Mn_3O_4) was compared with that of mixed metal oxide (MnCo-MO) catalysts for the oxidation of vanillyl alcohol and the results are shown in Fig. 2.16. Among these catalysts, Co_3O_4 showed significantly lower substrate conversion (48%) with higher selectivity to vanillin (88 %). The efficiency of Mn_3O_4 in terms of vanillin yield was marginally higher (54%) than that obtained for MnCo-MO catalyst (51 %), but the catalyst recycle experiment with Mn_3O_4 showed a substantially diminished conversion of 29% and also lower selectivity to vanillin (74%) owing to the higher oxygen storage capacity and faster oxygen absorption rates of manganese oxide

(MnOx), which led to the over-oxidation to vanillic acid. However, the MnCo-MO catalyst showed superior recyclability (discussed later) and selectivity to vanillin of 83% relative to catalysts containing only the single oxide of either cobalt or manganese.

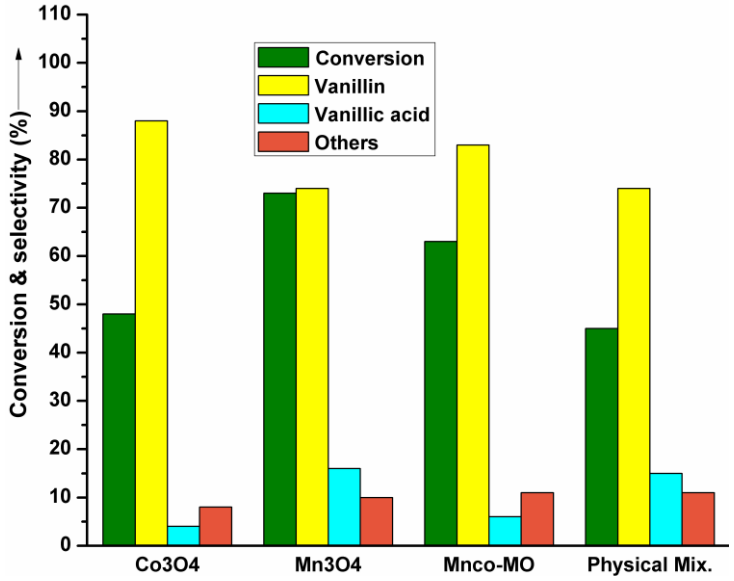

Fig. 2.16. Catalysts screening for oxidation of vanillyl alcohol. Reaction conditions: vanillyl alcohol, 3.24 mmol; catalysts (0.1 g), temperature, 140 ^{o}C; acetonitrile (70 ml), air pressure (21 bar); time, 2 h.

The higher activity of the MnCo-MO catalyst might result from spinel $CoMn_2O_4$ along with Mn species of varying oxidation states. A separate oxidation experiment performed by using a physical mixture of Mn_3O_4 and Co_3O_4 showed only 45% conversion of vanillyl alcohol with 74% selectivity to vanillin, which was close to that obtained for spinel Co_3O_4. The importance of Co/Mn composition in the mixed metal oxide was also studied by preparing and testing two mixed oxide samples with varying molar ratios of Mn and Co (MnCo 1:1 and 2:1). Both of these catalysts showed either inferior activity and/or selectivity relative to MnCo-MO catalyst with 1:2 molar ratio of Mn and Co. MnCo 1:1 catalyst showed 52% conversion and 83% selectivity to vanillin, whereas MnCo 2:1 showed 64% conversion of vanillyl alcohol with 74% selectivity to vanillin (Table 2.3).

Table 2.3. Catalyst screening for vanillyl alcohol oxidation

Catalyst	Conversion (%)	Selectivity (%)		
		Vanillin	Vanillic acid	Others
Coprecipitation CoMn–MO	22	85	3	12
CoMn (1:1)	52	83	5	12
MnCo (2:1)	64	73	12	15

The lower selectivity to vanillin in the case of MnCo 2:1 catalyst was owing to the over-oxidation of vanillin to vanillic acid. MnCo-MO having a Mn/Co ratio of 1:2, prepared by a co-precipitation method, [51] on testing for vanillyl alcohol oxidation showed inferior activity (22% conversion) to MnCo-MO prepared by a solvothermal method (Table 2.3). In spite of the fact that MnCo-MO prepared by co-precipitation had a pure $CoMn_2O_4$ phase, it had a very low activity because of its lower surface area (17 m^2g^{-1}) and higher crystallite size (62 nm) than MnCo-MO prepared by the solvothermal method, which had a higher surface area of 105 m^2g^{-1} and smaller crystallite size of 10 nm (Fig. 2.17).

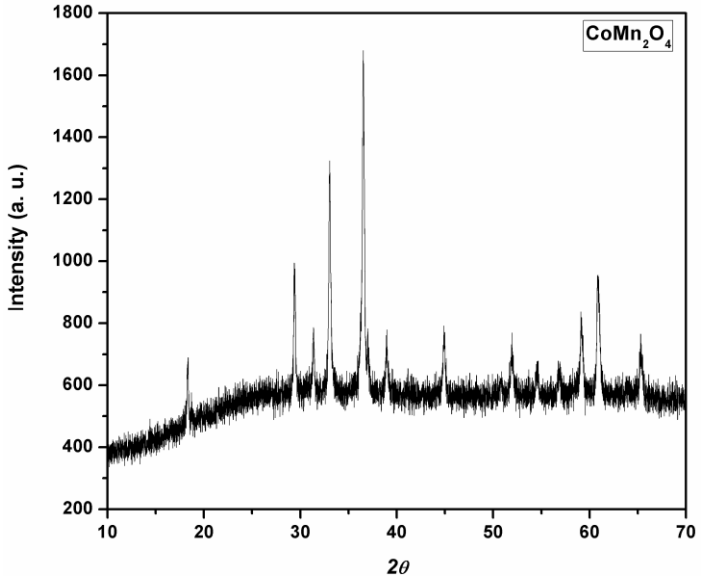

Fig. 2.17. XRD of $CoMn_2O_4$ prepared by co-precipitation method

Further, the nature of the solvent was also found to have a profound influence on vanillyl alcohol oxidation. The sequential oxidation of aldehyde to acid and other by-products may be inhibited through careful selection of the solvent. In a nonpolar solvent such as toluene, poor conversion of vanillyl alcohol was obtained (35%) owing to the lower solubility of vanillyl alcohol in toluene. Among the polar solvents, organic polar solvents showed a better performance than inorganic solvent (H_2O), which might be because of the higher solubility of oxygen in organic solvents.

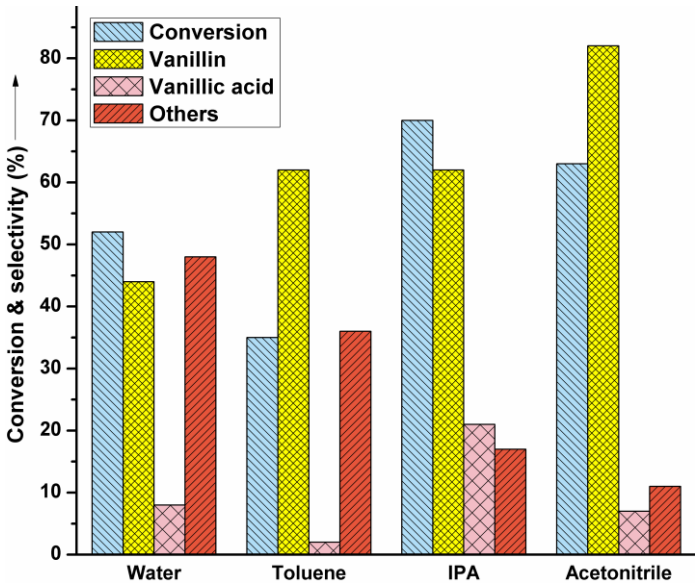

Fig. 2.18. Effect of solvent on oxidation of vanillyl alcohol. Reaction conditions: vanillyl alcohol, 3.24 mmol; MnCo–MO catalyst (0.1 g), temperature, 140 ^{o}C; solvent, (70 ml), air pressure (21 bar); time, 2 h.

As can be seen from Fig. 2.18, the conversion and selectivity were remarkably different in polar inorganic and organic solvents. In water, conversion of vanillyl alcohol was 52% and selectivity to vanillin was only 44% with majority formation of tar. Vanillyl alcohol is sparingly soluble in water; hence significant inhibition of the adsorption of the substrate onto the catalyst surface restricts the rate of reaction. However, in polar organic solvent, the solubility of the substrate was higher allowing easy adsorption of reactant molecules on the catalyst surface and the reaction was readily facilitated. Oxidation of

vanillyl alcohol in acetonitrile gave the highest conversion of 62% and selectivity of 83% to vanillin compared with oxidation in isopropyl alcohol (60% conversion of vanillyl alcohol with 62% selectivity to vanillin). The higher dielectric constant of acetonitrile (37.5) than that of isopropyl alcohol (17.9) facilitates better solubility of substrate and oxidant in the solvent, hence affecting the activity and selectivity pattern.

The effect of reaction time on vanillyl alcohol conversion and selectivity to vanillin was studied with MnCo-MO catalyst under optimized reaction conditions and the results are shown in Fig. 2.19.

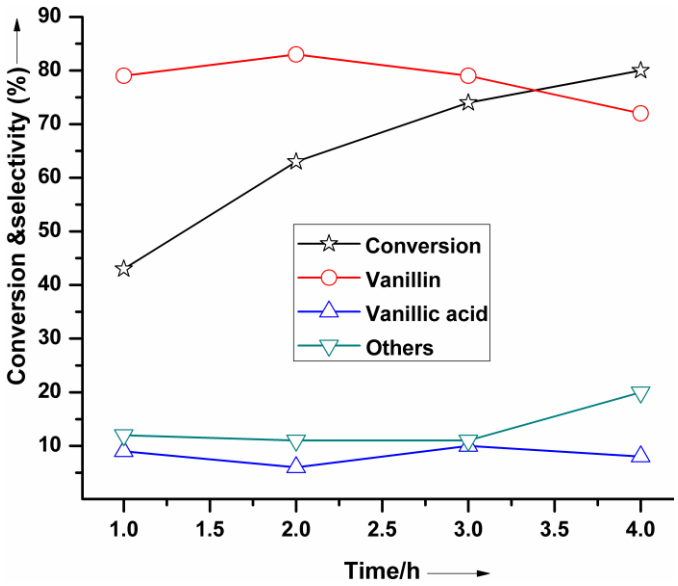

Fig. 2.19. Effect of time on oxidation of vanillyl alcohol. Reaction conditions: vanillyl alcohol, 3.24 mmol; MnCo–MO catalyst (0.1 g), temperature, 140 ^{o}C; acetonitrile, (70 ml), air pressure (21 bar).

The conversion of vanillyl alcohol increased from 43 to 63% and the selectivity to vanillin increased from 79 to 83% with an increase in reaction time from 1 to 2 h. A further increase in reaction time from 2 to 4 h enhanced the conversion of vanillyl alcohol from 63 to 80%; however, it led mainly to the formation of tar. As this could not be detected by HPLC, the material balance of the overall reaction was <90 %. The visible tarry product was separated out from the reaction crude, dried, weighed and accounted

for determining the vanillin selectivity as well. The selectivity of vanillin was found to decrease from 83 to 72% with increase in reaction time from 2 to 4 h.

The effect of temperature on vanillyl alcohol oxidation was examined over the MnCo-MO catalyst in a temperature range of 100–160 ^{o}C and the results are shown in Fig. 2.20. The conversion of vanillyl alcohol increased from 41 to 76% with an increase in reaction temperature from 100 to 160 ^{o}C. The selectivity to vanillin increased from 57 to 83% initially with an increase in reaction temperature from 100 to 140 ^{o}C, but a further increase in temperature to 160 ^{o}C caused a decrease in vanillin selectivity from 83 to 74% owing to the formation of over-oxidation products.

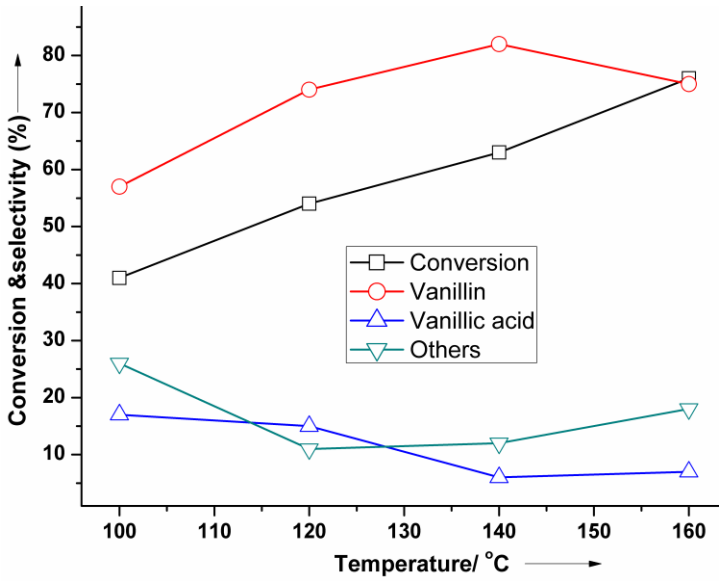

Fig. 2.20. Effect of temperature on oxidation of vanillyl alcohol. Reaction conditions: vanillyl alcohol, 3.24 mmol; MnCo–MO catalyst (0.1 g), temperature, 100-160 ^{o}C; acetonitrile, (70 ml), air pressure (21 bar); time, 2 h.

Catalyst concentration has a significant effect on the liquid phase oxidation of vanillyl alcohol. Experiments were conducted by varying the catalyst concentration in the range of 0.0007–0.0017 gcm^{-3} and the results are displayed in Fig. 2.21. The conversion of vanillyl alcohol increased with increase in catalyst loading from 0.0007 to 0.0014 gcm^{-3}, whereas the selectivity to vanillin remained almost constant at about 83%. The increase

in conversion with increase in catalyst loading was a result of the increase in the number of active sites available for participating in the reaction. Further increase in catalyst loading from 0.0014 to 0.0017 gcm^{-3} had a marginal effect on vanillyl alcohol conversion, thus implying that mass-transfer resistance could be significant under these conditions.

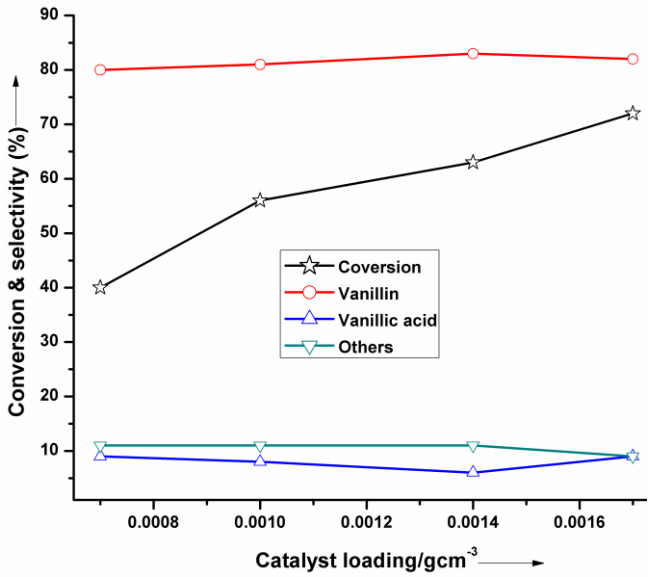

Fig. 2.21. Effect of catalyst concentration on oxidation of vanillyl alcohol. Reaction conditions: vanillyl alcohol, 3.24 mmol; MnCo–MO catalyst, 0.0007-0.0017 g/cm^3; temperature, 140 ^oC; acetonitrile, (70 ml), air pressure (21 bar); time, 2 h.

The effect of partial pressure of oxygen on conversion and selectivity was studied for vanillyl alcohol oxidation by varying the air pressure in the range of 7 to 28 bar at 140 ^oC and the results are shown in Fig. 2.22. Both the conversion of vanillyl alcohol and selectivity to vanillin increased gradually with an increase in air pressure from 7 to 21 bar, beyond which the conversion increased but the selectivity to vanillin started decreasing from 83 to 78%, thereby implying that a higher dissolved concentration of oxygen increased the formation of other by-products.

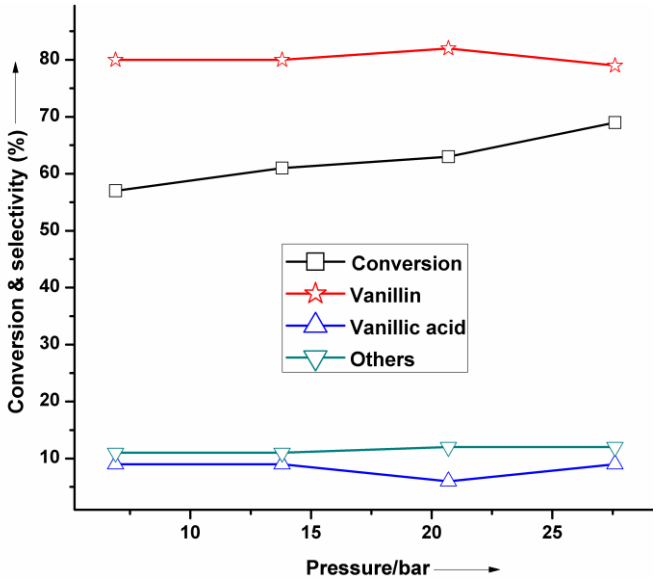

Fig. 2.22. Effect of pressure. Reaction conditions: vanillyl alcohol, 3.24 mmol; MnCo–MO catalyst, 0.1 g; temperature, 140 ^{o}C; acetonitrile, (70 ml), air pressure (7- 28 bar); time, 2 h.

The stability of the MnCo-MO catalyst for vanillyl alcohol oxidation was investigated by recycling studies in the following way: After the first oxidation run with fresh MnCo-MO catalyst, the reaction crude was allowed to settle and the clear supernatant product mixture was removed from the reactor. The catalyst remaining in the reactor was washed with methanol twice and then dried at 100 ^{o}C. The subsequent run was continued by adding a fresh charge to this catalyst. Fig. 2.23 shows that the activity decreased if only the dried reused catalyst was used (recycles 1 and 2), but the original activity could be regained (63%) if the reused catalyst (recycle 3) was calcined again at 450 ^{o}C for 1 hour. A small loss in the activity was observed, which resulted from handling of the catalyst.

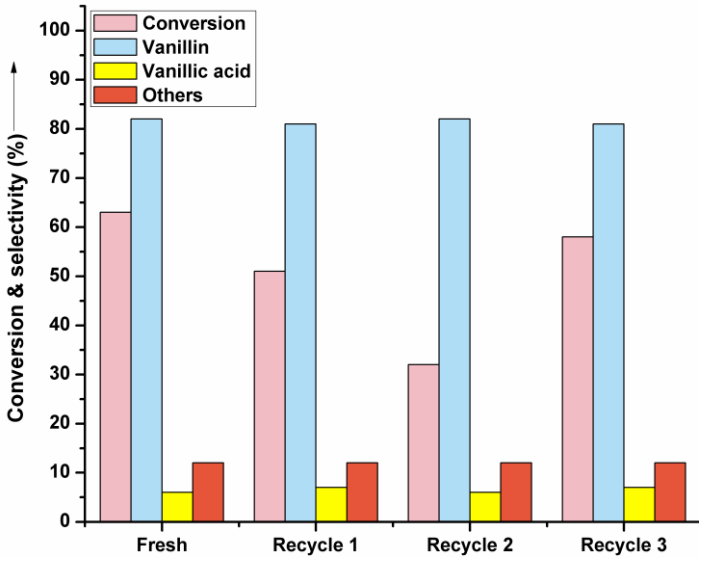

Fig. 2.23. MnCo–MO catalyst recycles studies. Reaction conditions: vanillyl alcohol, 3.24 mmol; MnCo–MO catalysts, 0.1 g; temperature, 140 ^{o}C; acetonitrile, (70 ml), air pressure (21 bar); time, 2 h.

To eliminate the possibility of a homogeneously catalysed reaction owing to dissolution of metal oxide, a leaching test was also performed and the results are shown in Fig. 2.24.

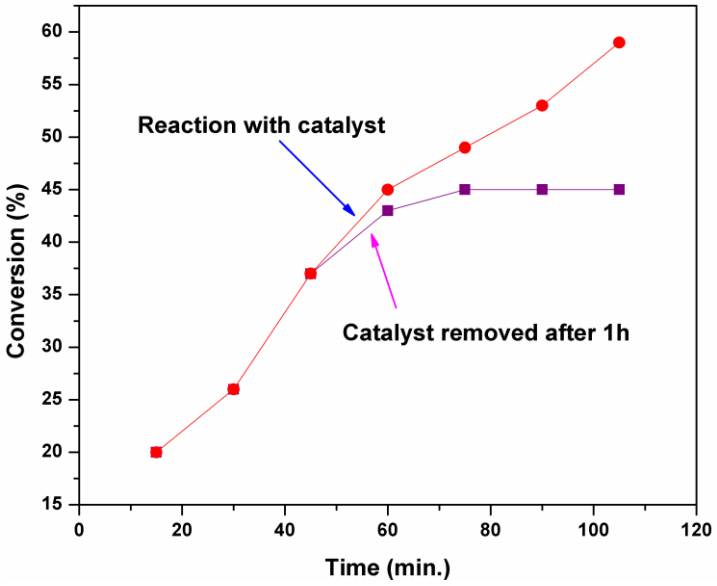

Fig. 2.24. Catalyst leaching test

The MnCo-MO catalyst was separated from the reaction mixture by simple filtration after a partial conversion of 43% in 1 h, and the filtrate was then employed in further reaction under similar conditions (21 bar air pressure at 140 ^{o}C), which did not give any further conversion. The absence of any metal species in the filtrate was confirmed by inductively coupled plasma spectrometry. These results clearly support the fact that the oxidation of vanillyl alcohol catalysed by MnCo-MO is truly heterogeneous in nature.

A plausible mechanistic pathway for oxidation of vanillyl alcohol catalysed by mixed oxide (MnCo-MO) to give vanillin is shown in Scheme 2.3. In the ground state, oxygen remains in the triplet form containing two unpaired electrons with parallel spins. Direct reaction of triplet oxygen with singlet organic molecules to give a singlet product is a spin-forbidden process and has a very slow reaction rate. This can be overcome by complexation of triplet oxygen with a paramagnetic transition metal ion [52].

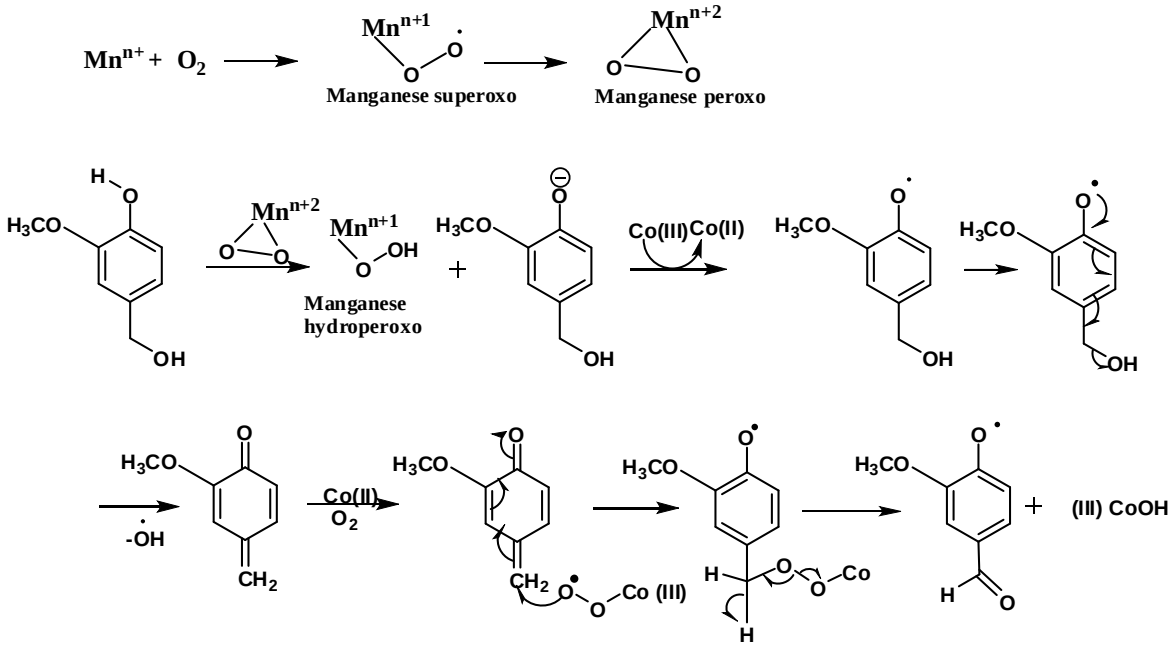

Scheme 2.3. Plausible mechanistic pathway for the formation of vanillin

As manganese with d^4 configuration has a more paramagnetic nature (2.8 BM) than cobalt with d^7 configuration (1.7 BM) in a tetragonal complex because of the Jahn–Teller effect, [53] it has a strong tendency to react with an oxygen molecule to give a

metal superoxo complex. This further converts into the metal peroxo complex, which readily forms a metal hydroperoxo complex by abstracting a proton from vanillyl alcohol to give the corresponding phenolate ions. The role of Mn is thus significant in eliminating the use of a free base (NaOH). The phenolate ions get oxidised to the phenoxy radical by means of reaction with Co^{3+} species present in the reaction medium [30]. The phenoxy radical then undergoes further reaction to form the quinomethide, which reacts with the cobalt superoxo complex to give a peroxycobalt (III) complex followed by its subsequent decomposition to the corresponding aldehyde with concomitant release of a hydroxycobalt (III) complex. The formed aldehyde with a free radical abstracts the proton from the reaction medium and is converted to vanillin. To examine the involvement of free radicals in the reaction, we performed the oxidation reaction in the presence of a small amount of radical scavenger, benzoquinone, under the same reaction conditions. The conversion of vanillyl alcohol dropped significantly from 62 to 25% without affecting the selectivity, thus supporting the role of free radicals in the reaction.

2.4. REDUCED GRAPHENE OXIDE COMPOSITE WITH REDOXIBLE MnCo-OXIDE FOR *p*-CRESOL OXIDATION

In this work, we present the research efforts to develop sustainable and clean pathway for the liquid phase oxidation of *p*-cresol [54]. The products formed, depending on the catalyst and the reaction conditions are *p*-hydroxybenzyl alcohol (PHBAlc), *p*-hydroxybenzaldehyde (PHBAld) and *p*-hydroxybenzoic acid (PHBAcid). All these compounds have versatile applications in industrial and pharmaceutical sectors [55]. Industrially, *p*-hydroxybenzaldehyde is synthesized by side-chain chlorination of *p*-cresol and by subsequent saponification of the resulting dichloromethyl group [56]. Sharma *et al.* reported the oxidation of *p*-cresol in methanol by using cobaltous chloride in the presence of NaOH giving 90% conversion with 59% selectivity to *p*-hydroxybenzaldehyde [57]. The drawbacks of these methods are the employment and the generation of chemicals detrimental to health and environment and took longer reaction time. The use of graphene based composite materials have attracted substantial attention due to their unique structure and extraordinary properties for various applications such as

electrocatalysts, electrodes, sensors and more specifically dispersion of metal oxide nanoparticles (NP) on graphene sheets potentially provides a novel way to develop catalysts for oxidation reactions [58]. A facile synthesis of graphene/metal oxide NP composites with good control of size and morphology is critical to the catalytic applications of practical relevance. The use of graphene oxide (GO) based composite material as a catalyst, for liquid phase oxidation of *p*-cresol, has never been reported before. The surface of GO hosts oxygen containing functional groups like hydroxyl (–OH) and epoxide groups located on the basal planes and carbonyl (>C=O) and carboxyl groups (–COOH) located at the edges of the GO [59]. These functional groups facilitate anchoring of metal nanoparticles, useful for performing redox reactions. GO is an excellent precursor for graphene synthesis, via either chemical or thermal reduction processes. A number of chemical reductants have been studied for reducing GO to form graphene/metal nanoparticle composites, e.g. hydrazine and its derivatives [60]. However, these reductants are highly toxic and explosive, which limit their usage on a larger scale operation. Therefore, we used ethylene glycol as a reducing agent, which is safe and environmentally suitable [61]. Although cobalt is an excellent catalyst for the relatively inert hydrocarbon C–H bond activation in oxidation reactions, incorporation of manganese along with it, is known to improve the overall oxidation activity and more particularly, influence the product distribution due to the formation of efficient redox couple between Co and Mn [62]. We have developed Co_3O_4, which was found to be an efficient catalyst for liquid phase aerobic oxidation of vanillyl alcohol to vanillin in the presence of NaOH. Further, we also developed mixed metal oxides catalyst by doping manganese with the cobalt oxide (MnCo−MO) that led to the formation of tetragonal $CoMn_2O_4$ phase, which was found to be active species for the oxidation reactions and catalyzed base-free oxidation of vanillyl alcohol to vanillin. In continuation of our efforts towards the substitution of reagent based oxidation processes by nonpolluting solid catalyst for industrially relevant oxidation reaction, we have synthesized the composite material of reduced graphene oxide with cobalt-manganese mixed oxide (r-GO-MnCoO) for liquid phase oxidation of *p*-cresol to *p*-hydroxybenzaldehyde (96%) with 71% product

yield. The activity of the catalyst was correlated with its physico-chemical characterization data obtained from various techniques.

2.4.1. Experimental

Reduced graphene oxide composite with manganese-doped cobalt oxide (r-GO-MnCoO) catalyst was prepared by solvothermal method and the details of which has been described in chapter 2 of Section A (section 2.3.2.4). The catalysts were characterized by XRD, O_2-TPD, CV and HR-TEM technique and the detailed characterization procedure is described in chapter 2 of Section A (sections 2.4.1, 2.4.10, 2.4.11, and 2.4.6). The activity of r-GO-MnCoO catalysts for *p*-cresol oxidation was carried out in batch-reactor and experimental procedure is described in Section A (2.5.2.3) of chapter 2.

2.4.2. Results and discussion

2.4.2.1. Catalyst characterization

The graphite powder showed a sharp diffraction line at $2\theta = 26.5^o$ corresponding to a d-spacing of 3.34 Å. (Fig. 2.25) However, graphene oxide (GO) shows the diffraction peak at $2\theta = 11.4^o$ with an increase in d-spacing to 7.5 Å. This is attributed to the oxidation of graphite involving introduction of oxygen containing functionalities [63]. XRD diffractograms of r-GO-MnCoO nanocomposite showed diffraction peaks at $2\theta = 33.4^o$ (103), 39.1^o (004) and 54.6^o (312) corresponding to the tetragonal phase of $CoMn_2O_4$ (JCPDF card no. 77-0471), while the peaks at $2\theta = 19^o$, 31.2^o, 36.7^o, 44.7^o, 59.3^o and 65.2^o, were ascribed to the cubic phase of the Co_3O_4 (JCPDF card No. 74-1657). The diffraction peaks at $2\theta = 31.2^o$, 36.7^o, 44.7^o, 59.3^o and 65.2^o, showed 0.2^o shift towards lower 2θ values as compared to the bare mixed metal oxides (MnCo-MO) (Fig. 2.10A), indicating interaction of r-GO with metal oxides. The average crystallite size of r-GO-MnCoO nanocomposite estimated from the full width half maximum of the (311) diffraction peak by applying the Scherrer equation was about 8 nm which was less than the bare MnCo-MO (10 nm). The broader and less intense XRD diffraction peaks

observed for r-GO-MnCo composite indicates nanocrystalline nature of the prepared catalyst.

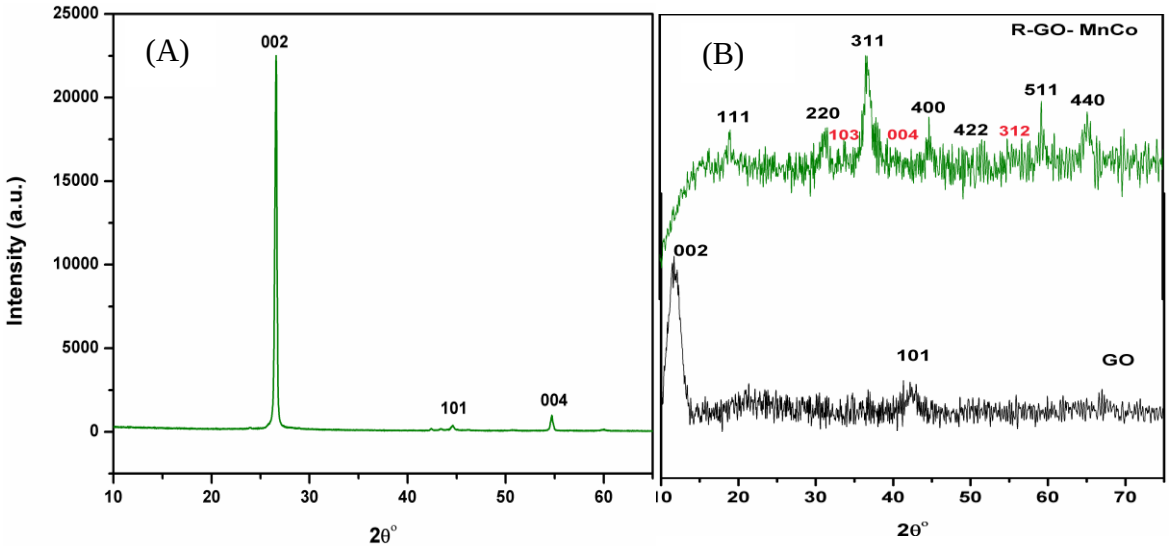

Fig. 2.25. XRD patterns of (A) graphite powder, and (B) r-GO-MnCoO and GO

X-ray photoelectron spectrum of r-GO-MnCoO was used for studying the electronic properties of metal oxide catalysts prepared in combination with GO. In C1s XPS spectrum of GO showed a broad carbon peak that could be fitted satisfactorily to four major peaks after deconvolution as shown in Fig. 2.26a. The peaks at 284.4, 286, 287.5 and 288.7 eV were due to C−C, C−O, C=O and O−C=O species, respectively. XPS of C1s in r-GO−MnCoO nanocomposite (Fig. 2.26b), showed reduction in the intensity of the peaks corresponding to C−O, C=O and O−C=O species as compared to GO, due to the removal of the oxygen containing groups and the recovery of sp^2 carbon network. The percentage distribution of different carbon species in GO and r-GO-MnCoO are shown in Table 2.4. In r-GO–MnCoO nanocomposite, Co $2p_{3/2}$ showed a broad peak that could be fitted satisfactorily to 3 principle peaks and one satellite peak after deconvolution as shown in Fig. 2.26c. The peak at 780 eV was assigned to Co^{3+} of Co_2O_3 while, the peak at 781 eV was assigned to Co^{2+} of $CoMn_2O_4$. Formation of $CoMn_2O_4$ was also confirmed by XRD and HR–TEM results. Another peak at 782.1 eV was also present due to Co^{2+} but from spinel Co_3O_4. A satellite peak at 784 eV was indicative of Co^{2+} in both the spinel Co_3O_4 and $CoMn_2O_4$. All the peaks showed the positive shift towards higher

binding energy (BE) as compared to the bare mixed metal oxides (MnCo-MO) (Fig. 2.12(a)), which was attributed to stronger metal–r-GO interactions that were induced by an increase in the number of defects in r-GO. It also indicates the decrease of electron density and a change in the electronic states of metals leading to the higher valence states. This trend can be interpreted as delocalization of *d* and *p*-orbital electrons of metals and carbon of r-GO, respectively.

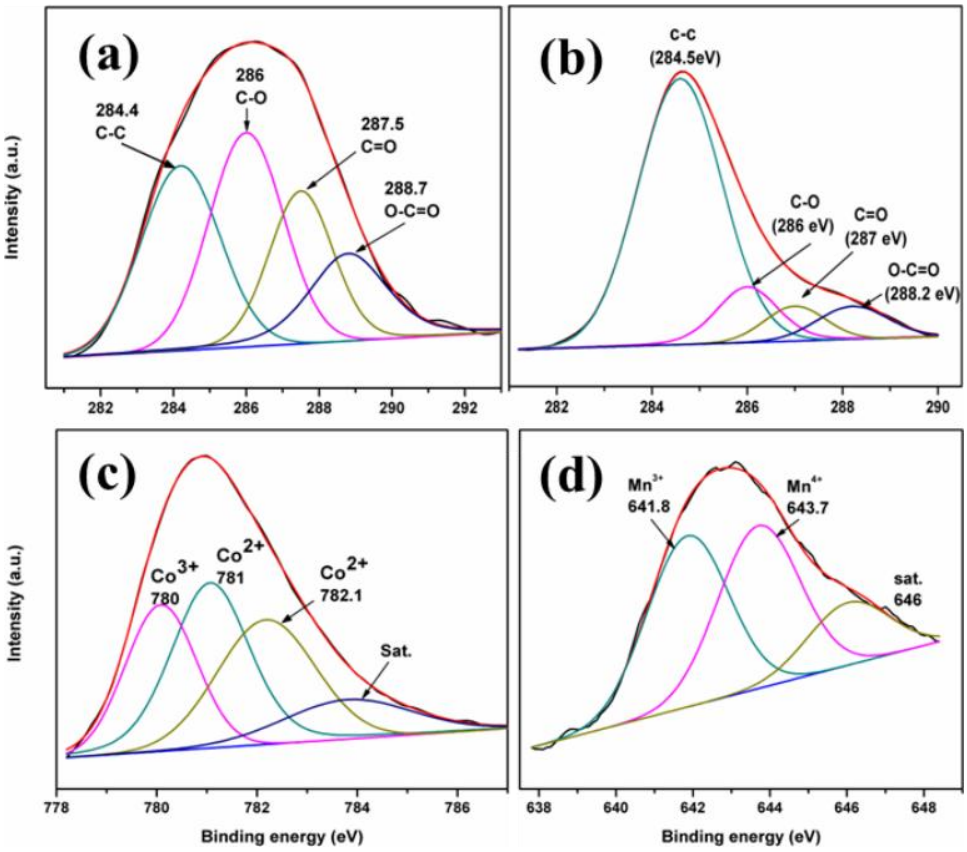

Fig. 2.26. XPS of (a) C 1s of GO, (b) C 1s of RGO−MnCoO, (c) Co $2p_{3/2}$, and (d) Mn $2p_{3/2}$ of r-GO−MnCoO nanocomposite

r-GO–MnCoO catalyst also showed a broad signal of Mn $2p_{3/2}$, which could be fitted satisfactorily to 2 major peaks and a satellite peak after deconvolution, as shown in Fig. 2.24d. The peaks at 641.8 and 643.7 eV, correspond to Mn^{3+} and Mn^{4+}, respectively, while the small peak at 646 eV corresponds to the satellite of Mn^{4+}.

Table 2.4. Percentage distribution of different carbon species

Carbon species in GO			Carbon species in RGO−MnCoO	
Chemical Species	**Binding energy (eV)**	**Area (%)**	**Binding energy (eV)**	**Area (%)**
C−C	284.4	30	284.6	74
C−O	286	33	286	12
C=O	287.5	21	287	7
O−C=O	288.7	16	288.2	7

It is reasonable therefore, to conclude that the Mn exists as Mn^{3+} in $CoMn_2O_4$ spinel oxides. Presence of $CoMn_2O_4$ spinel in r-GO–MnCoO catalyst was also confirmed by XRD diffraction peaks at $2\theta = 33.4^o$ (103). However, the presence of Mn^{4+} indicates the possibility of MnO_2, which we did not observe in XRD due to the peak broadening. The shift in the BE of Mn towards higher values was also observed as compared to bare mixed metal oxides that might be due to the extremely effective delocalized donor–acceptor interactions with the π-system of the r-GO and metal oxide [64]. The manner in which oxygen is bonded to metals, in r-GO–MnCoO nanocomposite can be determined through XPS of oxygen. Deconvolution of the O1s spectrum of r-GO-MnCoO produces three main peaks around 530.3, 532, and 533 eV as shown in Fig. 2.27.

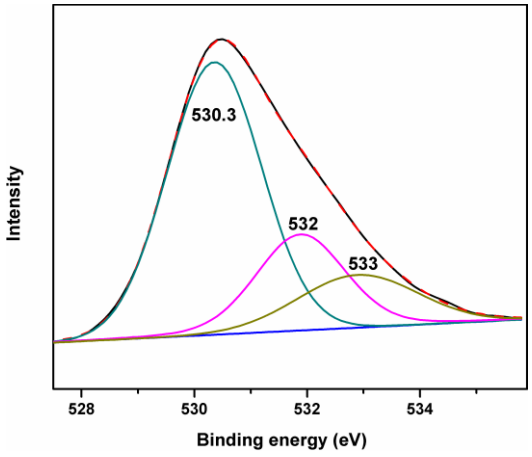

Fig. 2.27. XPS of O1s of r-GO-MnCoO nanocomosite

The peak at lower binding energy (530.3 eV) could be assigned to the oxygen species involved in metal oxide chemical bonds in the composite and must therefore correspond to Co–O and Mn–O bonds respectively [65]. However, the peaks at higher binding energies (532 and 533 eV) were assigned to C−O (oxygen singly bonded to aliphatic carbon) and phenolic (oxygen singly bonded to aromatic carbon) groups, respectively [66].

HR-TEM provides insight into the morphology and detailed structure of the prepared catalysts. Fig. 2.28a reveals that r-GO–MnCoO is a composite material of reduced graphene oxide and mixed metal oxide (MnCo-MO) having uniform nanotubes with size ∼25 nm in length and 6 nm in diameter. The morphology of the mixed oxide did not change after making composite with r-GO, as the bare mixed metal oxide also has the nano rod like morphology (Fig. 2.28b). The lattice fringe pattern of the r-GO–MnCoO nanocomposite is shown in Fig. 2.28c. The dominant exposed planes of r-GO–MnCoO were (103) and (004) with a lattice space of 0.26 nm and 0.22 nm, respectively, which was related with the spinel $CoMn_2O_4$. The other exposed planes were (111) and (400) with a lattice space of 0.46 and 0.20 nm, related with the spinel Co_3O_4. Fig. 2.28d showing the ED patterns of the r-GO–MnCoO nancomposite was used to determine the lattice constants which were in excellent agreement with those obtained from the XRD analysis. The FE-SEM images of the bare mixed oxide and r-GO-MnCo also supported the HR-TEM results. The bare MnCo-MO showed monodisperse nanorod like structure (Fig. 2.29A) and r-GO-MnCoO showed composite nature of material in which nanorods were attached over the surface of reduced graphene oxide (Fig. 2.29B). It has been demonstrated that both vacancies and edges in r-GO were effective trapping centers for metal oxide nanoparticles.

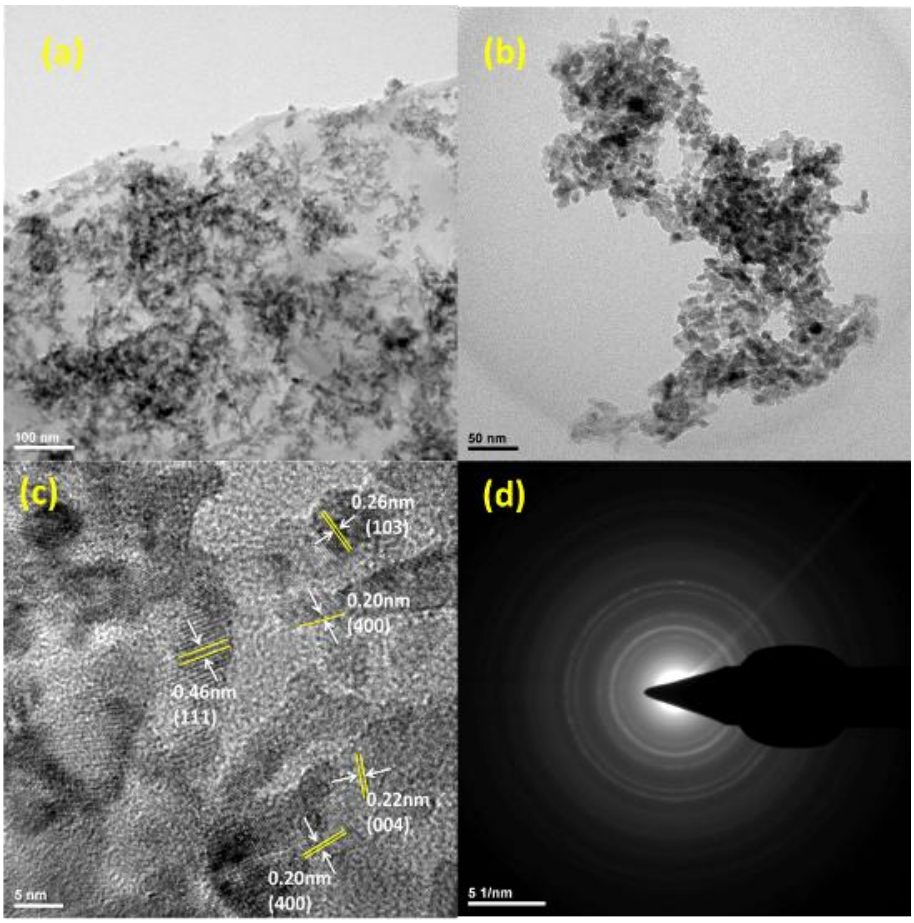

Fig. 2.28. HR-TEM images of (a) r-GO-MnCoO nanocomposite, (b) MnCo-MO, (c) lattice fringe patterns of r-GO-MnCoO and (d) SAED pattern of r-GO-MnCoO

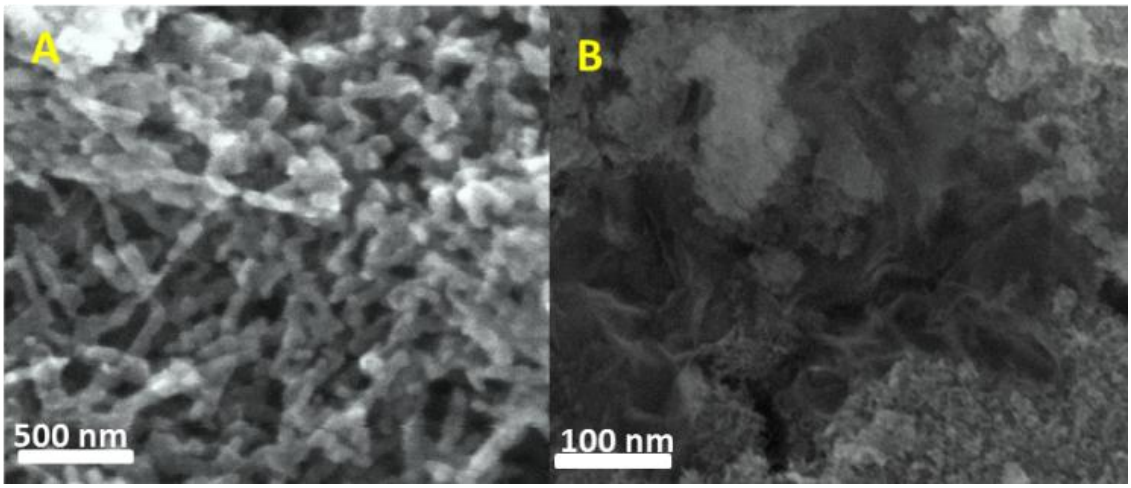

Fig. 2.29. FE-SEM images of (A) MnCo-MO and (B) r-GO-MnCoO

To investigate the types of active oxygen species, O_2-TPD measurement of r-GO–MnCoO nancomposite and MnCo−MO was performed and the results are shown in Fig. 2.30. Four peaks appearing in the TPD, which were designated as peaks α, β, γ and δ, indicated four kinds of oxygen species present in the samples. Generally, the adsorbed oxygen undergoes the following transformations: [67]

$$O_2\,(ad) \rightarrow O^{2-}(ad) \rightarrow O^{-}(ad) \rightarrow O^{2-}(lattice)$$

The physically adsorbed oxygen and O^{2-}(ad) species were desorbed at relatively lower temperature (<300 ^{o}C). In Fig. 2.28, peak α corresponds to O^{2-} (ad) species. The O^{-} species desorbs at higher temperature (> 400 ^{o}C), therefore it is more reasonable to assign β and γ peaks to the desorption of O^{-} species. Besides the three peaks, the lattice oxygen desorbs at a very high temperature (>800 ^{o}C), hence δ-peak could be assigned to the presence of lattice oxygen. In case of r-GO–MnCoO nancomposite β, γ and δ peaks shifted to lower temperatures compared to those in bare MnCo-MO. This suggests that the addition of r-GO into the mixed oxide (MnCo-MO), increased the surface oxygen mobility and facilitated the oxygen desorption from catalyst surface at lower temperatures. This in turn increased the rate of reaction as observed in case of r-GO-MnCoO nanocomposite (Table 2.5).

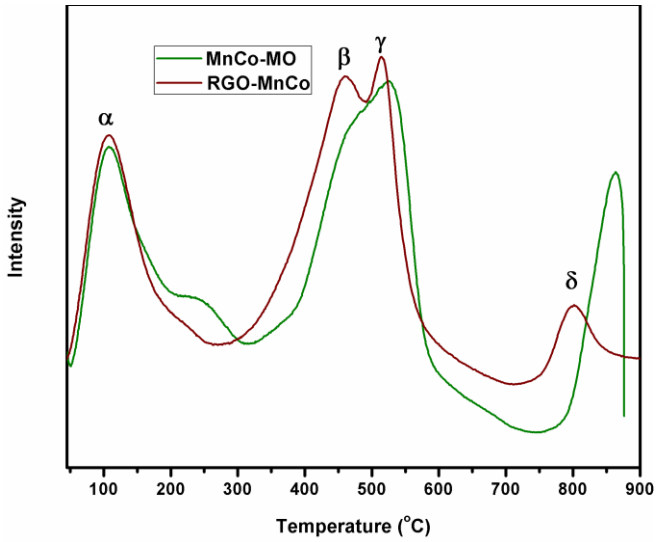

Fig. 2.30. O_2-TPD of bare MnCo-MO and r-GO-MnCoO

The active sites present in r-GO−MnCo catalyst could be approximately estimated by the cyclic voltammetry. Cyclic voltammetry measurements were performed at a scan rate of 100 mV s^{-1} over the potential range of 0–0.8 V in 0.5 M H_2SO_4 solution by using a glassy carbon electrode. Fig. 2.31 shows the plots of current density versus potential for the MnCo-MO and r-GO-MnCoO.

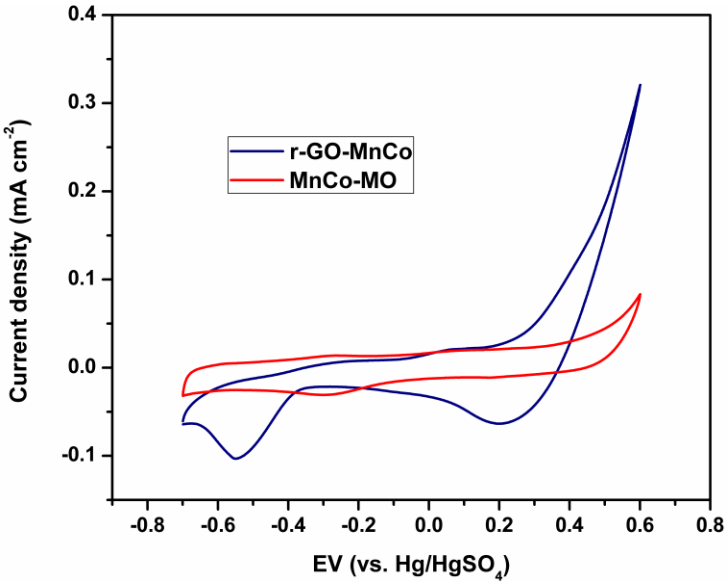

Fig. 2.31. Cyclic voltammetry curve of MnCo-MO and r-GO-MnCoO

From the graph it is clear that, r-GO-MnCoO nanocomposite presents the largest integrated area compared to the bare MnCo-MO, indicating that the redox potential of the nanocomposite has been significantly increased due to the addition of r-GO. The enhancement in redox potential of the r-GO-MnCoO nanocomposite material can be ascribed to the (i) large specific surface area (154 m^2/g) than bare MnCo-MO (85 m^2/g), (ii) smaller particle size (8 nm) and (iii) synergistic effect between the r-GO and MnCoO nanoparticles. Therefore, decrease in particle size increased the active surface that took part in the redox reactions [68]. Both the samples (MnCo-MO and r-GO-MnCoO nanocomposite) showed clearly the presence of oxidation and reduction peaks. In both cases, the first anodic peak in the low potential region (-0.3V) could be assigned to the oxidation of Mn^{2+} to Mn^{3+} or Co^{2+} to Co^{3+} while, the second one at 0.08V was attributed

to the oxidation of Mn^{3+} to Mn^{4+}. Similarly, the cathodic peak present at higher potential (0.2V) could be assigned to the reduction of Mn^{4+} to Mn^{3+} and the second one at lower potential (-0.55V) could be assigned to the reduction of Mn^{3+} to Mn^{2+} or Co^{3+} to Co^{2+}. As compared with the bare MnCo-MO, the substantially negative shift (from -0.28 to -0.55) of the cathodic peak was observed for the r-GO-MnCoO, which indicated the increased electron density of the Co^{2+} and Mn^{2+} species [69]. The reduction peak indicates the reduction ability of oxygen hence, as the potential value shifted to more and more negative value, the oxygen reduction ability increases that led to the higher oxidation ability of r-GO-MnCoO for *p*-cresol to *p*-hydroxybenzaldehyde. Similar study has been reported in case of Mn_3O_4 composite with multi walled carbon nano tubes (MWCNT) [70].

2.4.3. Catalytic activity of r-GO-MnCoO

The performance of different catalysts for *p*-cresol oxidation was studied under the same reaction conditions (Table 2.5). A blank run without catalyst gave only 6% product yield with higher selectivity to PHBAcid (60%). Table 2.5 shows that single component metal oxide catalysts exhibited lower activity than the bimetallic catalysts. r-GO-CoO catalyst was highly selective for PHBAld formation, however, r-GO-MnO catalyst was highly selective for PHBAlc formation. The addition of Mn to the cobalt oxide led to the complete change in the both selectivity patterns as well as catalyst activity. From Table 2.5, it is clear that mixed metal oxide (MnCo-MO) have higher catalytic activity compared with the catalyst with only single metal oxide, regardless, if it is either cobalt or manganese alone as an active phase. The higher activity of the mixed metal oxides was due to the cooperative effect among the metals towards an increment in the mobility of the oxygen as well as stabilizing the more active species. The redox cycles, which also permit the reactivation of the catalyst, are also favoured. Manganese in synergism with cobalt oxide, improves the superficial oxygen at the catalyst surface which is attributed by the high oxygen storage capacity of the manganese [71].

Table 2.5. Catalyst screening for *p*-cresol oxidation

Catalyst	Product Yield (%)	Selectivity (%)			
		PHBAlc	PHBAld	PHBAcid	PHBEth
*WO	6	2	38	60	-
r-GO-CoO	20	-	89	10	1
r-GO-MnO	28	100	-	-	-
MnCo (1:1)	42	1	95	3	1
r-GO-MnCoO (1:1)	71	-	96	3	1
r-GO-MnCoO (1:2)	57	-	97	2	1
r-GO-MnCoO (2:1)	60	1	95	3	1

*WO = without catalyst

Reaction conditions: *p*-cresol (55.5 mmol), NaOH, 155 mmol, catalyst (0.1 g), 100 ^{o}C, methanol (50 mL), oxygen pressure (2.7 bar), time 1 h.

MnCo mixed oxide, its composite with reduced graphene oxide (r-GO−MnCoO), showed higher catalytic activity (71% product yield) than those of bare mixed metal oxide (MnCo-MO) (42% product yield) without affecting the selectivity pattern. This observation suggests that GO doped catalyst was efficient for sustainable redox couple formation ($M^{n+} \leftrightarrow M^{n+1}$). The increment in the oxidising ability of the catalyst by increasing the electron density on to the metal oxide via delocalization of electrons through π–π interaction of r-GO was supported from CV analysis. Also GO based catalysts provide the anchoring sites for the aromatic substrate through π–π interaction, which increased the probability of adsorption of substrate on the catalyst surface, leading to higher reaction rate.

For *p*-cresol oxidation, catalysts were prepared by varying the ratios of cobalt and manganese with the constant amount of GO (1%). Among the screened catalysts, we observed that 1:1 ratio of cobalt and manganese showed highest catalytic activity (71%

product yield) than r-GO-MnCoO (1:2) and r-GO-MnCoO (2:1) showed 57% and 60 % product yield, respectively. As r-GO−MnCoO (1:1) catalyst gave better performance, further work on the optimization of the reaction parameters was carried out using this catalyst. Fig. 2.32 shows the time course of catalytic performances in the *p*-cresol oxidation with r-GO−MnCo catalyst at 2.7 bar of oxygen. It showed that product yield increased from 68 to 71% by extending the reaction time from 30 to 60 min. Thereafter, decrease in the product yield occurred from 71 to 60% in 2 hours that might be due to the formation of tarry product, which was detected only after the reaction was continued for longer reaction time (2 hours). However, selectivity to the PHBAlc, PHBAcid and PHBEth throughout the reaction remained only < 6% and selectivity for PHBAld was >96%.

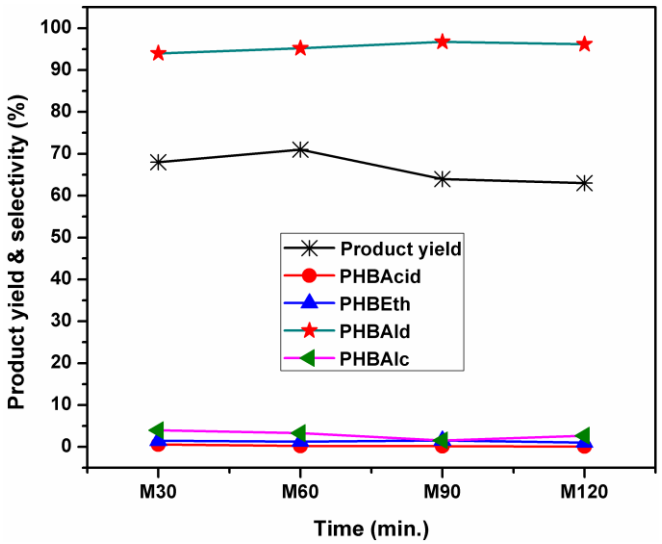

Fig. 2.32. Effect of time on oxidation of *p*-cresol. Reaction conditions: *p*-cresol (55.5 mmol), NaOH, 155 mmol, catalyst (0.1 g), 100 ^{o}C, methanol (50 mL), oxygen pressure (2.7 bar), time 2 h.

The stability of r-GO−MnCoO catalyst for *p*-cresol oxidation was established by its recycle experiments in the following way. After the first oxidation run with fresh r-GO−MnCoO nanocomposite, the catalyst was filtered and washed several times with methanol, dried at 100 ^{o}C for 6 h and reused for the subsequent runs by adding a fresh charge. Fig. 2.33 shows that the catalyst was found to retain its activity even after 3rd

recycle experiment without any loss of activity indicating the high efficiency of r-GO−MnCoO catalyst for the oxidation of *p*-cresol.

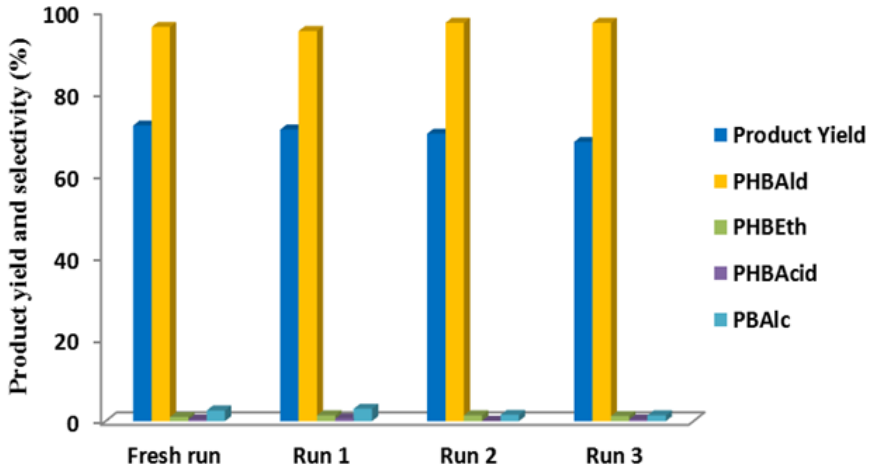

Fig. 2.33. Recycle study for *p*-cresol oxidation. Reaction conditions: *p*-cresol (55.5 mmol), NaOH, 155 mmol, r-GO-MnCoO catalyst (0.1 g), 100 ^{o}C, methanol (50 mL), oxygen pressure (2.7 bar), time 1 h.

To check the stability of the r-GO−MnCo catalyst and verify that the reaction is truly heterogeneously catalysed, a leaching experiment was also carried out. After 30 min. of reaction, the catalyst was filtered and the reaction was left to continue for another 30 min. in which the product yields measured before and after catalyst filtration were 68% and 66.5% respectively, confirming that the reaction was heterogeneous and also that there was no metal leaching under the reaction conditions.

2.5. MANGANESE OXIDE CATALYST FOR VERATRYL ALCOHOL OXIDATION

Activity of the catalyst strongly depends upon their morphology, crystallite size and the planes that they expose. These in turn depend upon the catalyst preparation methods [72]. During the past decade, the rapid development in the material science offers an opportunity to prepare metal and/or metal oxide with tailored structural characteristics for efficient catalysis. Among these, the most critical factor in the exposure of specific crystal

plane which would be responsible for type of number of active sites required in a particular reaction [32]. Our earlier studies on Co_3O_4 material showed that [111] plane of the cobalt oxide was highly active, due to presence of higher concentration of Co^{3+}, facilitating for the oxidation reaction [17]. From this perspective it was thought appropriate to compare two methods viz. co-precipitation and solvothermal for the preparation of mesoporous manganese and cobalt oxides as these are versatile oxidation catalysts.

Co-precipitation is a simple and well known method, reported for the synthesis of most of the metal oxides [73] whereas, solvothermal method has been reported as a powerful tool to synthesize the nanomaterial with the reproducibility, quality, and quantitative yield [74]. The prepared catalysts were evaluated for liquid phase oxidation of veratryl alcohol (Scheme 2.4). Manganese oxide used for this purpose because of its non-toxic and cost-efficient nature, and also predominantly due to the wide range of stable oxidation states (+2, +3, +4, and +7) of this element [75]. In heterogeneous catalysis, manganese oxides are used as selective catalysts for a wide range of catalytic applications, including ozone decomposition, [76] photocatalytic oxidation of organic pollutants, [77] nitric oxide reduction, [78] selective oxidation of carbon monoxide, [79] volatile organic compounds and decomposition of hydrogen peroxide [80]. Recently, spinel Co_3O_4, prepared by simple co-precipitation method has been reported for selective oxidation of veratryl alcohol in water by using molecular oxygen. The catalyst showed the highest conversion of 85% with 96% selectivity to veratryl aldehyde in 7 hours [73]. As a derivative of coniferyl alcohol (a primary monomer of lignin), veratryl alcohol bearing a 3,4-dimethoxy group has been extensively studied for understanding the chemistry of lignin valorization and exploring efficient transformation routes. Veratryl alcohol can be oxidized into veratraldehyde by using different catalysts such as enzymes 81], noble and non-noble metal porphyrin complexes, [82] cobalt (salen) complexes [83] and Co-zeolitic imidazolate frameworks (Co-ZIFs) [84]. However, catalyst preparation in these processes are complicated, require a longer reaction time, reaction mediated by the base (pyridine or NaOH), and suffer a major problem in its recovery and recyclability. Hence, it is of great practical importance to develop a simplified preparation protocol for

low cost, highly active and reusable heterogeneous catalysts with the capability to form strong redox couple and give controlled oxidation products.

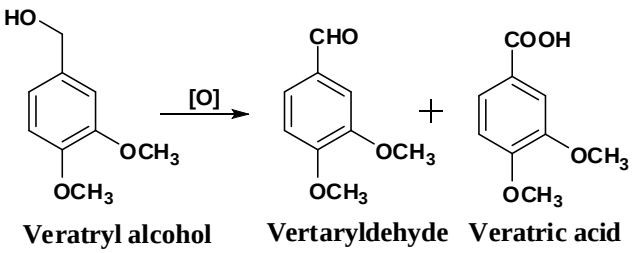

Scheme 2.4. Aerobic oxidation of veratryl alcohol

2.5.1. Experimental

Manganese oxide catalyst prepared by solvothermal and co-precipitation methods was designated as MnOx-ST and MnOx-CP, respectively. The details of catalyst preparation have been described in chapter 2 of Section A (section 2.3.2.2). The catalysts were characterized by XRD, XPS, H_2-TPR, and HR-TEM technique and the detailed characterization procedure is described in chapter 2 of Section A (sections 2.4.1, 2.4.8, 2.4.10, and 2.4.6). The activity of catalysts for veratryl alcohol oxidation was carried out in batch-reactor and experimental procedure is described in chapter 2 of Section A (2.5.2.4).

2.5.2. Results and discussion

2.5.2.1. Catalyst characterization

Manganese oxides crystallize in numerous different structures with varied proportions of Mn ions (Mn^{2+}, Mn^{3+}, and Mn^{4+}). The phases of the manganese oxide synthesized by solvothermal and co-precipitation methods were characterized by X-ray diffraction, and the result was shown in Fig. 2.34. The diffraction peaks of the sample obtained from solvothermal method have the mixed phases of the monoclinic Mn_5O_8 (JCPDS 39-1218) and tetragonal hausmannite of Mn_3O_4. The Mn_3O_4 can be considered as a spinel structure

of $Mn^{2+}(Mn^{3+})_2O_4$, in which Mn^{2+} and Mn^{3+} occupy the tetrahedral and octahedral site of the spinel respectively [85]. In case of solvothermal method, the octahedral Mn^{3+} ions in Mn_3O_4 might be oxidized to Mn^{4+} preferentially over Mn^{2+}, which leads to the formation of $(Mn^{2+})_2(Mn^{4+})_3O_8$, i.e. the Mn_5O_8 [86]. The formation of Mn_5O_8 was further proved by X-ray photoelectron spectroscopy. However, all the diffraction peaks of the sample obtained from co-precipitation were well matched to the pure tetragonal phase of Mn_3O_4 (JCPDS 24-0743).

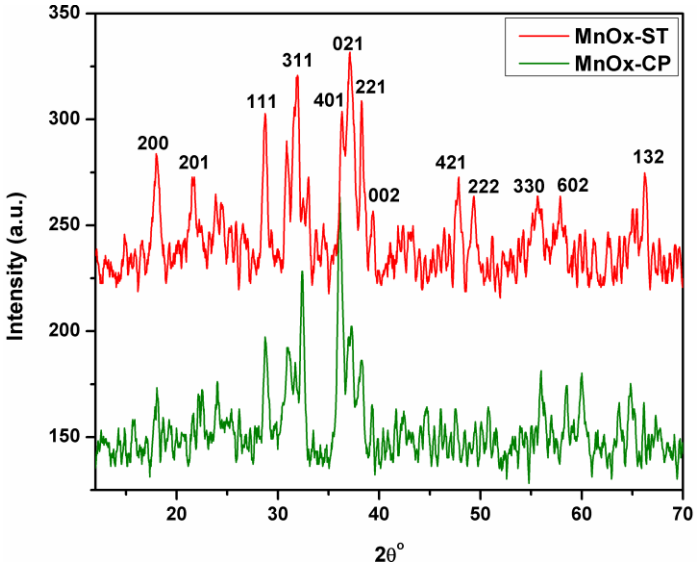

Fig. 2.34. XRD patterns of MnOx-ST and MnOx-CP

HR-TEM images of MnOx-ST and MnOx-CP are shown in Fig. 2.35. The oxides obtained from the solvothermal method shown hexagonal nanoplate like morphology having particles size in the range of 8-12 nm whereas the oxide obtained from co-precipitation gave mixed morphology of nano-octahedron and spherical shape with the particles size in the range of 18-34 nm. The clear lattice fringe pattern illustrates that the hexagonal nanoplates are highly crystalline in nature (Fig. 2.35b). The six side facets of the hexagonal nanoplates are well-defined. The inter-planer spacing was about 0.28 nm and 0.49 nm, which corresponds to the [311] and [200] planes of Mn_5O_8 and Mn_3O_4 respectively. Presences of these oxides phase were also confirmed from XRD of MnOx-ST. However, inter-planer spacing in case of MnOx-CP was 0.27 nm, which corresponds

to the [103] plane of Mn_3O_4. The field-emission scanning electron microscopy (FE-SEM) images in Fig. 2.36 (a–d) shows general morphology of the MnOx-ST, exhibited many hexagonal plates are agglomerate together into larger petal-like sheets and gave spherical flower like appearance. The surface of the nano-hexagonal plates appeared highly porous.

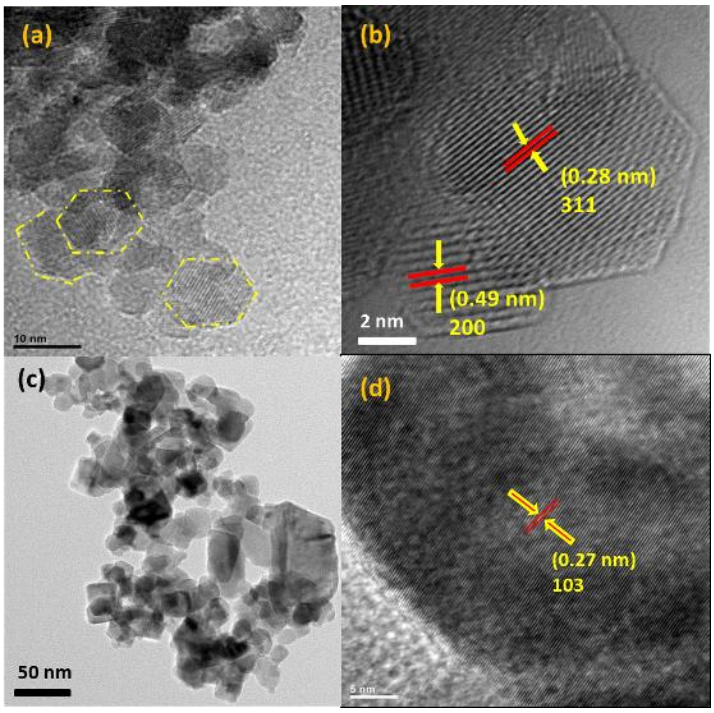

Fig. 2.35. HR-TEM images of (a) MnOx-ST, (b) lattice fringe pattern of MnOx-ST, (c) MnOx-CP, and (d) lattice fringe pattern of MnOx-CP

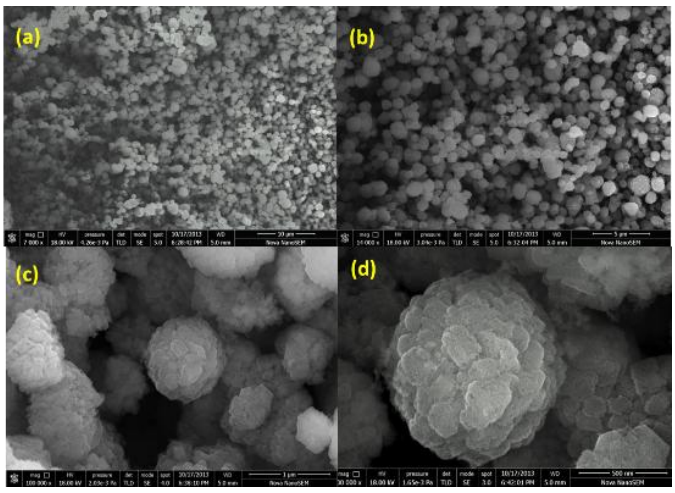

Fig. 2.36 a-d. FE-SEM images of MnOx-ST

The porous nature and specific surface area of the MnOx-ST were investigated by nitrogen adsorption-desorption measurements. Fig. 2.37 shows the isotherm and the corresponding Barrett–Joyner–Halenda (BJH) pore size distribution curves. The isotherm can be categorized as type IV, with a distinct hysteresis loop located in the range 0.3–1 p/p_o, which is a characteristic of mesoporous materials [87]. The hysteresis feature of the MnOx-ST at the relative pressure of 0.3-1 was classified as the H3 loop, suggesting the presence of crystalline metal oxide aggregates of sheet like shapes [88]. From the pore size distribution curve, it was observed that MnOx-ST showed a bimodal pore distribution that is micropores in the region of 0.5-2 nm and mesopores ranging from 2 to 5 nm. The BET specific surface area of the MnOx-ST was 97 m^2 g^{-1}, which is much higher than that of the MnOx-CP (the surface area is only 32.3m^2 g^{-1}).

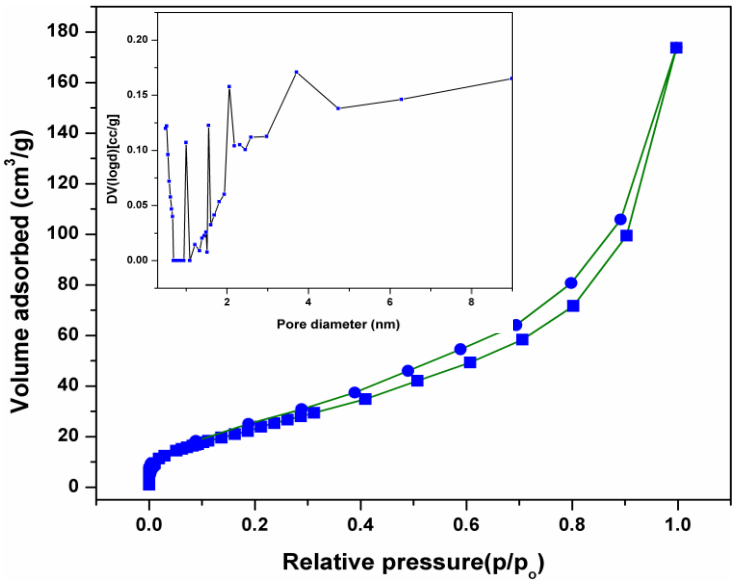

Fig. 2.37. N_2-adsorption-desorption isotherm for MnOx-ST and inset pore size distribution of MnOx-ST

H_2-TPR profiles of MnOx-ST and MnOx-CP are shown in Fig. 2.38. In general, the TPR patterns strongly depend on the morphology and oxidation states of the sample. The TPR profiles of both the samples showed two steps reduction process. MnOx-CP showed the low temperature peak around 322 ^oC, corresponds to the reduction of Mn^{3+} ions located in octahedral holes in the hausmannite lattice. As the Mn_3O_4 particles were firstly get

reduced, the formed relatively stable MnOx species would cover the inner core, hindering further reduction, and they were totally reduced to MnO at high temperature (459 ^{o}C). The broad and unsymmetrical nature of the second reduction peak during reduction of MnO_x to MnO was due to the mixed morphology of MnOx-CP as also suggested by HR-TEM. However, MnOx-ST, showed two very sharp and symmetrical reduction peaks at higher temperature relative to MnOx-CP (343 ^{o}C and 494 ^{o}C respectively). The low temperature reduction peak (343 ^{o}C) was attributed to the reduction of Mn_5O_8 to Mn_3O_4 and the high temperature reduction peak (494 ^{o}C) was corresponds to the reduction of Mn_3O_4 to the MnO [89]. The H_2 consumption of MnOx-CP was 4.46 mmol/g, which is similar to the theoretical amount of Mn_3O_4 (4.37 mmol/g) [90]. However, in case of MnOx-ST, H_2 consumption was 6.7 mmol/g, which are much higher than the theoretical amount of Mn_3O_4, indicating the increase of oxygen species due to the formation of Mn_5O_8 along with Mn_3O_4.

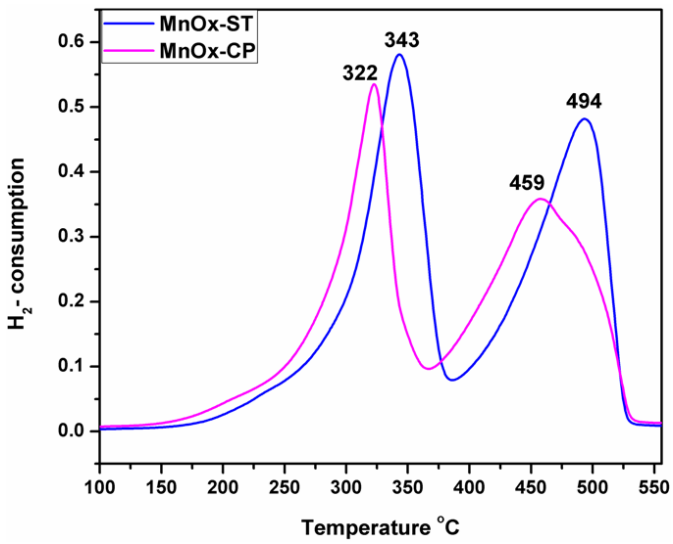

Fig. 2.38. H_2-TPR profiles of MnOx-ST and MnOx-CP

X-ray photoelectron spectroscopy (XPS) was used to monitor the different oxidation states of manganese in MnOx-ST. For the MnOx-ST, a broad, strong Mn $2p_{3/2}$ peak was observed suggesting Mn ion exists as more than one oxidation states. A broad signal of Mn $2p_{3/2}$ could be fitted satisfactorily to two principal peaks and two satellite peaks after deconvolution, as shown in Fig. 2.39A. The peaks at 641.5 and 642.7 eV correspond to

Mn^{3+} and Mn^{4+}, respectively, whereas the peaks at 644 and 646.2 eV correspond to the satellite of Mn^{3+} and Mn^{4+} ions respectively, which originated from the charge transfer between the outer electron shell of the ligand and the unfilled 3d shell of Mn during the creation of the core-hole in the photoelectron process [91]. Existence of two types of manganese oxide (Mn_3O_4 and Mn_5O_8) in MnOx-ST was also proved by the XRD and TPR results.

The manner in which oxygen is bonded to metal in metal oxides can be determined through XPS of oxygen. The chemical environment of oxygen in metal oxide catalysts played an important role in their catalytic properties. In the O1s spectrum of MnOx-ST, three peaks were fitted satisfactorily after deconvolution, attributed to three types of oxygen species as shown in Fig. 2.39B. The peak at BE of 529–530 eV was ascribed to the lattice oxygen while, the peak at BE of 531–532 eV was ascribed to defective oxides or surface oxygen ions with low coordination. Another peak at a higher BE (above 533 eV) corresponded to adsorbed water [45].

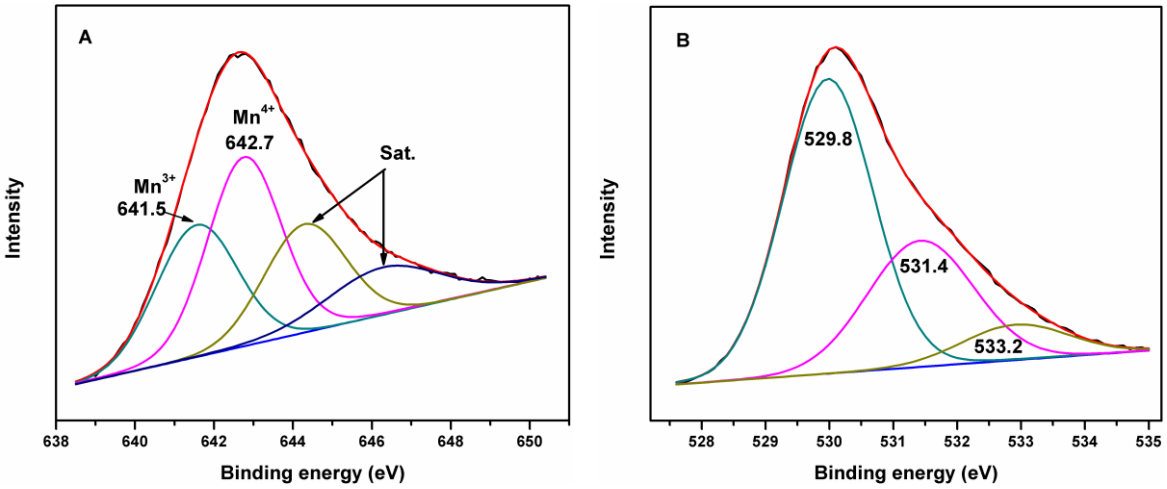

Fig. 2.39. XPS spectra of (A) Mn $2p_{3/2}$ and (B) O 1s of MnOx-ST catalyst

2.5.3. Activity measurement

The activity of manganese and cobalt oxide, prepared by solvothermal (ST) and co-precipitation (CP) methods was compared for the liquid-phase air oxidation of veratryl alcohol and the results are shown in Fig. 2.40. All the reactions were performed under optimum reaction conditions in the absence of a base.

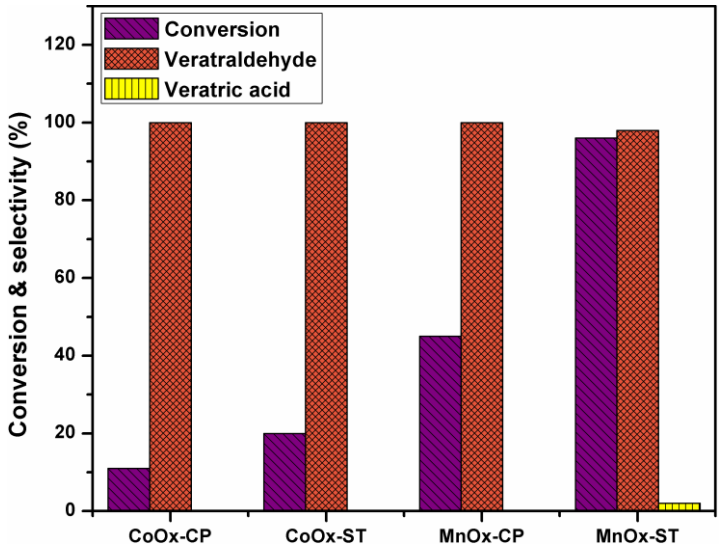

Fig. 2.40. Catalysts screening for veratryl alcohol oxidation. Reaction conditions: veratryl alcohol 0.5 g, catalyst (0.1 g), 120 ^{o}C, acetonitrile (60 mL), air pressure (21 bar), time 90 min

Among the screened catalysts, cobalt oxide catalysts showed significantly lower conversion (CoOx-CP =11% and CoOx-ST =20%) than manganese oxide catalysts (MnOx-CP = 45% and MnOx-ST =96%) with almost similar selectivity to veratryl aldehyde (100%). The difference in activity was due to the following reasons: i) Mn has higher oxygen storage capacity, ii) wide range of oxidation states, and iii) it has strong reduction potential (−1.19) than Co (−0.27), which facilitate the oxidation process. In addition to this, the catalysts prepared by solvothermal method were found to be highly reactive than the catalysts prepared by co-precipitation method. The cause of higher activity of these solvothermal catalysts was due to the morphological and structural differences that enable fabrication of catalytic materials with exposing more reactive crystal planes, and favouring the oxidation reactions. As it was also confirmed from HR-TEM results; MnOx-CP has mixed morphology of octahedron and spherical shape with (103) plane while, MnOx-ST having uniform regular hexagonal nanoplates with (200) and (331) planes. In spite of this the catalysts prepared by solvothermal method have higher surface area (97 m^2/g) and lower particles size (8-12 nm) measured from BET and HR-TEM, respectively. This could be the also reason for higher activity of the

solvothermal catalyst. In spite of this, highly porous nature of the material, as confirmed by FE-SEM and HRTEM, might be also responsible for the higher activity of the catalysts. As porous materials enhanced the diffusion rate of the substrate and product through it and avoids the deactivation the catalyst by pore blocking.

The effect of reaction time on veratryl alcohol conversion and selectivity to veratraldehyde was studied with MnOx-ST catalyst under optimised reaction conditions and the results are shown in Fig. 2.41. The conversion of veratryl alcohol increased from 48 to 96% with an increase in reaction time from 15 min. to 2 hours. As we observed from Fig. 8, the rate of conversion of veratryl alcohol, after 60 min. became slow and the decrease in veratraldehyde selectivity began to start. Hence, 90 min. reaction time was found to be the optimum time, at which conversion was 90% and selectivity to veraraldehyde was 98%.

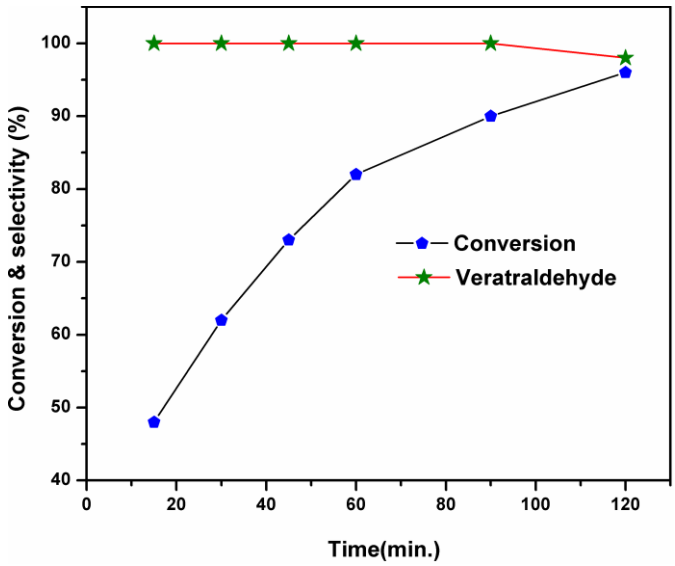

Fig. 2.41. Effect of reaction time on veratryl alcohol oxidation. Reaction conditions: veratryl alcohol 0.5 g, catalyst (0.1 g), 120 ^{o}C, acetonitrile (60 mL), air pressure (21 bar), time 2 h.

The stability of catalyst for veratryl alcohol oxidation was established by its recycle experiments in the following way. After the first oxidation run with fresh MnOx-ST, the catalyst was filtered and washed several times with methanol, dried at 100 ^{o}C for 2h and reused for the subsequent runs by adding a fresh charge. Fig. 2.42 shows that the catalyst

was found to retain its activity even after 3rd recycle experiment with minor loss in activity (from 90% conv. to 85%) indicating the high efficiency of MnOx-ST catalyst for the oxidation of veratryl alcohol. To check the stability of the MnOx-ST catalyst and verify that the reaction is heterogeneously catalyzed, a leaching experiment was also carried out. After 1h of reaction, the catalyst was filtered and the reaction was left to continue for another 1h, in which the conversion measured before and after catalyst filtration were 81% and 82.5% respectively, thus practically the same within experimental error, showing that the reaction was heterogeneous and also indicating that there was no metal leaching under the reaction conditions.

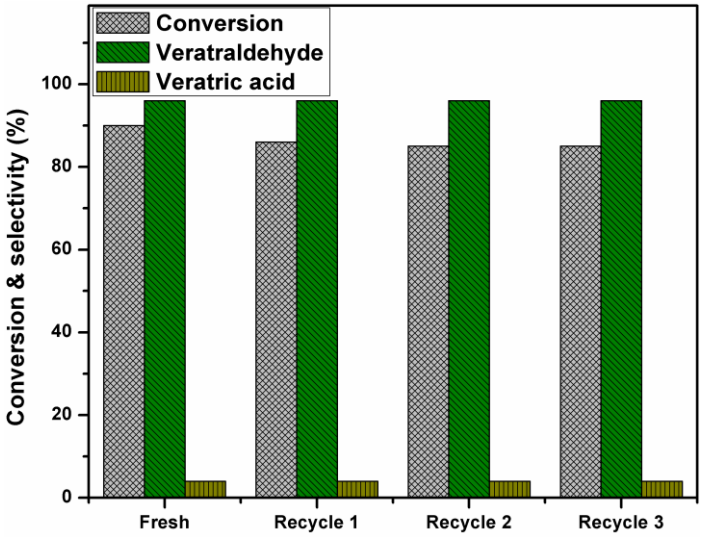

Fig. 2.42. MnOx-ST catalyst recycling studies. Reaction conditions: veratryl alcohol 0.5 g, catalyst (0.1 g), 120 ^{o}C, acetonitrile (60 mL), air pressure (21 bar), time 90 min.

2.6. CONCLUSIONS

Various cobalt and manganese based catalysts viz. Co_3O_4, Mn_3O_4, mixed oxides of Co-Mn and reduced graphene oxide supported Co-Mn oxide were prepared by solvothermal as well as co-precipitation methods. Comparison between commercial and prepared Co_3O_4 catalyst showed that the latter was a better catalyst for vanillyl alcohol oxidation in the presence of NaOH. The higher activity of the prepared Co_3O_4 was due to its smaller crystallite size (14 nm), higher surface area (87 m^2 g^{-1}) and higher exposure of Co^{3+}

species over the Co_3O_4 surface as confirmed by CV measurement. In case of mixed metal oxide (MnCo-MO) catalyst prepared by solvothermal method, doping of manganese into the Co_3O_4 framework led to the formation of tetragonal $CoMn_2O_4$ and Mn_3O_4 spinel phases. The existence of $CoMn_2O_4$ was confirmed by XRD, HRTEM and XPS. TPR also gave additional evidence of the formation of mixed Co–Mn oxides by the appearance of a reduction peak at a higher temperature (637 ^oC). TPO of a mixed oxide exhibited higher oxygen adsorption capacity than that of a single metal oxide, which was the reason for the higher activity of the mixed oxide catalyst for aerobic oxidation of vanillyl alcohol, in the absence of a base. Reduced graphene oxide (r-GO) proved to be highly efficient support for the mixed metal oxide (MnCo-MO) catalyst in liquid phase oxidation of *p*-cresol to *p*-hydroxybenzaldehyde. The structural characteristics of r-GO provided the active sites for adsorbing *p*-cresol through π-π stacking interaction. In addition, r-GO support caused transfer of charge leading to the enhancement in redox potential of the MnCo mixed oxide. Both these factors led to the increase in rate of oxidation giving 71% product yield with >96% selectivity to *p*-hydroxybenzaldehyde in 1 h for *p*-cresol oxidation under mild reaction conditions. Solvothermal and co-precipitation methods of preparation for manganese and cobalt oxide catalysts were compared for veratryl alcohol oxidation. Between these, manganese oxide catalyst prepared by solvothermal method (MnOx-ST) exhibited higher activity than that of Co_3O_4 catalyst. MnOx-ST catalyst was also found to be more efficient (90% conversion) than MnOx-CP (49% conversion) with almost complete selectivity to veratraldehyde.

2.7. REFERENCES

1. M. B. Gawande, R. K. Pandey, R. V. Jayaram, *Catal. Sci. Technol.* 2012, 2, 1113.
2. R. J. Farrauto, C. H. Bartholomew, Fundamentals of Industrial Catalytic Processes; John Wiley and Sons: Chichester, UK, 2003.
3. G. Centi, F. Cavani, Selective Oxidation by Heterogeneous Catalysis; Kluwer Publication: New York, 2001.
4. B. K. Hodnett, Heterogeneous Catalytic Oxidation: Fundamental and Technological Aspects of the Selective and Total Oxidation of Organic Compounds; John Wiley & Sons: New York, 2000.
5. G. C. Bond, Catalysis by Metals, Academic Press, New York, 1962.
6. U. Menon, V. V. Galvita, G. B. Marin, *J. Catal.* 2011, 238, 1.
7. E. W. McFarland, H. Metiu, *Chem. Rev.* 2013, 113, 4391.
8. S. Todorova, H. Kolev, J. P. Holgado, G. Kadinov, C. Bonev, R. Pereńíguez, A. Caballero, *Appl. Catal. B* 2010, 94, 46.
9. D. A. Aguilera, A. Perez, R. Molina, S. Moreno, *Appl. Catal. B* 2011, 104,144.
10. V. S. Kshirsagar, A. C. Garade, K. R. Patil, R. K. Jha, C. V. Rode, *Ind. Eng. Chem. Res.* 2009, 48, 9423.
11. R. K. Marella, C. K. P. Neeli, S. R. R. Kamaraju, D. R. Burri, *Catal. Sci. Technol.* 2012, 2, 1833.
12. T. Mitsudome, A. Noujima, T. Mizugaki, K. Jitsukawa, K. Kaneda, *Adv. Synth. Catal*, 2009, 351, 1890.
13. S. E. Davis, M. S. Ide, R. J. Davis, *Green Chem.* 2013, 15, 17.
14. A. C. Garade, N. S. Biradar, S. M. Joshi, V. S. Kshirsagar, R. K. Jha, C. V. Rode, *Appl. Clay Sci.* 2011, 53, 157.
15. V. S. Kshirsagar, A. C. Garade, K. R. Patil, M. Shirai, C. V. Rode, *Top. Catal.* 2009, 52, 784.
16. V. S. Kshirsagar, S. Vijayanand, H. S. Potdar, P. A. Joy, K. R. Patil, C. V. Rode, *Chem. Lett.* 2008, 37, 310.
17. A. Jha, C. V. Rode, *New. J. Chem.* 2013, 37, 2669.

18. J. F. Stanzione, J. M. Sadler, J. J. La Scala, K. H. Reno, R. P. Wool, *Green Chem.* 2012, 14, 2346.
19. A. D. Bulam, S. V. Nekrasov, B. V. Passet, V. G. Foshkin, *J. Appl. Chem.* 1988, 61, 859.
20. S. R. Rao, G. A. Ravishankar, *J. Sci. Food Agric.* 2000, 80, 289.
21. Y. Chang, M. Zhang, L. Xia, J. Zhang, G. Xing, *Materials* 2012, 5, 2850.
22. J. Hu, Y. Hu, J. Mao, J. Yao, Z. Chena, H. Li, *Green Chem.* 2012, 14, 2894.
23. Y. Zhang, X. Li, X. Cao, J. Zhao, *Res. Chem. Intermed.* 2013 DOI: 10.1007s11164–013–1039-x.
24. R. Xu, H. C. Zeng, *J. Phys. Chem. B* 2003, 107, 12643.
25. P. Arnoldy, J. A. Moulijn, *J. Catal.* 1985, 93, 38.
26. W. J. Xue, Y. F. Wang, P. Li, Z. Liu, Z. P. Hao, C. Y. Ma, *Catal. Commun.* 2011, 12, 1265.
27. J. Xu, P. Gaob, T. S. Zhao, *Energy Environ. Sci.* 2012, 5, 5333.
28. Z. P. Xu, H. C. Zeng, *J. Mater. Chem.* 1998, 8, 2499.
29. F. Svegl, B. Orel, I. Grabec-Svegl, V. Kaucic, *Electrochim. Acta*, 2000, 45, 4359.
30. B. Barton, C. G. Logie, B. M. Schoonees, B. Zeelie, *Org. Process Res. Dev.* 2005, 9, 62.
31. I. Fernández, J. R. Pedro, A. L. Roselló, R. Ruiz, I. Castro, X. Ottenwaelder, Y. Journaux, *Eur. J. Org. Chem.* 2001,1235.
32. A. Jha, T. N. Chandole, C. V. Rode, 2013, *Communicated to RSC Advances.*
33. A. Jha, K. R. Patil, C. V. Rode, *ChemPlusChem.* 2013, 78, 1384.
34. J. Trawczyński, B. Bielak, W. Miśta, *Appl. Catal. B Env.* 2005, 55, 277.
35. M. Baldi, E. Finocchio, F. Milella, G. Busca, *Appl. Catal. B* 1998, 16, 43.
36. X. Xie, Y. Li, Z. Liu, M. Haruta, W. Shen, *Nature Lett.* 2009, 458, 746.
37. F. Wang, G. Yang, W. Zhang, W. Wu, J. Xu, *Chem. Commun.* 2003, 1172.
38. J. Li, X. Liang, S. Xu, J. Hao, *Appl. Catal. B* 2009, 90, 307.
39. F. Morales, D. Grandjean, A. Mens, F. M. F. de Groot, B. T. Weckhuysen, *J. Phys. Chem. B* 2006, 110, 8626.

40. C. D. Wagner, J. F. Moulder, L. E. Davis, W. M. Riggs, Handbook of X-ray Photoelectron Spectroscopy, 1st ed (Ed.: G. E. Muilenberg), Perkin-Elmer Corporation, Eden Prairie, 1979.
41. B. Tan, K. J. Klabunde, P. M. A. Sherwood, *J. Am. Chem. Soc.* 1991, 113, 855.
42. S. Ponce, M. A. Pena, J. L. G. Fierro, *Appl. Catal. B* 2000, 24, 193.
43. D. Delimaris, T. Ioanides, *Appl. Catal. B* 2008, 84, 303.
44. C. Liu, Q. Liu, L. Bai, A. Dong, G. Liu, S. Wen, *J. Mol. Catal. A* 2013, 370, 1.
45. J. Li, S. Xiong, X. Lia, Y. Qian, *J. Mater. Chem.* 2012, 22, 23254.
46. M. Ferrandon, J. Carnö, S. Järås, E. Bjçrnbom, *Appl. Catal. A* 1999, 180, 141.
47. J. Luo, M. Meng, X. Li, *J. Catal.* 2008, 254, 310.
48. W. J. Xue, Y. F. Wang, P. Li, Z. Liu, Z. P. Hao, C. Y. Ma, *Catal. Commun.*2011, 12, 1265.
49. C. Shi, Y. Wang, A. Zhu, B. Chen, C. Au, *Catal. Commun.* 2012, 28, 18.
50. K. Jirátová, J. Mikulová, J. Klempa, T. Grygar, Z. Bastl, F. Kovanda, *Appl. Catal. A* 2009, 361, 106.
51. S. A. Hosseini, D. Salari, A. Niaei, F. Deganello, G. Pantaleo, P. Hojati, *J. Environ. Sci. Health Part A* 2011, 46, 291.
52. R. A. Sheldon, R. A. van Santen, Catalytic Oxidation: Principles and Applications, World Scientific, Singapore, 1995, page.12.
53. J. E. Huheey, E. A. Keiter, R. L. Keiter, O. K. Medhi, Inorganic Chemistry: Principles of Structure and Reactivity, Pearson Education, Upper Saddie River, NJ, 2008, page. 489.
54. A. Jha, S. H. Patil, A. P. C. Ribeiro, C. A. N. Castro, K. R. Patil, A. Coronas, C. V. Rode, 2013, *Communicated to ACS Applied Material & Interfaces*.
55. H. V. Borgaonkar, B. C. Sampatraj, *J. Chem. Tech. Biotechnol.* 1984, 34, 107.
56. A. Thoer, G. Denis, *Synth. Commun.* 1988, 18, 2095.
57. S. N. Sharma, B. C. Sampatraj, *J. Chem. Tech. Biotechnol*. 1990, 49, 141.
58. B. F. Machadoab, P. Serp, *Catal. Sci. Technol.* 2012, 2, 54.
59. V. Georgakilas, M. Otyepka, A. B. Bourlinos, V. Chandra, N. Kim, K. C. Kemp, P. Hobza, R. Zboril, K. S. Kim, *Chem. Rev*. 2012, 112, 6156.

60. S. Wang, X. Wang, S. P. Jiang, *Phys. Chem. Chem. Phys.* 2011, 13, 6883.
61. C. Xu, X.Wang, J. Zhu, *J. Phys. Chem. C* 2008, 112, 19841.
62. D. A. Aguilera, A. Perez, R. Molina, S. Moreno, *Appl. Catal. B Environ.* 2011, 104, 144.
63. S. Stankovich, D. Dikin, R. Piner, K. Kohlhaas, A. Kleinhammes, Y. Jia, Y. Wu, S. Nguyen, R. Ruoff, *Carbon* 2007, 45, 1558.
64. J. Zhu, A. Holmen, D. Chen, *ChemCatChem*, 2013, 5, 378.
65. Z. S. Wu, W. Ren, L. Wen, L. Gao, J. Zhao, Z. Chen, G. Zhou, F. Li, H. M. Cheng, *Nano* 2010, 4, 3187.
66. D. Chen, H. Feng, J. Li, *Chem. Rev.* 2012, 112, 6027.
67. Y. Z. Wang, Y. X. Zhao, C. G. Gao, D. S. Liu, *Catal Lett.* 2008, 125, 134.
68. J. Zhu, A. Holmen, D. Chen, *ChemCatChem* 2013, 5, 378.
69. J. Xu, P. Gao, T. S. Zhao, *Energy Environ. Sci.* 2012, 5, 5333.
70. M. Biswal, V. V. Dhas, V. R. Mate, A. Banerjee, P. Pachfule, K. L. Agrawal, S. B. Ogale, C. V. Rode, *J. Phys. Chem. C* 2011, 115, 15440.
71. Q. Zhang, X. Liu, W. Fan, Y. Wang, *Appl. Catal. B Environ.* 2011, 102, 207.
72. H. Topsøe, *J. Catal.* 2003, 216, 155.
73. V. R. Mate, M. Shirai, C. V. Rode, *Catal. Commun.* 2013, 33, 66.
74. Y. Xia, Y. J. Xiong, B. Lim, S. E. Skrabalak, *Angew. Chem. Int. Ed.* 2009, 48, 60.
75. N. N. Tušar, S. Jank, R. Gläser, *ChemCatChem*, 2011, 3, 254.
76. Y. Xi, C. Reed, Y. K. Lee, S. T. Oyama, *J. Phys. Chem. B*, 2005, 109, 17587.
77. H. Caot, S. L. Suib, *J. Am. Chem. Soc.* 1994, 116, 5334.
78. A. Patela, P. Shuklaa, J. Chena, T. E. Ruffordb, V. Rudolpha, Z. Zhu, *Catal. Today*, 2013, 212, 38.
79. J. Xu, Y. Q. Deng, Y. Luo, W. Mao, X. J. Yang, Y. F. Han, *J. Catal.* 2013, 300, 225.
80. S. C. Kima, W. G. Shim, *Appl. Catal. B Env*. 2010, 98, 180.
81. M. Diaz-Gonzalez, T. Vidal, T. Tzanov, *Appl. Microbiol. Biotechnol*. 2011, 89, 1693.
82. C. Crestini, A. Pastoni, P. Tagliatesta, *J. Mol. Catal. A: Chem*. 2004, 208, 195.

83. J. J. Bozell, B. R. Hames, D. R. Dimmel, *J. Org. Chem*. 1995, 60, 2398.
84. J. Zakzeski, A. D. Ebczak, P. C. A. Bruijnincx, B. M. Weckhuysen, *Appl. Catal., A* 2011, 394, 79.
85. Z. Tian, P. M. Kouotou, N. Bahlawane, P. H. Ngamou, *J. Phys. Chem. C* 2013, 117, 6218.
86. J. Pike, J. Hanson, L. Zhang, S. W. Chan, *Chem. Mater*. 2007, 19, 5609.
87. A. Jha, A. C. Garade, S. P. Mirajkar, C. V. Rode, *Ind. Eng. Chem. Res*. 2012, 51, 3916.
88. K. Kaneko, *J. Memb. Sci*. 1994, 96, 59.
89. A. A. Mirzaei, H. R. Shaterian, M. Habibi, G. J. Hutchings, S. H. Taylor, *Appl Catal A.* 2003, 253, 499.
90. Q. F. Deng, T. Z. Ren, Z. Y. Yuan, *Reac. Kinet. Cat.* 2013, 108, 507.
91. C. C. Li, L. Mei, L. B. Chen, Q. Li, T. H. Wang, *J. Mater. Chem*. 2012, 22, 4982.

Chapter 3

Summary and conclusions

In this thesis, a detailed study on developing various non-noble catalytic systems, their characterization and evaluation for the industrially important hydroxyalkylation and liquid phase oxidation reactions has been carried out. Section A deals with solid acid catalysts developed for hydroxyalkylation reactions of various phenolic compounds with an aldehyde or a ketone. A variety of solid acid catalysts developed in this work are: (i) phosphotungstic acid (PTA) impregnated on different supports like MCM-41 and montmorillonite for hydroxyalkylation of phenol with phthalic anhydride to give phenolphthalein, (ii) sulphonic acid graphated magnetically separable solid acid catalysts for hydroxyalkylation of guaiacol to give selectively vanillin alcohol and (iii) metal cations exchanged montmorillonite clay for *p*-Cresol hydroxyalkylation to give 2, 2'-methylenebis (4-methylphenol) [DAM]. Scetion B of the thesis includes the development of non-noble metal oxide catalysts for liquid phase oxidations of phenolic compounds some of which are considered to be the sub-structures of lignin. The products of these oxidations are valuable intermediates and/or end products used in flavoring or perfumery industries. The major outcome of the thesis was the understanding of structure-activity correlation through detailed catalyst characterization and activity evaluation studies. The main conclusions of this work are summarized below.

- Three different solid acid catalysts developed for hydroxyalkylation reactions were: PTA/MCM-41, SO_3H-Fe_3O_4@MCM-41 and metal cation exchanged montmorillonite catalyst was developed with both Brönsted and Lewis acid sites which mainly contributed to give highest selectivity of 91% to phenolphthalein. The same catalyst was also found to be highly efficient for the hydroxyalkylation reaction of p-cresol and formaldehyde to give DAM. In another attempt, water tolerant magnetically separable solid acid catalyst SO_3H-Fe_3O_4@MCM-41was developed for guaiacol hydroxyalkylation to give vanillyl alcohol. The acidity of the catalyst was due to $–SO_3H$ functionalization confirmed by FT-IR and TGA studies. Third category of solid acid catalysts developed was montmorillonite clay incorporated with metal cations among which Al-mont showed the highest Brönsted acidity. This was due to polarization of interlayer water molecules by

highly charged Al^{3+} cations. Because of highest acidity and delamination, Al-mont gave the highest p-cresol conversion and almost completes selectivity to DAM. The recyclability of this catalyst was also proved up to 8 times.

- Four different catalysts developed for liquid phase oxidations include mono – metallic Co and Mn oxides as well as mixed oxides of both the metals. These were prepared by solvothermal as well as co-precipitation methods between which mixed oxides of Co and Mn prepared by solvothermal method exhibited the highest activity for oxidation of vanillyl alcohol to vanillin. Formation of tetragonal $CoMn_2O_4$ and MnO_2 spinel phase was established by XRD,XPS and HR-TEM. A very novel catalyst for the oxidation of *p*-cresol to *p*-hydroxybenzaldehyde developed was the composite of r-GO and mixed metal oxide (MnCo). The structural characteristics of r-GO provide active sites for *p*-cresol adsorption through π-π stacking. Also, r-GO caused charge transfer leading to the enhancement in redox potential of MnCo mixed oxide. For veratryl alcohol oxidation to aldehyde, MnOx preapered by solvotheraml method gave higher activity than that of both MnOx and Co_3O_4 prepared by co-precipitation method.

List of Publications

Research paper published in peer reviewed journals

1. **A. Jha**, A. C. Garade, S. P. Mirajkar, C. V. Rode, MCM-41 supported phosphotungstic acid for the hydroxyalkylation of phenol to phenolphthalein. *Ind. Eng. Chem. Res.* 2012, 51, 3916−3922.

2. **A. Jha**, C. V. Rode, Highly selective liquid-phase aerobic oxidation of vanillyl alcohol to vanillin on cobalt oxide (Co_3O_4) nanoparticles. *New J. Chem.* 2013, 37, 2669-2674.

3. **A. Jha**, A. C. Garade, M. Shirai, C.V. Rode, Metal cation-exchanged montmorillonite clay as catalysts for hydroxyalkylation reaction. *Appl. Clay Sci.* 2013, 74,141–146.
4. **A. Jha**, C. R. Patil, A. C. Garade, C. V. Rode, Magnetically separable single-site Ti-Fe_3O_4@MCM-41 catalyst for selective epoxidation of olefins. *Ind. Eng. Chem. Res.* 2013, 52, 9803−9811.
5. **A. Jha**, K. R. Patil, C. V. Rode, Mixed Co-Mn oxide catalyzed selective aerobic oxidation of vanillin alcohol to vanillin in base free conditions. *ChemPlusChem* 2013, 78, 1384–1392.
6. **A. Jha**, D. Mhamane, A. Suryawanshi, S. M. Joshi, S. Ogale, C. V. Rode., Triple nano-composites of $CoMn_2O_4$, Co_3O_4 and reduced graphene oxide for oxidation of aromatic alcohols. 2013, *Communicated to Catalysis Science & Technology*.
7. **A. Jha**, S. H. Patil, A. P. C. Ribeiro, C. A. N. Castro, K. R. Patil, A. Coronas, C. V. Rode, Reduced graphene oxide composite with redoxible MnCo-oxide for *p*-cresol oxidation using molecular oxygen. 2013, *Communicated to ACS Applied Material & Interfaces*.
8. **A. Jha**, T. N. Chandole, C. V. Rode, Solvothermal synthesis of mesoporous manganese oxide with enhanced catalytic activity for veratryl alcohol oxidation. 2013, *Communicated to RSC Advances*.

9. A. C. Garade, V. S. Kshirsagar, **A. Jha**, C.V. Rode, Structure–activity studies of dodecatungstophosphoric acid impregnated bentonite clay catalyst in hydroxyalkylation of *p*-cresol. *Catal. Commun.* 2010, 11, 942–945.
10. V. R. Mate, **A. Jha**, U. D. Joshi, K. R. Patil M. Shirai, C. V. Rode, Effect of preparation parameters on characterization and activity of Co3O4 catalyst in liquid phase oxidation of lignin model substrates. 2013, *Communicated to Appl. Catal. A: Gen.*

Posters/Oral presentation for national/international symposium

1. **Ajay Jha**, C. V. Rode, "Effect of activity tuning of montmorillonite clay on the activity of hydroxyalkylation of *p*-cresol".

   Poster presented in Chemical Constellation Cheminar-2012, organized by NIT-Jalandhar, India, September 2012.

2. **Ajay Jha**, C. V. Rode, "PTA/MCM 41 as a solid acid catalyst for phenolphthalein synthesis".

   Poster presented in National seminar on recent advances in synthetic chemistry and nanomaterials, organized by Shivaji University, Kolhapur-2012. (**Best Poster award**).

3. **Ajay Jha**, Ajit C. Garade, C. V. Rode, "Synthesis of Phenolphthalein by using solid acid catalysts".

   Poster presented in Science Day, organized by CSIR-NCL, India, February 2010.

4. Ajit C. Garade, **Ajay Jha**, C. V. Rode, "Acidity tuning of fumed silica for the hydroxyalkylation of phenol to bisphenol".

   Poster presented in International Workshop on Nanotechnology& Advanced Functional Materials (NTAFM-09), organized by Material Research Society of India (Pune Chapter) & Indian Institute of Science Education & Research, Pune (India), 2009.

5. **Ajay Jha**, C. V. Rode, "Magnetically separable catalyst for olefin epoxidation reaction".

   Poster presented in Science Day, organized by CSIR-NCL, India, February 2012.